A Novel, Hierarchically Developed Surface Kinetics for Oxidation and Reforming of Methane and Propane over Rh/Al_2O_3

Zur Erlangung des akademischen Grades eines
DOKTORS DER NATURWISSENSCHAFTEN

(Dr. rer. nat.)
Fakultät für Chemie und Biowissenschaften
Karlsruher Institut für Technologie (KIT) - Universitätsbereich
genehmigte

DISSERTATION

von

MSc.Chem.Eng. CANAN KARAKAYA

aus

ARDAHAN, Türkei

Dekan: Prof. Martin Bastmeyer
Referent: Prof. Olaf Deutschmann
Korreferent: Prof. Jan-Dierk Grunwaldt
Tag der mündlichen Prüfung: 21 Dezember 2012

Elif Ipek´e….
Sevgilerimle.

Abstract

This thesis focuses on the development of a surface reaction mechanism for oxidation of H_2 and CO, water-gas shift (WGS) as well as reverse water-gas shift (R-WGS) reactions and partial/total oxidation and steam/dry reforming of methane and propane over Rh/Al_2O_3 catalyst. The study aims at providing a better understanding of the reaction kinetics of synthesis gas production.

A stagnation-flow reactor set-up has been developed and constructed to study the reaction kinetics of various gas fuels (e.g., H_2, CO, CH_4, C_2H_6, C_3H_8) and evaporated liquids (e.g., water, ethanol, methanol, iso-octane). The reactor configuration facilitates one-dimensional (1D) modeling of coupled diffusive and convective transport within the gas-phase boundary layer with detailed heterogeneous chemistry model. As a result, well-defined boundary conditions are created, and heat and mass transport effects are eliminated from the kinetic model. Boundary-layer composition profiles of the species are measured by using a micro-probe sampling technique. Gas-phase concentrations of the species are simultaneously analyzed by MS and FTIR.

The stagnation disk is coated with a Rh/Al_2O_3 catalyst by spin-spray technique. Light microscopy (LM), scanning electron microscopy (SEM), and transmission electron microscopy (TEM) are applied for the determination of the physical properties of the catalyst to reveal the interaction between the support and the active phase. A new CO chemisorption TPD technique is developed for the measurement of the catalytically active surface area of the stagnation disk.

The experiments are conducted in the stagnation-flow reactor following a hierarchical approach in the development of suitable kinetic model for oxidation and reforming of light hydrocarbons. All possible reaction paths of partial oxidation and reforming of methane and propane are considered. The complexities of the systems are augmented by increasing the complexity of fuel type and reactant composition. H_2 oxidation, CO oxidation, preferential oxidation of CO, WGS, R-WGS, catalytic partial oxidation (CPOx), steam reforming (SR), and dry reforming (DR) of CH_4 and C_3H_8 reactions are investigated. The reactions are examined under varying fuel composition and over a wide range of temperature. For each case, the reaction temperature is chosen so that only heterogeneous reactions occur and that gas-phase reactions can be neglected. Furthermore, ignition studies are conducted to understand the adsorption and desorption behavior of the species (H_2, CO, CH_4, C_2H_6 and C_3H_8). Numerical simulations are performed using the CHEMKIN SPIN and DETCHEM^{STAG} codes.
The obtained data are used to assist in the development of an elementary-step-like surface reaction mechanism based on the mean-field approximation. Thermodynamic consistency is ensured. The applicability of the reaction mechanism is shown by simulation of different continuous-flow reactor models from different research groups using DETCHEM^{CHANNEL} software.

Kurzfasssung

Kern dieser Arbeit ist die Entwicklung eines Oberflächenreaktionsmechanismus für die Oxidation von Wasserstoff und CO, die Wasser-Gas-Shift-Reaktion (WGS) und ihre Umkehrung (R-WGS) sowie für die katalytische Verbrennung, Partialoxidation (CPOx), Dampf- und Trockenreformierung von Methan und Propan über Rh/Al_2O_3-Katalysatoren. Ziel ist dabei ein verbessertes Verständnis der Reaktionskinetik der Synthesegas-Produktion.

Ein Staupunktströmungsreaktor wurde entwickelt, um die Reaktionskinetik verschiedener gasförmiger Brennstoffe (H_2, CO, CH_4, C_2H_6, C_3H_8) sowie verdampfter Flüssigkeiten (Wasser, Ethanol, Methanol, Iso-Oktan) zu untersuchen. Die Reaktorgeometrie ermöglicht eine 1D-Modellierung der Gasphasen-Grenzschicht unter Berücksichtigung der heterogen-katalytischen chemischen Reaktionen sowie der konvektiven und diffusiven Transportprozesse in der Gasphase. Aufgrund wohldefinierter Randbedingungen sind keine zusätzlichen Annahmen bezüglich wärme- und stofftransportlimitierender Prozesse erforderlich. Die Konzentrationsprofile in der Grenzschicht werden mit Hilfe einer Mikrosonde vermessen. Die Analyse der Stoffzusammensetzung erfolgt durch simultane Messung mit MS und FTIR.

Die Beschichtung der Staupunktprobe mit Rh/Al_2O_3 erfolgt durch die Spin-Spray-Technologie. Lichtmikroskopie (LM), Rasterelektronenmikroskopie (REM) und Transmissionselektronenmikroskopie (TEM) werden zur Charakterisierung der physikalischen Eigenschaften des Katalysators herangezogen, um die Struktur von Träger und aktiver Phase sichtbar zu machen. Ein neues TPD-Verfahren zur Bestimmung des chemisorbierten CO wurde entwickelt, mit dem die aktive katalytische Oberfläche der Staupunkprobe bestimmt wird.

Die Experimente im Staupunktreaktor bauen in der Weise aufeinander auf, wie sie durch ein hierarchisches Modell der Oxidation und Reformierung leichter Kohlenwasserstoffe beschrieben werden. Alle möglichen Reaktionspfade der Partialoxidation und der Reformierung von Methan und Propan werden berücksichtigt. Die Komplexität des Reaktionsnetzwerks nimmt mit steigender Komplexität des Brennstoffes und der Produktzusammensetzung zu. Oxidation von Wasserstoff und CO, die bevorzugte Oxidation von CO sowie WGS, R-WGS, CPOx, Dampf- und Trockenreformierung von CH_4 und C_3H_8 werden untersucht. Dabei werden die Brennstoffzusammensetzung und die Temperatur variiert. Die Reaktionstemperatur wurde jeweils so gewählt, dass nur Oberflächenreaktionen berücksichtigt werden müssen und Gasphasenreaktionen ausgeschlossen werden können. Weiterhin wird der Light-Off beobachtet, um die Adsorptions-/Desorptions-Kinetik der Spezies H_2, CO, CH_4, C_2H_6 und C_3H_8 zu verstehen. Numerische Simulationen werden mit den Programmen CHEMKIN SPIN und DETCHEM^{STAG} ausgeführt.

Anhand der gemessenen Daten wird ein elementarer Oberflächenreaktionsmechanismus im Rahmen der Mean-Field-Näherung entwickelt. Thermodynamische Konsistenz wird gewährleistet. Zur Validierung des Reaktionsmechanismus werden Messwerte aus Strömungsreaktorexperimenten verschiedener Gruppen mit Ergebnissen aus Simulationen mit DETCHEM^{CHANNEL} verglichen.

CONTENTS

1. INTRODUCTION

Enormous efforts have been made recently in science and technology to optimize the chemical processes for better utilization of feed stocks via environmental friendly processes [1]. Among others natural gas is the most abundant fuel with its main component being over 80 vol.% CH_4 [2]. Although oil is expected to be replaced by natural gas in the future, the utilization of gas is facing several problems. Natural gas sources are mostly located at remote places and because of the possible leakages; transportation of the gas through thousands of kilometers of pipelines does not fulfill the expectations of low cost and safety. These problems can be eliminated by gas-to-liquid technologies where natural gas is mainly converted to higher liquid hydrocarbons [2, 3].

A major step in gas-to-liquid technologies is the conversion of natural gas to synthesis gas (a mixture of H_2 and CO). The synthesis gas can be utulized as a feed stock for ammonia synthesis and for the production of synthetic liquid fuels (such as methanol) by Fisher-Tropsch synthesis [4-6]. Moreover, the produced synthesis gas can be used for on-board or stationary power generation by fuel cell applications [7-9]. Furthermore, synthesis gas is used in conventional vehicles internal engines to decrease the pollutant emissions during the start-up time when the catalytic converters do not work because of their operating temperatures are not reached yet. The driving force behind using the feedstocks via more environmentally friendly and efficient technologies requires converting higher hydrocarbons and oxygenated fuels (i.e. propane, ethanol, iso-octane) to synthesis gas so that they can directly be used in auxiliary power units (APU) applications [1, 10].

Catalytic partial oxidation and reforming of methane are efficient ways of producing synthesis gas and have been studied on an industrial and academic level. Methane can mainly be converted to synthesis gas via catalytic partial oxidation (CPOx), steam reforming (SR), autothermal reforming (ATR) and dry reforming (DR) [11-14].

CPOx of CH_4 has been studied extensively since the early 1940s [15]. Today, the technology can be used for medium to small-scale on-board or stationary synthesis gas applications by using compact reactors. Overall synthesis gas yield of > 90 % can be achieved in miliseconds (10^{-2}-10^{-4} s) of contact time in the reactor without carbon formation [14, 16-18].

$$\mathrm{CH_4} + \frac{1}{2}\mathrm{O_2} \rightarrow \mathrm{CO} + \mathrm{H_2} \qquad \Delta_\mathrm{R}\mathrm{H}^\mathrm{o} = -35.9\ \mathrm{kJ/mol} \qquad 1.1$$

However, the strong competition between the total oxidation and the partial oxidation results in high operating temperatures, above 1173 K, at which homogeneous gas-phase reactions may take place leading to the occurrence of flames, which causes hot spots in the catalytic region and results in explosions. Besides, high operating temperature may cause a thermal stress on the catalyst and its support as well as catalyst deactivation because of active metal sintering.

Among the technologies which are currently applicable, synthesis gas production via catalytic steam reforming is one of the most applied commercial technologies leading to high synthesis gas selectivity. Furthermore, the process is favoured because it enables using low cost materials, e.g., Ni as a catalyst at high temperatures, above 1173 K [19].

$$CH_4 + H_2O \leftrightarrow CO + 3H_2 \qquad \Delta_R H^o = +206.2\ \mathrm{kJ/mol} \qquad 1.2$$

Although the process efficiency is high, the ratio of H_2/CO is larger (H_2/CO = 3-5) than required (Eq.1.2) for Fisher-Tropsh synthesis [20]. If steam reforming processes are used for gas-to-liquid applications, the reaction is often carried out at high pressure (10-30 bar) in order to avoid an expensive compression. However, high pressure is not favorable since the pressure has a dramatic effect on the methane conversion because of the equilibrium limitations. To overcome this problem, the reaction is carried out at high temperatures with an excess amount of steam which also avoids carbon formation [21]. The process has its drawbacks which are high construction costs and high energy demand due to the endothermicity of the reaction. Because SR requires larger reactor sizes than a CPOx reactor, the applicability of the process to on-board synthesis gas units, such as fuel cells, is also limited. However, this drawback has been overcome in recent years by using micro channel reactors which enables achivening high synthesis gas yield in short contact times in compact reactor configuration [22, 23].

A combination of partial oxidation and steam reforming (autothermal reforming) is realized when steam reforming of methane is carried out in the presence of oxygen (Eq.1.3). The process combines the advantages both processes; steam reforming and partial oxidation. This way, the high energy demand of steam reforming can be decreased and a high synthesis gas yield can be achieved without deactivation of the catalyst [24]. The reaction path can be selected to be under exothermic, endothermic or thermo-neutral conditions depending on the ratio of CH_4-O_2-H_2O [25]. Besides, when using a low steam/carbon ratio (S/C=0.6), carbon formation can be disfavored/avoided and synthesis gas ratio with a H_2/CO = 2, which is suitable for Fischer–Tropsch synthesis, can be produced [26].

$$CH_4 + {}^{x}/_{2}\, O_2 + (1-x)H_2O \rightarrow CO + (3-x)H_2 \qquad \Delta_R H^o = 206.2 - 241.8x\ \mathrm{kJ/mol} \qquad 1.3$$

In recent years the reforming of CH_4 with CO_2 has also been studied in industry and academia. Using CO_2 rather than H_2O is preferable since the process yields low H_2/CO ratios (Eq.1.4), which is suitable for Fisher-Tropsch synthesis reactions. The process also has an advantage of reducing CO_2 which is known as a greenhouse gas [27, 28].

$$CH_4 + CO_2 \rightarrow 2CO + 2H_2 \qquad \Delta_R H^o = +247\ \mathrm{kJ/mol} \qquad 1.4$$

The reaction is highly endothermic and high temperature and operating pressure are needed to achieve high conversion and product yields. However, due to coke deposition and/or sintering of active metal and support phases, these severe operating conditions may cause deactivation of the catalyst [28].

Alternatively, reactors are designed to operate in combination of different reforming or oxidation processes to meet the final processes requirements, i.e., selectivity of H_2, the right ratio of H_2/CO and overall heat management of the reactor. An ATR process is designed as a combination of CPOx and SR. Furthermore, combinations of SR, DR and CPOx processes, in which CH_4, O_2, H_2O and CO_2 are all introduced as reactants also takes place in the industrial applications [21].

On the other hand, product selectivity highly depends on the active metal and its interaction with the support media. An optimum catalyst design requires meeting the expectations of high synthesis gas selectivity, long life time, durability against sintering and coke formation, and also a cost effective design for large scale commercial applications.

Noble metals, such as Rh, Pt, Pd, Ru, and Ir, dispersed on a support material are efficiently used for CPOx and reforming of methane. Product selectivity strongly varies depending on the catalyst. Among others, Pt and Rh are the most effective catalyst. Although Pt yields more total oxidation products than Rh, both catalysts are durable, and suitable for high temperature applications. On the other hand, due to high costs and limited availability, research has also focused on designing non-noble metal-based catalysts for large-scale commercial applications.

In last decades, many attempts have been made to substitute noble metals with alkaline earth metals (Ni, Co, Fe) supported on different oxides (Al_2O_3, MgO, ZrO_2) for reforming reactions. Among those Ni shows a promising catalytic activity and product selectivity for SR and DR reactions carried out at high temperatures (923-1273 K) and pressures (10-30 bar). On the other hand, the reactions promptly result in carbon formation which leads to a deactivation of the catalyst. Although current studies focused on designing new catalysts, those with a small amount of noble metals are used in combination with Ni and Co catalyst to reduce the catalyst costs [21, 29]. Among the other nobel metals, Rh is known as the most effective catalyst for CPOx and reforming of CH_4 and it is mostly used in industrial applications [1, 5, 30].

Today, the challenge of these processes is not only to discover new catalytic materials but also to optimize and advance the catalytic processes for development of cost effective environmentally-friendly technologies [3]. Therefore, it is important to contribute a fundamental understanding of the reaction mechanism over the catalyst (metal) and reveal its interaction with the support at the molecular level [31, 32].

Although the reaction schemes for CPOx and reforming of CH_4 are two separate processes, studies show that, there is not a distinct boundary between these two catalytic processes [33]. Exemplarily, Horn et al. showed that CPOx of CH_4 is a complex process; SR, water-gas shift (WGS) as well as reverse water-gas-shift (R-WGS) reactions may also take place during the reaction [34, 35]. Similarly reverse water-gas reaction takes place during SR of CH_4 [36]. Furthermore, Hanneman et al. resolved the spatial and temperatre profile along the catalyst bed in a plug-flow reactor using in-situ X-ray absorption spectroscopy. They pointed out that change in the structure of the catalyst is also the sign that oxidation and reforming zones exist in the catalyst bed during the partial oxidation of methane [37].

Therefore, a unified surface reaction mechanism is neccessary which involves all possible reaction steps between the the chemical species under consideration and which is valid for a wide range of temperatures and pressures.

The development of a reliable surface reaction mechanism relies on the well-defined concentration and temperature profiles in the catalytic region in which heat and mass transport effects are minimized for an exact computational solution of the chemical and physical properties of reactive flow [35]. Despite its simplicity, disponibility of a laboratory scale fixed-bed flow configuration rector is usually limited for kinetic investigations as the concentration gradients in a few millimetres of the catalyst bed strongly vary due to the exothermic or endothermic nature of the catalytic processes [16, 38]. Although the recent advances in reaction engineering enables understanding the reaction kinetics on the atomic level under realistic conditions, the modeling of heterogeneous and homogeneous chemistry in a two-dimensional (2D) set-up including elementary-step-like reaction mechanisms is quite complex. Therefore simplifying assumptions are usually made to model heat and mass transport effects [39-43].

Alternatively, a stagnation-flow reactor can be used to facilitate 1D modeling of heterogeneous chemistry coupled with diffusive and convective transport within the gas-phase boundary-layer.

This study focuses on the development of a surface reaction mechanism for partial oxidation and reforming of CH_4 and C_3H_8 over Rh/Al_2O_3 catalyst based on the mean-field approximation. Furthermore, the presented reaction mechanism can be used to simulate the $H_2/CO/CO_2/H_2O$ systems (e.g., H_2 and CO oxidation, preferential oxidation of CO and WGS, R-WGS reactions). A stagnation-flow reactor is developed for studying the catalytic chemisty and gas-phase concentration profiles are measured under steady-state conditions (Chapter 3).

A newly-developed CO chemisorption method is presented for charecterization of flat stagnation surface (catalyst) (Chapter 4).

Numerous experiments are carried out in the stagnation-flow reactor under varying fuel composition and over a wide range of temperature (Chapter 5). By following a hierarchical approach, H_2 oxidation, CO oxidation, preferential oxidation of CO in H_2 and O_2 mixtures, water-gas shift and reverse water-gas shift reactions as well as CPOx, SR, and DR of CH_4 are studied consecutively. Catalytic ignition studies are conducted as well to understand the adsorption and desorption kinetics of the reactive species (H_2, CO, CH_4, C_2H_6, C_3H_8). In the development of the mechanism, reaction path analyzes are conducted. The reaction rate parameters are evaluated using the 1D stagnation-flow reactor data. Thermodynamic consistency is ensured between 273-1273 K. The validation of the proposed reaction mechanism is also shown by means of a number of experiments under varying fuel composition and at different temperatures for laboratory-scale continuous-flow reactors and for different catalyst structures. Finally, the reaction mechanism is extended to C_3H_8 by studying CPOx and SR of C_3H_8.

This study can serve as a model for the development of elementary-step-like surface reaction mechanisms with the associated kinetics for complex catalytic reaction schemes. Following the similar hierarchical approach presented here, the surface reaction steps of further C_2, and C_4 species as well as oxygenated fuels and higher hydrocarbons (i.e., ethanol, iso-octane) can be incorporated in to the model. Developed reaction kinetics can be used for optimization of chemical systems that will lead to the development of cost-effective and environmentally friendly technologies for future.

2. FUNDAMENTALS

2.1 Modeling and Simulation of Heterogeneous Reactions

The term catalyst was first introduced by Berzelius in 1835 to refer to a substance that increases the rate of a chemical reaction without being consumed. Today, more than 90 % of industrial processes involve catalysis, e.g., production of fine chemicals, petrochemicals and agrochemicals, and the production of pharmaceuticals, cosmetics, foods, and polymers [44, 45]. Moreover, catalysts are also used in environmentally friendly technologies by helping in the abatement of pollutants and providing cleaner chemicals, synthetic products [45].

As more complex catalytic processes were developed, the emphasis of the research shifted to improving their selectivity. Today's technology requires the development of catalytic processes with optimum operating conditions, that consume less reactants, minimize the need for expensive and difficult separation processes, and create less polluting by-products [46]. An important basis for designing an optimum chemical reactor at the industrial level starts with attempts at understanding the relation between chemical kinetics, heat and mass transport at the molecular level [47].

2.2 Reaction Kinetics

A chemical reaction is a series of molecular level processes that lead to transformations of one species to another by re-arrangement or exchange of atoms. The general reaction equation can be expressed as

$$\sum_i v'_{ik} A_i \rightarrow \sum_i v''_{ik} A_i \quad . \tag{2.1}$$

with the stoichiometric coefficients of v'_{ik} and v''_{ik} for species of reactant or product A_i. The rate of formation or consumption of a species in a chemical reaction is called *reaction rate*. For the species i, the rate equation can be expressed as

$$\frac{dc_i}{dt} = (v''_{ik} - v'_{ik}) k_f \prod_i c_i^{a'_{ik}} \quad . \tag{2.2}$$

In this equation, c_i is the concentration of species i, k_f is the reaction rate coefficient and a'_{ik} is the reaction order with respect to species i.

For elementary-step reactions in which every reaction step is an equilibrium reaction and written in pairs of forward and reverse reaction steps, a'_{ik} is equal to stoichiometric coefficient of species i (v'_{ik}) whereas for global rate equations, the order of the reaction may vary. For the forward reaction rate, the rate coefficient k can be expressed by the Arrhenius model (Eq.2.3)

$$k_{\mathrm{f}_k} = \mathrm{A}_k T^{\beta_k} \exp\left[\frac{-E_{a_k}}{RT}\right] \quad . \tag{2.3}$$

Here, A_k is the pre-exponential factor, β_k is the temperature exponent and E_{a_k} is the activation energy.

For surface reactions, pressure has no direct effect on the rate coefficients, whereas for gas-phase reactions, an additional pressure dependency of the rate coefficient is necessary for dissociation and recombination reactions [43].

Reaction steps occurring on a gas-solid interface at the microscopic level basically involve adsorption, surface reactions, desorption and diffusion steps. These processes are briefly summarized in Figure 2.1. The processes are exemplarily shown on a catalyst with pellet structure.

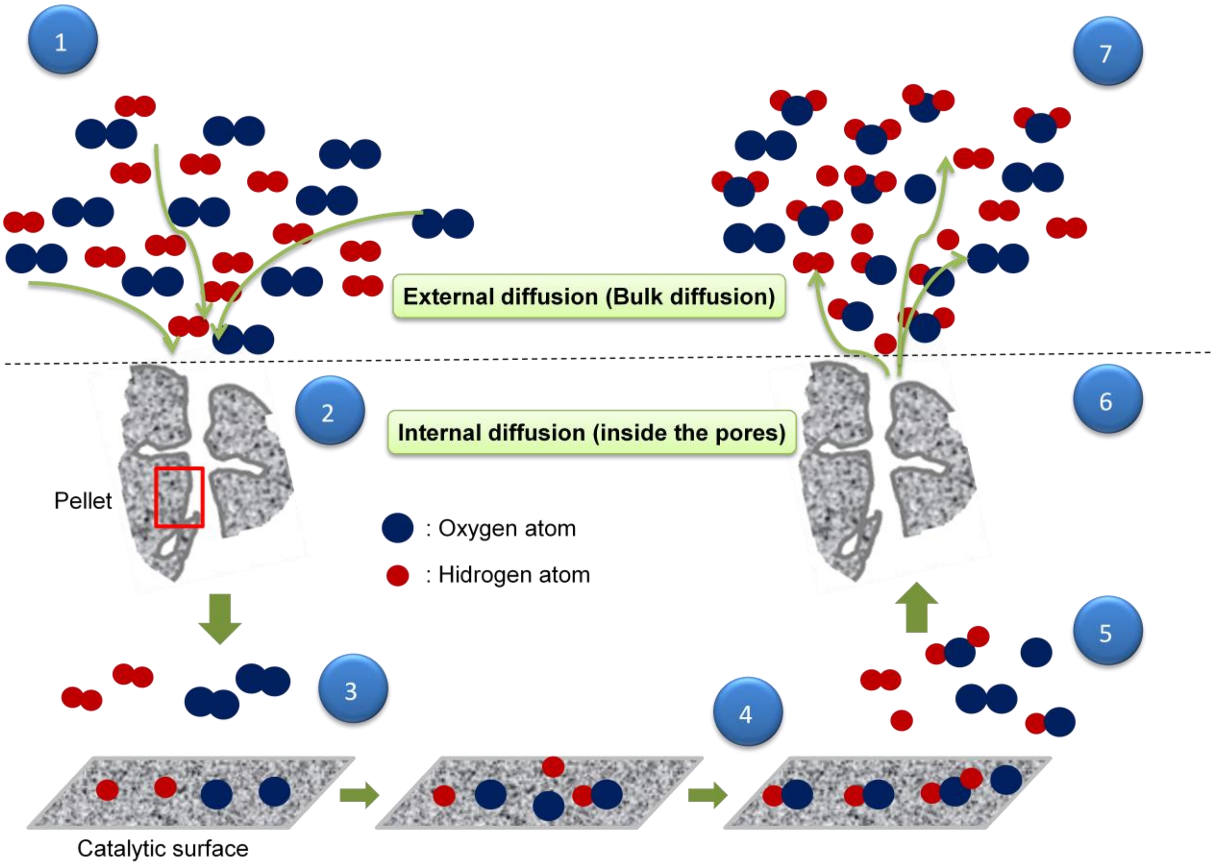

Figure 2.1. A catalytic reaction scheme for H_2 oxidation.

Reaction starts with the mass transfer (diffusion) of the reactants from the bulk fluid (step1, Figure 2.1) (i.e., gas-phase) to the external surface of the catalyst. The reactant molecules diffuse in to the catalyst pore to the immediate vicinity of the internal catalytic surface (step 2, Figure 2.1). The catalyst provides an alternative pathway for the reactions by lowering the activation energy barrier. The reactants adsorb on the surface physically (weakly-bonded via Van der Waals forces) or chemically; so called chemisorption (step 3, Figure 2.1). The heat of the adsorption of chemisorption is higher than that of physisorption. Although chemical reaction only occurs for chemisorbed species (dissociation, recombination or reaction of one chemisorbed species with another adsorbed or gas-phase species), they both have an impact on the reaction kinetics [48].
After the reaction has taken place (step 4, Figure 2.1), products desorb from the surface (step 5, Figure 2.1) and diffuse from the interior of the catalyst (i.e., the pellet) to the pore mouth (step 6, Figure 2.1). Finally, the step of external diffusion of the products from the pore mouth back to the bulk fluid follows. These steps are shown in Figure 2.1 on a catalyst with a pellet form [49].

2.2.1 Global Kinetics versus Elementary-Step Reaction Mechanism

The combination of reaction kinetics and reactor design has been studied as a major subject of catalytic reaction engineering since 1950s. Early studies used global rate expressions to determine the reaction rate. Purely empirical algebraic expressions were used to express the chemical reaction rate.

If a reaction occurs on a molecular level in exactly the way it is described by the reaction equation, it is called an *elementary reaction* (micro-kinetic model). Otherwise it is a *global reaction, overall reaction or net reaction* (macro-kinetic) [3].

Macro-kinetic models are widely used for isothermal reactor design [3, 50]. The global reaction rate law is derived from laboratory-scale experiments measuring temperature, species, concentration and pressure. It is only valid in the limited range of conditions in which the kinetic data is derived. Furthermore, it is prohibitive to extrapolate global rate expressions, as differences between the real and the assumed mechanism may invalidate the expression outside the range of conditions to which the parameters are fitted [51]. Besides, such models cannot be used for modeling non-steady-state operations for complex reaction systems [3]. On the other hand, the micro-kinetic approach attempts to describe reactions using their most fundamental set of elementary reaction steps. By this, the model can be applied to predict reaction kinetics accurately over a wide range of temperature and pressure. As a result, one model can be used to validate various sets of reaction conditions in a quick and cost-efficient manner, thus allowing the optimal processing conditions to be determined [52]. The model can be used to estimate the reactor behavior for all external conditions such as high pressure and high temperatures which are difficult to realize in laboratory conditions. One drawback of this approach is that large numbers of kinetic parameters are required for a complex reaction mechanism. Data from different fields, such as ultra-high vacuum (UHV) studies, thermodynamic, spectroscopy, quantum mechanical approaches or semi-empirical approaches for the calculation of the activation energy barriers and laboratory-scale kinetic investigations can be incorporated into micro-kinetic models. A

methodology for the development of a micro-kinetic model and the relation between all these fields are shown in
Figure 2.2.

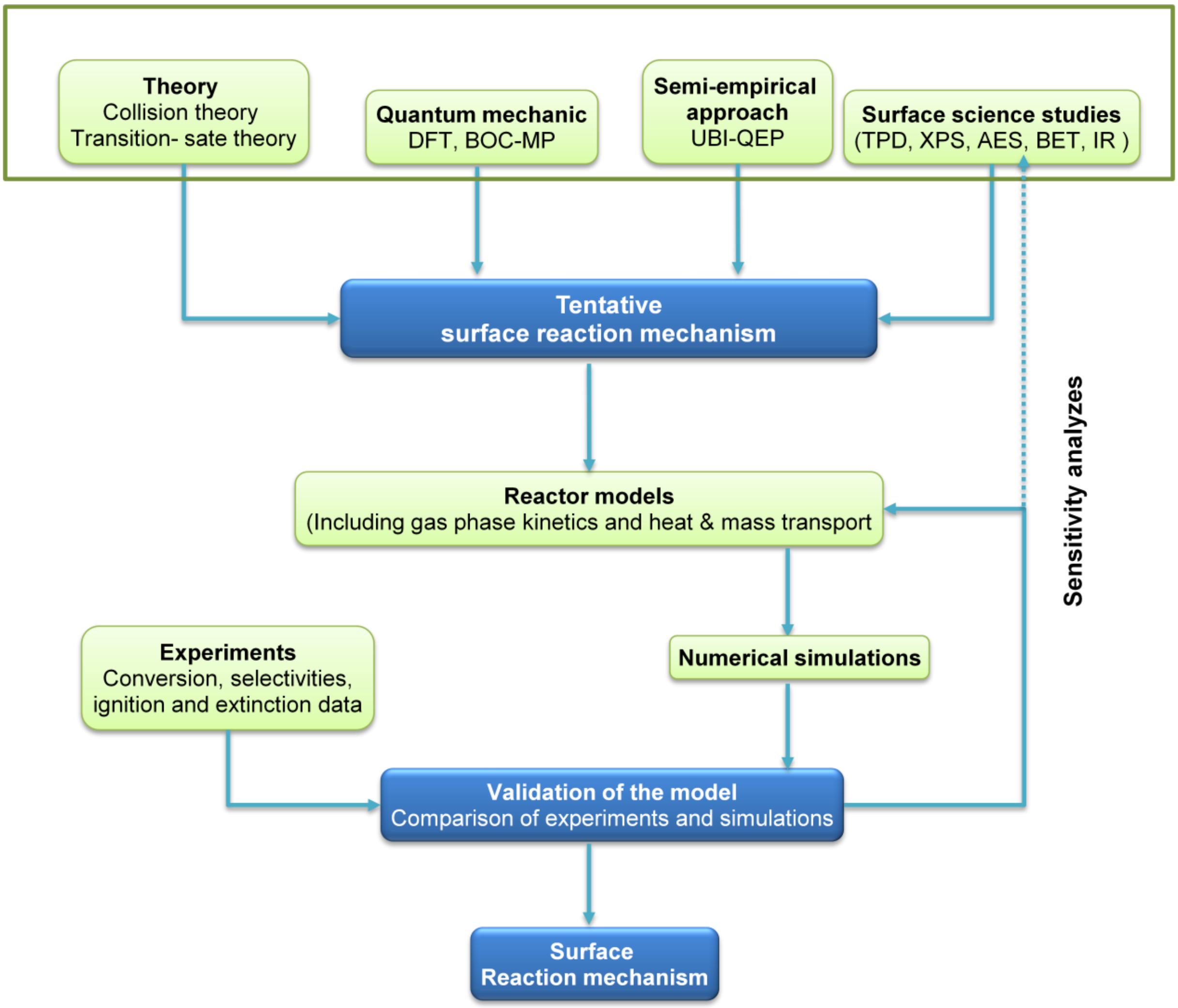

Figure 2.2. Development of a surface reaction mechanism: methodology, adapted from [3].

2.2.2 Surface Reactions and Mean-Field Approximation

In most cases, the adsorption step is the critical step for surface reactions. There are three main approaches to describe the reaction mechanism based on the adsorption phenomena.
The first model, the *Langmuir-Hinshelwood mechanism,* assumes that the reaction is generated between the adsorbed species only. Gas-phase species of A and B adsorb on the active metal sites of the catalyst, forming $A(s)$ and $B(s)$.The reaction proceeds between these adsorbed species. The reaction rate is controlled by the reaction of the adsorbed molecules. The rate expression can be derived to be a function of surface coverage's of species A and B [53].

$$A(s) + B(s) \rightarrow C(s) \tag{2.4}$$

$$r_A = -k\theta_A\theta_B \qquad \theta_A + \theta_B \leq 1 \quad . \tag{2.5}$$

Another approach, the Eley-Rideal mechanism, assumes that a chemically adsorbed species $(A_{(s)})$ may directly react with gas-phase species B. The formation of CO_2 over Pd supported catalysis is found likely to occur via this model. Gas-phase CO reacts with the adsorbed oxygen atom $O_{(s)}$ and forms a CO_2 molecule in the gas-phase and thus produces a free adsorption site S [53, 54]. In Figure 2.3 comparison of these two models is sketched for CO oxidation.

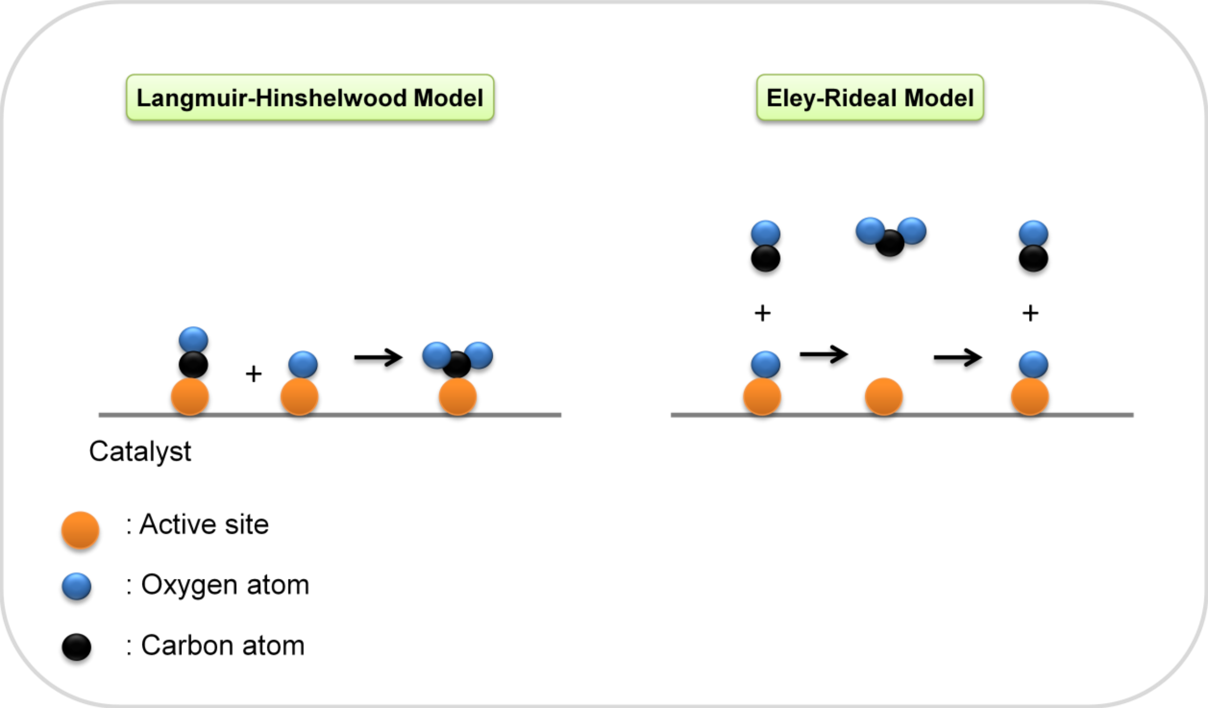

Figure 2.3. Comparison of Langmuir-Hinshelwood and Eley-Rideal models.

Lastly, the *Mars-van Krevelen model* has been proposed for catalysts that have oxygen in their lattice structure such as PtO_x, PdO_x and CeO_2. Hendriksen and Frenken have proposed that this mechanism is valid for CO oxidation over Pt(110) under oxygen rich conditions at high pressures. Adsorbed CO reacts with this lattice oxygen of PtO_x and after the desorption of CO_2, the reduced catalyst is re-oxidized by oxygen molecules in the gas-phase [55].

Although the main goal of micro-kinetic modeling of heterogeneous catalysts is to describe the system on its most fundamental level, simplifications are necessary because of the complexity of a catalytic reaction which varies in several orders of length and time scales [52, 53].
Nowadays, the mean-field approximation is a popular method for modeling technical chemical reactors. This method allows using all adsorption models i.e., Langmuir-Hinshelwood, Ridel Eley and Mars-van Krevelen. However, the reaction mechanism

presented in this study is developed based on the Langmuir-Hinshelwood adsorption model. According to mean-field approximation, the surface is assumed to be uniform. The structure of the surface is associated with a surface site density Γ that describes the maximum number of species that can adsorb on a unit surface area, e.g., (mol/m^2). Adsorbates are randomly distributed on the surface while adsorbate-adsorbate interactions are neglected and lateral interactions are not taken into account [43]. Hense on a macroscopic level, the state of the surface is described by the mean surface coverages of the adsorbed species and temperature [3].

On the other hand in the real systems, the state of the catalytic surface varies with position catalyst bed [3]. Novel discoveries show that, over time, the catalyst surface may change with reaction conditions. Grunwaldt et al. used in situ EXAFS (Extended X-ray Absorption Fine Structure) technique for methanol synthesis reaction over Cu based catalysts and they found out that the structure of the Cu particles depends on the reduction potential of the reaction gas. Thus, the structure of the Cu particles will depend on the conversion of the reactants or the sampling position in the reactor [56].

Based on the mean-field approximation, the modeling of a surface reaction should cover all processes of adsorption and the reactions between adsorbed species as well as all processes of desorption and diffusion of species into and from the bulk phase. For such a multi-step reaction mechanism, derivation of the molar net production rate $\dot{s}_i$ of a gas-phase or an adsorbed species are well documented in Ref [43] and they are briefly summarized here.

$$\dot{s}_i = \sum_{k=1}^{K_s} v_{ik}\, k_{\mathrm{f}k} \prod_{i=1}^{N_g+N_s+N_b} c_i^{v'_{ik}} \qquad \left(i = 1, \ldots., N_g + N_s + N_b\right) \quad . \tag{2.6}$$

The mechanism consists of K_s surface reactions among N_g gas-phase, N_s surface and N_b bulk species. The net production rate $\dot{s}_i$ of a surface species is linked to its coverage θ_i (Eq. 2.7).

$$\dot{s}_i = \frac{\Gamma}{\sigma_{\mathrm{i}}}\frac{d\theta_i}{dt} \qquad \left(i = 1, \ldots., N_g + N_s + N_b\right) \qquad \text{and} \qquad \sum_{i=1}^{N_s} \theta_i = 1 \quad . \tag{2.7}$$

In this equation, σ_{i} is the coordination number, i.e., the number of surface sites covered by each species of i. The surface coverage θ_i varies due to the local changing of temperature and concentrations of the species in the reactor, which enormously affects the surface reaction rates. Thus, the additional parameters μ_{i_k} and ε_{i_k} should be introduced for the definition of θ_i. By introducing these parameters into the Eq. 2.3, the expression of $\mathrm{k}_{\mathrm{f}_k}$ becomes more complex:

$$\mathrm{k}_{\mathrm{f}_k} = A_k T^{\beta_k} \exp\left[\frac{-E_{a_k}}{RT}\right] \prod_{i=1}^{N_s} \theta_i^{\mu_{i_k}} \exp\left[\frac{\varepsilon_{i_k}\theta_{\mathrm{i}}}{\mathrm{RT}}\right] \quad . \tag{2.8}$$

Besides, for the adsorption reactions, sticking coefficients are commonly used. The relation between the rate coefficient and the sticking coefficient is shown in Eq. 2.9. S_i^0 denotes the initial sticking coefficient for an uncovered surface:

$$k_{\mathrm{f}_k}^{ads} = \frac{S_i^0}{\Gamma^\tau} \sqrt{\frac{\mathrm{RT}}{2\pi M_i}} \quad \text{and } \tau = \sum_{i=1}^{N_s} v'_{ik} \quad . \qquad 2.9$$

At the catalytic surface, the net production rate of the species i via catalytic reactions is calculated according to Eq. 2.6. The net production rate of each chemical species in the gas-phase is balanced with the diffusive flux of that species in the gas-phase at steady-state conditions by assuming that, no deposition or ablation of chemical species occurs on/from the catalyst surface occurs:

$$\rho Y_i V_i = F_{\mathrm{cat/geo}} \dot{s}_i W_{ii} \quad . \qquad 2.10$$

The term $F_{\mathrm{cat/geo}}$ is introduced as a scaling factor as a ratio of the active catalytic surface area A_{catalyst} which is derived from the CO chemisorption measurements and the geometric surface area of the stagnation disk $A_{\mathrm{geometric}}$.

$$F_{\mathrm{cat/geo}} = \frac{A_{\mathrm{catalyst}}}{A_{\mathrm{geometric}}} \quad . \qquad 2.11$$

Furthermore, (η_i) denotates the effectiveness factor and it has been incorporated in the equations to introduce the internal mass transport limitations in the reaction.

The effectiveness factor is the ratio of the observed reaction rate to that which would occur in case of the diffusion limitations was eliminated.

Assuming that the reaction rate of the consumption of the reactants follows the first-order low, the reaction rate can be rewritten in the form of the rate coefficient k_{f} and the concentration C_i of the reactant i:

$$\dot{s}_i = -k_{\mathrm{f}} C_i \quad . \qquad 2.12$$

Furthermore, at given reaction conditions, the diffusion coefficient is assumed to be constant. For a catalyst with a slab geometry, the washcoat is assumed to be thick enough to sustain the zero concentration gradient at the deepest point of the washocat (L). On these assumptions, the effectiveness factor is defined as

$${}_i = \frac{\tan \phi_i}{\phi_i} \quad \text{and} \quad \phi_i = L \sqrt{\frac{k_{\mathrm{f}}}{D_{\mathrm{ef}_i}}} \quad . \qquad 2.13$$

ϕ_i is defined to be the Thiele modulus, while η_i and ϕ_i are calculated for the user-defined species. The effective diffusion coefficient (D_{ef_i}) can be calculated by taking into account the Knudsen diffusion coefficient (D_{Knud_i}) and the molecular diffusion coefficient (D_{mol_i}) of the species k in the mixture [57, 58].

$$D_{ef_i} = \frac{\varepsilon_p}{T} D_i \quad . \tag{2.14}$$

$$\frac{1}{D_i} = \frac{1}{D_{mol_i}} + \frac{1}{D_{Knud_i}} \quad . \tag{2.15}$$

In the equations above, ε_p and T represent the porosity and tortuosity respectively.

2.2.3 Thermodynamic Consistency

One of the major issues in developing a detailed surface reaction mechanism is thermodynamic consistency. Even though the recently-published reaction mechanisms ensure enthalpic consistency, many of them are not consistent with respect to entropy, which is due to the lack of knowledge about the transition states of the individual reaction steps. Thus, there is not sufficient information for a theory-based determination of pre-exponential factors in the rate equations. However, an independent choice of the rate coefficients causes an inconsistent entropy change in the overall reaction, which leads to an incorrect prediction of equilibrium states [43, 59, 60].

In this chapter, derivations of the equations are written as they are given in Ref. [60].

A reliable reaction mechanism should ensure enthalpic and entropic consistency. The equilibrium of a chemical reaction for an arbitrary reaction,

$$\sum_i \nu'_{ik} \mathrm{A}_i \underset{k_{rk}}{\overset{k_{fk}}{\rightleftarrows}} \sum_i \nu''_{ik} \mathrm{A}_i \tag{2.16}$$

only depends on the thermodynamical properties of the species involved. The equilibrium constant, K_{pk}, which describes the equilibrium composition in terms of equilibrium activities, a_i^{eq}, and their stoichiometric coefficients, $\nu_{ik} = \nu_{ik}'' - \nu_{ik}'$, is a function of temperature T

$$K_{pk} = \prod_i \left(a_i^{\mathrm{eq}}\right)^{\nu_{ik}} = \exp\left(-\frac{\Delta_k G^0}{RT}\right) \quad . \tag{2.17}$$

R is the gas constant. The change of free enthalpy $\Delta_k G^0$ at normal pressure p^0 can be written as

$$\Delta_k G^0 = \sum_i \nu_{ik} \, G_i^0(T) \quad . \qquad 2.18$$

Here, the $G_i^0(T)$ is the standard free entalpy of the species i, i.e., the chemical potential at normal pressure.

In equilibrium, the rate coefficients of forward and reverse reactions obey the equation

$$\frac{k_{\mathrm{f}k}}{k_{\mathrm{r}k}} = K_{\mathrm{p}k} \cdot \prod_i \left(c_i^0\right)^{\nu_{ik}} \quad . \qquad 2.19$$

The c_i^0 are reference concentrations at normal pressure, i.e., $c_i^0 = p^0 / RT$ for gas-phase species and $c_i^0 = \Gamma / \sigma_i$ for surface species, in which Γ is the surface site density (2.72 10^{-5} mol/m^2 for Rh) and σ_i is the number of the surface sites occupied by the species i.The rate coefficients of each reaction have to fulfill the Eq.2.19. However, some of the G_i^0 involved on the right hand side of the equation are unknown. Usually, there are more reversible reactions than unknown chemical potentials. Thus, we have an over-determined system of equations with respect to the unknown G_i^0.

In logarithmic form, we can write Eq. 2.19 as

$$\ln k_{\mathrm{f}k} - \ln k_{\mathrm{r}k} = -\frac{1}{RT} \sum_i \nu_{ik} \, G_i^0(T) + \ln\left(\prod_i \left(c_i^0\right)^{\nu_{ik}} \right) \quad . \qquad 2.20$$

For a fixed temperature, this is a linear equation system in terms of the chemical potentials G_i^0 and the logarithms of the rate coefficients. After removal of the unknown G_i^0 by Gaussian elimination, an under-determined system of linear equations for $\ln k_{\mathrm{f}k}$ and $\ln k_{\mathrm{r}k}$ are left. Allowing a change of rate coefficients of selected reactions, the minimal changes required to satisfy the linear equation system at a fixed temperature can be calculated using a weighted least-square fit. This procedure is repeated for several temperatures and new Arrhenius parameters are fitted to the new temperature dependency of the rate coefficients.

The weights in the adjustment procedure using a code of the DETCHEM software package are chosen in accordance with a sensitivity analysis of the reaction mechanism using SPIN. The rate coefficients of sensitive reactions are shifted less or remained unchanged.

2.3 Modeling Mass and Heat Transfer

The simulation of a chemical reactor requires the simultaneous solution for heterogeneous chemical kinetics coupled with mass transport and heat transport problems. Comprehensive models are based on a three-dimensional (3D) dimensional solution of Navier-Stokes equations.

The most of the laboratory-scale or commercial reactor applications involve a cylindrical reactor structure i.e., a tubular reactor, monolithic channel geometry or foam structure catalysts. Therefore the reactive flow is mostly modeled for multi-component fuels in laminar flow regimes with ideal gas behavior in a cylindrical coordinates [61, 62].

2.3.1 Navier-Stokes Equations for Tubular Channel Flow Model

2D solution of Navier Stokes Equations

Mathematical modeling of chemically reacting flows in a tubular channel can be performed in 2D at steady-steady conditions based on the solution of Navier-Stokes equations in cylindrical coordinates for axisymmetric flow field in radial and axial coordinates.

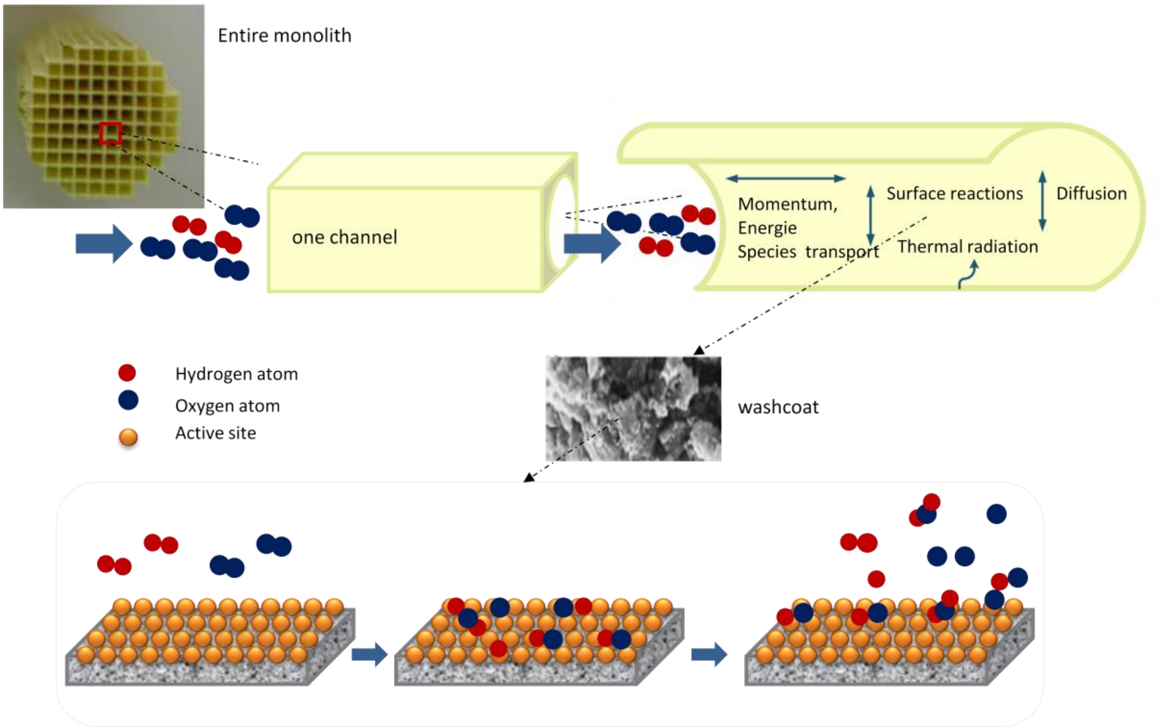

Figure 2.4. Modeling of chemically reacting flow in channel geometry.

Mass continuity:

$$\frac{\partial(\rho u)}{\partial z}+\frac{1}{r}\frac{\partial(r\rho u)}{\partial r}=0 \quad . \qquad 2.21$$

Axial momentum:

$$\rho u\frac{\partial u}{\partial z}+\rho v\frac{\partial u}{\partial r}=-\frac{\partial p}{\partial z}+\frac{\partial}{\partial z}\left[2\mu\frac{\partial u}{\partial z}-\frac{2}{3}\mu\left(\frac{1}{r}\frac{\partial(\rho u)}{\partial r}+\frac{\partial u}{\partial z}\right)\right]+\frac{1}{r}\frac{\partial}{\partial r}\left[\mu r\left(\frac{\partial v}{\partial z}+\frac{\partial u}{\partial r}\right)\right] \quad . \qquad 2.22$$

Radial momentum:

$$\rho u \frac{\partial v}{\partial z} + \rho v \frac{\partial v}{\partial r} = -\frac{\partial p}{\partial z} + \frac{\partial}{\partial z}\left[2\mu \frac{\partial v}{\partial r} - \frac{2}{3}\mu\left(\frac{1}{r}\frac{\partial(\rho u)}{\partial r} + \frac{\partial u}{\partial z}\right)\right] + \frac{\partial}{\partial z}\left[\mu\left(\frac{\partial v}{\partial z} + \frac{\partial u}{\partial r}\right)\right] + \frac{2\mu}{r}\left[\frac{\partial v}{\partial r} - \frac{v}{r}\right] \quad . \tag{2.23}$$

Species Continuity:

$$\rho u \frac{\partial Y_i}{\partial z} + \rho v \frac{\partial Y_i}{\partial r} = -\frac{\partial J_{i,z}}{\partial z} - \frac{1}{r}\frac{\partial\left(r j_{i,r}\right)}{\partial r} + R_i^{\mathrm{hom}} \quad \left(i = 1, \ldots\ldots, N_g\right) \quad . \tag{2.24}$$

Thermal energy:

$$\rho \rho c_p \left(u \frac{\partial T}{\partial z} + v \frac{\partial T}{\partial r}\right) = u\left(\frac{\partial p}{\partial z} + v \frac{\partial p}{\partial r}\right) + \frac{\partial}{\partial z}\left(\lambda \frac{\partial T}{\partial z}\right) + \frac{\partial}{\partial r}\left(r\lambda \frac{\partial T}{\partial r}\right) - \sum_{i=1}^{K} c_{pi}\left(J_{i,z}\frac{\partial T}{\partial z} + J_{i,r}\frac{\partial T}{\partial r}\right) - \sum_{i=1}^{K} h_i\, R_i^{\mathrm{hom}} \quad . \tag{2.25}$$

State:

$$p = \frac{\rho R T}{\bar{M}} \quad . \tag{2.26}$$

In these equations, r and z are the independent variables in radial and axial coordinates respectively. The dependent variables are, axial velocity u, radial velocity v, species mass fractions Y_i, temperature T and pressure p. The other variables are, density ρ, viscosity μ, thermal conductivity λ, species entalphy h_i and specific heat c_p. In species continuity thermal energy equations, the diffusive mass flux term appears as J_i. The term R_i^{hom} represents the mass of i produced by the gas-phase reactions. The equations are expressed in steady-state conditions, while gravitational forces and mass sources are neglected.

Beyond these assumptions, such simplifications are necessary because of the high computational costs and the long CPU time for the solution of Navier-Stokes equations. Navier-Stokes equations are a set of elliptical diferential equations, that is, complete flow field must be solved simultaneously in accordance with specific boundary conditions defined along the entire boundary of the flow [62].

1D solution of Navier-Stokes Equations: Plug-Flow Model

The plug-flow model is a simple model in which the reactor is modeled one-dimensionally. All the axial diffusive terms are neglected by assuming that, convective transport is dominant in the axial direction. All the radial variations are neglected by assuming that diffusive transport (mixing) is fast in the radial direction. With these assumptions, mass and continuity equations can be written in one dimension (Eq. 2.27)

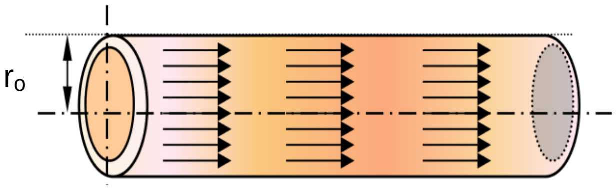

Figure 2.5. Plug-flow model.

$$\rho u A_c \frac{\partial Y_i}{\partial z} + Y_i A'_s \sum_{i=1}^{K} R_i^{\mathrm{het}} = \left(A'_s R_i^{\mathrm{het}} + A_c R_i^{\mathrm{hom}}\right) \qquad \left(i = 1, \ldots., N_g\right) \quad . \tag{2.27}$$

For a tubular flow with a diameter of r_o as shown in Figure 2.5 the cross sectional areas A_c and the circumferential length A'_s can be derived as follows:

$$A_c = \pi r_o^2 \quad \text{and} \quad A'_s = 2\pi r_o \quad . \tag{2.28}$$

The second term on the left hand side of Eq. 2.27 represents the net mass addition or depletion to/from the fluid by adsorption and desorption of the species on the catalyst wall. This term vanishes under the condition that there is no accumulation (ablation or deposition). The terms on the right hand side represent the net production rate (addition or depletion) of the gas-phase species i by heterogeneous R_i^{het} and homogeneous R_i^{hom} reactions.

Although the solution of a chemically reacting flow based on plug-flow assumptions is computationally inexpensive and requires only a few seconds of computational time, the range of the validity is limited.

Boundary-layer Model for Laminar Tubular Channel Flows

The boundary-layer theory was first introduced in 1904 by Ludwig Prandtl. His discovery was an important contribution to exact solution of Navier-Stokes for practical applications such as calculating the lift and drag on airplanes. According to Prandtl “A very satisfactory explanation of the physical process in the boundary-layer (Grenzschicht) between a fluid and a solid body could be obtained by the hypothesis of an adhesion of the fluid to the walls, that is, by the hypothesis of zero relative velocity between fluid and wall”. A schematic sketch of this explanation is shown in Figure 2.6 for a fluid flow over an immersed body.

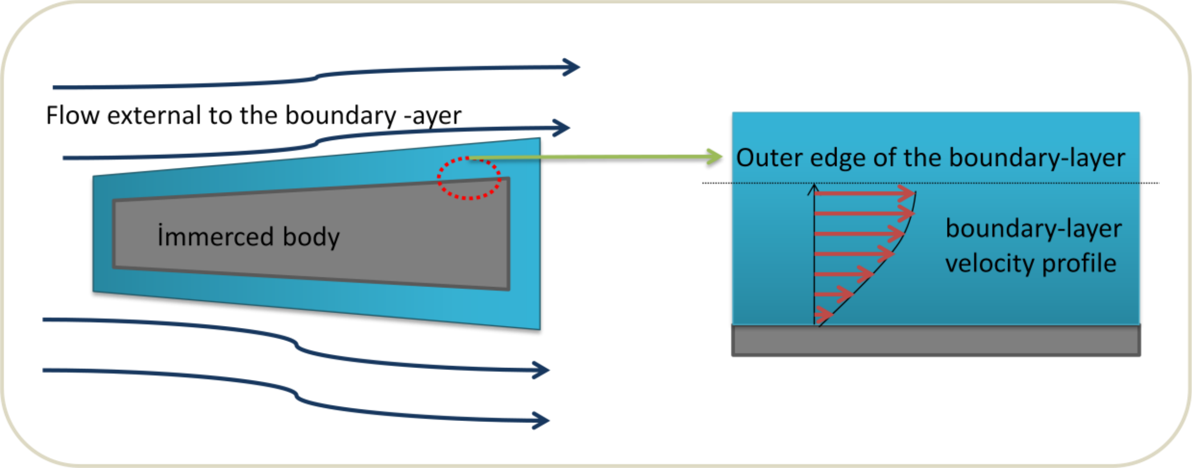

Figure 2.6. Boundary-layer model.

For a chemically reacting flow, it is assumed that, axial diffusive transport is diminished in comparison to radial diffusion and convective transport. This means that all second derivatives in the axial z dimension are eliminated. They are neglected because they are small compared to others, although they do not truly vanish. Boundary-layer equations retain a full two-dimensional representation of all the field variables [63].

Mass continuity:

$$\frac{\partial(\rho u)}{\partial z}+\frac{1}{r}\frac{\partial(r\rho u)}{\partial r}=0 \quad . \tag{2.29}$$

Axial momentum:

$$\rho u\frac{\partial u}{\partial z}+\rho v\frac{\partial u}{\partial r}=-\frac{\partial p}{\partial z}+\frac{1}{r}\frac{\partial}{\partial r}\left[\mu r\frac{\partial u}{\partial r}\right] \quad . \tag{2.30}$$

Radial momentum:

$$\frac{\partial p}{\partial r}=0 \quad . \tag{2.31}$$

Species continuity:

$$\rho u\frac{\partial Y_i}{\partial z}+\rho v\frac{\partial Y_i}{\partial r}=-\frac{\partial J_{i,z}}{\partial z}-\frac{1}{r}\frac{\partial\left(r j_{i,r}\right)}{\partial r}+R_i^{\mathrm{hom}} \quad \left(i=1,\ldots\ldots,N_g\right) \quad . \tag{2.32}$$

Thermal energy:

$$\rho c_p\left(u\frac{\partial T}{\partial z}+v\frac{\partial T}{\partial r}\right)=\frac{\partial}{\partial r}\left(r\lambda\frac{\partial T}{\partial r}\right)-\sum_{i=1}^{K} c_{pi}\,J_{i,r}\frac{\partial T}{\partial r}-\sum_{i=1}^{K} h_i\,R_i^{\mathrm{hom}} \quad . \tag{2.33}$$

The resulting problem is a set of algebraic-differential equations and can be solved by means of the finite-difference or the finite-volume discretization method. When the boundary-layer approximation is valid, the characteristics of the steady-state governing equations change. In contrast to elliptical form of Navier-Stokes equations, boundary layer equations are a set of parabolic differential equations. This is a huge simplification leading to efficient computational algorithms. The boundary-layer theory is especially valid for high flow rates as long as the laminar-flow regime is established (high Peclet numbers) [62, 64].

2.3.2 Stagnation-Flow Model

For the reactive systems in which a large number of species are involved in the conservation equations, it should be noticed that huge simplifications are made to reduce the computational time. Mostly, these simplifications bring about uncertainties regarding the exact solution of the system. For this reason, studies on the development of detailed surface reaction mechanism require coupling experimental studies with numerical simulations of reactor configurations, whose flow fields are well known and easy to model such as channel geometries, wire flows and stagnation-flows [65].

Among others the stagnation-flow represents a class of flow configurations for which the Navier-Stokes equations, together with thermal energy and species continuity equations, can be solved as a boundary-layer problem. Mathematical solution of the system is performed by solving a set of the ordinary differential equations [64].

A stagnation-flow reactor is a useful tool for kinetic measurements because it represents a well-defined flow field, which enables modeling both heterogeneous and homogeneous chemistry [66, 67]. The basic stagnation-flow solution is derived from the Hiemenz solution, in which the flow is in the direction of a solid plate [65]. Even though the flow field is 2D, with realistic assumptions, conservation equations can be reduced to a 1D boundary-layer problem [68, 69]. Stagnation-flow reactors have extensively been used for chemical vapor deposition (CVD) experiments. The flow is directed a disk by creating stagnation point on the disk to achieve a thick and uniform deposition across the substrate [70, 71]. The simplicity of the flow pattern allows the mathematical modeling of the material growth with mass, momentum, and energy balance equations in 1D [70, 72-74].

Today, stagnation-flow reactors (SFR) are widely used in combustion research to study the effects of fluid-mechanical strain on flame behaviour [64]. A number of groups have studied catalytic chemistry in a stagnation-flow configuration to incorporate detailed chemistry into catalytic combustion simulations [27, 38, 66, 67, 75-83]. Ljungström et al. have studied the H_2O formation kinetics in H_2/O_2 mixtures on a Pt foil by introducing a laser beam into a stagnation foil surface [75]. Song et al. have studied the ignition criteria of H_2 and propane on stagnation-flow geometry and showed that the SFR geometry provides accurate data on the bifurcation analysis where heterogeneous and homogeneous reactions take place [76].

Many studies have been performed in order to model the ignition criteria of H_2/O_2 mixtures on Pt surfaces using the stagnation-flow geometry that enables the 1D boundary-layer solution of Navier Stokes equations [67, 78, 79, 84, 85]. Deutschmann et al. studied the ignition behavior of CH_4, CO, and H_2 as well as of CH_4/H_2 mixtures by using the simplified 1D stagnation-flow field approximation [53, 86]. Furthermore, the SFR configuration has been used to investigate the detailed surface reaction kinetics for complex reactions such as methane partial oxidation and steam reforming on noble metals [27, 66, 80, 83, 87].

Recently, McGuire et al. studied dry reforming of methane over Rh supported strontium-substituted hexaaluminate catalysts in a stagnation-flow reactor [27]. The information obtained was used to modify the surface reaction mechanism of Hartmann et al.[88].

In this chapter, the derivation of a 1D stagnation-flow field is provided. Since the reactor used in this study has no circumferential velocity, all the equations are given for stationary disk applications. Navier-Stokes equations are solved for axisymteric flow configuration in the $z-r$ plane at steady-state.

Derivation of the equations is well documented elsewhere [70, 89, 90] and here the equations are given in as they are derived by Kee et al.[90].

Generally speaking the derivation of the stagnation-flow equations relies on two important conjectures.

Assumption 1: The velocity field is presumed to be described in terms of a streamfunction written in the form of:

$$\rho\Psi(z,r) = r^2 U(z) \quad . \tag{2.34}$$

Here $U(z)$ symbolizes an unspecified function of z alone. This satisfies the mass continuity equations exactly.

Assumption 2: Temperature, composition and density are presumed to vary only in axial directions. The pressure is assumed to be constant throughout the flow but varies in a very special way, which appears in the equations as an eigen value problem. Besides, the magnitude of the pressure variations is assumed to be too small compared to the mean thermodynamic pressure (Figure 2.7).

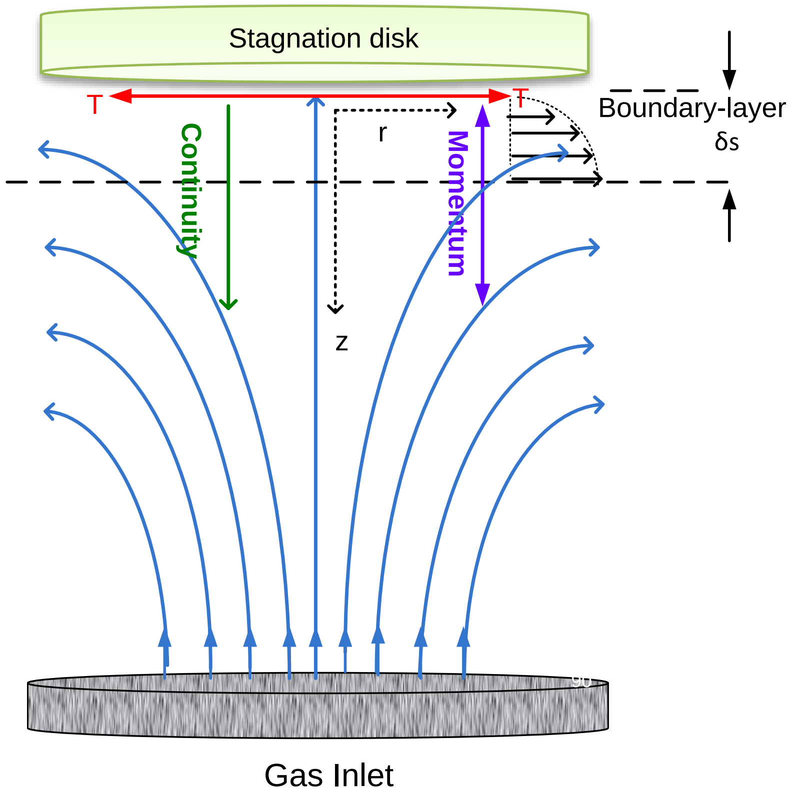

Figure 2.7. Axisymmetric stagnation-flow.

Using these assumptions, the 2D Navier Stokes equations (Eq. 2.29-2.33) are simplified. Then, derivation of axial (u) and radial velocity (v) as well as the stream functions in radial and axial coordinates are expressed follows:

$$\frac{\partial \Psi}{\partial r} = \rho u r = 2rU. \qquad \rho u = 2U. \qquad \frac{\partial u}{\partial z} = 2\frac{\partial}{\partial z}\left(\frac{U}{\rho}\right) \quad . \tag{2.35}$$

Since density is a function of z only:

$$\frac{\partial u}{\partial r} = 2U\frac{\partial}{\partial r}\left(\frac{1}{\rho}\right) = 0 \quad . \tag{2.36}$$

$$-\frac{\partial \Psi}{\partial z} = \rho v r = -r^2\frac{dU}{dz} \qquad \rho v = -r\frac{dU}{dz} \qquad \frac{\partial v}{\partial z} = -r\frac{\partial}{\partial z}\left(\frac{1}{\rho}\frac{dU}{dz}\right) \quad . \tag{2.37}$$

$$\frac{\partial v}{\partial r} = -\frac{dU}{dz}\frac{\partial}{\partial r}\left(\frac{r}{\rho}\right) = -\frac{1}{\rho}\frac{dU}{dz} \quad . \tag{2.38}$$

Substituting the equations derived (Eq 2.35-2.38) into the Navier-Stokes equations yields only axial derivatives of U and ρ. Thus, the following ordinary differential equations remain:
Axial momentum:

$$\frac{\partial p}{\partial z} = -4U\frac{d}{dz}\left(\frac{U}{\rho}\right) + \frac{4}{3}\frac{d}{dz}\left[2\mu\frac{d}{dz}\left(\frac{U}{\rho}\right) + \frac{\mu}{\rho}\frac{dU}{dz}\right] - 2\mu\frac{d}{dz}\left(\frac{1}{\rho}\frac{dU}{dz}\right) \quad . \tag{2.39}$$

Radial momentum:

$$\frac{1}{r}\frac{\partial p}{\partial r} = 2U\frac{d}{dz}\left(\frac{1}{\rho}\frac{dU}{dz}\right) - \frac{1}{\rho}\left(\frac{dU}{dz}\right)^2 - \frac{d}{dz}\left[\mu\frac{d}{dz}\left(\frac{1}{\rho}\frac{dU}{dz}\right)\right] \quad . \tag{2.40}$$

Since $\partial p/\partial z$ is known to be a function of z only, its radial derivative must vanish. Therefore, $(1/r)\,\partial p/\partial z$ is a constant that is called $_r$.

$$\frac{1}{r}\frac{\partial p}{\partial r} = {}_r \quad . \tag{2.41}$$

If unspecified function $U(z)$ is definded as scaled velocity $V = v/r$ and rewritten in terms of V, the resulting stagnation-flow equations become as follows:

$$\frac{\partial(\rho u)}{\partial z} + 2\rho V = 0 \quad . \tag{2.42}$$

$$\rho u\frac{\partial u}{\partial z} + \frac{\partial p}{\partial z} - 2\mu\frac{\partial V}{\partial z} - \frac{4}{3}\frac{\partial}{\partial z}\left(\mu\frac{\partial u}{\partial z}\right) + \frac{4}{3}\frac{\partial}{\partial z}(\mu V) \quad . \tag{2.43}$$

$$\rho u\frac{\partial V}{\partial z} + \rho V^2 - \frac{\partial}{\partial z}\left(\mu\frac{\partial V}{\partial z}\right) + \; = 0 \quad . \tag{2.44}$$

$$= \frac{1}{r}\frac{\partial p}{\partial r} \quad . \tag{2.45}$$

Thermal energy and species continuity equations for a species i are also shown below in 1D:

$$\rho c_p u\frac{\partial T}{\partial z} - \frac{\partial}{\partial z}\left(\lambda\frac{\partial T}{\partial z}\right) - u\frac{\partial p}{\partial z} + \rho\sum_{i=1}^{N_g}\left(c_p Y_i V_i\right)\frac{\partial T}{\partial z} + \sum_{i=1}^{N_g} h_i\, W_i\dot{\omega}_\iota = 0 \quad . \tag{2.46}$$

$$\rho u\frac{\partial Y_i}{\partial z} + \frac{\partial}{\partial z}(\rho Y_i V_i) - W_i\dot{\omega}_\iota = 0 \qquad i = 1, \ldots\ldots N_g \quad . \tag{2.47}$$

In addition, the equation of state is written as below:

$$\rho = \frac{p}{RT}\frac{1}{\sum_{i=1}^{N_g} Y_i/W_i} \quad . \tag{2.48}$$

In these equations, temperature T, species mass fractions Y_i, axial velocity u, and the scaled radial velocity $V = v/r$, in which v is the radial velocity and r is the radial coordinate are functions of z only. V_i represents the diffusion velocity of species i in the z direction and is evaluated as

$$V_i = \frac{1}{X_i \overline{W}} \sum_{i \neq j}^{N_g} W_j D_{ij} \frac{\partial X_j}{\partial z} - \frac{D_i^T}{\rho Y_i} \frac{1}{T} \frac{\partial T}{\partial z} \quad . \tag{2.49}$$

In which X_i represents the mole fractions, $\overline{W}$ is the mean molecular weight, D_{ij} is the multi-component diffusion coefficient, and D_i^T is the thermal diffusion coefficient of species i Further symbols denote molecular viscosity (μ), thermal conductivity (λ) mixture specific heat c_p, molecular weight of species i, (W_i), enthalpy of formation (h_i), molar reaction rate of gas-phase reactions (ω_i), and the number of gas-phase species (N_g) [64].

The boundary conditions at the inlet of the reactor are given as

$$T = T_{in} \qquad u = u_{in} \qquad v = 0 \qquad Y_i = Y_{i_{in}} \quad . \tag{2.50}$$

The remaining boundary conditions at the gas-catalyst interface are:

$$u = 0 \qquad V = 0 \qquad T = \mathrm{T}_s \quad . \tag{2.51}$$

2.4 Numerical Tools

The modeling of stagnation-flow reactor experiments is performed by using SPIN code which is part of the CHEMKIN package and DETCHEM$^{\text{STAG}}$ which is recently developed as a part of DETCHEM software package. Continuous-flow reactor experiments are modeled by using DETCHEM$^{\text{CHANNEL}}$ and equilubrium calculations are performed by using DETCHEM$^{\text{EQUIL}}$. In this chapter, a brief introduction of these softwares will be given.

2.4.1 CHEMKIN SPIN Code [69]

SPIN is the software developed for the solution of 1D rotating disk and stagnation-flow reactor models. The program computes species, temperature and velocity profiles as well as the deposition rate (for CVD applications) at steady-state by coupling fluid mechanics and gas-phase chemical kinetics of the reactive flow. The SPIN program accounts for finite-rate gas-phase and surface chemical kinetics and multicomponent molecular transport. The governing set of differential equations is solved by a modified Newton algorithm for nonlinear algebraic equations.

The kinetic data, thermodynamic as well as the transport properties of the reactive flow are supplied by CHEMKIN GAS-PHASE, SURFACE CHEMKIN and TRANSPORT packages.

The user should first supply the information of the chemical species and the chemical reaction for a particular reaction mechanism in the *chem.inp* file. Furthermore, the thermodynamic properties of these species will be extracted from the data base called *therm.da*”. The information from the user input and the thermodynamic properties are stored in the CHEMKIN linking file, *chem.asc*. Similarly, the transport properties of these species are written in a file called *trans.dat.* Polynomial representations of temperature dependent viscosities, thermal conductivities and binary diffusion coefficients of each individual species are given in the *trans.da*” file. CHEMKIN subroutine library uses a fitting program called t*ran*, and all this transport information is computed and stored in a CHEMKIN linking file called *tran.asc..*

For heterogeneous reactions, SURFACE CHEMKIN interpreter must also be executed. Surface reaction properties such as, surface and bulk species names, surface site types and surface reaction steps are provided by the user in the input file *surf.inp.* SURFACE CHEMKIN reads this information entered by the user and writes a SURFACE CHEMKIN linking file named *surf.asc*.

Reaction conditions such as temperature, concentration of the species and the solution parameters are defined by the user in the file named *spin.inp*. SPIN then reads this input file and produces the solution. For all input files, SPIN generates text files such as; *spin.out*, *chem.out* and *surf.out*.

2.4.2 DETCHEM Code

The DETCHEM (DETailed CHEMistry) software package is a numerical tool used for a detailed description of physical and chemical processes of a reactive system by coupling transport and chemistry. The DETCHEM software package is written in FORTRAN. Reaction rates and transport coefficients, i.e., binary diffusion coefficients, thermal conductivity, viscosity for each species and bulk phase, are calculated using library routines. Detailed gas-phase and surface reaction mechanisms are considered. However, only heterogeneous reaction mechanisms are investigated in this study. Since the reaction temperatures are considerably low, homogenous reactions are neglected [48, 58]. The heterogeneous reaction model is based on the mean-field approximation. This way, an exact computational solution of different reactor models and flow configurations is possible. The names of the applications refer to the flow configuration or the reactor type modeled, such as DETCHEM^{PLUG} for the 1D solution of continuous-flow reactor applications and DETCHEM^{CHANNEL} for 2D solution of reactive flows in a single channel of the monolithic catalyst. Furthermore entire monolith can be modeled in 2D or 3D by using DETCHEM^{MONOLITH}. Moreover, equilibrium concentrations in given reaction conditions can be computed by DETCHEM^{EQUIL}. Detailed information about the entire DETCHEM package is given elsewhere [58].

The numerical solution of the flow reactor system is modeled by channel geometry and equilibrium calculations are performed using DETCHEM^{EQUIL}. In this chapter, further details of DETCHEM^{STAG}, DETCHEM^{CHANNEL} and DETCHEM^{EQUIL} will be discussed.

2.4.2.1 DETCHEM^{STAG}

This program has recently been developed as apart of DETCHEM software to solve 1D stagnation-flow field. The program computes, veleocity, temperature, concentration profiles of the species at steady-state or transient conditions. Further information can be found elsewhere [58].

2.4.2.2 DETCHEM$^{\text{CHANNEL}}$

The DETCHEM$^{\text{CHANNEL}}$ code was developed for the simulation of chemically reacting flows at steady-steady conditions for the 2D solution of axisymmetric flows. DETCHEM$^{\text{CHANNEL}}$ considers the flow through a cylindrical or annular channel. Transport effects and chemical kinetics in a single channel are modeled at the micro-kinetic level (Figure 2.4). The boundary-layer approximation is valid with a sufficiently high velocity of the fluid or sufficiently small diameter of the channel. Typical channel diameters for 600 and 900 cells per square inch (cpsi) monoliths are 4.90 mm and 4.24 mm, respectively. Diffusion limitations of the surface reaction rates are also considered. The user supplies the geometric properties of the channel in *channel.inp* file. The reaction conditions i.e., temperature, pressure, flow rate and reactant composition are also supplied in the *channel.inp* file. The reaction mechanisms can be included in the *channel.inp* file or it can be provided via external input files. The thermochemical properties of the species are calculated as polynominal functions using the *thermdata* and *moldata* databases that are located in the same directory file [58].

The total continuity, axial momentum, energy and species continuity equations are solved using the governing equations which are given in Chapter 0. In addition, here, the calculation of the reaction rate in terms of unit catalyst area is given in detail.

2.4.2.3 DETCHEM$^{\text{EQUIL}}$ [58]

Equilibrium concentrations are calculated by the software DETCHEM$^{\text{EQUIL}}$. A closed system of temperature T, pressure p and molar amounts of substance n_i is in equilibrium, if the Gibbs free energy reaches a minimum with respect to all possible combinations of n_i.

$$G(T,p,n_i) = \sum_i n_i \left(G_i^o(T) + RT \ln \frac{p_i}{p^o} \right) \quad . \qquad 2.52$$

$G_i^o(T)$ is the standard molar free energy at pressure p^o, i. e., the chemical potential at standard pressure. Assuming ideal gas law for the mixture, the partial pressures (p_i) can be replaced by the amounts of the species :

$$p_i = \frac{n_i RT}{V} \quad . \qquad 2.53$$

For a reaction k with stoichiometric coefficients v_{ik}, the change of Gibbs free energy is given by:

$$\Delta_k G^o(T) = \sum_i v_{ik} G_i^o(T) \quad . \qquad 2.54$$

If the reaction k is in equilibrium, solution of Eq. 2.52 yields

$$\Delta_k G^o(T) = -RT \ln K_p(T) \quad . \qquad 2.55$$

where K_p is defined as thetemperature dependent equilibrium constant with respect to partial pressures:

$$K_p = \prod_i \left(\frac{p_i}{p^o}\right)^{v_{ik}} \quad . \qquad 2.56$$

DETCHEM$^{\mathrm{EQUIL}}$ calculates the equilibrium mole composition of the system at a given temperature and pressure. The program requires and input file *equil.inp,* in which the user supplies the reaction conditions under examination. Enthalpy and entropy of each species are calculated as polynomial functions using the *thermdata* database. Although the equilibrium molar compositions are calculated for constant T and p in this study, the program can also solve the problem to find the adiabatic temperature for constant H and p.

3. EXPERIMENTAL SET-UP

This chapter focuses on the development and construction of the stagnation-flow reactor. Therefore, detailed information on the reactor configuration, operating conditions and analytical tools are given.

The experimental set-up basically consists of a stagnation-flow reactor, a gas feeding system and analytics (Figure 3.1). The system has been designed to work for a wide range of gases and evaporated liquids. In this chapter, detailed information about the reactor and each unit will be given.

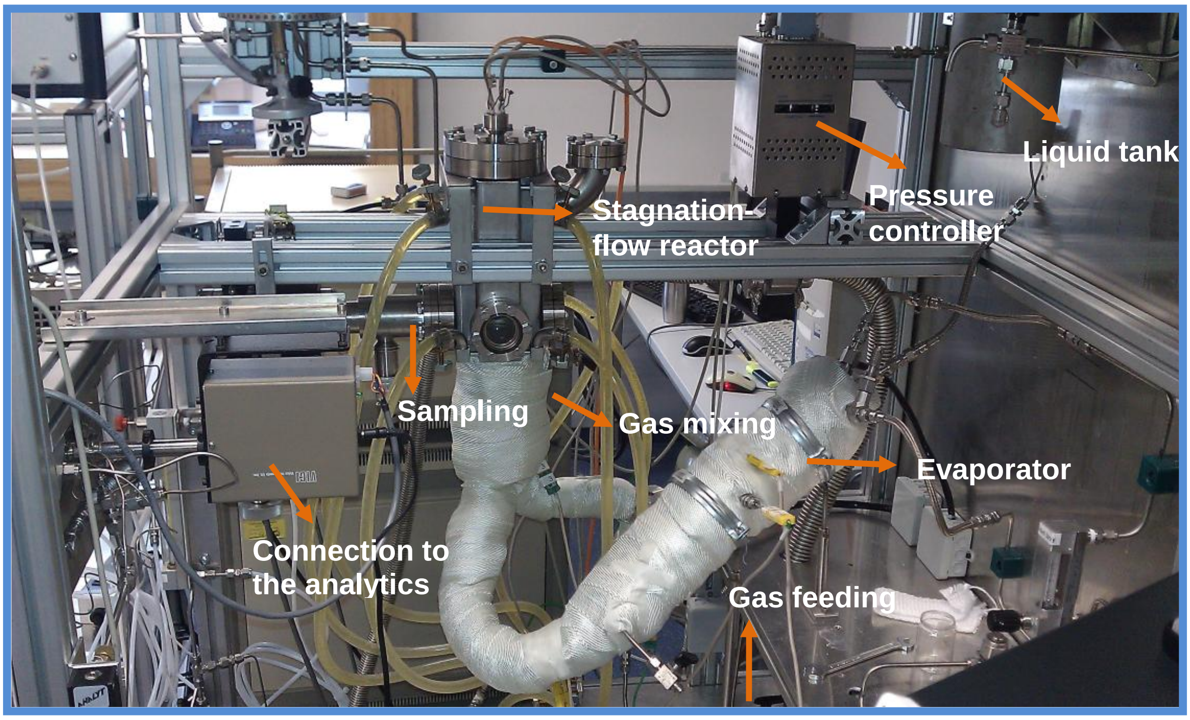

Figure 3.1. Experimental set-up.

3.1 Stagnation-Flow Reactor

A stagnation-flow reactor has been developed for the detailed investigation of heterogeneous kinetics over Rh/Al_2O_3 catalyst and applied in this study for oxidation and reforming of CH_4 and C_3H_8 (Figure 3.2). A similar reactor configuration was constructed in the Colorado Fuel Cell Center laboratory (Colorado School of Mines, USA) [83].

The main reactor chamber is constructed by MKS instruments (Boulder, USA). The reaction chamber is made of stainless steel, which is isolated from the ambient atmosphere by hot ethylene glycol circulation via a chiller; recirculating water bath (Thermo Neslab RTE7, -298 K to +423 K) to keep the reactor wall temperature constant.

The stagnation-flow reactor set-up enables working at 100-1100 mbar, and the pressure is controlled by a butterfly valve (MKS, T3BIA). The reactor body is designed to be operated at a maximum of 4 bar. For this high-pressure application, the reactor body contains a safety window. If the operating pressure exceeds 4 bar, the safety window automatically opens and prevents possible damages to the reactor.

The reactor can be operated at temperatures of 298-1173 K. Gases such as O_2, CO, H_2, CH_4, C_2H_6, C_3H_8 and vaporized liquids such as water, ethanol, methanol or iso-octane can be used as reactants (Figure 3.3).

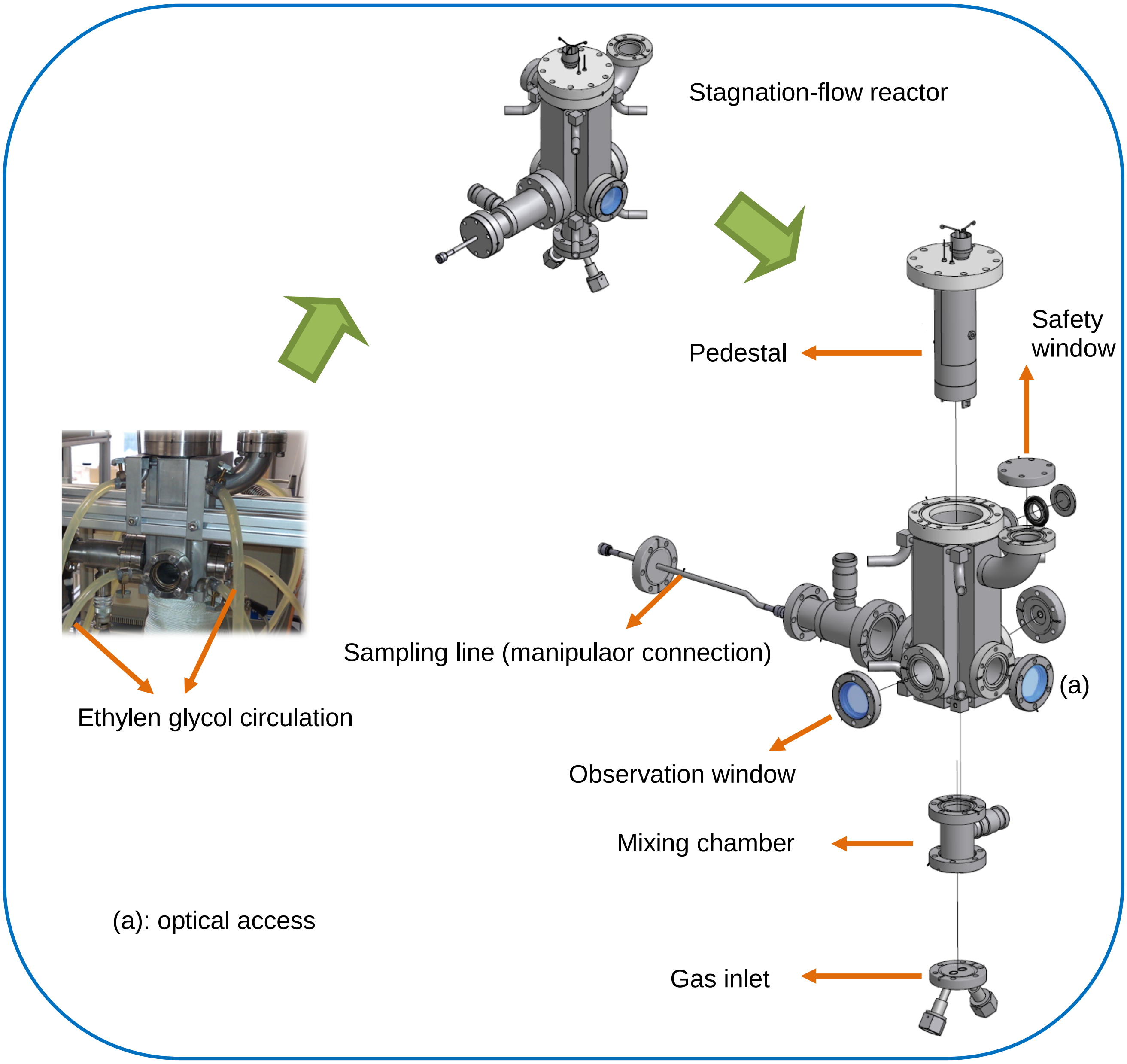

Figure 3.2. Stagnation-flow reactor.

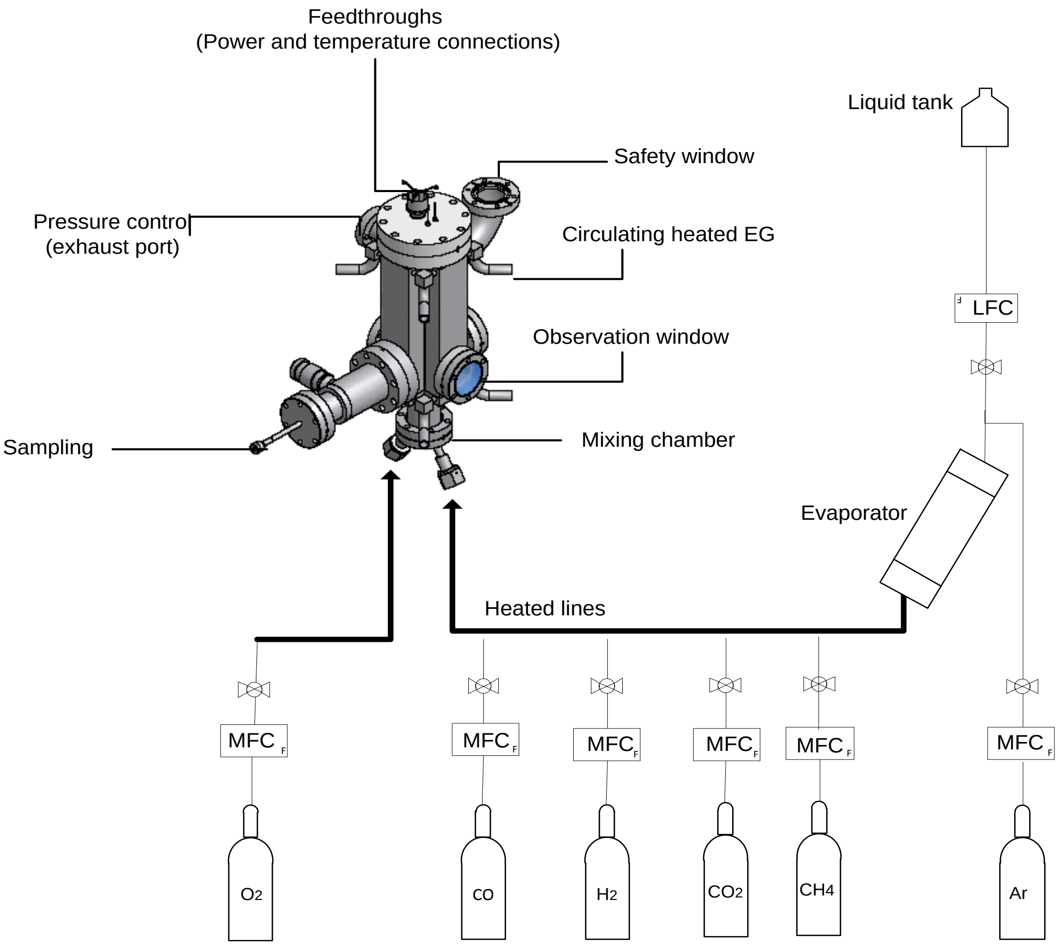

Figure 3.3 Flow diagram.

The experimental set-up consists of the feeding system, the reactor chamber, the sampling device and analytical tools.

3.1.1 Feeding System

All gases are dosed via mass flow controllers (MFC, Bronkhorst). For liquid fuels, a liquid mass flow controller (MFC, Bronkhorst) is used and a microstructure nozzle evaporation technique is applied [91]. Ar diluted hydrogen and oxygen are fed to the reactor from two separate channels. These gases are premixed in a mixing unit before they enter the reaction zone (Figure 3.4). The mixing chamber is made of a 7.6 cm deep stainless steel cylinder and is filled with glass beads that are 2 mm in diameter. A 2 mm thick porous sintered metal (stainless-steel type 316L, Mott Corporation) is placed on top of the glass bead layer.

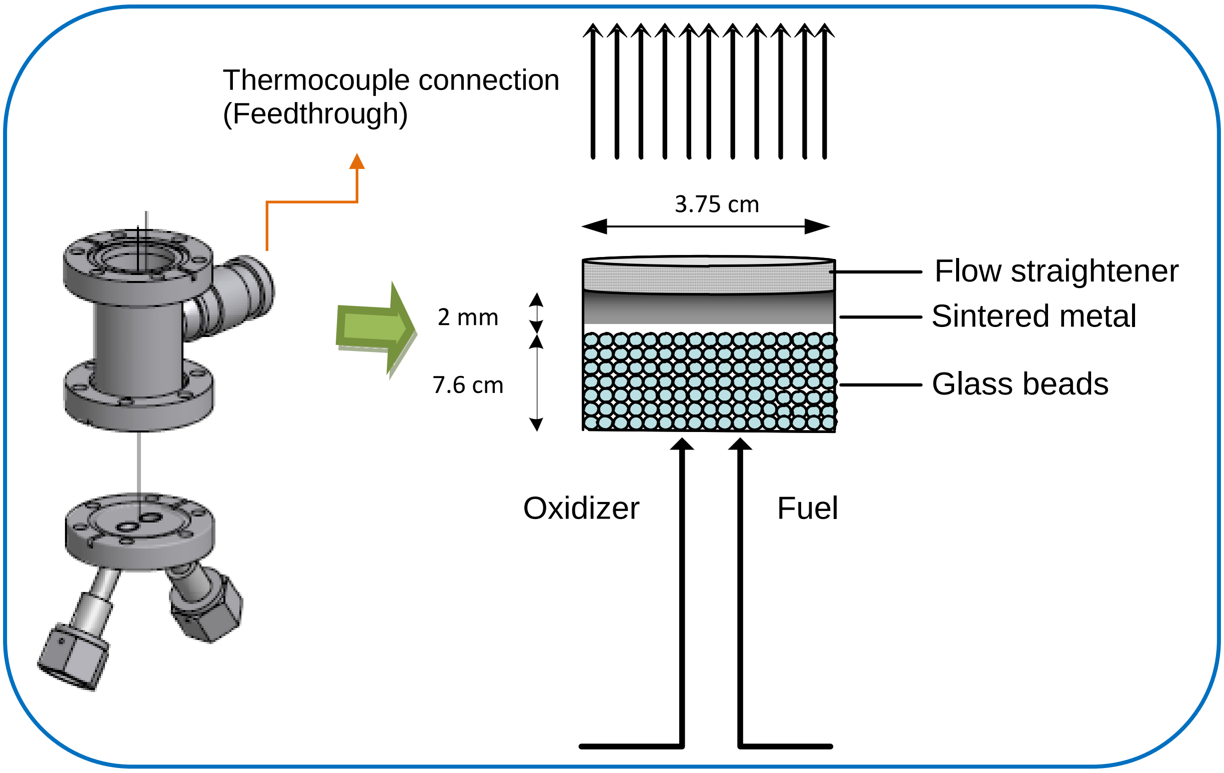

Figure 3.4. Mixing chamber.

The pore size of 0.1 mm of the sintered metal is chosen to be smaller than the quenching distance of any flammable mixture to prevent flashbacks [92]. A K-type thermocouple is embedded in the center of the mixing chamber to measure the inlet temperature of the gases.

The gas mixture is directed to the catalytic surface through a flow straightener (3.75 cm in diameter) made of stainless steel (304-CrNiMo, Indy Honeycomb) with a 0.8 mm cell size honeycomb structure. The distance between the flow straightener and the catalytic surface is 3.9 cm.

The flow configuration is oriented upwards so that the buoyancy effect on the stagnation-flow field is diminished. This configuration provides a stagnation-flow field with a radially uniform velocity profile at the inlet. Gas lines are also heated to prevent the condensation of the liquids.

The gases are exhausted through an annular pipe and burned in Bunsen burner which is also housed in the reactor. Operating pressure is selected to be 500 mbar to obtain an optimum boundary-layer thickness. A detailed investigation on definition of the optimum operating pressure is given in Chapter 3.1.6

3.1.2 The Reactor Chamber

The reactor chamber consists of a pedestal where the catalytic surface, heater and the power connections of this heater are housed (Figure 3.5).

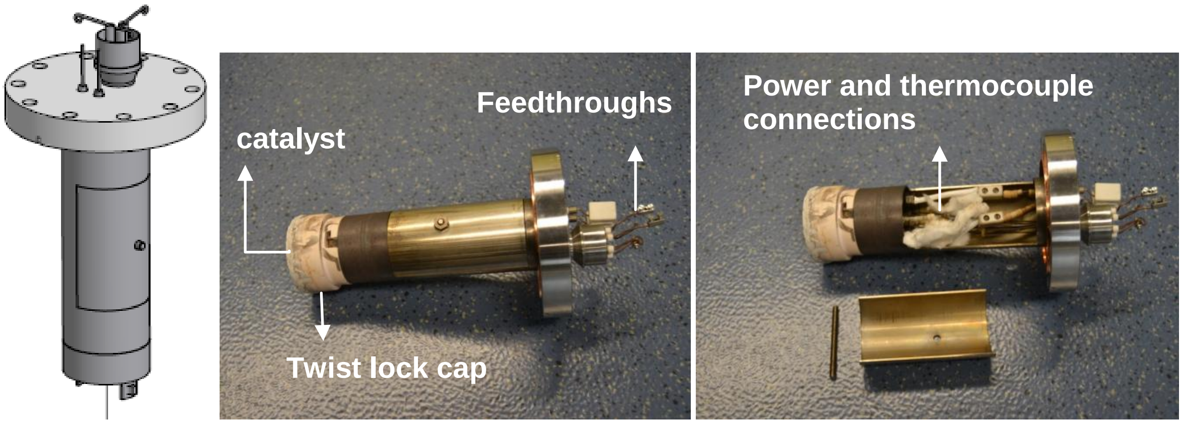

Figure 3.5 Pedestal.

Catalytic Surface

The catalyst is coated on a flat stagnation disk which is made of alumina. The disk (5.5 cm in diameter) is created using a high-temperature castable ceramic resin and hardener (COT Rescor 780, Cotronics Corporation). Appropriate amounts of resin and hardener are mixed to yield 100 g. The blend is well-mixed and moulded in a silicon rubber form and it is subjected to an ultrasonic bath for 5 min for degassing of the blend. An R-type (rhodium-platinum) thermocouple with 0.2 mm thickness (Omega Newport) is embedded in the center of the stagnation surface during casting. The thermocouple wires are isolated by using a round, two hole ceramic insulator (0.254 mm OD, Omega). These steps are shown in Figure 3.6

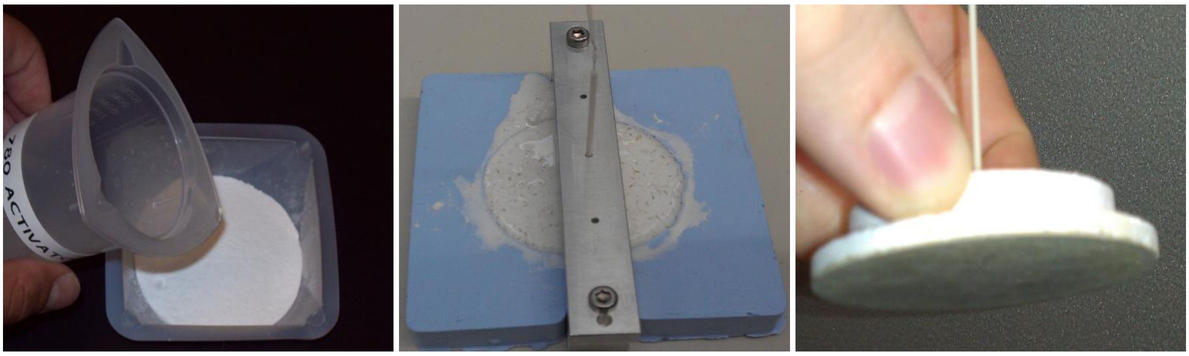

Figure 3.6. Preparation of the stagnation surface.

The surface is dried at 403 K for 2 h and cured at 873 K for 2 hours. The resulting ceramic structure consists of 99 wt.% Al_2O_3.

3.1.3 Heater Design

The stagnation surface is directly heated by a resistive heater which is located right above the surface. Firstly, a slilicon carbide (SiC) resistive heater (total resistivity of 1.4 Ω at room temperature (Morgan Advanced Ceramic), is used. Power is supplied (maximum 20V at full range) to the heater by a PID controlled power unit (Eurotherm 818) through tantanum (Ta) or molybdenum (Mo) rods. Ta/Mo nuts/ferrules are used for the connection between the rods and the heater. Although these materials are well-known as high temperature stable materials, they tend to oxidize easily at elevated temperatures (> 573 K), leading to a lack of power supply to the heater (Figure 3.7).

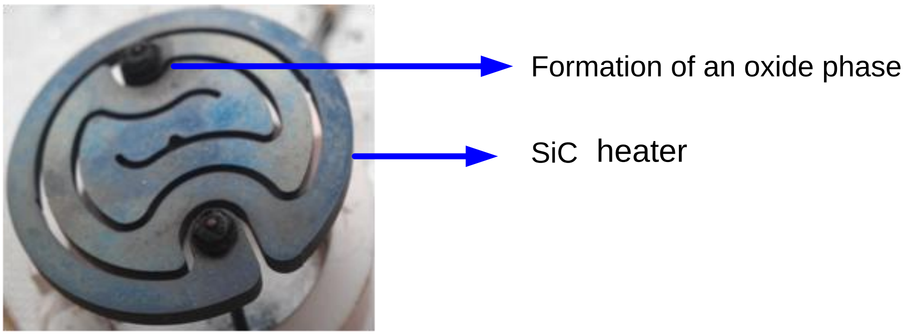

Figure 3.7. SiC heater.

Therefore, a new resistive heater has been designed. The heater is made of FeCrAl alloy, which is commercially known as Kanthal A1 (Sandvik materials technology). This material has been designed for high temperature applications and is durable up to temperature of 1673 K. A specific shape was designed to achieve a homogeneous heat distribution on the catalyst surface. Total resistivity is calculated to be 1.3 Ω with a total resistance length of 0.9 m and thickness of 2 mm. The material was machined by laser technique by “Technishe Infrastructure und Dienste”, Karsruhe Institute of Technology (KIT). The heater is directly located above the catalytic surface (Figure 3.8). Techical details of the heater are given in Figure 3.9 .

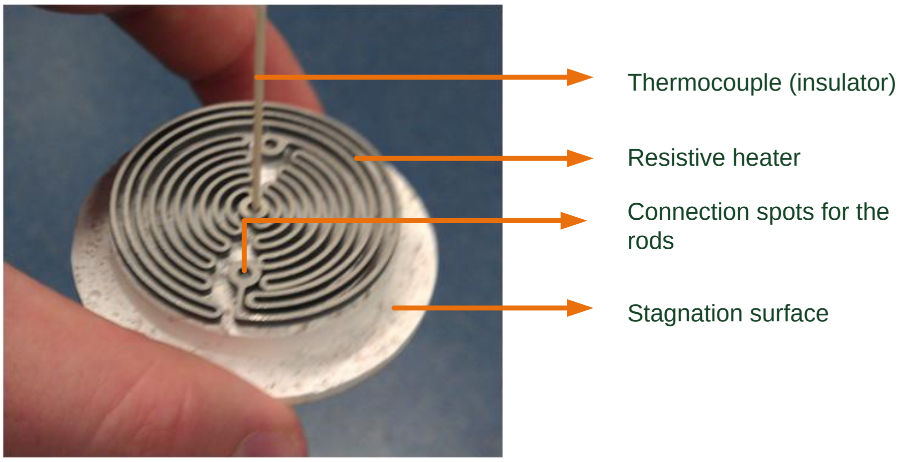

Figure 3.8. Newly designed resistive heater.

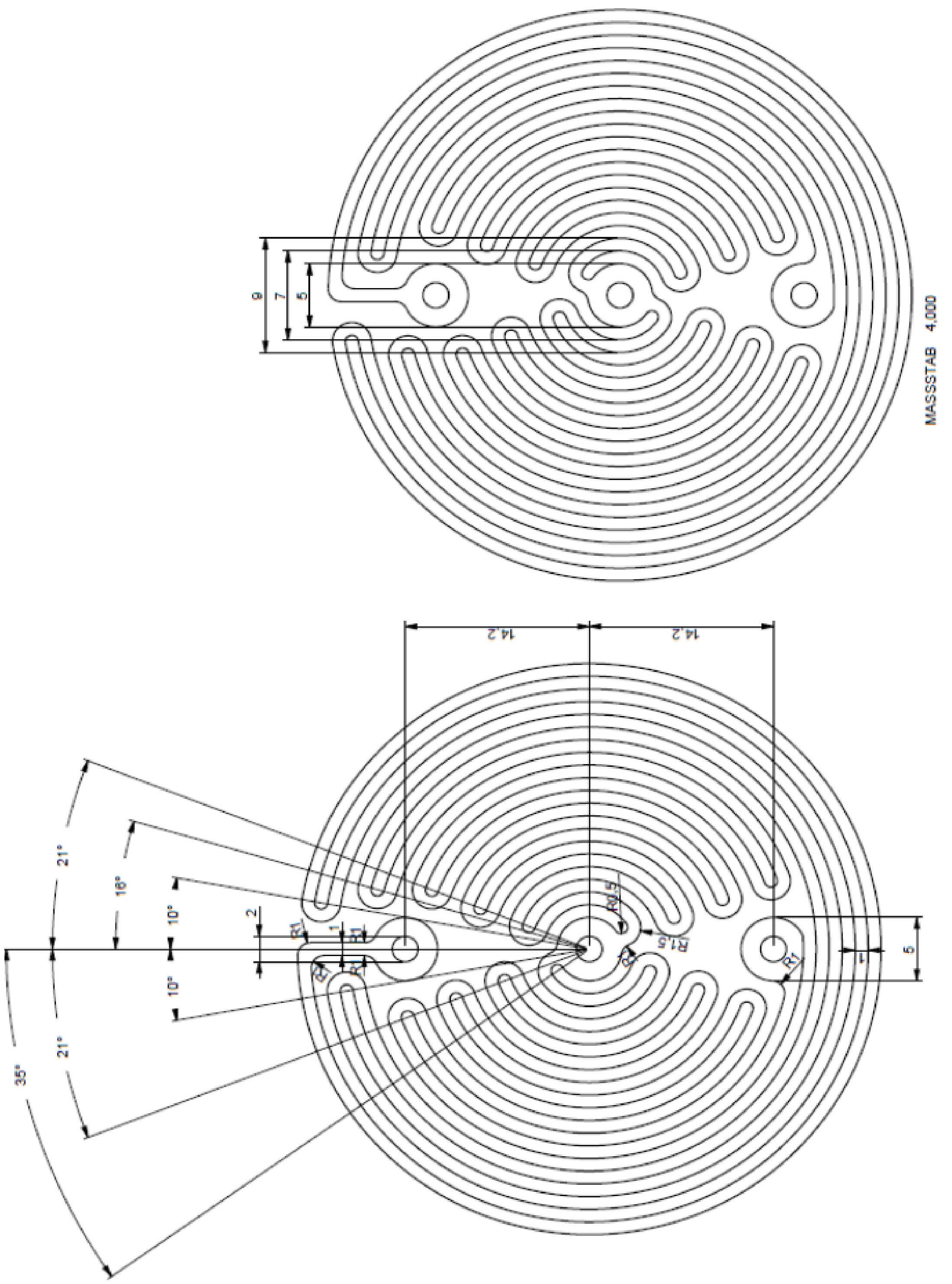

Figure 3.9.Technical details of the resistive heater

Stainless steel (316L, 1.4404) rods which have 2 mm radius and 7 cm length, are used for power connection. Nuts and washers are also made of the same material. The heater and the catalyst are placed in a ceramic housing and attached to the pedestal as shown in Figure 3.5

.

3.1.4 Analytics

A chemical ionisation mass spectrometer (MS) (Airsense 500, V&F) and a H_2 sensor (H-Sense, V&F) as well as FTIR (MKS, MultiGas^{TM} 2030 Model) are used simultaneously to analyze the product composition. O_2 is detected by the MS, H_2 is detected by the H-Sensor and the FTIR is used for the detection of CO, CO_2 and hydrocarbon species (CH_4, C_2H_6 and C_3H_8) as wet-basis. H_2O is calculated via O_2 mass balance. The properties of the analytics are briefly given in this chapter.

Mass Spectrometer

Principally, mass spectrometers work based on the separation of ionized molecules or their fragments according to their mass-to-charge ratios (m/z). Mass spectrometers work under high vacuum to avoid any collisions between the ionized molecules and to ensure a free mean path until they reach the detector.

The Airsense 500, V&F model mass spectrometer was preliminary designed for automotive gas after-treatment applications in which fast analyses of outlet gas compositions with high flow rates are desired. It is a chemical ionization mass spectrometer. A sample is ionized through the exchange of charges between the charged source gas ions and the molecules under examination. Each type of source-gas ion has its characteristic energy krypton (Kr) 14.0 eV, Xenon (Xe) 12.13 V and mercury (Hg) 10.54 eV). The source-ion gases are selected by the user occording to the species that will be analyzed. For example, for O_2, Xe is selected as the source gas whereas for CO and CO_2 species Kr should be selected. The ionizied species are detected by a quadrupole mass filter coupled with an ion molecule reaction (IMR) technique, which ensures fast and selective detection without interference. The detection range of the mass filter is 0-500 atomic mass unit (amu) [93].

H_2-Sensor: H-Sense [94]

Since H_2 can not be detected by the mass spectrometer used in this study, a H_2 sensor (H-Sense, V&F) is additionally used. H-Sense is an electron pulse ionization mass spectrometer. The sample ions are energized, focused and separated further on in a magnetic field in order to detect only H_2 and He (Figure 3.10).

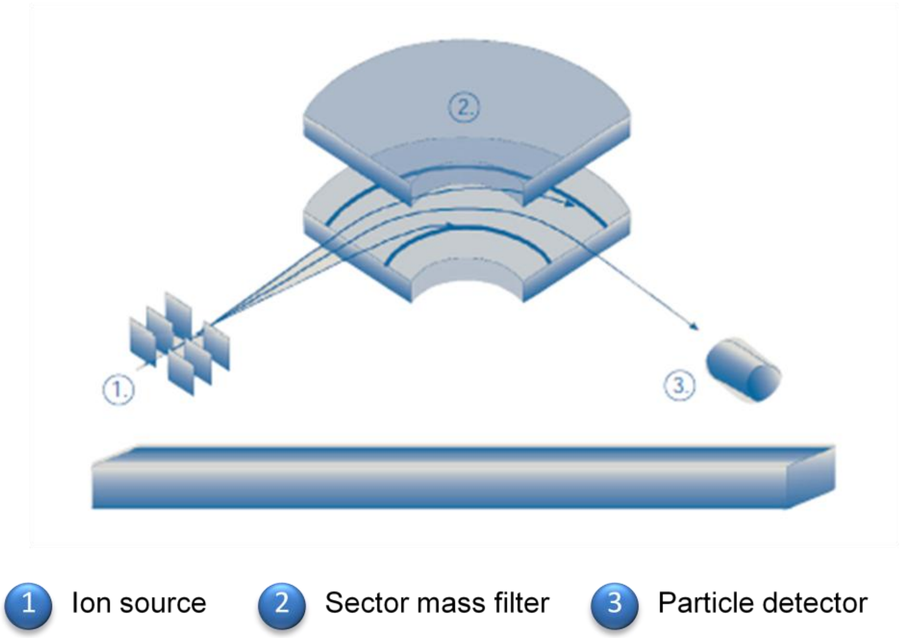

Figure 3.10 Working principle of H-Sense.

The analytic is optimized to measure mass range of 2-4 amu with the overall response time less than 1 second in a fast, dynamic and on-line manner.

Fourier Transform Infrared (FTIR) Spectrometer [95, 96]

Fourier transform infrared spectroscopy (FTIR) is a rapid and non-destructive measurement technique for qualitative and quantitative analysis of organic or inorganic compounds either in solid, liquid or in gas-phase. The measurement technique is based on absorption spectroscopy. When a material is irradiated with infrared radiation, the absorbed IR radiation usually excites molecules into a higher vibrational state. Chemical bonds vibrate at a characteristic frequency representative of their structure, bond angle and length. Individual molecules have the ability to interact with incident radiation by absorbing the radiation at a specific wavelength. A qualitative analysis of the sample is determined by the definition of a specific absorption band which is like a finger print of the molecule. Traditional infrared spectrometers are of the dispersive type. This means that, the instrument separates the individual frequencies of energy emitted from the infrared source. The technique has limitations due to the slow scanning process. In a sample containing multiple species, a method is needed for measuring all of the infrared frequencies simultaneously, rather than individually. The FTIR technique was developed as a the solution of this problem.

FTIR spectroscopy works based on the idea of the interference of radiation between two beams yielding an interferogram. The latter is a signal produced as a function of the change of path length between the two beams. The two domains of distance and frequency are interconvertible by Fourier transformation. The basic components of an FTIR spectrometer are schematically shown in Figure 3.11. The radiation emerging from the source is passed to the sample through an interferometer before reaching a detector. Upon amplification of the signal, in which high-frequency contributions have been eliminated by a filter, the data are converted to a digital form by an analog-to-digital converter and transferred to the computer for the fourier transformation

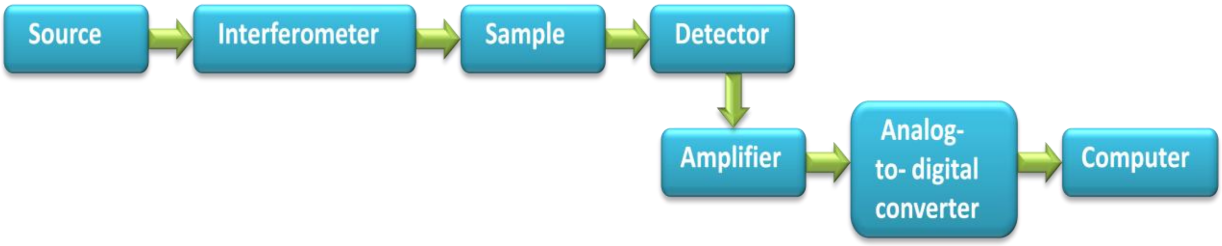

Figure 3.11 Basic components of a FTIR spectrometer.

Like most common FTIR spectrometers, MKS MultiGas^{TM} 2030 Model FTIR includes a Michelson interferometer, which consists of two perpendicular plane mirrors, one of which can travel in a direction perpendicular to the plane. Detailed information can be found elsewhere [96].

3.1.5 Gas Sampling and Measurement Technique

The concentration profiles of the species within the boundary-layer are measured by a microprobe sampling technique. A quartz microprobe with a 50 µm opening and a bend angle of 15^{o} is used. The microprobe has the dimensions of 3 mm OD and 1mm ID, however, on the tip where the sampling is performed the microprobe OD is <0.4 (Hilgenberg GmbH). This configuration allows close contact to the catalyst surface. The probe is positioned at a radial distance of nearly 0.8 cm from the center to eliminate the edge effect and provide as little disturbance to the flow field as possible (Figure 3.12).

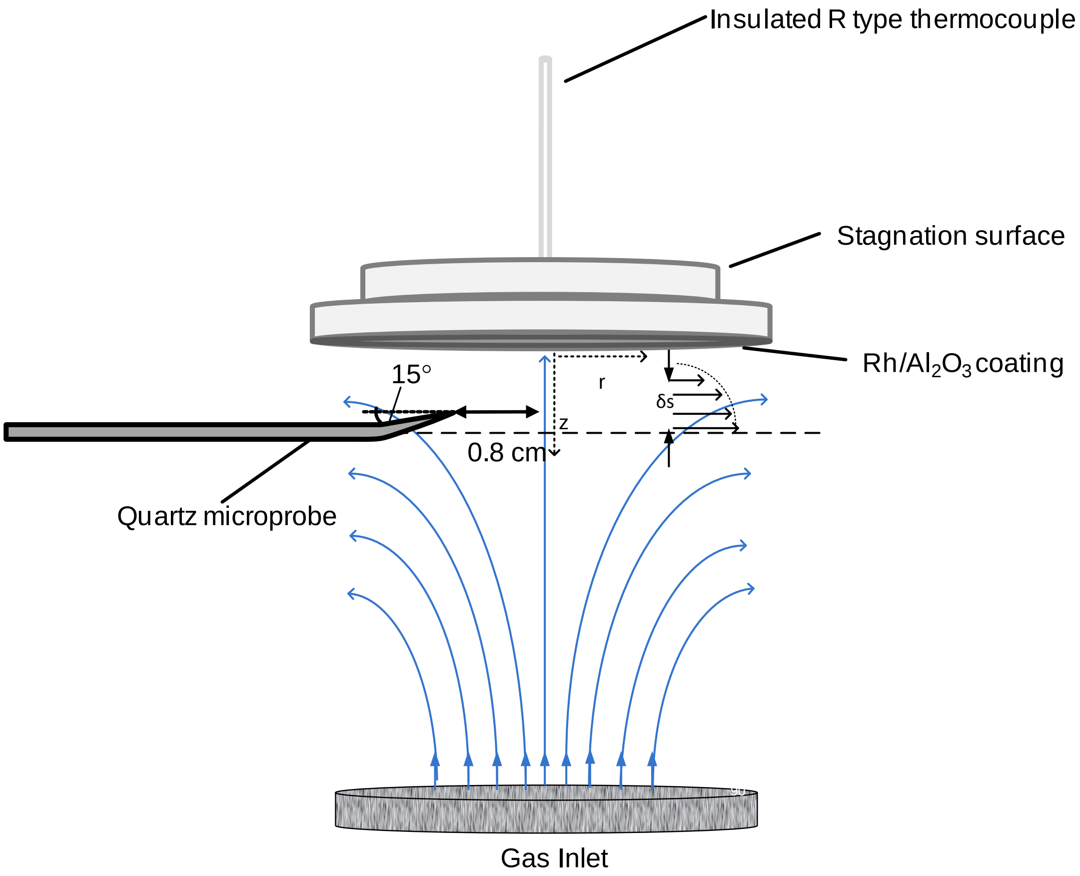

Figure 3.12. Stagnation-flow regime and sampling technique.

The position of the microprobe in the boundary-layer is controlled by a step motor controller (Thermionics Northwest, Inc.). Initially, the microprobe is positioned on the surface and the probe-surface contact is determined visually. Starting from the position of this zero point, the probe is moved downward through the boundary-layer in steps of 0.5 mm. The concentration profile of the species is detected at steady-state temperature.

All analytics used in this study are designed for continuous-flow measurements. To analyze a small amount of sample taken from the reaction zone, a six-port valve (VICI Valco Instruments Co. Inc) configuration is adapted (Figure 3.13).

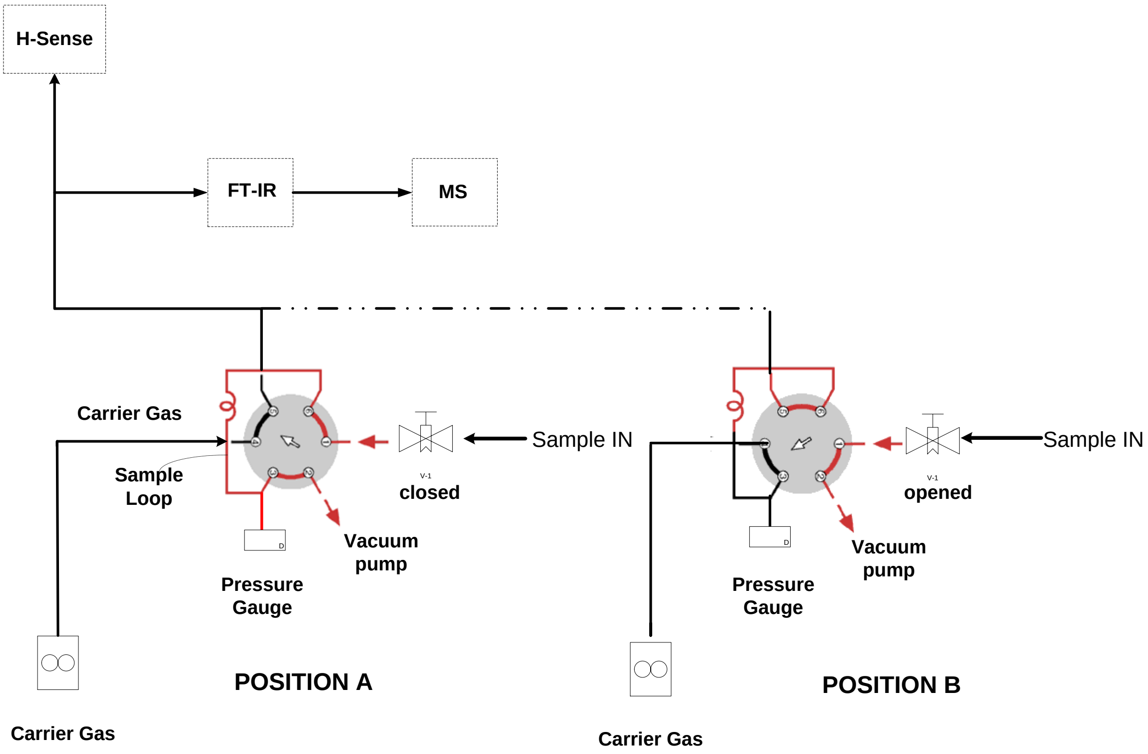

Figure 3.13. Six-port valve configuration and sampling technique

At the each axial measurement point, a defined amount of gas is sampled and injected to the analytics via the six-port valve configuration. At the valve position A, the sample loop (2 ml) is directly connected to the vacuum pump and evacuated. In this position the valve between the sample loop and the reactor is closed. By opening this valve, the loop is filled with the sample at a constant pressure and at room temperature (420 mbar under the conditions that reactor is working at 500 mbar). Changing the valve position to B, this defined amount (with given pressure, volume, and temperature) is injected into the analytics by Ar carrier gas. The total flow rate is 1.4 SLPM (standard liter per minute at 293 K and 1 atm) and the flow is split into two directions by using a regulating valve. 0.9 SLPM of the total flow is fed to the H-Sense and the rest is fed to the FTIR and the outlet of the FTIR is connected to MS inlet. By this way CO, CO_2 and hydrocarbon species simultaneously analyed by FTIR and MS, whereas O_2 is detected by MS. Injections are repeated four times for each measurement point (at axial position of the tip) to assure repeatability. To avoid possible disturbance effects during the sampling, the system is held four minutes between the injections to achieve a new steady-state.

After the boundary-layer is resolved, the catalyst is regenerated before starting the next experiment in which the catalyst temperature or inlet composition has changed. The catalyst is oxidized at 773 K for 30 min with 5 vol.% O_2 diluted in Ar and reduced for 30 min with 5 vol.% H_2 diluted in Ar with 5 SLPM.

1 vol.% H_2 (Air liquide N50) is used to calibrate the H-Sense. Direct calibration of MS is performed by using 250 ppm O_2 in Ar dilution (Air liquide) and furthermore 1.5 vol.% O_2 in Ar dilution (Air liquide 4.8) is used for sampling loop calibration. The FTIR is calibrated by two

different gas mixtures that contain: 2 vol.% CO, 2 vol.% CO_2 in Ar dilution and 4.94 vol.% CH_4 as well as 5.03 vol.% C_3H_8, 4.99 vol.% C_2H_6, 5 vol.% C_3H_6, 5 vol.% C_2H_4 and 5 vol.% C_2H_2 diluted in Ar (Basi gas).
The six-port valve is connected to the calibration gas mixtures, and by varying the injection pressure, multi-point calibration curves are created in the desired range of detection. To assure the repeatability, injections are repeated four times for each calibration point as well.

As a result of the injection mode, Gaussian peak signals are observed in all analytics used. Quantitative analysis of the species are performed based on the integration of these Gaussian peaks using the trapezoidal rule [97].

3.1.6 Resolution of the Boundary-Layer: Effect of the Operating Pressure

The selection of the operating pressure is crucial for obtaining a well-defined stagnation-flow. In the laminar regime, the Reynolds number (Re) lies in the range of 500≤Re≤2000. High axial flow rates are necessary to direct the flow to the stagnation surface without distortion and vorticity (potential flow).
The flow is nearly inviscid over most of the domain, whereas viscous and diffusive transport effects become important in a thin region near the surface where boundary-layer is formed. There are momentum and thermal boundary-layers present in this region denoted by δ_s and δ_T respectively. If that the viscous diffusion effect is stronger than the thermal diffusion, $\delta_s > \delta_T$ [89].
When the uniform stagnation-flow field is established, the effect of the Re number on the momentum boundary-layer thickness is given with the expression here below:

$$\delta_s = \frac{z}{Re^{1/2}}\left[\frac{0.2365}{Re^{1/2}} + \left(1.892 + \frac{0.0559}{Re}\right)^{1/2}\right] \quad . \qquad 3.1$$

$$Re = \frac{zu\rho}{\mu} \quad . \qquad 3.2$$

The resolution of the thermal and momentum boundary-layer thickness with enough experimental data is crucial for stagnation-flow reactor experiments. To create a potential flow, instead of using high flow rates at atmospheric pressure, the inlet velocity is increased while decreasing the operating pressure:

$$\rho = \frac{pM}{RT}, \qquad \rho = \frac{m}{u} \quad and \quad \frac{p_1}{p_2} = \frac{u_2}{u_1} \qquad 3.3$$

If p_1 is selected to be a reference pressure of 1 bar, decreasing the pressure (< 1 bar) will increase the axial flow velocity [49]. According to Eq. 3.2, increasing the flow rates will yield a higher Re number which will result in a decreased boundary-layer thickness (Eq. 3.1)

A series of CO oxidation experiments were carried out at three different working pressures to define the optimum working pressure (Table 3.1). The stagnation disk is coated with a Rh/Al_2O_3 catayst. Detailed information on catalyst preparation will be given in Chapter 4. The experiments are carried out with a total flow rate of 15.5 SLPM. 2.67 vol.% CO and 2.23 vol.% O_2 are diluted in Ar and fed to the reactor. The inlet temperature was measured to be 313 K. Boundary-layer profiles of CO and CO_2 were measured at a surface temperature of 473 K. Only MS was coupled for resolution of the boundary-layer. The calculated density (ρ) and inlet velocity (u) are given in Table 3.1.

Table 3.1 Effect of pressure on inlet velocity and density.

Pressure, p mbar	Density, ρ (kg/m^3)	Inlet velocity, u m/s
300	0.21	0.82
500	0.35	0.50
750	0.53	0.33

A comparison of the CO concentration profiles along the boundary-layers is presented in Figure 3.14. Physical appearance of the boundary-layer is assumed to start at the point where the CO concentration reaches its inlet value.

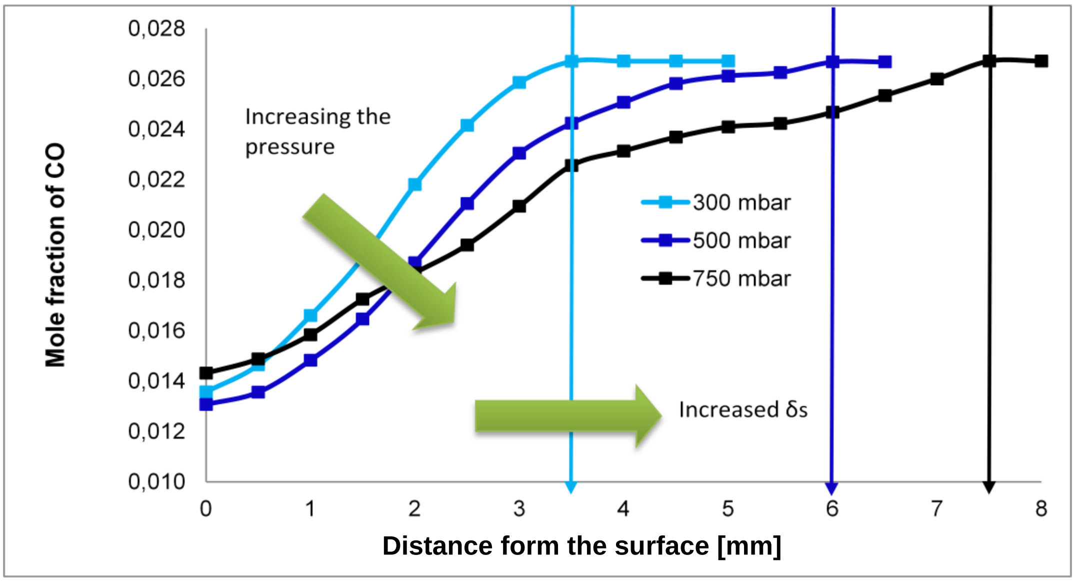

Figure 3.14. Effect of pressure on boundary-layer thickness.

At a working pressure of 300 mbar, the CO concentration profile reaches its inlet value at 3.5 mm, thus, increasing the pressure results in an increased boundary-layer thickness as expected. At a working pressure of 750 mbar, the boundary layer is considerably thick (7.5 mm). Since the surface temperature is quite low, at high temperature regimes (> 873 K) an increased boundary-layer thickness is expected due to the effect of the temperature on molecular diffusion. For the pressure of 300 mbar, enough data points are collected within the boundary-layer. However a problem arises due to the accuracy in sampling and measurement due to the detection limit of the analytics. The amount of the sample taken from the reactor is limited by the working pressure. At 300 mbar working pressure, the sampling loop pressure is 220 mbar. The concentration of the species in the sampling loop is proportional to sampling loop pressure. This pressure range does not satisfy the detection limit of the analytics.

On the other hand, at 500 mbar working pressure, the boundary-layer thickness (6 mm) is measureable and the measurements show a good sampling accuracy. All catalytic measurements investigated in this study are carried out at 500 mbar, whereas the ignition studies (Chapter 5.1) are carried out at 300 mbar.

4. CATALYST PREPARATION AND CHARACTERIZATION

4.1 Catalyst Preparation

The flat stagnation disk is coated with Rh/Al_2O_3 catalyst. Appropriate amounts of aqueous solution of rhodium (III) nitrate (Umicore) (9 wt.% Rh)) and boehmite (AlOOH) (20 % boehmite) are mixed to obtain a 5 wt.% Rh/ Al_2O_3 composition. The solution is diluted with water and applied to the disk by the spin-spray technique to ensure a homogeneously distributed catalytic layer on the surface. Coating a flat surface with a well-defined particle size and morphology is essential for the stagnation-flow reactor application [98, 99]. For this purpose a simple laboratory-scale spray apparatus has been developed. The stagnation surface is heated to 373 K and held on a rotary support which spins at 1000 rpm. The solution is sprayed by compressed air via a spray gun. The surface is dried at 403 K for 10 min and the procedure is repeated until the desired coating thickness of 100-130 μm is achieved. The coated stagnation surface is then calcined at 973 K for 2 h in air. Prior to the measurements, the surface is oxidized by 5 vol.% O_2 diluted in Ar at 773 K for 2 h. The resulting rhodium oxide phase is reduced by 5 vol.% H_2 diluted in Ar at 773 K for 2 h.

Then the catalyst is attached to the ceramic twist lock cap by using a ceramic glue (Resbond 989) (Figure 3.5).

4.2 Catalyst Characterization

The catalyst is subjected to light microscopy (LM), scanning electron microscopy (SEM) and high resolution transmission electron microscopy (HR-TEM) investigations to examine bulk structure, the Rh particles and the active metal-support interactions. The active metal surface area is measured by CO chemisorption. In this chapter, the LM, SEM and HR-TEM characterization methods are briefly introduced and the results are discussed. Since there is no available chemisorption measurement technique for stagnation surfaces, a continuous-flow chemisorption measurement technique is developed. Detailed information on the development of this method is given in Chapter 4.2.4.

4.2.1 Light Microscopy

A metallurgical light microscope works based on the measurement of reflected light from the material. A specimen is illuminated through the objective lens by light from a lamp or arc source. This light is focused by the condenser lens into a beam that is directed approximately parallel to the optical axis of the microscope by a half silvered mirror. The light then passes through the objective and falls onto the specimen. It is then reflected from the surface of the specimen, back through the objective, the half silvered mirror, and the ocular to the observer's eye, or to a camera port or a film plane. The magnification of the analytics is 1000 and it has a limit of resolution of ~2000 Å [100, 101].

A metallurgical light microscope (LM: Rechert MEF4A) is used for the determination of the catalytic layer on the stagnation disk. The coating thickness and the homogeneity of the layer are investigated by means of LM technique.

Figure 4.1 shows a LM image of the cross-sectional area of the used catalyst after the experiments. In this image, a Rh/Al_2O_3 layer of roughly 100 μm is deposited on the stagnation disk. Since the Al_2O_3 substrate has a porous structure, the coating first fills these pores, and it is shown in the image that a second layer is created which is roughly 30 μm thick and behaves like a flat surface, as is expected from a stagnation surface.

The repeatability of the procedure is tested by coating a second disk which shows a total coating thickness of 130 μm and a second coating layer of 25 μm.

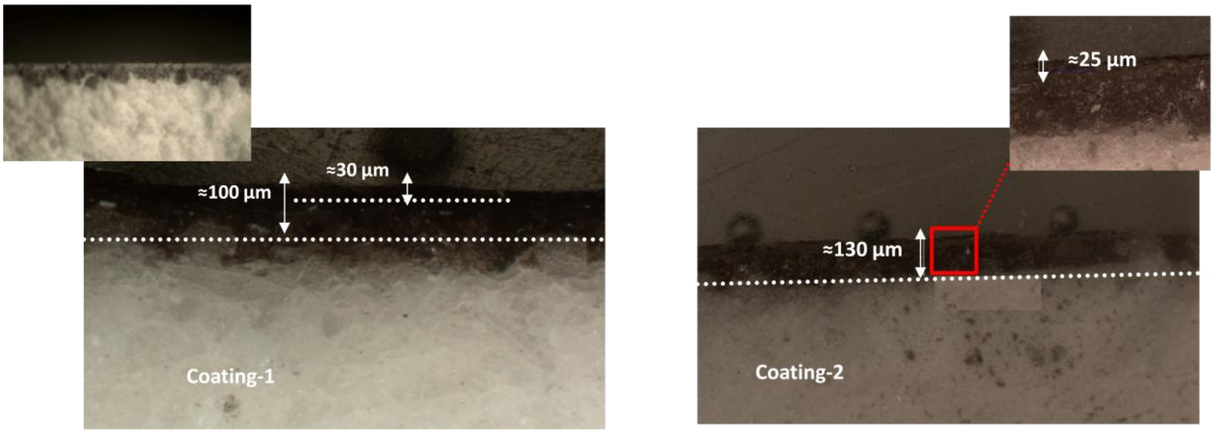

Figure 4.1. LM images of the catalyst.

4.2.2 Scanning Electron Microscopy [101, 102]

A scanning electron microscope provides detailed high resolution images of the sample with magnifications of up to $1x10^5$ by rastering a focused electron beam across the surface and detecting secondary or backscattered electron signals. An energy dispersive X-Ray analyzer (EDX or EDA) is also used to provide elemental identification and quantitative compositional information. This technique allows submicron scale features to be observed, which is well beyond the range of optical microscopes.

A normal scanning electron microscope operates at a high vacuum. The basic principle is that a beam of electrons is generated by a suitable source, typically a tungsten filament or a field emission gun. The electron beam is accelerated by a high voltage (typically 30 kV) and passes through a system of apertures and electromagnetic lenses to produce a thin beam of electrons. Then, the beam scans the surface of the specimen by means of scan coils. Electrons are emitted from the specimen by the action of the scanning beam and collected by a suitably-positioned detector.

Scanning electron microscopy (SEM: Hitachi S570), in combination with energy-dispersive X-ray spectroscopy (EDX), is applied to characterize the support and the metal interaction. Rh metal particles are investigated after the catalytic measurements. SEM images reveal a porous alumina structure where Rh particles ~100-150 nm diameter are attached to the surface (Figure 4.2).

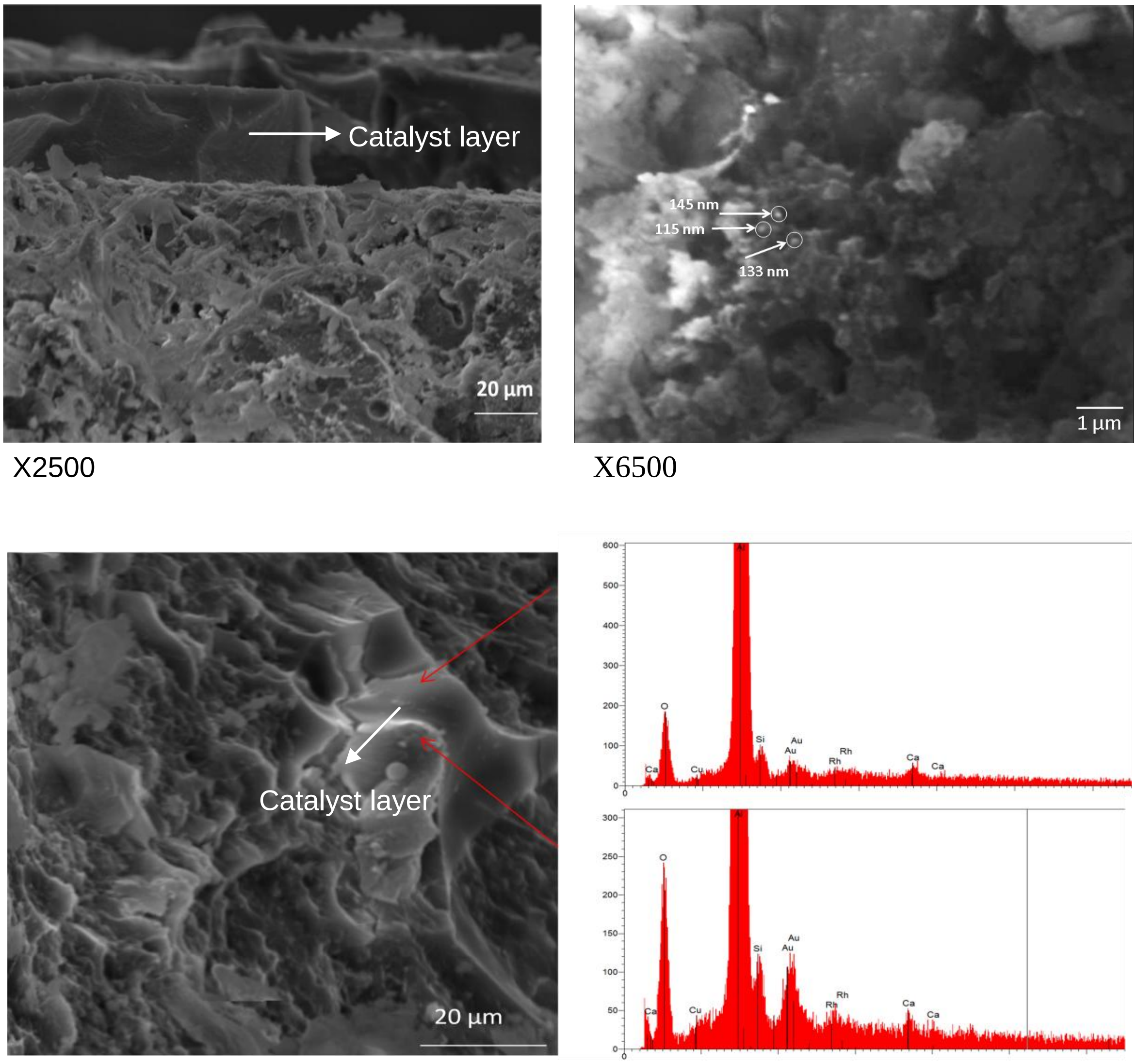

X2500

X6500

X2200

Figure 4.2. SEM-EDX images of the catalyst.

The Rh particles are also detected by EDX. Also, large amounts of silica are detected that originates from the boehmite solution.

4.2.3 High Resolution Transmission Electron Microscopy (HR-TEM) [103, 104]

The transmission electron microscope is used for a detailed investigation of the lattice structure of the specimen. This technique uses a high energy electron beam transmitted through a very thin sample to image and analyze the microstructure of materials with atomic scale resolution. Lattice images of the specimen can be obtained by selection of a large objective aperture that allows many beams to pass including the direct beam. The image is formed by the interference of the diffracted beams with the direct beam (phase contrast). If the point resolution of the microscope is sufficiently high and a suitable crystalline sample is oriented along a zone axis, high-resolution TEM (HR-TEM) images are obtained. In many cases, the atomic structure of a specimen can directly be investigated by HR-TEM. Magnification can be up to X200000.

HR-TEM (Philips CM200 FEG) is used to characterize the catalyst after catalytic measurements. Unlike in the SEM investigations, smaller Rh particles of 15-50 nm are mostly detected. Besides, some Rh particles smaller than 10 nm are also visible (Figure 4.3). The diverse particle size distribution can be attributed to the possible agglomeration of the smaller Rh particles during the catalytic reactions.

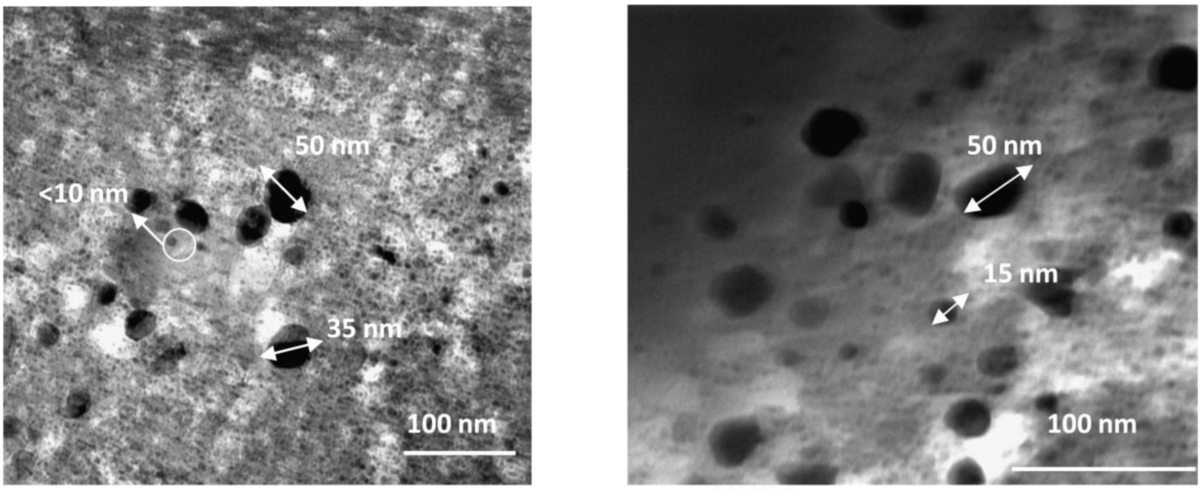

Figure 4.3.TEM images.

4.2.4 CO Chemisorption: Development of a Continuous-flow CO Chemisorption Measurement Technique

The active metal surface area of the catalyst is measured by a CO chemisorption technique. Although there are commercially available techniques for the catalyst in powder, pellet or crushed monolithic structure, no technique is available for the measurement of a flat catalytic surface which is used in the stagnation-flow reactor experiments. All the data derived from commercial techniques are based on the small sample which is thought to be representative for the whole bulk structure of the catalyst. Besides, since the catalyst is destroyed, a direct comparison of the chemisorption data from before and after the catalytic measurements is not possible.

In this chapter, the development of a continuous-flow CO chemisorption technique is discussed. The aim of this study is to establish a simple and rapid chemisorption technique for the quantification of metal dispersion on different types of supported metal catalysts as well as of the different structures, such as monoliths, pellets, and granules, without using a sophisticated apparatus and UHV conditions. Such a technique cannot only help to

understand the catalytic behavior under operating conditions, i.e., at atmospheric pressure and in flow, but the same apparatus can also be used to repeatedly study the kinetics and temperature programmed desorption (TPD) upon certain treatments (aging, poisoning, and storage of adsorbates). Here, exemplarily results are presented for diesel oxidation catalysts (DOC). The catalyst is Pt/Al_2O_3, which is washcoated onto a honeycomb-structured cordierite monolith. In order to compare the dispersion data, which were achieved by means of the method, which is presented here, with data from commercial devices, the monoliths were crushed and used in a fixed-bed reactor configuration. The method has been validated by different techniques from different research institutes/commercial set-ups.
The application of the method on a technical Rh/Al_2O_3 catalyst in a monolithic structure is shown in chapter 4.2.5 Furthermore, the CO chemisorption measurement on the stagnation surface is explained in detail in chapter 4.2.6.

4.2.4.1 Theoretical Background

Gas adsorption is a very frequently used method for the characterization of heterogeneous catalysts in order to quantify the active surface area of the supported metal catalysts such as Pt, Pd, and Rh [105, 106] and determine the metal dispersion of fresh and used catalysts. In exhaust gas after-treatment, for instance, the reduction in conversion of pollutants due to on-road aging of the catalysts (Pt, Pd, and Rh) is directly related to the total number of adsorption sites available for CO chemisorption [107, 108]. The effects of catalyst agglomeration, loss, and poisoning on the overall reaction rate could be governed by a single scalar, i.e. the number of active sites available for CO chemisorption.

Metal dispersion is expressed as the ratio of the total number of metal atoms on the metal surface accessible to the adsorbate species to the total number of metal atoms in the sample [109]. H_2 and CO are the most frequently used probe molecules [110, 111]. In the past, the understanding of surface properties of transition metals and metal oxides was often based on the studies of ultra-high vacuum conditions (UHV). However, chemisorptive and catalytic properties at atmospheric conditions may significantly differ from those at UHV conditions [110].

CO TPD under continuous-flow has been studied before. Foger and Anderson [112] showed that a considerable amount of CO_2 was detected when TPD of chemisorbed CO was carried out on Pt/Al_2O_3 catalysts. They also showed that a considerable amount of CO_2 desorbed above 450 K and the desorption spectra reached their maxima at 820 K. It was generated by a reaction between CO and the residual water that originated from the dehydrated ɣ-alumina support [112]. Dropsch and Baerns worked with Pd/Al_2O_3 catalyst and showed that CO_2 was generated via the Boudouard reaction of CO when CO_2 reached a significant level above 500 K [113]. Another study performed by Lear et al. showed that CO oxidation was significant above 500 K and reached its maximum at around 760 K when water gas shift reaction took place between chemisorbed CO and the hydroxyl groups associated with the alumina support [114]. Föttinger et al. also showed that WGS reaction is generated between the adsorbed CO and OH species on the support of Pd/Al_2O_3 catalyst [115].

In this study, a considerable amount of CO_2 desorption was observed during CO chemisorption TPD on a Pt/Al_2O_3 catalyst. To investigate the origin of the CO_2 formation, a CO pulse technique was applied to measure the adsorbed amount of CO and quantify the desorbed amount of CO and CO_2. Adsorption studies were carried out at different temperatures to investigate the oxidation behavior of the adsorbed amount of CO on the surface. Dispersion results based on the measured CO and CO_2 signals were compared with CO chemisorption and H_2 dispersion data obtained in commercial devices. Additionally, CO oxidation was studied in the same continuous-flow apparatus by measuring the CO conversion as a function of temperature.

4.2.4.2 Experimental

Catalyst

The catalyst studied is a commercial honeycomb-structured diesel oxidation catalyst made of cordierite with 0.114 wt.% Pt loading dispersed in an Al_2O_3 washcoat (DOC20). The specific surface area of the catalyst is determined by nitrogen adsorption at 77 K with the Brunauer Emmett Teller (BET) method. The BET measurements are carried out in a Belsorb Mini II apparatus.

Experimental Set-up

A continuous-flow reactor set-up was designed to be used for both adsorption and desorption studies under atmospheric pressure as shown in (Figure 4.4). Ar, H_2, and CO gases are fed to the reactor by mass flow controllers (MKS) for the continuous-flow applications.

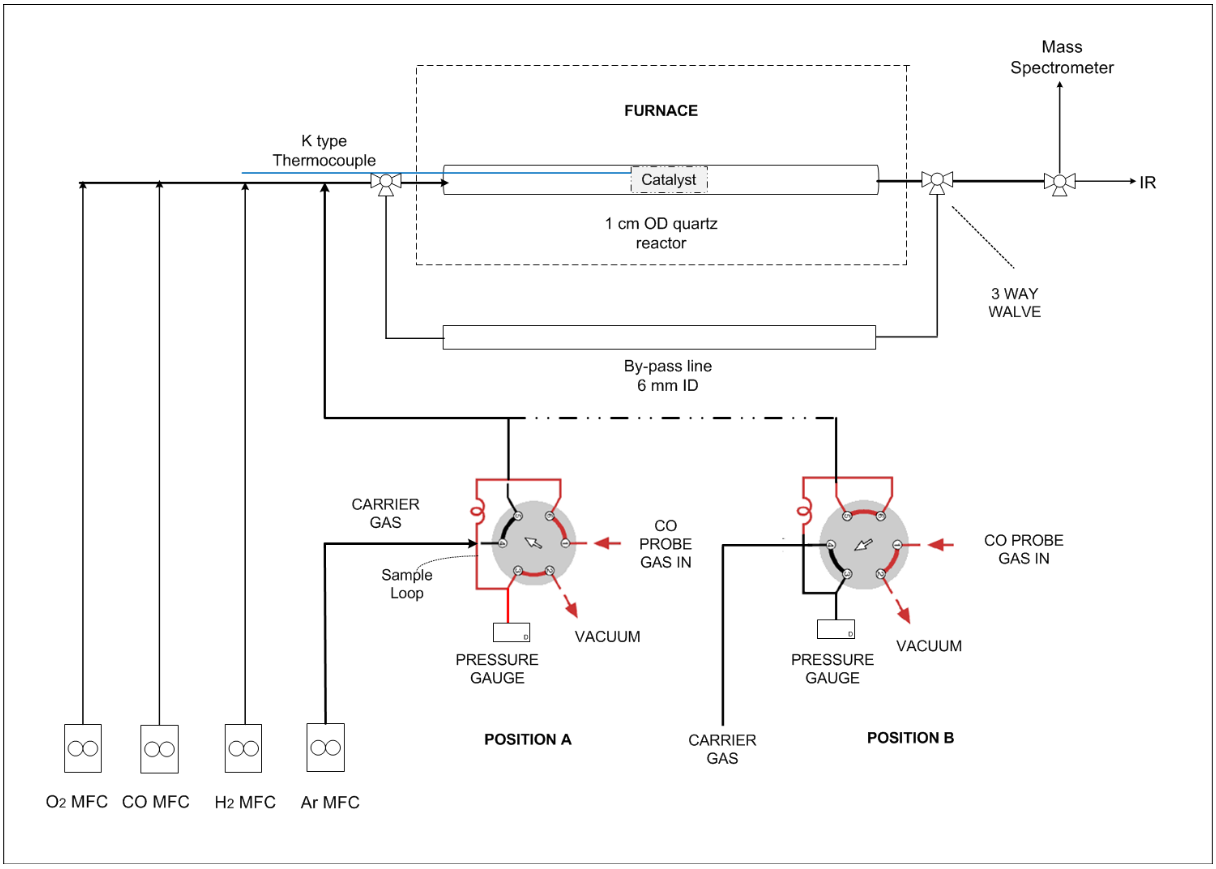

Figure 4.4 Experimental set-up for continuous-flow CO Chemisorption TPD and CO pulse adsorption measurements

An automated six-port valve (VICI Valco Instruments Co. Inc.) configuration is applied to generate pulses for the adsorption studies. When the six-port valve is at position A, it is connected to a vacuum pump and the sample loop (0.26 cm^3) is evacuated. Then the loop is filled with pure CO at constant pressure (600 mbar) and room temperature. Having thus defined volume, pressure, and temperature, $6.3x10^{-3}$ mmol CO is loaded in the sample loop. By changing the six-port valve's position to B, this defined amount of CO in the sample loop is pulsed to the reactor. The system works with different structures of catalyst supports, such as pellets, powders, or monoliths. For this purpose, two different reactor configurations are established. In this study, the catalyst was crushed and placed in a 10 mm outer diameter (OD) quartz reactor to reduce dead volume. For monolithic structures, a 25.4 mm OD quartz reactor is used instead. The catalyst is positioned in the center of the reactor and fixed there with quartz wool.

The reactor is housed in a temperature-controlled furnace and the temperature inside the catalyst bed is measured by a K-type thermocouple (NiCr-Ni, 3 mm thick). The system has a by-pass line with 6 mm OD made of stainless steel, which is designed for sample loop calibrations. Flow directions between the reactor and the by-pass line can be controlled by three-way valves. The outlet gas is connected to a chemical ionization mass spectrometer (MS) (Airsense 500, V&F) and an infrared detector (IR) (BINOS 100, Emerson Process). MS is used for detailed investigations, and O_2, CO, and CO_2 species are detected, whereas for repeated measurements, IR is chosen to measure CO and CO_2 species. Flow direction between MS and IR is controlled by means of a three-way valve configuration.

Measurements without Catalyst

For the quantification of amount of possible adsorbed CO by the sealings and quartz wool, the reactor is first operated without catalyst. The empty reactor (10 mm OD with quartz wool) is subjected to the continuous-flow CO adsorption measurement. The pre-treatment procedure is applied and a TPD measurement is carried out. CO, CO_2, and O_2 species are analyzed in the outlet gas composition by using an MS.

Continuous-flow TPD Studies

The amount of 1 gram of the crushed monolith catalyst is placed in a quartz tube reactor leading to a 30 mm catalyst bed. The total flow rate in the reactor always is 1 SLPM. Since MS requires high flow rates, measurement are carried out with 1SLPM total flow, whereas in case that IR is used measurement are carried out with total flow rate of 0.5 SLPM.

Before the analysis, the catalyst is subjected to a pre-treatment procedure. For this purpose, the catalyst is first oxidized by 21 vol.% O_2 (Air Liquide, 99.95 % purity), diluted in Ar (Air Liquide, 99.996 % purity), with a total flow rate of 1 SLPM for 1 h at 773 K. After flushing with Ar for 30 min, the catalyst is reduced by 4 vol.% H_2 (Air Liquide, 99.996 % purity) in Ar at 673 K for 1 hour.

For the TPD measurement, the reactor is cooled down to room temperature (290 K). Then, 1 vol.% CO (Air Liquide, 99.97 % purity), diluted in Ar, is fed to the reactor for 1 h to saturate the metal surface. Physisorbed CO is removed by flushing with Ar gas for another 30 min at room temperature. TPD is performed with a heating rate of 28 K/min from room temperature to the maximum temperature of 790 K under continuous Ar flow. The heating rate of 28 K/min was chosen for achieving a better signal/noise ratio. Similar heating rates were also used in literature (3-50 K/min) [112-114, 116]. The heating rate only affects the desorption profile of the peaks. Higher heating rates yield sharp peaks, whereas lower heating rates result in wider peak shapes. 28 K/min is the maximum heating rate of the oven and yields reasonably sharp peak spectra that permit repeatable analysis.
The outlet gas composition is monitored during the TPD.

CO Pulse Adsorption at Room Temperature

To investigate the origin of CO_2 peaks derived during continuous-flow CO TPD measurements, a CO pulse technique is applied at atmospheric pressure and room temperature. First, the pre-treatment procedure is applied for the continuous-flow TPD measurements. CO pulses are injected by means of the automated six-port valve configuration. The defined amount of pure CO ($6.30x10^{-3}$ mmol) is pulsed to the reactor in 1 SLPM Ar carrier gas. Between the pulses, the reactor is kept under 1 SLPM Ar flow. The outlet gas composition is monitored by the MS. Desorption of CO and CO_2 species is detectable as Gaussian peaks. The pulsation is continued until desorption peaks reach the saturation value. In practice the pulsation was terminated when two consecutive CO peaks resulted in an equal amount of CO observed according to the peak area. The CO pulsation is followed by a TPD measurement carried out between the temperatures of 290 K and 790 K with a fixed ramp of 28 K/min.

CO Pulse Adsorption at High Temperatures

CO pulse adsorption measurements are also carried out at higher temperatures. After the same pre-treatment procedure as described above, the reactor temperature is raised to the 367 K, 427 K, 527 K, 573 K temperature points, respectively, in Ar carrier gas. CO is pulsed at these temperatures and pulse measurements are carried out. CO and CO_2 species are detected by an MS coupled to the outlet gas stream. After saturation is observed, a TPD is carried out again.

CO Pulsing on a O_2 Pre-covered Pt Surface

To analyze the effect of pre-adsorbed O_2, CO pulse adsorption is carried out on an O_2 pre-covered surface. The pre-treatment procedure is applied as described above (oxidation and reduction). After the reduction, 10 vol.% O_2 is continuously fed to the reactor and the surface is saturated by O_2 at room temperature (290 K). After flushing the physisorbed O_2 with Ar carrier gas, CO pulses are injected at room temperature. CO pulsation and TPD studies are conducted.

Determination of Metal Dispersion

For the TPD studies, the desorption profiles of both CO and CO_2 species yield Gaussian-like peaks. Calculations of the desorbed amounts of CO and CO_2 are performed on the basis of the trapezoidal rule method [97]. The calculation relies on the assumption that all desorbed C species, i.e., CO and CO_2, are originated from adsorbed CO. The metal dispersion is calculated by assuming an adsorption stoichiometry of CO/Pt and CO_2/Pt of unity [109, 117, 118].

In the pulse adsorption studies, the amount of CO adsorbed on the catalyst is calculated by the difference of the total amount of CO pulsed into the reactor and the total amount of CO detected in the outlet gas stream. In case CO_2 is generated during the pulsation, the amount of CO adsorbed on the catalyst is calculated by subtracting the moles of CO_2 and CO in the outlet gas stream from the total moles of CO pulsed (Eq. 4.1)

$$n_{CO}^{ads} = n_{CO}^{injected} - n_{CO}^{outlet} - n_{CO_2}^{outlet} \tag{4.1}$$

In the case that CO_2 is detected in the outlet stream during the pulsation, the carbon balance is additionally tested by also sending pulses over the by-pass line after the measurement. In all cases, the sum of CO and CO_2 moles in the outlet stream equaled the moles of CO pulsed into the reactor (6.30×10^{-3} mmol).

Metal dispersion is calculated on the basis of the ratio of the total numbers of adsorbed CO molecules to the total number of Pt metal atoms in the sample.

Method Evaluation

H_2 chemisorption measurements are performed by using a commercial chemisorption set-up (Quantochrome Autosorb Automated Gas Sorption System) running under UHV (Institute of Micro Process Engineering, KIT). Metal dispersion was calculated by assuming a 1:1 ratio of H atoms to the surface metal atoms, although it was known that hydrogen molecules may adsorb dissociatively or non-dissociatively on Pt [119].
Chemisorption measurements are carried out in a commercial CO chemisorption set-up (BELCAT). It was reported that CO may adsorb on Pt in different ways, such as dissociatively, by linear bonding, and by bridge bonding. Since literature also emphasizes that CO mostly bonds linearly, it is presumed that there is only linearly bonded CO [112, 115, 116, 119-121]. Thus, the adsorption stoichiometry between the metal atom and the CO molecule is assumed to be unity. The results are compared with the room temperature CO chemisorption results obtained in this study.

CO Oxidation Measurements

CO oxidation measurements are carried out in the same continuous-flow reactor on the same catalyst (1 g). A gas mixture of 1000 ppm CO and 12% O_2 diluted in Ar is fed to the reactor with a total flow rate of 1.25 SLPM. Oxidation is studied between 290 K and 423 K in steps of 50 K at isothermal conditions. Steady-state conversion is ensured at each temperature. CO and CO_2 in the outlet gas composition are quantified by MS measurements.

4.2.4.3 Results and Discussion

Catalyst

A diesel oxidation catalyst (DOC) exhibiting 0.114 wt% Pt of the entire monolithic structure loaded on Al_2O_3 washcoat (Pt/Al_2O_3) in a honeycomb structure is used. The BET surface area is measured to be 29.6 m^2/g. The DOC material is used as crushed material to reduce the dead volume in the reactor. An amount of 1 g DOC material was used in a packed-bed reactor structure; this corresponds to 5.87×10^{-3} mmol Pt.

Measurements

Blank measurements show that no CO adsorption takes place when there is no catalyst in the reactor. All desorption spectra originate from CO adsorption on the catalyst. However, when the reactor is running under continuous-flow of 1 SLPM Ar, MS detects 20 ppm O_2 at the outlet gas stream. Even though no O_2 is co-fed during the analysis, the Ar carrier gas contains maximum 6 ppm level of O_2, and since the system is running at atmospheric pressure, it is believed that a very small amount of O_2 from the atmosphere may diffuse into the lines through the reactor as well.

The total amount of 4.36×10^{-3} mmol CO and CO_2 desorbs from the sample resulting in 74 % Pt dispersion. The TPD desorption profiles of the continuous-flow CO chemisorption measurements at room temperature (Figure 4.5) show that a considerable amount of CO_2 (2.61×10^{-3} mmol, i.e. 60% of the total moles of desorbed carbon) leaves the reactor.

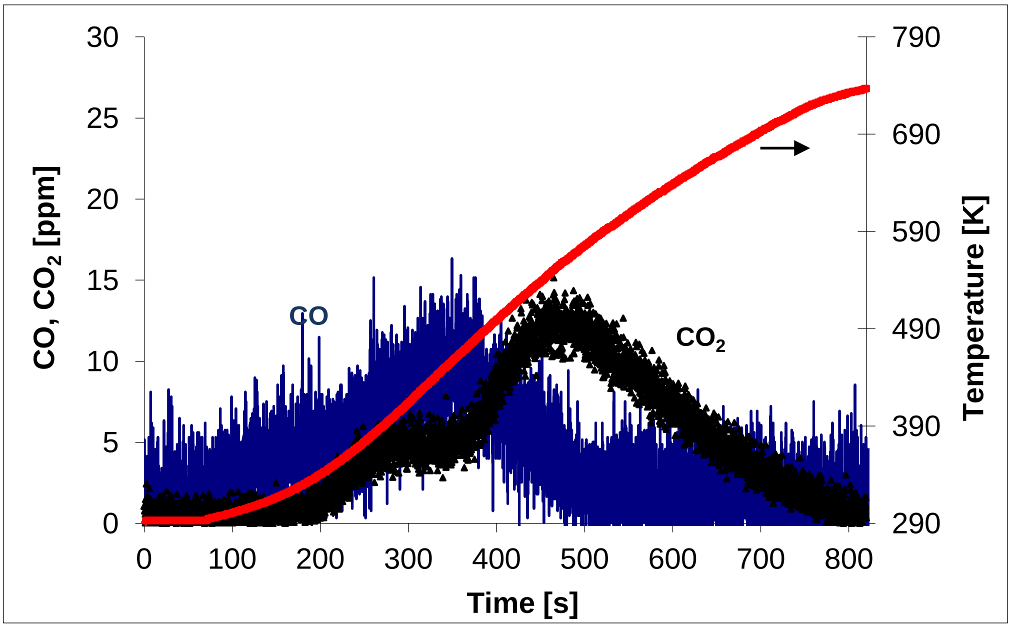

Figure 4.5. Continuous-flow CO chemisorption TPD spectra of CO and CO_2 species and catalyst temperature (ramp applied) as a function of time.

The CO_2 desorption profile exhibits two peaks; a low temperature CO_2 peak with its maximum at around 395 K and a larger peak with its maximum at 543 K. On the other hand, CO yields one peak that reaches its maximum at around 443 K.

The oxidation of CO during TPD studies has been investigated earlier for different types of precious metals (PM) and supports [112-114]. Foger and Anderson studied Pt catalysts with different types of supports (Pt/aerosil, Pt/γ-Al_2O_3, and Pt-Au/aerosil). They proposed three different possible ways for CO_2 generation during TPD: CO oxidation via atomic oxygen (Eq. 4.2) [122], Boudouard reaction (Eqs. 4.3 and 4.4), and water gas shift reaction (WGS) (Eqs. 4.5 and 4.6) [112].

$$CO(s) + O(s) \rightarrow CO_2(s) \qquad 4.2$$

The oxidation of CO with chemisorbed oxygen (Eq. 4.2) involves elementary-steps and the reaction proceeds between the linearly adsorbed CO species and the adsorbed O species (Langmiur-Hinshelwood model) [33, 79, 123-125]. If this is the main reaction in the system leading to CO oxidation, it is presumed that the possible oxygen source of adsorbed oxygen atoms (O(s)) in the system is the oxygen occurring at the ppm level in the carrier gas. For the continuous-flow CO chemisorption measurements, the oxidized amount of CO is calculated to be 2.6×10^{-3} mmol. On the other hand, during the measurement, when only Ar carrier gas is fed to the reactor i.e, during cooling down the reactor to the adsorption temperature and purging processes, (this procedure takes nearly 1h) 11.3 mmol O_2 is fed to the reactor, equaling an O_2 level of 6 ppm in the Ar carrier gas. This provides enough adsorbed oxygen for the oxidation of CO during the subsequent TPD.

The second possible route for the oxidation is the dissociation of the adsorbed CO species (Boudouard reaction), which results in C deposition on the precious metal (PM) surface [113]:

$$2CO(s) \rightarrow C(s) + CO_2(s) \qquad 4.3$$

This C deposition reaction may also occur via the Eley-Rideal mechanism [112]:

$$CO + CO(s) \rightarrow C(s) + CO_2 \qquad 4.4$$

The dispersion calculations rely on the assumption that all desorbed CO_2 originates from adsorbed CO. For this reason,1 mol desorbed CO_2 is counted as 1 mol CO adsorbed on the surface. According to reactions (4.3) and (4.4), it is obvious that the disproportionation reaction of 2 moles of adsorbed CO species leads to 1 mol of adsorbed C and 1 mol of CO_2. In this case, the dispersion calculation would not be valid. Dropsch and Baerns studied this disproportionation of CO during TPD on a Pd/Al_2O_3 catalyst and agreed that this reaction was one of the main sources of CO_2 generation [113]. In order to examine this reaction path, in the study, 10 vol.% O_2 diluted in Ar is fed to the reactor gas stream after the TPD measurement is finished. Then, the temperature is raised to 873 K to oxidize the C_{ads}. Neither CO_2 nor CO species are detected by BINOS or MS in the experiment. However, since the potentially expected amounts of CO and CO_2 are rather low (micromole range) at high flow rate (1 SLPM), CO and CO_2 concentrations might be under the detection limit of the analytic (signal-to-noise ratio of 1). This high signal-to-noise ratio may also affect the precision of the calculation because the CO chemisorptions measured in the set-up differ slightly from the commercial ones.

Lastly, CO oxidation via the water-gas shift (WGS) route (Eqs. 4.5 and 4.6) is also examined. Since the surface of γ-Al_2O_3 contains OH groups and due to the difficulty to completely dehydrate the high surface-area oxide support, this reaction is considered as one of the favorable oxidation routes [112-114, 126]:

$$CO(s)/gas + OH_{support} \rightarrow CO_2 + \frac{1}{2}H_2 \qquad 4.5$$

$$CO(s)/gas + H_2O \rightarrow CO_2 + H_2 \qquad 4.6$$

Foger and Anderson studied TPD on Pt/Al_2O_3 at atmospheric conditions [112]. During the desorption spectra, they detected several CO peaks with their maxima at 388 K, 530 K, 591 K, and 781 K in one desorption spectra. They also found a considerable amount of CO_2 corresponding to 12 % of the total amount of CO and CO_2 desorbed. The spectra of both CO and CO_2 species showed peak broadenings in the high temperature range. The CO_2 desorption started at around 580 K and reached its maximum at around 733 K. They explained this behavior by WGS reaction of CO species with OH from the support. Holmgren et al. studied oxygen storage capacity of Pt/Al_2O_3 catalysts and proposed that at 673 K, CO oxidation was mainly generated from WGS reaction with OH groups on alumina support [126]. In this study, CO_2 desorption, with its maxima of 395 K and 543 K, cannot be explained by WGS reaction because these temperatures are quite low for WGS reactions [127]. Beside the temperature limitations, it was also shown that not all OH/H species present on the alumina are energetically able to participate in the reaction path of the WGS [128].

It is, therefore, concluded that the main reaction leading to CO oxidation during the TPD in the experiment is the oxidation of CO with the adsorbed oxygen contained in the Ar carrier gas.

CO Pulse Adsorption

This measurement is carried out to study the potential disproportionation reaction (Bouduard reaction), and to assure that the total amount of C calculated from the TPD spectra is equal to the amount of CO adsorbed. Figure 4.6 shows the CO concentration in the outlet gas measured by MS as a function of time during the pulsation. The temperature is kept constant at 290 K. A large degree of the adsorption (3.48×10^{-3} mmol, equivalent to 82 % of the total adsorption) takes place at the first pulse and the surface is nearly saturated after the third injection. Pulses are repeated two more times (the fourth and the fifth injection) after the saturation point to ensure that the surface is fully covered by CO.

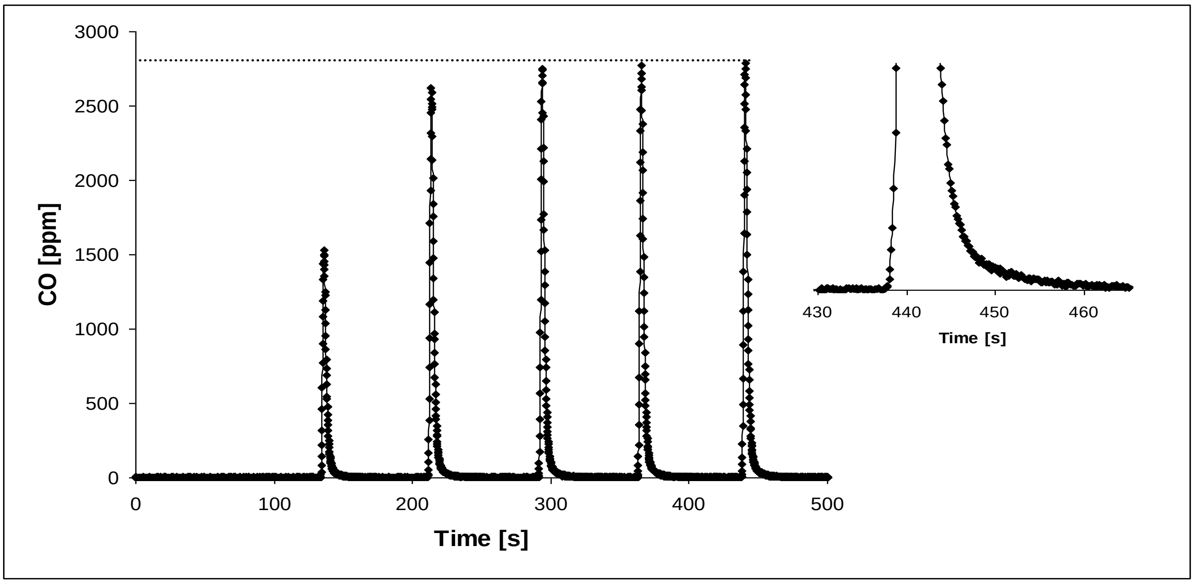

Figure 4.6. CO pulse adsorption at room temperature (290 K).

The time interval between the pulses is 1-2 min, which accounts for the rather large dead volume between the catalyst bed and the analytics. Although the injection time is only 1.5 seconds and the residence time in the catalyst bed is only 90 ms, a significant CO signal in the exhaust can be observed for 22 seconds (Figure 4.6).

After the saturation, a TPD measurement is carried out using the same procedure as described in previous section “Continuous-flow TPD Studies”. Results are shown in Figure 4.7. The resulting TPD spectra agree well with the one obtained in the continuous-flow TPD experiments (Figure 4.5).

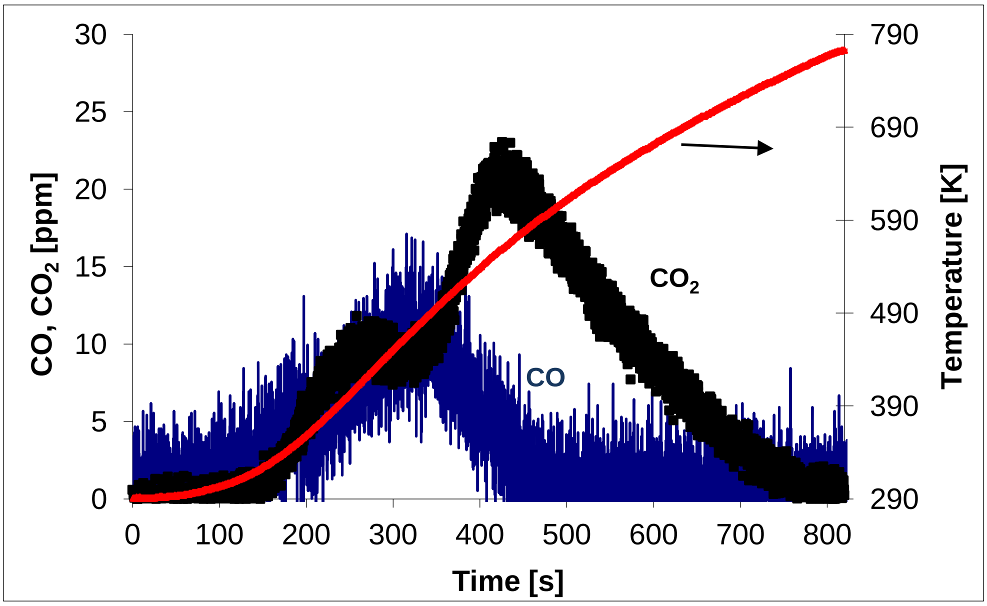

Figure 4.7. TPD spectra of CO, CO species after CO pulse adsorption at room temperature (290 K).

From the pulse adsorption measurement (Figure 4.6), the total amount of adsorbed CO was calculated to be 4.24x10^{-3} mmol correlating to 72 % Pt dispersion; total number of Pt atoms in the sample is 5.88x10^{-3} mmol. This result agrees well with the continuous-flow TPD measurement study giving 74 % Pt dispersion based on the total amount of CO and CO$_2$ desorbed, which is 4.36x10^{-3} mmol (Figure 4.5). This agreement also supports the conclusion that CO$_2$ observed in the outlet stream of the TPD study is generated by oxidation of adsorbed CO.

Table 4.1. Comparison of chemisorption data and dispersion results based on adsorption and desorption measurements and commercial set-ups.

	Adsorbed CO, mmol/g	Desorbed CO, mmol/g	Desorbed CO$_2$ mmol/g	Total C CO+CO$_2$ mmol/g	Dispersion %
Continuous-flow TPD	-	1.75 x10^{-3}	2.61 x10^{-3}	4.36 x10^{-3}	74
CO Pulse adsorption	4.24x10^{-3}	-	-	4.24 x10^{-3}	72
TPD after CO pulse adsorption	-	1.21 x10^{-3}	3.51 x10^{-3}	4.72 x10^{-3}	80
CO chemisorption-BELCAT Commercial set-up	-	-	-	-	76
H2 chemisorption-Quantachrom Autosorb Commercial set-up	-	-	-	-	81

The dispersion derived from both techniques also well agree with the dispersion data obtained using commercial devices with CO chemisorption (BELCAT) and H$_2$ chemisorption (Quantachrome Autosorb) as given in Table 4.1. The small difference between H$_2$

chemisorption results and CO chemisorptions results is due to the different adsorption states of hydrogen molecules on Pt [119, 129].

CO Pulses at Different Temperatures

To analyze the oxidation behavior of the catalyst during the pulsation, CO pulse adsorption measurements were carried out at different temperatures (367 K, 427 K, 527 K and 573 K). For each temperature point, the same pre-treatment procedure was applied.

Figure 4.8 and Figure 4.9 show the adsorption and desorption behaviors of the catalyst at 367 K. During the first pulsation, 1.7x10^{-4} mmol CO_2 is generated. No further CO_2 is generated with the repeating pulses. Saturation is achieved after the fourth pulse. It is possible that, the CO_2 peak created in the first pulse is sourced via the reaction of CO with adsorbed oxygen on the surface. Since the Boudouard reaction is neglected and the temperature of 367 K is too low for WGS reaction, this CO_2 peak can be attributed to the oxidation of CO by the oxygen covering the surface [130].

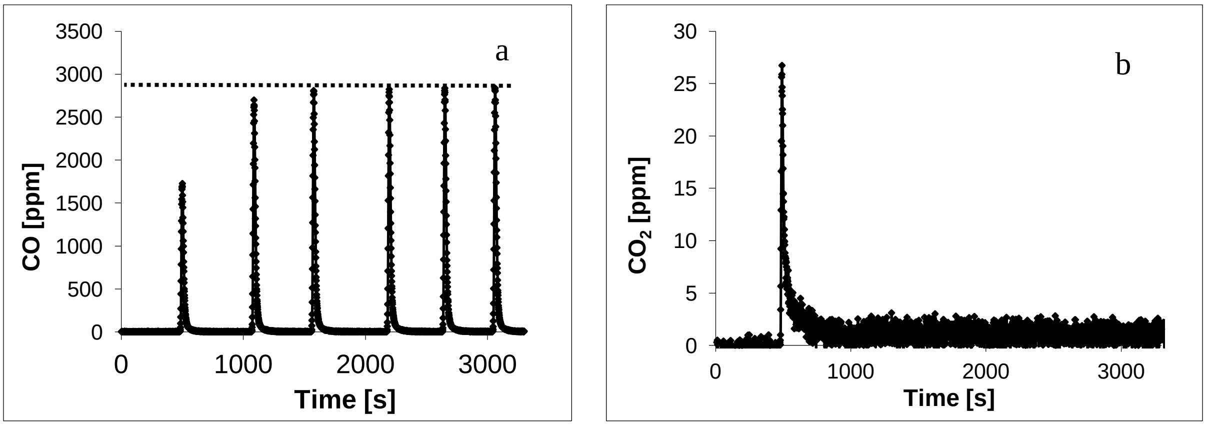

Figure 4.8. CO pulse adsorption at 367 K, CO signals detected during the pulsation (a) CO_2 formation during the pulsation (b).

As shown in Figure 4.9, desorption spectra of CO and CO_2 show similar behavior to that in Figure 4.5. The CO peak reaches its maximum at around 454 K with a decreased amount of desorbed CO, compared to the room temperature adsorption study. The CO_2 desorption spectra are also similar to room temperature adsorption study, since it gives two main peaks with maxima at around 425 K and 542 K, respectively.

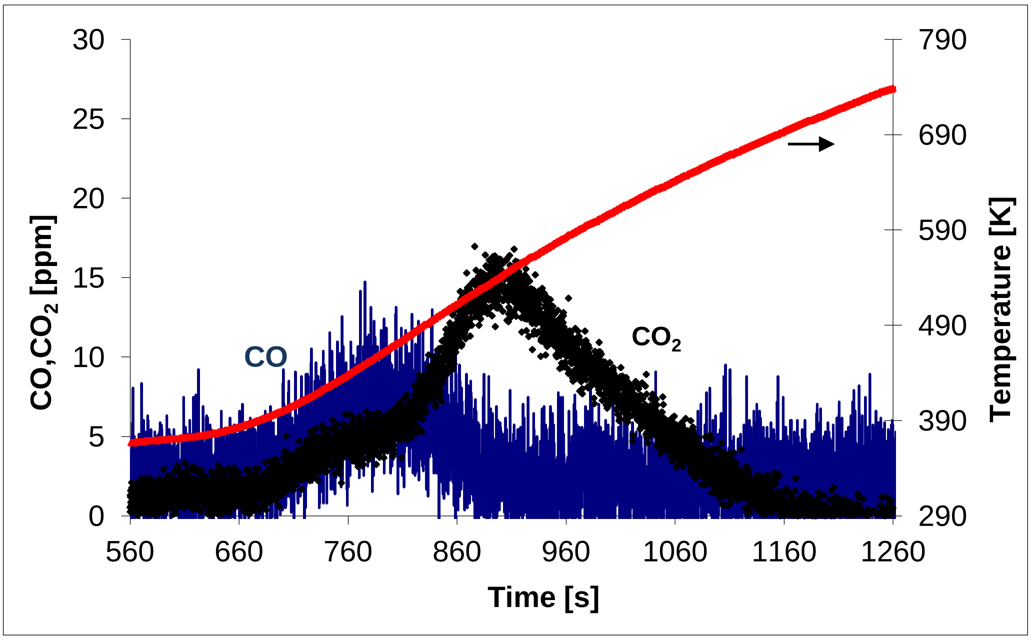

Figure 4.9. TPD spectra of CO and CO_2 after CO pulse adsorption measurements at 367 K.

The desorbed amount of CO_2 does not change in a noticeable amount. 2.56×10^{-3} mmol CO is desorbed after the adsorption study at 367 K, on the other hand 3.51×10^{-3} mmol CO_2 is desorbed at the room temperature continuous–flow TPD measurement (Table 4.2).

Table 4.2. Dispersion calculations according to pulse adsorption technique and TPD measurements as a function of temperature.

Temp. [K]	Adsorbed CO, mmol/ g Pulse adsorbtion	Generated CO_2 during the pulsation	Desorbed CO, mmol/g TPD	Desorbed CO_2 mmol/g TPD	Total amount of desorbed C $CO+CO_2$ mmol/g - TPD	Dis. %
290	4.24×10^{-3}	-	1.20×10^{-3}	3.51×10^{-3}	4.71×10^{-3}	80
367	3.83×10^{-3}	1.77×10^{-4}	1.01×10^{-3}	2.56×10^{-3}	3.57×10^{-3}	61
427	2.91×10^{-3}	1.15×10^{-3}	2.77×10^{-4}	2.05×10^{-3}	2.32×10^{-3}	40
527	1.42×10^{-3}	7.87×10^{-3}	-	1.04×10^{-3}	1.04×10^{-3}	18
573	6.61×10^{-4}	7.46×10^{-3}	-	5.16×10^{-4}	5.16×10^{-4}	9

The same procedure is repeated for higher temperatures, and the results show that increasing the adsorption temperature results in an increased amount of CO oxidation during pulsation. An example of the CO pulse adsorption at 573 K is shown in Figure 4.10. The first CO pulsation results in a high amount of CO_2 generation, whereas repeating the pulses results in less CO oxidation. After the seventh pulsation, the detected CO and CO_2 amounts are repeatable. At this point the sum of the CO detected and the molar amount of CO_2 generated are equal to the base value (6.3×10^{-3} mmol).

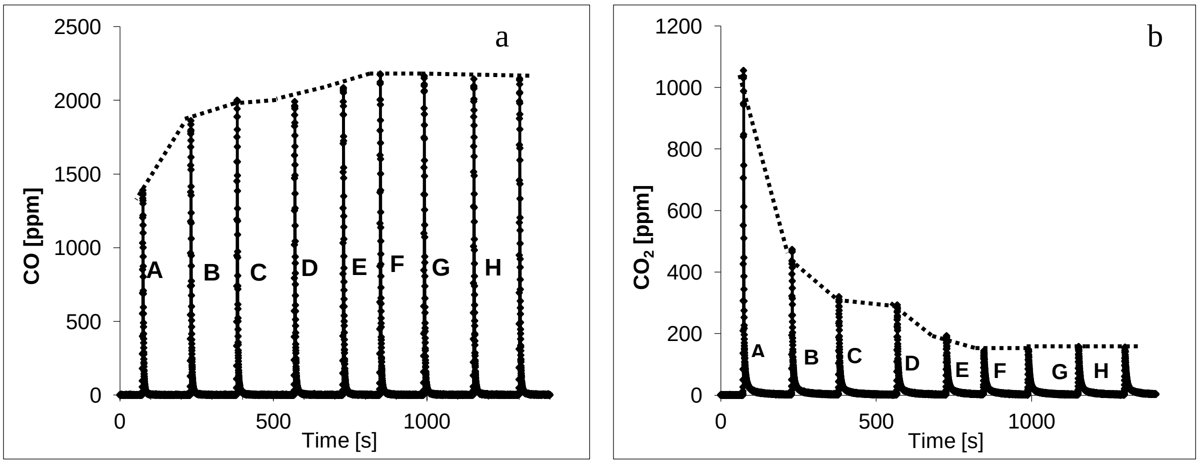

Figure 4.10. CO Pulse adsorption at 573 K, CO signals detected during the pulsation (a), CO_2 formation during the pulsation (b).

The TPD spectra of CO and CO_2 species between 290 K and 573 K are presented in Figure 4.11 as a comparison. Increasing the temperature yields lower amounts of CO and CO_2 desorbed since the coverage is lower at high temperatures, whereas the ratio of oxidation increases with the increasing temperature.

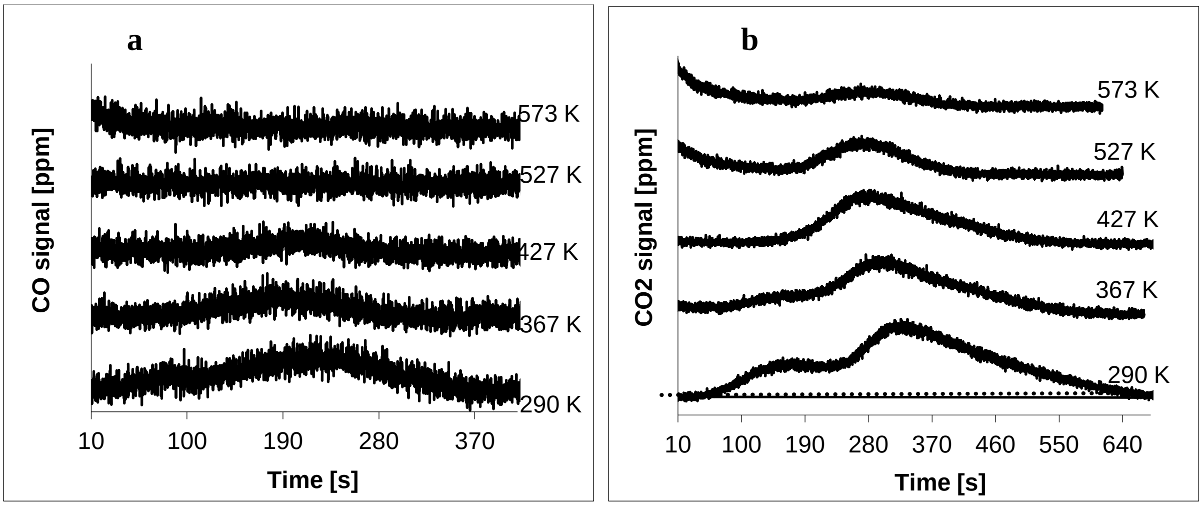

Figure 4.11. Comparison of the desorption profiles of CO (a) and CO_2 (b) at the temperatures of 290-573 K.

To compare the calculated amounts of adsorbed and desorbed species, coverage data are presented in Figure 4.12, assuming that at room temperature the surface metal is completely covered by CO (coverage, θ=1).

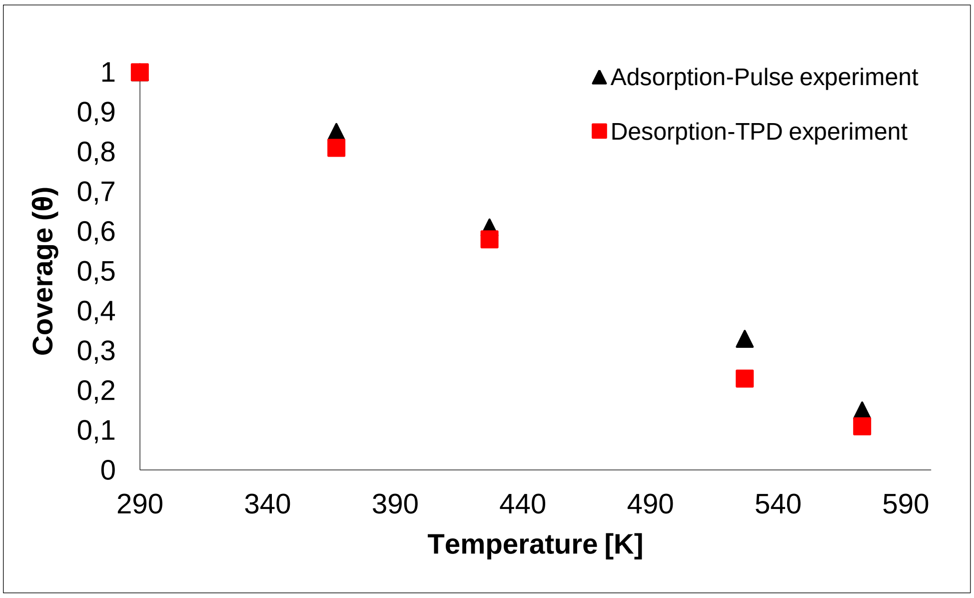

Figure 4.12. Temperature dependency of coverage, calculated based on CO pulse adsorption and desorption methods.

Increasing the temperature yields a linear decrease of coverage and the coherence of the adsorption and desorption results were noticeable. The coverage derived from the pulse adsorption and the subsequent TPD show small deviations at higher temperatures.

CO Pulsing on an O_2 pre-covered Pt Surface

Even though the studies show that adsorption and desorption studies are compatible, the next concern is the adsorption of CO in the presence of O_2 since the adsorbed O_2 may have occupied the active metal surface during the CO chemisorption.

Firstly, CO pulse adsorption is generated on an O_2 pre-covered Pt surface at room temperature (290 K) (Figure 4.13). The first pulse results in a high amount of CO_2 generation ($8x10^{-4}$ mmol) and repeating pulses yield less CO_2. The total amount of CO_2 generated during the pulsation is $1.96x10^{-3}$ mmol and the total amount of CO adsorbed is calculated as $2.92x10^{-3}$ mmol. 50 % metal dispersion is calculated based on the assumption that CO_2 is chemisorbed CO originated.

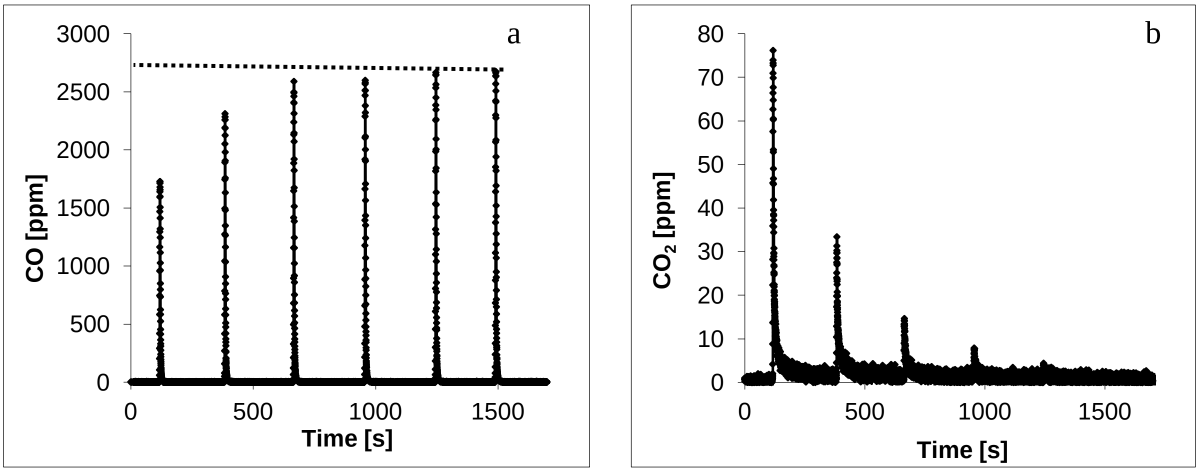

Figure 4.13. CO Pulse adsorption on the O_2 pre-covered surface. CO (a) and CO_2 (b) signals

On the other hand when the surface is free of oxygen the total amount of CO absorbed is 4.24 x10^{-3} mmol, resulting in 72 % dispersion (Figure 4.7). After the adsorption studies, TPD is carried out from room temperature to its maximum of 790 K. The resulting spectra only show a single CO_2 desorption peak with its maximum at around 370 K (Figure 4.14). A calculated value of 3.29 x10^{-3} mmol CO_2 yields 56 % metal dispersion.

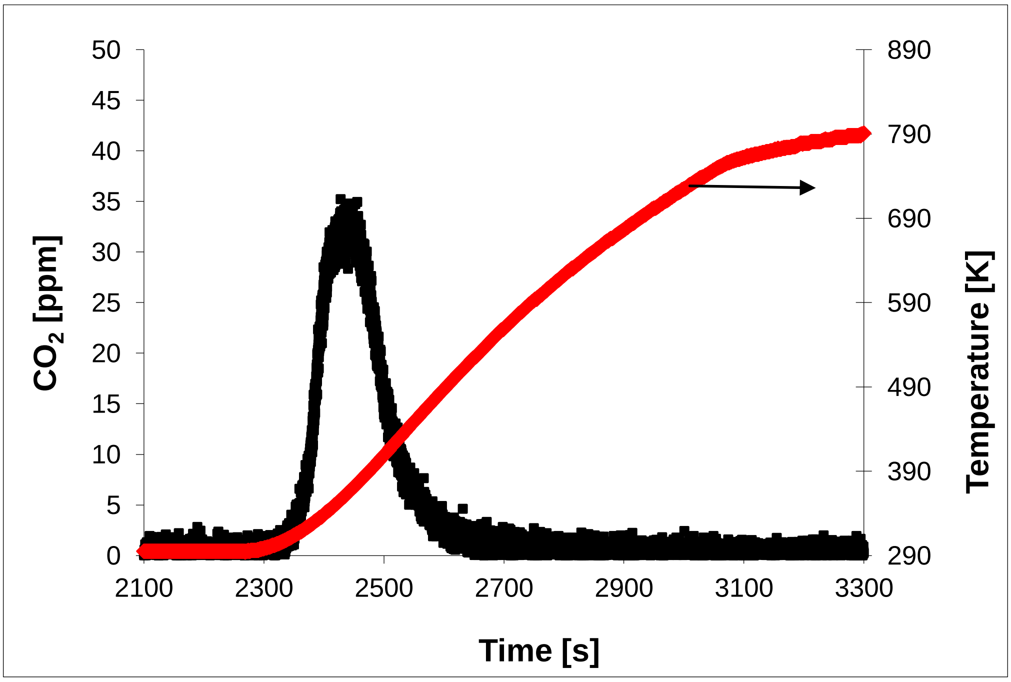

Figure 4.14. TPD profile after CO pulse adsorption on O_2 pre-covered surface.

80 % metal dispersion is calculated based on the room temperature CO pulse adsorption-TPD measurements on an oxygen-free surface. For both studies (adsorption and desorption), the difference in the dispersions between an O_2 pre-covered surface and a free surface is nearly 30 %. This difference shows that, when the O_2 pre-covered Pt surface was exposed to CO molecules, it can still be covered with a high amount of CO. Bourane and

Bianchi [123] studied the adsorption behavior of CO in the presence of O_2. They tried to cover the CO-saturated surface with O_2 and claimed that linearly-bonded CO was not modified in the presence of O_2 for CO/O_2 ratios > 2. According to their study (at 300 K), CO would not desorb to liberate some sites for the adsorption of oxygen. Segner et al. studied the adsorption of CO on Pt surfaces and concluded that, in case the surface is already saturated with O, it can still adsorb CO molecules [131].

According to the H_2 chemisorption results in the study, the calculated average crystal size for Pt/Al_2O_3 catalyst is 1.4 nm. In contrast, high resolution transmission electron microscopy (TEM) images show particles between 10-20 nm as well as particles smaller than 10 nm [132]. This small particle size distribution supports the assumption that CO is predominantly covering the surface since the particle size is relatively small. An effect of the 6 ppm O_2 in the carrier gas on dispersion data derived by the techniques seems very unlikely, also because the CO/O_2 ratio is far above 2.

CO Oxidation Measurements

The oxidation behavior of CO is well-explained in the literature [123, 128, 131, 133-135]. During the pulse adsorption studies, it is observed that CO oxidation may take place at room temperature (290 K) in the case that the surface is O_2 pre-covered (Figure 10b). Thormählen et al. have shown that, when the surface (Pt) is pre-oxidized, CO conversion may even start at 225 K [134].

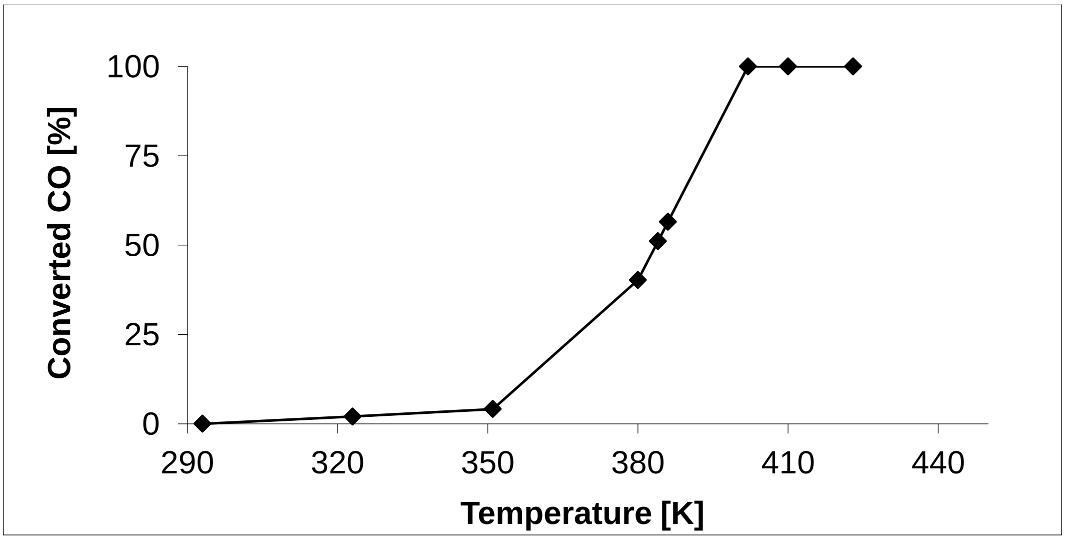

Figure 4.15. CO oxidation light-off curve with a gas mixture of 1000 ppm CO and 12 % O_2 diluted in Ar with a total flow rate of 1.25 SLPM.

To understand the oxidation behavior of the catalysts during pulsation and TPD, CO oxidation is studied in an O_2-rich atmosphere at temperatures of 293-423 K (Figure 4.15). The light-off temperature (at 50 % conversion) is 383 K, which is compatible with the results presented in Figure 4.14 for the desorption profile of CO on an O_2 pre-covered surface where the maxima of CO_2 peak is detected as 374 K. This result also supports the conclusion that the main oxidation source of CO is the oxygen from the Ar carrier gas.

4.2.4.4 Conclusion

CO chemisorption on a technical catalyst was studied by two methods in a simple continuous-flow reactor at atmospheric pressure: TPD of pre-adsorbed CO and CO pulse adsorption. The metal dispersion derived from the results of both methods agree very well and were also reproduced by commercial CO and H_2 chemisorption devices.

In the TPD spectra, a large amount of CO_2 molecules was found in the outlet stream. Therefore, the effect of the observed oxidation of the adsorbed CO on the method was investigated. By using the pulse adsorption technique, it was shown that the CO_2 comes from the oxidation of adsorbed CO with O_2 that occurs at ppm level in the Ar carrier gas. WGS is negligible and Boudouard reaction does not take place. The effect of the adsorbed oxygen on the availability of Pt adsorption sites is negligible. Hence, the dispersion can be calculated by assuming an adsorption stoichiometry of CO/Pt and CO_2/Pt of unity.

CO TPD in a continuous-flow reactor at atmospheric pressure is suitable for the measurement of metal dispersion in technical catalysts. With the proposed simple set-up a quick technique is available for CO chemisorption studies. This technique brings several advantages briefly listed here:

- Measurements can be performed in simple continuous-flow reactor set-up, which is mainly available in most of the laboratories.
- No sophisticated techniques such as ultra high vacuum are necessary. The technique can be applied under realistic operating conditions, i.e atmospheric pressure and room temperature.
- The method is not limited by the catalyst structure and size.
- The catalyst is not destructed; by this way, dispersion data can be correlated with the aging or catalytic activity measurements.

4.2.5 CO chemisorption on Rh Surface

In this chapter application of the continuous-flow CO chemisorption method on Rh/Al_2O_3 catayst is discussed. 0.28 wt % Rh/Al_2O_3 catalysts (Umicore AG & Co KG) of monolithic structure (900 cpsi) is used for the measurements. Similar to Pt/ Al_2O_3, the catalyst is subjected to continuous-flow TPD and pulse adsorption measurements. 0.9 g crushed catalyst is used for the measurements. Pulse adsorption measurements are carried out at 290 K and continuous-flow TPD measurements are performed consecutively (Figure 4.16). Experimental conditions are the same as described in chapter 4.2.4.2. However pretreatment procedure differs slightly. The catalyst is first oxidized by 21 vol.% O_2 (Air Liquide, 99.95 % purity), diluted in Ar, with a total flow rate of 1 SLPM for 1 h at 823 K. After flushing with Ar gas for 30 min, the catalyst is reduced by 4 vol.% H_2 in Ar dilution at 723 K for 1 hour. The metal dispersion is calculated by assuming an adsorption stoichiometry of CO/Rh and CO_2/Rh of unity [136].

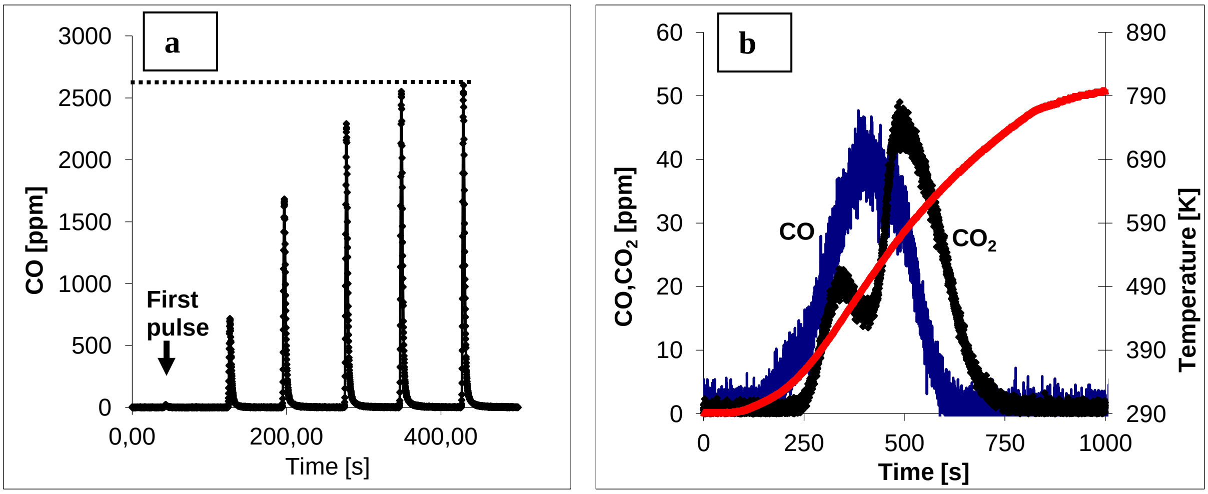

Figure 4.16. Pulse adsorption at 290 K (a) and continuous-flow TPD measurements (b) on Rh/Al_2O_3 catalyst

Similar to the Pt catalyst, TPD results with oxidation of adsorbed CO with oxygen sourced at ppm level in the Ar carrier gas. Dispersion data are validated by H_2 chemisorption measurement data as well (Institute of Micro Process Engineering, KIT). Results are summarized in Table 4.3.

Table 4.3. Comparison of the dispersion data of Rh/Al_2O_3 catalyst.

	H_2 chemisorption	CO Pulse Adsorption	TPD after CO Pulses
Dispersion %	59	56	57

4.2.6 CO chemisorption on the Stagnation Surface

The catalytic active surface area of the catalyst used in stagnation-flow experiments are measured by continuous-flow CO chemisorption TPD measurements. The quartz tubular reactor (Figure 4.4) is replaced by a new flow reactor. The reactor is designed for the measurement that allows characterizing the entire catalyst surface without destruction (Figure 4.17). After the catalyst is attached to the ceramic housing (Chapter 3.1.2), it is placed in the reactor. The resistive heaters as well as the power and thermocouple feedthroughs are contained inside this ceramic housing. The reactor has inlet and outlet flow connections made of stainless steal (6mm OD). Heating is supplied by leading the power through the feedthroughs. Temperature is measured by an R-type thermocouple and controlled by a Carbolite 2416 model control unit.

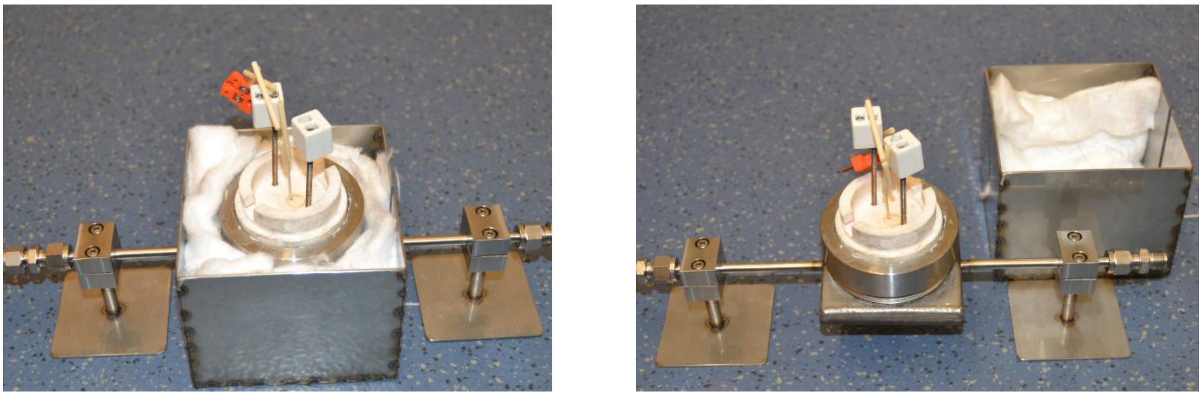

Figure 4.17. CO chemisorption reactor for the flat catalyst (disk) used in stagnation-flow experiments.

Instead of a quartz tube reactor, the flow reactor in Figure 4.17 is used. However, with regard to the flow controllers, the same experimental set-up is used. A pre-treatment procedure is applied as described in chapter 4.2.5 and the experiments are carried out with the total flow rate of 0.5 SLPM. An IR detector (BINOS 100) is connected to the outlet gas composition to measure the desorbed species of CO and CO_2. The measurement is carried out on a fresh catalyst, before the catalytic measurements.

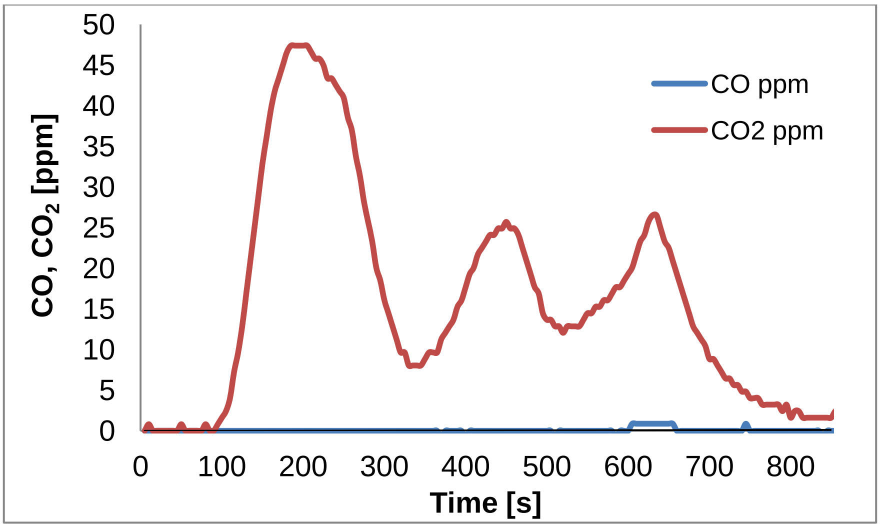

Figure 4.18. Continuous-flow CO chemisorption TPD spectra.

TPD spectra show only CO_2 species (1.96×10^{-3} mmol). Similar to the tubular flow reactor experiments (Chapter 4.2.4 and 4.2.5), the oxygen which is only at ppm level in the sytem leads the CO oxidation during TPD and all adsorbed CO molecules are oxidized. The total catalyst amount on the stagnation disk is calculated based on the thickness of the catalyst layer. An average of 100 µm of catalytic layer is taken into account based on the LM investigations (Chapter 4.2.1, Figure 4.1). A detailed sketch of the stagnation disk (catalyst substrate) and the coating layer is shown in Figure 4.19. The density of Al_2O_3 is assumed to be 3.65 g/cm^3 with 60 % porosity. Detailed information about coating layer (ɣ-Al_2O_3) is given in Table 4.4.

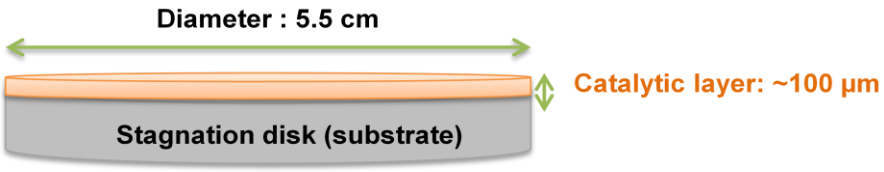

Figure 4.19. Stagnation disk (catalyst substrate) and catalyst layer.

Table 4.4. Properties of coating layer (ɣ-Al_2O_3).

	Radius, cm	Thickness, cm	Volume, cm^3	Porosity, %	Net weight, g
Material ɣ-Al_2O_3	5.5	0.01	0.237	60	0.347

By assuming a surface site density (Γ) of 2.72x10^{-5} mol/m^2 for a closed packed Rh(111) surface, active surface area is calculated to be 0.21 m^2/g. Dispersion is calculated to be 1.2 % (Eq. 4.7 and 4.8).

$$D = \frac{n_{adsorbed_{\mathrm{CO}}}}{n_{Rh}}.100\ \% \qquad n_{adsorbed_{\mathrm{CO}}} = n_{desorbed\ \mathrm{CO_2}} \tag{4.7}$$

$$n_{Rh} = \frac{m_{Rh}}{M_A} \qquad m_{Rh} = \mathrm{Net\ weight}\,.\,\%\ \mathrm{Rh} \tag{4.8}$$

The final derivation of $F_{cat/geo}$ can be written as below:

$$F_{\mathrm{cat/geo}} = D.\frac{m_{Rh}}{M_A}.\frac{1}{\Gamma}.\frac{1}{A_{\mathrm{geometric}}} \tag{4.9}$$

Geometrical surface are of the disk ($A_{\mathrm{geometric}}$) is calculated to be 2.38x10^{-3} m^2. With this information $F_{\mathrm{cat/geo}}$ value ($(F_{\mathrm{cat/geo}})_{\mathrm{Experimental}}$) of the stagnation surface (disk) is calculated to be 30.

Since the catalyst has a considerably thick (~100 μm) washcoat layer, the calculated $F_{\mathrm{cat/geo}}$ value can not directly be used. Diffusion limitation should be taken into account by intoroducing the effectiveness factor (Eq. 2.10). However, effectivess factor can not be introduced in the CHEMKIN SPIN and DETCHEM$^{\mathrm{STAG}}$. Therefore, effective $F_{\mathrm{cat/geo}}$ value (Eq.4.10) has been used for the simulations.

$$\text{Effective } F_{\mathrm{cat/geo}} = i \cdot (F_{\mathrm{cat/geo}})_{\mathrm{Experimental}} \tag{4.10}$$

Exemplarily, the WGS reaction is considered (Chapter 5.4). The reaction temperature is selected to be 873 and the reactor the inlet mole composition is defined to be 4.75 vol. % CO and 5.18 vol.% H_2O diluted in Ar. The reactor is operated at 500 mbar and CO is chosen to be the effective species. Under these reaction conditions, CO flux at the catalyst surface is

calculated to be -4.4x10^{-3} mole/m^2s and the reaction rate is calculated to be 3.2x10^7 mole/m^3s.
For a washcoat layer of 100 µm, a pore diameter of 50 nm and a porosity of 60 % are assumed. The tortuosity value is assumed to be 3. With these data, the effectiveness factor for is calculated to be 0.01.

With this information effective $F_{\mathrm{cat/geo}}$ value is calculated to be 0.3. Since the reactions (e.g., CO and H_2 oxidation, WGS, R-WGS, CPOx) examined over a wide range of temperature and fuel compositions, the value of effective $F_{\mathrm{cat/geo}}$ used in numerical simulations varies.

5. DEVELOPMENT OF A MULTI-STEP SURFACE REACTION MECHANISM

This chapter focuses on the development of a unified thermodynamically consistent surface oxidation and reforming reaction mechanism for CH_4 and C_3H_8 over Rh/Al_2O_3 surfaces.
The development of reliable reaction kinetics depends on kinetic investigations with well defined reactor parameters. A fixed-bed flow reactor configuration is mostly used in laboratory experiments. However, unless the profiles are resolved in time and space domain, it is usually limited for kinetic investigations because of the exothermic or endothermic nature of the catalytic processes where temperature and concentration gradients occur within a few millimeter of the catalyst bed [35, 38, 137, 138] As an alternative, TAP (temporal analysis of products) reactor configuration can be used to investigate the reaction kinetics, assuming that adsorption, desorption, and the reaction steps are the processes that occur under isothermal conditions. The only transport mechanism of the molecules is through Knudsen diffusion. On the other hand, the application of the TAP reactor is not representing the practically relevant conditions since the reactor operates under isothermal, low–pressure conditions and with highly-diluted reactive mixtures [139, 140].

Salinger and Eigenberger studied a fixed-bed reverse-flow reactor configuration for propane combustion to analyze hysteresis of the reaction and its effect on product yield under real operating conditions. They used direct calculation of periodic states in 2D to predict optimum operating conditions, i.e., fuel concentrations and flow rates. Although their method was successful, they pointed out the long CPU time for 2D calculations [141].
Horn et al. revealed the necessity of a well-defined reactor configuration that makes it possible to measure concentration and temperature profiles in the catalytic region for a reliable computational solution of chemical and physical properties of reactive flow under realistic conditions [5, 34, 35]. They presented a capillary sampling technique and with this method they were able to analyze spatial and temporal resolved data inside the catalyst bed for technical systems under transient and steady-state conditions. Donazzi et al. used a similar technique for a micro-kinetic study of partial oxidation of hydrocarbons in a specially-designed annular reactor configuration [16, 30]. Even though those techniques ensure quality information, under realistic operating conditions, modeling of the heterogeneous and homogeneous chemistry in two dimensions (2D or 3D), including chemistry and transport in the reactive flow field is quite complex because the boundary conditions can not be exactly determined due to the heat transport effects. Thus, simplifying assumptions are made for modelling of heat and mass transport effects [39-43].

A stagnation-flow reactor (SFR) geometry is instead a rather simple and easy-to-handle but very useful tool for kinetic measurements because it represents a well-defined flow field with a zero-dimensional catalytic surface, which enables coupled modeling of heterogeneous chemistry and reactive flow at steady-state and transient conditions [66, 67].

In this study the catalytic measurements are carried oiut in the stagnation-flow reactor (given in detail in Chapter 3.1). A hierarchical approach is followed to examine the reaction kinetics. Thus, starting from a single fuel, the complexity of the reaction is augmented by increasing the number of the components in the reactive gas mixture. H_2 oxidation, CO oxidation, preferencial oxidation of CO in H_2 and O_2 mixtures, water-gas shift, reverse and water-gas shift reactions as well as CPOx, SR and DR of CH_4 are studied consecutively. Furthermore, CPOx and SR of C_3H_8 are conducted. A schematic diagram is shown in Figure 5.1 describing the hierarchical approach followed in conducting the stagnation-flow reactor experiments.

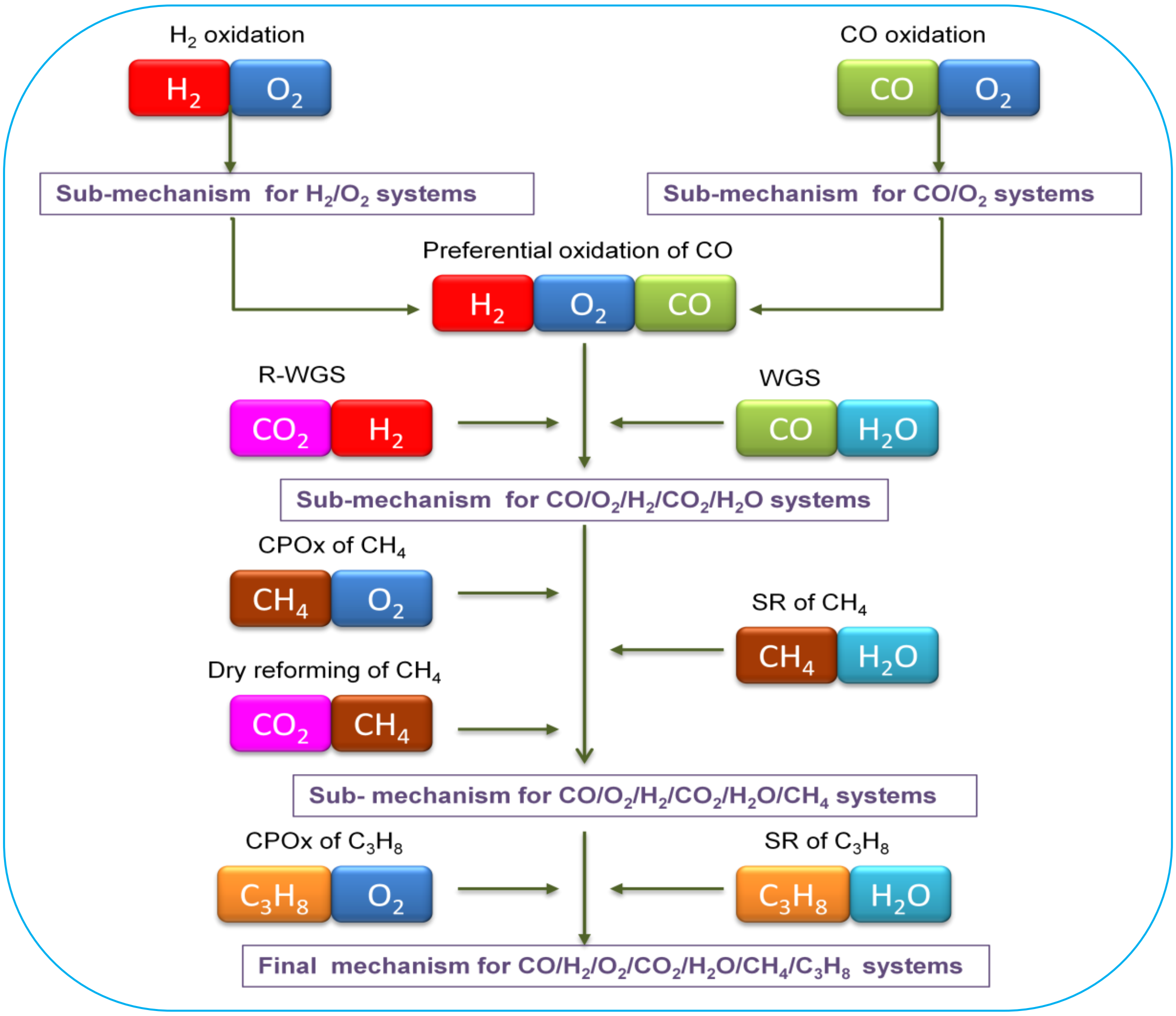

Figure 5.1. Stagnation-flow reactor experimental path by following the hierarchical approach.

To optimize the reaction kinetics, reactions are examined for varying fuel/oxygen ratios and over wide range of temperature. The catalytic ignition studies are also conducted to understand the adsorption and desorption kinetics of the reactive species (H_2, CO, CH_4, C_2H_6 and C_3H_8). The reaction rate parameters are adjusted according to the experimental data derived from the stagnation-flow reactor. In each step, the fidelity of the reaction mechanism is shown by testing the reaction mechanism for different reactor types under varying experimental conditions.

5.1 Catalytic Ignition of Light Hydrocarbons

In this chapter, the ignition of the oxidation of CO, H_2, CH_4, C_2H_6, and C_3H_8 over Rh/Al_2O_3 catalyst is discussed. The literature serves valuable data on the ignition behavior of light hydrocarbons (C_1-C_3), H_2 and CO, on Pt [142-148]. However the ignition behaviors of only ethane [149], CO [150], and H_2 [151] are known for Rh. In the cases of CO and H_2, the ignition studies did not account for a wide range of fuel/oxygen ratios for Rh. This study systematically extends the literature on the ignition kinetics of ligh hydrocarbons, CO and H_2 over Rh-based catalysts and, hence, supports the development of reliable surface reaction mechanisms for oxidation and reforming over rhodium [27, 33, 83, 88, 151, 152].

5.1.1 Theoretical Background

Ignition studies provide valuable information for the construction of surface reaction mechanisms for a better understanding of adsorption-desorption and equilibrium kinetics and intrinsic reaction rates [142, 147, 148].

Hohn et al.[148] define catalytic ignition as the point in which the temperature of a reaction mixture maintains without additional external heating due to the sufficient heat release of the chemical reaction. Alternatively, Rinnemo et al.[143, 144] define catalytic ignition as a sudden transition from a kinetically limited pre-ignition state to a mass-transport limited post-ignition state for an exothermal catalytic reaction. The reaction ignites, when the Frank-Kamenetskii-condition (F.-K.-condition, Eq. 5.1) is fulfilled.

$$\gamma \equiv \frac{\frac{dQ_c}{dT}}{\frac{dQ_l}{dT}} > 1 \qquad 5.1$$

Q_c is the heat, which is released by the chemical reaction, and Q_l represents the heat loss. If the Frank-Kamenetskii factor is higher than unity ($\gamma > 1$), the temperature of the system will increase due to the excess of released heat in comparison to the heat losses. Catalytic ignition of an exothermic reaction is usually associated with a sudden transition from a kinetically limited pre-ignition state to a mass transport-limited post-ignition state [143, 144].

Former studies on Pt catalyst illustrate that the ignition behavior of a reaction mixture is highly dependent on fuel type and fuel/oxygen ratios in the feed composition. Increasing the concentration of hydrocarbons in the gas mixture yields a decrease in ignition temperature on Pt catalysts due to the high oxygen coverage of catalytic surface in pre-ignition state. [153-155] However an opposite tendency– an increasing fuel/oxygen ratio with increasing ignition temperature - is also explored for the oxidation of carbon monoxide, hydrogen and alkenes by Behrendt et al.[154] and Cho and Law respectively [153].

Packed bed reactors are mostly used for determination of the catalytic ignition. Although reactor configuration is ideal for determination of light-off and steady-state conversion profiles of the fuels, their application to ignition studies is limited due to the heat and mass transfer limitations in the reactor. As an alternative, stagnation-flow reactors can be used.

Catalytic wires/foils are also used as catalysts in tubular reactor configuration. Heat can be supplied to foil directly and temperature is measured on the foil surface [153-155]. The flow is supplied perpendicular to the foil creating a 1D stagnation flow. This configuration minimizes the dependence of the ignition temperature on the flow properties [153].

A number of groups studied catalytic ignition in a stagnation-flow configuration to incorporate detailed reaction mechanisms into catalytic combustion simulations [67, 75, 76, 78, 86]. Deutschmann et al. used catalytic ignition data for development of a surface reaction mechanism for CH_4 on Pt surfaces [86]. Ziauddin et al. studied the ignition properties of ethane/air mixtures on different catalysts (Pt, Pd, Rh, Ir, and Ni) in a stagnation-flow configuration as well. They proposed that the ignition temperatures vary significantly due to the different chemisorption properties of the catalysts [149]. Rh, Ir, and Ni form oxides in fuel-lean operating conditions because they exhibit higher affinity to oxygen than Pt. This will lead to high ignition temperatures due to the deactivation of the catalytically active sites. Pt, however, is not known to form stable oxides under the conditions used for catalytic oxidation of light hydrocarbons; consequently, Pt can be used for catalytic oxidation of light hydrocarbons at both fuel-lean and fuel-rich operating conditions.

5.1.2 Experimental Procedure

The dependency of the ignition temperature on varying fuel/oxygen ratios, which are represented by the α-value (a ratio of mole fractions (x) of fuel and oxygen) is experimentally explored for the oxidation reaction of CO, H_2, CH_4, C_2H_6, and C_3H_8 in the range of 0.25 (fuel-lean) < α < 0.9 (fuel-rich). The reaction gases are diluted with 88 vol. % of Ar for all experiments.

$$\alpha = \frac{x_{\text{fuel}}}{x_{\text{fuel}} + x_{\text{oxygen}}} \quad . \qquad 5.2$$

For the detection of the ignition temperature, the catalytic surface is heated by linearly increasing the input power of the resistive heater. The voltage is kept constant until thermal steady-state is reached. Because of the low thermal conductivity of the ceramic support, the steady-state is not reached until some minutes. After reaching the steady-state, temperature as a function of the voltage is recorded and the voltage is increased stepwise until it reaches the next steady-state. The catalytic ignition is explored by a sudden increase in temperature compared to with an inert gas measurement. At the ignition point, a transition from a kinetically limited pre-ignition state to a mass transport-limited post-ignition state starts.

5.1.3 Results and Discussion

The ignition of oxidation of the CO and H_2 (α=0.4 for both fuels) are shown in Figure 5.2. The temperature curve as a function of voltage is generally composed of the pre-ignition, ignition, and post-ignition state.

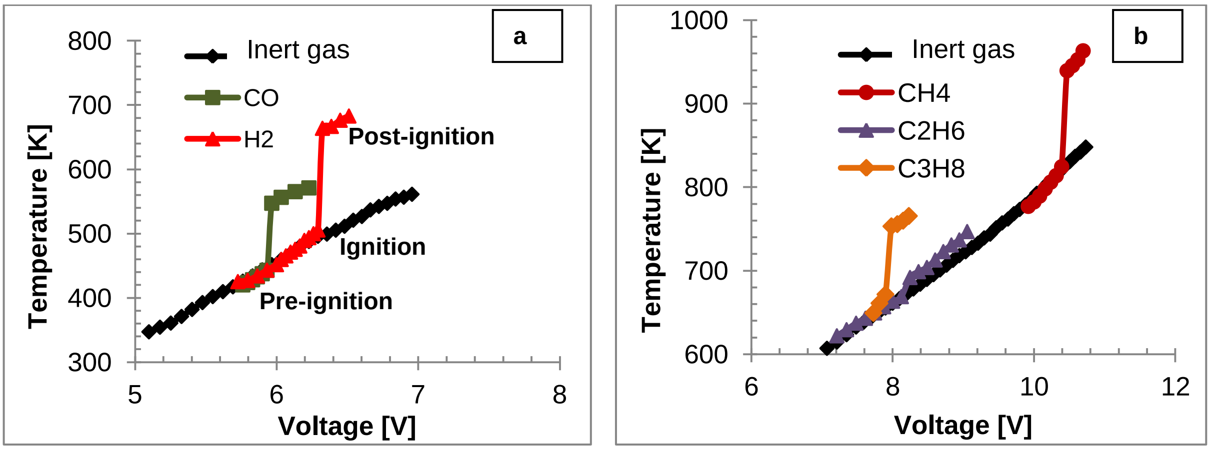

Figure 5.2. Temperature as a function of voltage of the resistive heater, displaying the ignition graph of carbon monoxide and hydrogen oxidation (a) and methane, ethane and propane (b) with a gas composition of α = 0.4 compared to an inert measurement. Ignition states are shown for H_2.

In the pre-ignition region, no surface reaction can be observed, and the recorded temperature data represent the heating rate of the catalytic system (Figure 5.2, a) According to simulations of Deutschmann et al.[86] and Warren et al.[146], during this kinetically-limited pre-ignition state, the catalytic surface is mainly covered by one species. Exemplarily, in fuel rich conditions for CO/O_2 mixtures, CO(s) is the main surface species whereas in O_2 rich conditions (fuel lean) the surface is mainly covered by oxygen. After reaching the ignition point, the reaction starts, which can be seen from a sudden increase in temperature. The detected temperature curves have the same slope before and after ignition. At post-ignition, however, the curve is shifted to higher temperatures. This temperature difference between pre-ignition and post-ignition state differs for each reaction and α-value due to the varying conversion and different heat release. Especially for ethane oxidation, the temperature difference is very low (ΔT = 25 K), which is due to the low conversion (Figure 5.2, b).

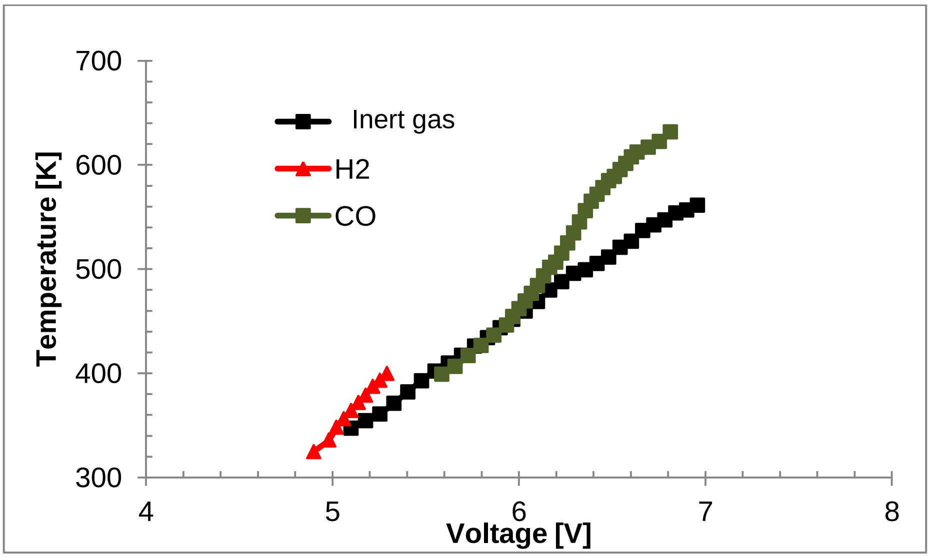

Figure 5.3. Temperature as a function of voltage of the resistive heater, displaying the ignition graphs of CO and H_2 oxidation. Catalytic ignition does not occur for α = 0.4 for H_2 andα= 0.7 for CO oxidation.

For ignition of H_2 oxidation for α= 0.4 and CO oxidation for α =0.7, no sudden temperature increases are detected (Figure 5.3). This was the case for all reactions in fuel-lean conditions (α < 0.4). Ziauddin et al. and Veser et al.[149, 155] explain this behavior as a result of low catalytic activity of rhodium at high temperatures and fuel-lean conditions. Furthermore, no ignition was detected in the case of CO oxidation in fuel-rich conditions. This is attributed to the CO poising effect since the surface is fully CO covered. Oxygen adsorption is disfavored and ignition is inhibited for α ≥ 0.7. However, comparing the graph of the CO oxidation (α = 0.7, Figure 5.3) to the measurement with inert gas shows a temperature difference (ΔT > 100 K) between experiment and inert measurement, that is, the catalytic reaction occurs even though no ignition is observed. The light-off is inhibited when the heat release is smaller than the heat losses of the system, which is due to low conversion. In this case, the Frank-Kamenetskii condition (Eq. 5.1) is not fulfilled.

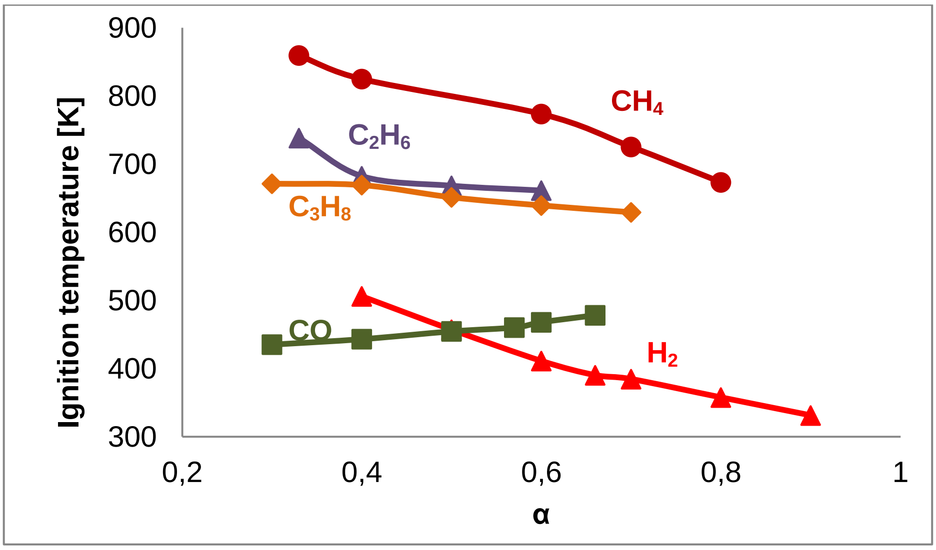

Figure 5.4. Ignition temperature with respect to the gas composition (α, Eq.5.2) of various fuel/oxygen mixtures.

For each reaction the ignition temperature varies with varying fuel/oxygen ratios (Figure 5.4). Compared to the other fuels, the oxidation of methane ignites at high temperatures of around 723–873 K. However, for the higher hydrocarbons, the ignition temperature is never above 773 K. For H_2 and CO oxidation, ignition temperature ranges between room temperature and 423 K. Increasing the α in oxidation of H_2, CH_4, C_2H_6, and C_3H_8 results in a decrease in ignition temperature. For oxidation of CO, however, an increase in oxygen concentration leads to lower ignition temperatures.

The ignition behavior is generally attributed to the surface coverage before the catalytic reaction is initiated. If the Langmuir-Hinshelwood mechanism is assumed, both reactants need to be adsorbed for the catalytic reaction. In the pre-ignition state, however, the catalytic reaction is kinetically limited due to the favored adsorption of one species, which is commonly referred to as the most abundant reaction intermediate species (MARI) [86, 156, 157]. For starting the catalytic reaction, a critical amount of adsorbed co-reactant is needed. This critical amount can be reached by rising the temperature in order to shift the adsorption/desorption equilibrium towards desorption of the MARI. At the ignition temperature, enough free adsorption sites are generated for the critical amount of adsorbed co-reactant. In the case that concentration of MARI on the surface is higher, ignition does not occur since generation of the critical amount of free adsorption sites is not established. That is, the reaction does not start and leads to a higher ignition temperature. Because desorption is favored at higher temperatures that generates fee adsorption sites for the other species.

As a result of the increase of ignition temperature during decrease of oxygen amount in the gas, CO is the most abundant intermediate species (MARI) in the pre-ignition state for the CO oxidation. For the oxidation of the hydrocarbon species and hydrogen, however, there is an opposite trend. An increasing fuel/oxygen ratio results in a lower ignition temperature. In these oxidation reactions, oxygen is the MARI. Therefore, oxygen has a higher sticking probability than the fuel species hydrogen, methane, ethane, and propane if the desorption reaction is neglected at low temperature in the pre-ignition state. The ignition behavior of hydrocarbons can additionally be correlated with the bond-dissociation energy of the fuel species. This is due to the fact that dissociated species are necessary for a catalytic reaction. The higher the bond-dissociation energy, the more energy, provided by heat, is needed to initiate the catalytic reaction. This behavior is similar to hydrocarbon oxidation on Pt [77, 142, 155].

5.1.4 Conclusion

For the construction of reaction mechanisms, these ignition studies provide valuable data to understand the trends of sticking behaviors, heats of adsorption, and desorption rate of the relevant species in the reaction system. Increasing the fuel/oxygen ratios for H_2, CH_4, C_2H_6, and C_3H_8 reduces results in decrease of the ignition temperatures. For the oxidation of CO, however, the decrease of the fuel/oxygen ratio results in lower ignition temperatures. This behavior is explained by the different surface coverage tendencies of the fuel/oxygen mixtures. Decreasing the amount of fuel (i.e., increasing the amount of O_2) in the gas mixtures results in an oxygen-poisoned surface, which inhibits the catalytic ignition. Furthermore, if the concentration of CO during CO oxidation is increased, the resulting high surface coverage of CO shifts the ignition temperature to higher values. The ignition behavior of hydrogen on rhodium differs from the behavior on platinum

.

5.2 H_2 oxidation Kinetics

In this chapter, H_2 oxidation on Rh/Al_2O_3 catalysts has been studied experimentally and numerically to achieve a better understanding of hydrogen oxidation kinetics which is also of interest in partial and total oxidation as well as reforming of hydrocarbons. The reaction mechanism presented is thermodynamically consistent and predicts the water formation in a wide range of temperature and fuel/oxygen ratios. Experiments are carried out in the stagnation-flow reactor configuration, which enables 1D modeling of heterogeneous chemistry coupled with diffusive and convective transport within the gas-phase boundary-layer.

The experimental results are used for developing an elementary-step-like reaction mechanism for H_2/O_2 mixtures. The validation and applicability of the mechanism is shown by simulating H_2 oxidation measurements in a laboratory type flow reactor with different flow rates.

5.2.1 Theoretical Background

Since Döbereiner´s discovery of the catalytic effect of Pt on H_2 and O_2 mixtures in 1823, heterogeneous oxidation of H_2 on transition metals has been studied extensively [67, 143, 144, 158-164]. Besides its simplicity, with only a few reaction steps of adsorption and desorption of the reactants and products, it is one of the key reactions in many catalytic processes of industrial importance [165, 166]. In microreactor technology, H_2 oxidation is carried out to test the flexibility of the reactor at different operating conditions without the occurrence of a flame [167-169]. Due to the low ignition temperature of H_2/O_2 mixtures, small amounts of H_2 can be applied in CH_4/O_2 systems to decrease the light-off temperatures, e.g. for catalytic combustor and turbine applications [53]. Furthermore, this reaction has a strong impact on exhaust gas after-treatment. During sudden acceleration of a car, formation and consequently oxidation of small amounts of H_2 in the exhaust gas may cause hot spot formations in the catalyst and lead to altering of catalytic converters [170, 171].

There is also a continued interest in developing a better understanding of hydrocarbon fuel processing technologies for syngas (H_2+CO) production in a wide range of operating conditions in order to increase reaction efficiency and reduce pollutants [5, 35, 172-176]. All fuel processing technologies i.e., partial oxidation, steam reforming, or auto thermal reforming, include the formation and/or oxidation of H_2 in their reaction pathways [172].

Development of a detailed kinetic mechanism for such complex reaction schemes necessarily begins with a H_2-O_2 sub-system which is also a critical step as the overall reaction efficiency is determined by H_2 selectivity to H_2O [173].

Among the catalysts belonging to group VIII transition metals (Rh, Pt, Ru, Ni), Pt and Rh are the most effective catalysts for synthesis gas production [5, 158, 166]. Although the reaction pathways and the existing surface species of H_2 oxidation on Pt and Rh are quite similar, the kinetic parameters differ considerably. Pt shows higher water formation activity than Rh as the energy barrier for the formation of formate hydroxyl species is lower than for Rh. This makes Rh a better catalyst for syngas production [166, 177]. Although H_2 oxidation kinetics on Pt surfaces has been studied extensively, the work on Rh is limited [53, 75, 78, 144, 153, 157, 161, 178-181]

In 1979, Yates, Thiel and Weinberg published a series of papers to examine the adsorption, desorption, and surface reactions of H_2 and O_2 on Rh(111) surfaces using low-energy electron diffraction (LEED) and thermal desorption (TDS) studies. They explained the H_2 and O_2 adsorption as coverage-dependent where oxygen pre-coverage blocks surface sites, and this inhibits subsequent H_2 adsorption. If O_2 is co-adsorbed with H_2, the activation energy for H_2 desorption is decreased. Due to the LEED technique, their experiments were limited to temperatures below 375 K [158-160, 182].

Padowitz and Sibener proposed an elementary-step reaction mechanism on Rh(111) surfaces by following the approach of Yates, Thiel and Weinberg. Using molecular beam technique, they were able to examine the reactions at temperatures of 450-1250 K for reactant pressures below 10^{-4} Torr. In their mechanism, they introduced oxygen dissolution into bulk metal at high temperatures and showed that water formation mainly follows the path of combination of adsorbed O and H species to yield hydroxyl intermediates, and that the reaction of H is sequenced. The reaction mechanism does not assume any dissociation of water, although all other elementary-steps are reversible. They concluded that the adsorption of H_2 and O_2 was coverage-dependent. For high temperature regimes with high oxygen and low hydrogen coverage conditions, the reaction regime shows linear, nonlinear, and possibly oscillatory behavior [162].

Zum Mallen et al. studied H_2 oxidation on polycrystalline Rh foils and compared it with Pt. In their study, they measured the OH formation rate for surface temperatures between 1000 and 1800 K by laser-induced fluorescence (LIF), and proposed a potential-energy diagram which emphasizes that the oxygen desorption energy is slightly higher on Rh than on Pt, and that OH surface species are less stable on Rh. In this diagram, it was shown that the high OH formation activation energy (83.6 kJ/mol) via the reaction of O and H is higher than Pt (10.5 kJ/mol) [177].

Further, Wilke et al. presented a theoretical study of H_2 oxidation kinetics on Rh and Pt surfaces using density-functional theory (DFT) to create the potential-energy diagram for water formation [166]. In their study, they succeeded in reproducing the potential-energy diagram for Rh with little difference compared to Hickman and Schmidt [183]. This difference was attributed to the execution of real experiments in industrial working conditions as compared to computer experiments simulated under high vacuum and on a single crystal.

Dewaele et al. studied the adsorption of H_2 and O_2 on supported (γ-Al_2O_3) Rh catalysts to point out the effect of real catalyst properties with low amounts of active metal on support [184]. In their study, they examined the desorption kinetics of H_2 and O_2 using a TAP (Temporal Analysis of the Products) reactor. They concluded that their kinetics data derived was in good agreement with the predicted adsorption and desorption rate of H_2 with respect to the second-order dependency of gas-phase H_2 concentration and adsorbed H on the surface. They also estimated the desorption activation energy for H_2 to be 56.6 kJ/mol which is considerably less than reported in the literature (80-100 kJ/mol) [184]. This difference is attributed to the support effect.

In recent years, Mhadeshwar and Vlachos studied H_2 ignition on Rh foils in a microreactor at atmospheric conditions in fuel-lean regimes. They pointed out that, unlike on Pt catalysts, ignition temperature decreases with increasing H_2 concentration in the fuel mixture [151]. Using the ignition data, they proposed a H_2 oxidation reaction mechanism as well. In their mechanism, they emphasized that desorption activation energies of oxygen and hydrogen are coverage-dependent. Maestri et al. used this heterogeneous reaction mechanism to examine the effect of H_2/O_2 homogeneous reactions at moderate temperature ranges in H_2-

rich regimes for varying flow rates. [185, 186]. They used an annular duct reactor for kinetic investigations and showed that the gas-phase reactions are negligible in a temperature range of 323-873 K. They pointed out that the heterogeneous model overestimates the measured O_2 conversions at intermediate temperatures and at the lowest flow rate (2 Nl/kg.cat). On the other hand, at high temperatures, the model underestimates the experimental O_2 conversion values. The difference between the experiments and predicted values becomes more evident with increasing flow rates. Besides the mass transfer limitations due to the reactor behavior, they explain these differences as a result of possible non-uniformity of the deposits in the boundaries of the catalyst bed and the uncertainty between the beginning and the end of the reactor [186]. This conclusion emphasizes the necessity of a well-defined reactor type for kinetic investigations.

5.2.2 Experimental Procedure

H_2 oxidation is studied at different temperatures and hydrogen/oxygen ratios. Operating pressure is selected to be 500 mbar and total flow rate is 15.5 SLPM. Ar-diluted gas mixtures are fed to the reactor and boundary-layer profiles of the species are measured at steady-state temperature. The thickness of the boundary-layer and the data points collected vary depending on the temperature. The maximum boundary-layer thickness measured in this study is 7 mm. The calculated flow velocity is 51 cm/s at 500 mbar working pressure and at the temperature of 313 K. Boundary-layer distributions of the species are measured. Detailed description of the measurement technique is given in Chapter 3.1.5.

5.2.3 Kinetic Parameters

The heterogeneous reaction mechanism of Deutschmann et al. for catalytic conversion of hydrocarbons over Rh catalyst [33, 88] is taken to be as a reference for the elementary-step-like reactions and the enthalpy values for $H_2/O_2/Rh$ systems. Reaction rate parameters are optimized on the basis of the stagnation-flow reactor experiments. The thermodynamical consistency has been ensured. The thermodynamic consistency has been ensured for a temperature range of 273-1273 K. The proposed reaction mechanism consists of six reversible elementary-steps including three gas-phase and six surface species (Table 5.1). This reaction mechanism follows Langmuir-Hinshelwood kinetics.

Adsorption, desorption and surface reactions between adsorbed species are modeled based on the mean- field approximation.

Table 5.1. Proposed surface reaction mechanism for H_2 oxidation kinetics.

	Reaction	*A*(cm, mol, s)	*β*(-)	E_a(kJ/mol)
R1	$H_2 + Rh(s) + Rh(s) \longrightarrow H(s) + H(s)$	3.000 x 10^{-2}	stick. coeff.	
R2	$O_2 + Rh(s) + Rh(s) \longrightarrow O(s) + O(s)$	1.000 x 10^{-2}	stick. coeff.	
R3	$H_2O + Rh(s) \longrightarrow H_2O(s)$	1.000 x 10^{-1}	stick. coeff.	
R4	$H(s) + H(s) \longrightarrow Rh(s) + Rh(s) + H_2$	5.574 x1 0^{19}	0.239	59.69
R5	$O(s) + O(s) \longrightarrow Rh(s) + Rh(s) + O_2$	5.329 x 10^{22}	-0.137	387.00
R6	$H_2O(s) \longrightarrow H_2O + Rh(s)$	6.858 x 10^{14}	-0.280	44.99
R7	$H(s) + O(s) \longrightarrow OH(s) + Rh(s)$	8.826 x 10^{21}	-0.048	73.37
R8	$OH(s) + Rh(s) \longrightarrow H(s) + O(s)$	1.000 x 10^{21}	0.045	48.04
R9	$H(s) + OH(s) \longrightarrow H_2O(s) + Rh(s)$	1.743 x 10^{22}	-0.127	41.73
R10	$H_2O(s) + Rh(s) \longrightarrow H(s) + OH(s)$	5.408 x 10^{22}	0.129	98.22
R11	$OH(s) + OH(s) \longrightarrow H_2O(s) + O(s)$	5.735 x 10^{20}	-0.081	121.59
R12	$H_2O(s) + O(s) \longrightarrow OH(s) + OH(s)$	1.570 x 10^{22}	0.081	203.41

The rate coefficients are given in the form of $k=AT^{\beta}\exp(-E_a/RT)$; adsorption kinetic is given in form of sticking coefficients; the surface site density for Rh (111) is Γ=2.72 x 10^{-9} mol cm^{-2}

It is assumed that, H_2 and O_2 dissociatively adsorb on the Rh surface with sticking coefficients of 0.3 and 0.1, respectively.

Table 5.2. Comparison of sticking probabilities of H_2, O_2 and H_2O on Rh active site.

Sticking coefficen s_o (unitless)	Thiel et al.,1979b	Yates et al.,1979b	Hickman and Schmidt, 1993	Zum Mallen et al.,1993
H_2		0.65	1.60 x 10^{-1}	3.20 x 10^{-1}
O_2	0.2	-	1.00 x 10^{-2}	1.00
H_2O	-	-	1.60 x 10^{-1}	1.60 x 10^{-1}

The sticking coefficients of H_2 and O_2 vary in a wide range [88, 151, 177, 183, 184]. Zum Mallen et al. presented an elementary-step-like reaction mechanism for H_2 oxidation. In their mechanism, H_2 and O_2 dissociatively adsorb on the Rh surface with sticking probabilities of 0.3 and 1.0, respectively [177], whereas Hickman and Schmidt proposed these coefficients to be 0.16 and 0.01. A detailed summary of the literature values for sticking coefficients of H_2 and O_2 is given in Table 5.2. Desorption of recombined hydrogen and oxygen is modeled as second orders in adsorbed hydrogen and oxygen atoms respectively. The activation energy of desorption of H_2 varies in the range of 75-85 kJ/mol [88, 152, 177, 183]. In the calculations, this energy was set to be 59.69 kJ/mol. According to the calculations, in the case that higher activation energy of desorption of H_2 is introduced surface is fully hydrogen covered in a H_2-rich atmosphere. That is, ignition is inhibited. Decreasing the activation energy of H_2 provides free active sites for oxygen. This altering is also in good agreement with the TAP study of Dewaele et al. (56.60 kJ/mol) [184].

On the other hand, in order to ensure the enthalpic consistency, activation energy of desorption of O_2 is increased from 355.20 kJ/mol to 387.00 kJ/mol [88] which is justifying by the fact that O_2 desorption activation energy varies in a wide range (104.5-355.3 kJ/mol) in the literature [177]. Due to the high activation energy barrier of O_2 desorption, in O_2 rich conditions, the surface is predominantly oxygen covered and this pre-coverage blocks subsequent H_2 adsorption [162]. This indication is in good agreement with experimental studies of Bär et al. In their study, ignition temperature was found to be increased by increasing oxygen/hydrogen ratios [187] This behavior was explained by poisoning effect of high oxygen coverage. Since the O_2 desorption step is much slower than H_2 desorption, in O_2 rich atmosphere oxygen covers the metal surface and blocks the free sites for subsequent H_2 adsorption. This behavior leads to higher ignition temperatures with increasing oxygen/hydrogen ratios.

However, a relatively high sticking coefficient of 0.3 is chosen for H_2 adsorption to provide sufficient amount of adsorbed hydrogen species to yield the reaction.

After the adsorption of reactants, the reaction mechanism follows the reaction path between adsorbed O and H species to form OH and H_2O adsorbates. The formation of $H_2O(s)$ formation from OH(s) and H(s) is the fastest step with the lowest activation barrier of 41.73 kJ/mol.

5.2.4 Results and Discussion

The surface reaction kinetics is developed based on the experimental results of stagnation-flow reactor and already published data of Tavazzi et al. [188]. Reaction rate on the stagnation-flow reactor catalyst surface is calculated based on the measured concentration fluxes along the boundary-layer and model development is achieved with the comparison of experimental and numerical values.

Sensitivity Analysis

Normalized sensitivity coefficients S_{ik} are computed by using SPIN in the form of logarithmic derivatives (Eq. 5.3), in which Y_i presents the mass fraction of the i -th gas or surface species.

$$S_{ik} = \frac{\alpha_k}{Y_i^{max}} \frac{\partial Y_i}{\partial \alpha_k} \qquad 5.3$$

Here, the maximum value of each variable on the catalyst surface is considered Figure 5.5 a, b show a comparison of model sensitivity to gas-phase and surface species in O_2-rich conditions before (330 K) and after the ignition temperatures. 600 K is selected for sensitivity analysis after ignition since the ignition is sustained in wide range of H_2/O_2 ratios at this temperature [151, 187]. Before ignition (330 K), the formation of OH(s) and $H_2O(s)$ and their reaction with H(s) are the important reaction steps (R1, R2, R3, R6, R7 and R9). In this case the surface is mainly covered (67 %) by oxygen whereas the hydrogen coverage is calculated to be only 0.2 %. Since the formation of H_2O mainly fallows the path of OH formation and consequently OH recombination reaction as well as, adsorption and desorption of hydrogen are the critical reaction steps those effect the formation of $H_2O(s)$ and H_2O.

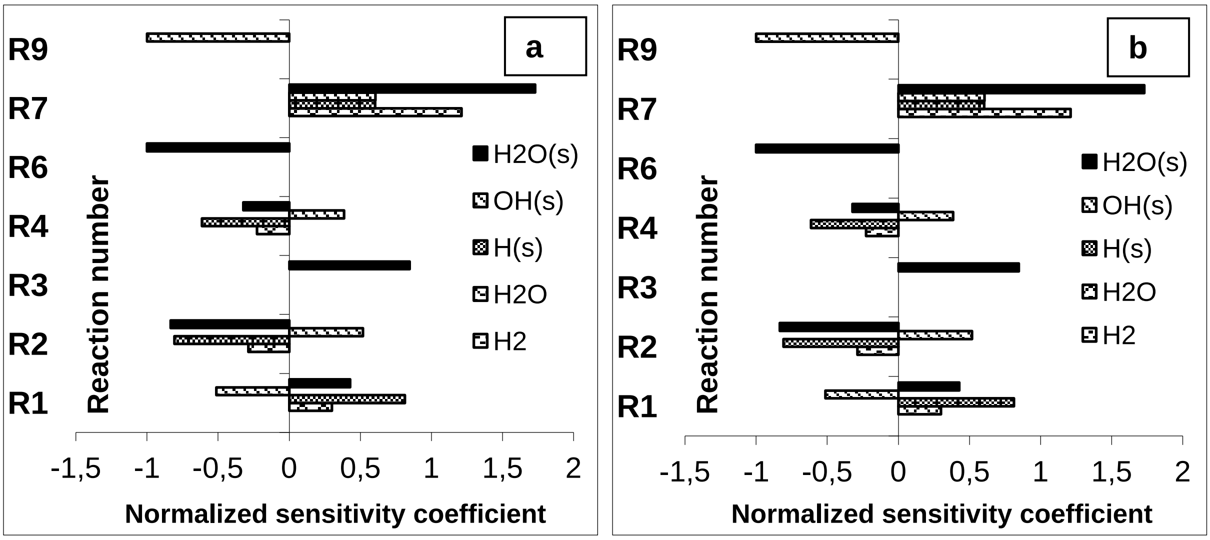

Figure 5.5. Normalized sensitivity coefficients for molar H_2/O_2 ratio of 0.67 before (a) and after (b) ignition.

Before ignition, surface is fully oxygen covered. On the other hand after ignition, hydrogen surface coverage is increased to be 40 % although the surface is still highly O_2 covered (60 %). In this case, gas-phase hydrogen concentration is controlled by R1 and R2 reaction steps. Besides, formation of OH(s) is highly sensitive to reaction R7 where the reaction between adsorbed O and H takes place.

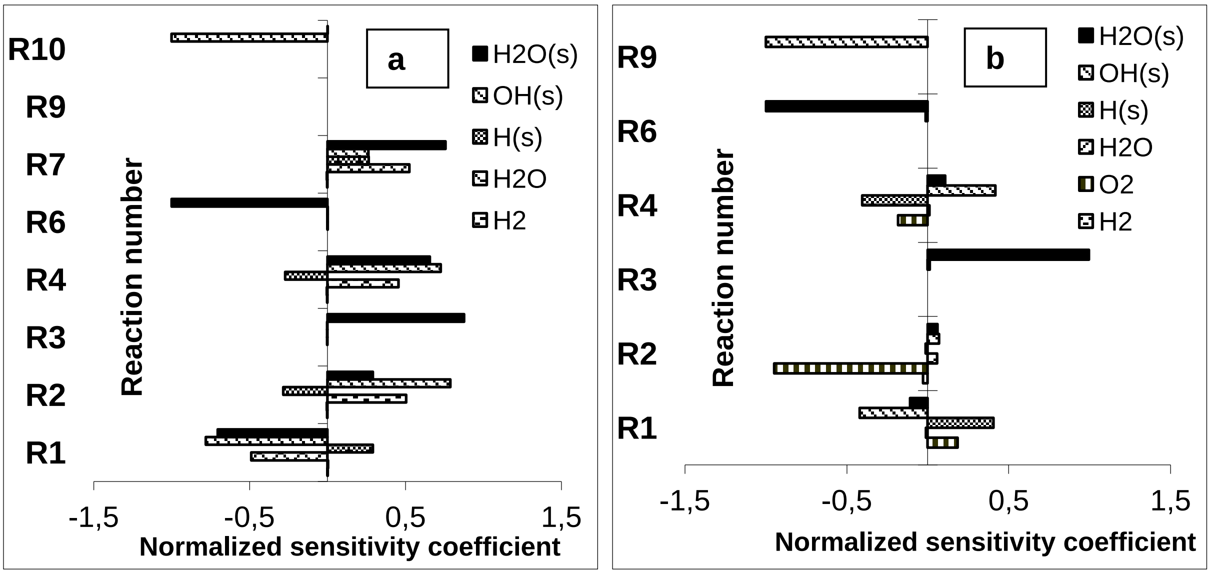

Figure 5.6. Normalized sensitivity coefficients for molar H_2/O_2 ratio of 2.33 before (a) and after (b) ignition.

Sensitivity analyses for H_2 rich conditions are shown in Figure 5.6 a,b before and after the catalytic ignition. Before ignition (330 K), although the surface is highly hydrogen covered (72 %), oxygen molecules still find free sites to adsorb (26 % oxygen covered). The reaction steps R1, R2, R4, R6, R7 and R10 are the critical reaction steps with respect to the gas-phase H_2O concentration as well as OH(s) and H_2O(s) concentrations (Figure 5.6 a). After ignition (600 K), the surface coverage of oxygen is nearly zero (0.08 %) Therefore, adsorption of gas-phase oxygen becomes an important step (R2). Formation of H_2O is controlled by R3 and R6 reaction steps where adsorption and desorption of H_2O take place. On the other hand, concentration of OH(s) is sensitive to R9 where H_2O(s) is formed (Figure 5.6 b).

Stagnation-Flow Reactor Experiments

Stagnation-flow reactor experiments are carried out at 673 K and 873 K with stoichiometric amount of H_2:O_2 mixtures (H_2/O_2 mole fractions: 0.0573/0.0287 baseline conditions) and with O_2 rich conditions, where equimolar H_2 and O_2 are fed into the system.

Figure 5.7 shows the catalytic oxidation of H_2 for the base-line case. Results from measurements (points) and from simulation (lines) of O_2 and H_2 concentrations are depicted in the boundary-layer. Simulations are performed by using CHEMKIN SPIN and DETCHEM^{STAG}. $F_{\mathrm{cat/geo}}$ value of 1 (effective $F_{\mathrm{cat/geo}}$) is used for numerical simulations. H_2O concentrations are calculated (points) by ensuring the oxygen mass balance.

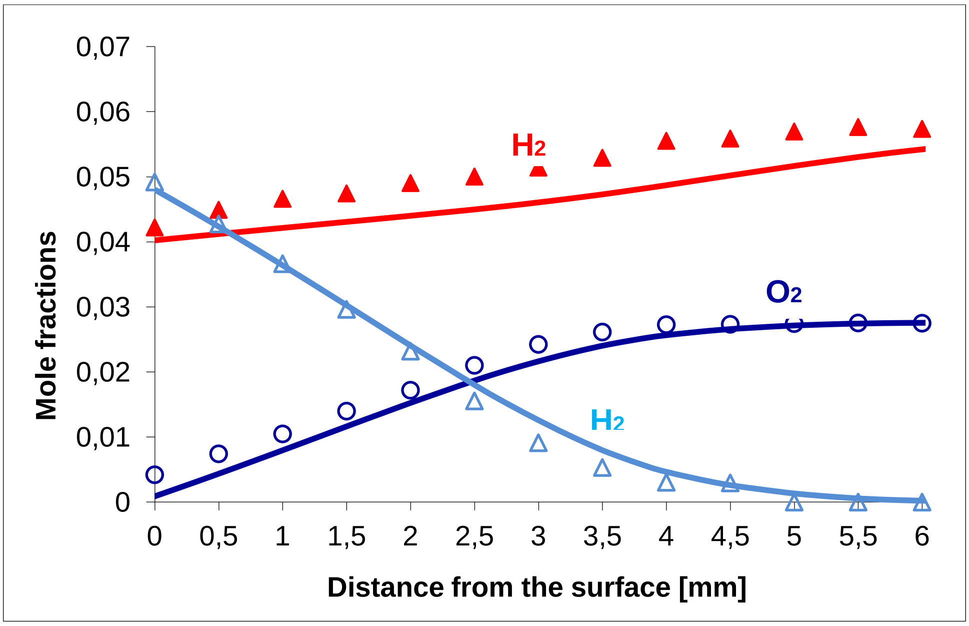

Figure 5.7. Comparison of experimental (symbols) and simulation results (lines) for catalytic oxidation of H2 at 673 K for baseline conditions (H_2/O_2=2) at 500 mbar with an inlet velocity of 51cm/s.

The concentration profiles of the reactant reach the inlet conditions at the edge of the boundary-layer. According to the O_2 profile, reaction is transport-limited because O_2 is almost completely consumed at the surface whereas the decrease in H_2 concentration reaches only 30 % of its inlet value. This behavior is due to the high diffusion rate of H_2 in Ar compared to that of O_2. As long as H_2 is consumed on the surface, the high mass transport properties of H_2 result in the fast diffusion to the surface.

To analyze the transport limitations, the measurement is conducted for O_2-rich conditions. Equimolar H_2 and O_2 are fed to the reactor and catalytic oxidation is observed at 673 K. According to Figure 5.8, O_2 is completely consumed on the surface whereas the concentration of H_2 is close to zero. Only heterogeneous chemistry is involved at this temperature. Again, the faster H_2 diffusion cases the difference. Increasing the oxygen concentration limits the mass transport of hydrogen molecules to the surface, that is, reaction rate is increased and more water molecule is produced.

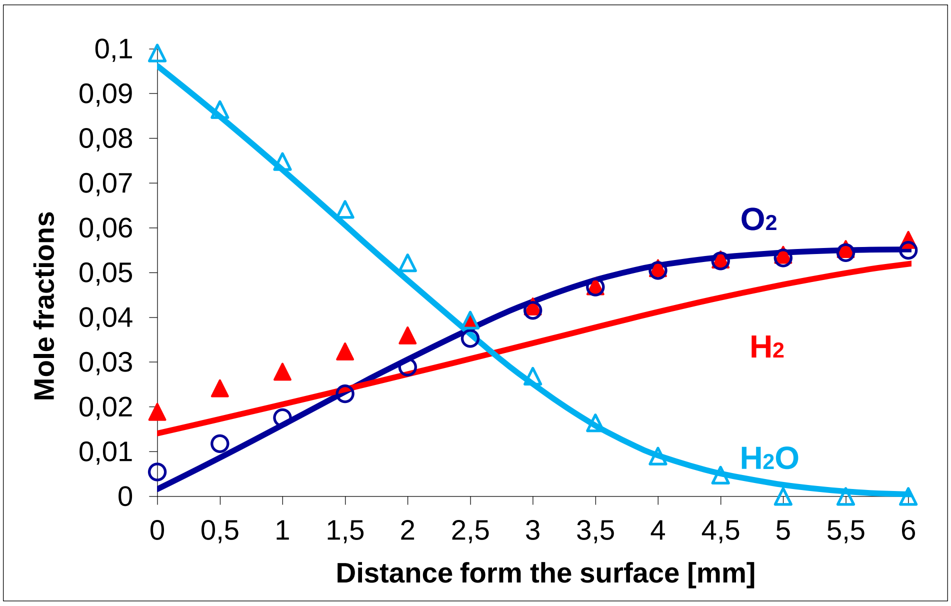

Figure 5.8. Comparison of experimental (symbols) and simulation results (lines) for catalytic oxidation of H_2 at 673 K (H_2/O_2=1) and at 500 mbar with an inlet velocity of 51cm/s.

Figure 5.9 and Figure 5.10 illustrate H_2 oxidation at 873 K for the baseline condition and O_2-rich conditions. The similarities between Figure 5.7 and Figure 5.9 as well as between Figure 5.8 and Figure 5.10 are remarkable. Since the reaction is transport-limited, increasing the temperature does not have a significant influence on the product distribution on the catalyst surface. However, the boundary-layer thickness is increased (7 mm) since H_2 mobility is highly affected by temperature.

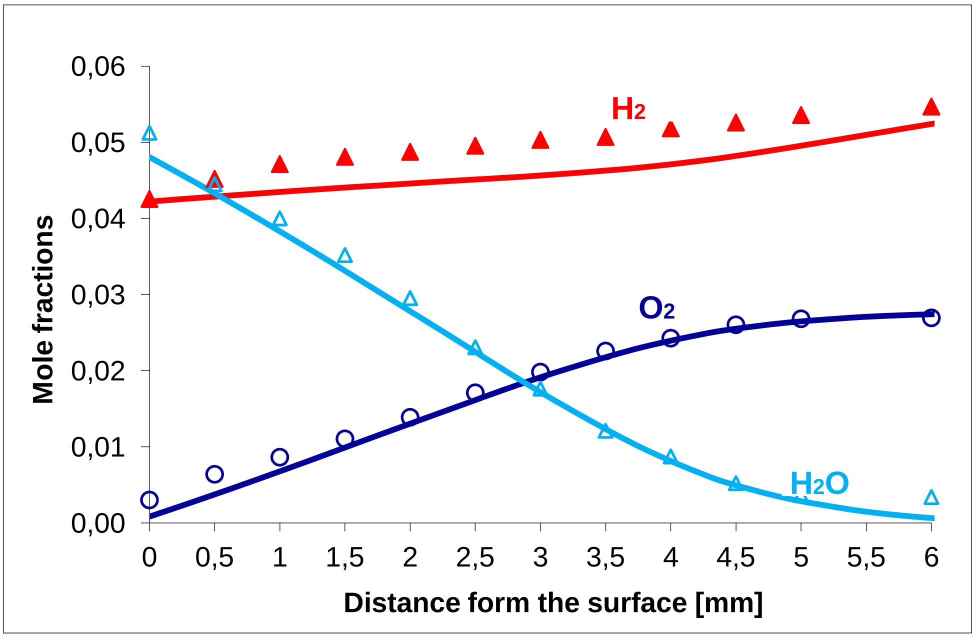

Figure 5.9. Comparison of experimental (symbols) and simulation results (lines) for catalytic oxidation of H_2 at 873 K for baseline conditions (H_2/O_2=2) at 500 mbar with an inlet velocity of 51cm/s.

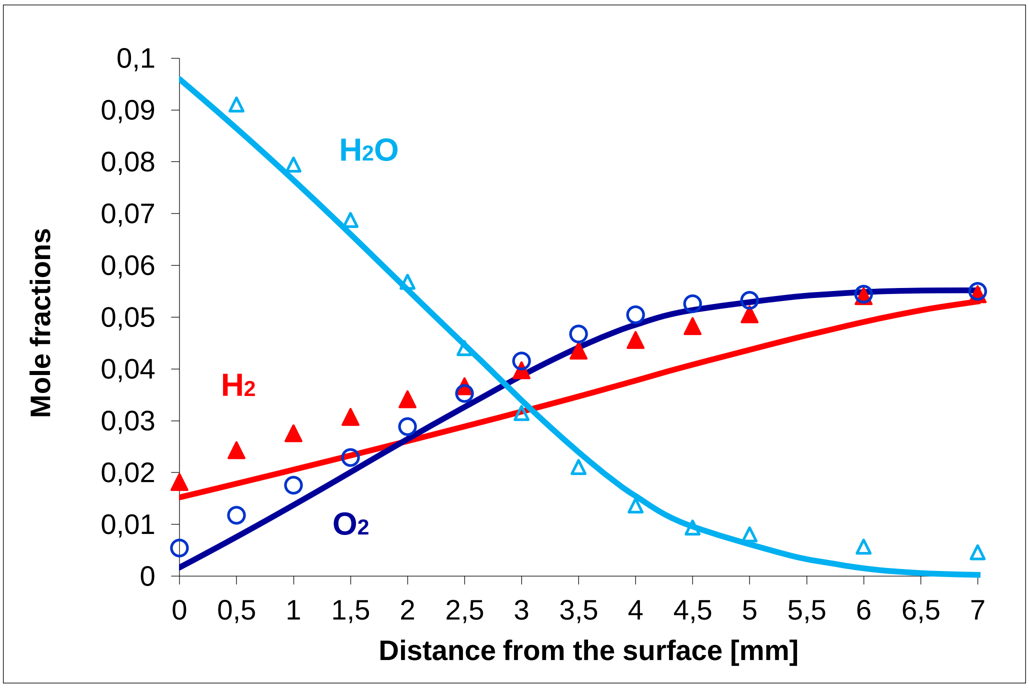

Figure 5.10. Comparison of experimental (symbols) and simulation results (lines) for catalytic oxidation of H_2 at 873 K (H_2/O_2=1) and at 500 mbar with an inlet velocity of 51cm/s.

For all cases, model simulations predict the surface concentration of H_2, O_2, and H_2O in good agreement. On the other hand, diffusion behavior of H_2 along the boundary slightly differs in the model compared to experimental results (Figure 5.8 and Figure 5.10). This difference can be attributed to the transport properties of H_2 in the mixtures. Based on the calculations with CHEMKIN SPIN, mixture-averaged transport properties are evaluated from the pure species properties using averaging procedures. Each species' diffusion velocity is calculated in terms of a diffusion coefficient and a species gradient.

$$V_i = -\frac{1}{X_i} D_{ij} \frac{dX_j}{dz} - \frac{D_i^T}{\rho Y_i} \frac{1}{T} \frac{dT}{dz} \quad . \tag{5.4}$$

$$D_{im} = \frac{1 - Y_i}{\sum_{j \neq i}^{i} X_j / \text{Đ}_{ji}} \quad . \tag{5.5}$$

In these expressions, X_i is the mole fraction for the $i-$ th species, Đ_{ji} is the binary diffusion coefficient matrix, D_{im} is the matrix of binary diffusion coefficients, and is D_i^T the thermal diffusion coefficient for the $i-$ th species [69]. Thermal diffusion plays an important role especially on small molecules such as H_2. Besides, it is believed that this behavior affects the microprobe sampling accuracy as well, since H_2 molecules tend to diffuse faster to the probe opening at high temperatures.

Application of the Reaction Kinetics: Flow Reactor Experiments

To show the applicability of the developed reaction kinetics, the H_2 oxidation measurement by Tavazzi et al.[188] in a flow reactor are reproduced. Their experiments were carried out in an annular type of reactor. A mullite tube with a radius of 2.35 mm was coaxially inserted into an outer quartz tube which has a 4.50 mm radius. 0.5 wt/wt % Rh/Al_2O_3 catalyst was coated on the inner tube (Figure 5.11).

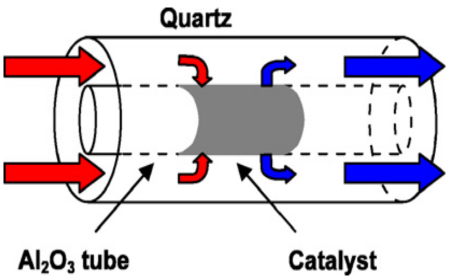

Inner Radius (mm)	2.35
Outer Radius (mm)	4.50
Reactor Length (mm)	15
Operating Pressure (atm)	1
Catalyst dispersion	70 %

Figure 5.11. Annular reactor used in the experiments of Tavazzi et al. [188].

The catalyst layer was 40-50 µm thick and it had 15 mm length. 70 % metal dispersion was calculated. With these data, the proposed reaction mechanism was evaluated by simulating the experiments by using the DETCHEM^{CHANNEL} software (Figure 5.12) [58]. Simulation results show reasonably good agreement with the experimental data. At low flow rates, the model overestimates the O_2 conversion where the reaction is in a transition state between the kinetically-controlled to mass transport-limited regime.

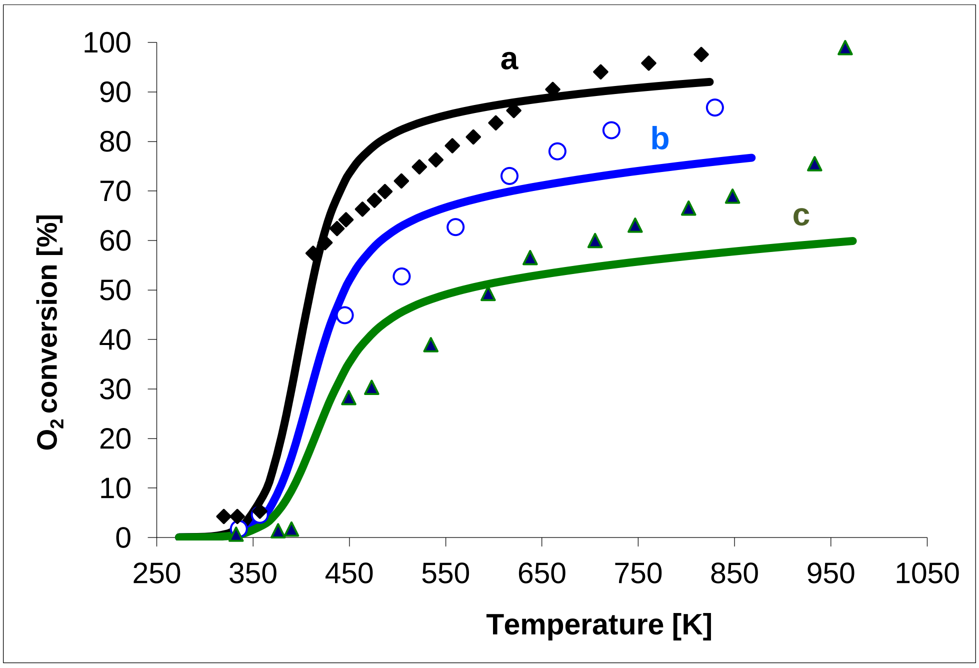

Figure 5.12.Comparsion of H_2 oxidation simulations (lines) and experiments (points) under H_2 rich conditions $H_2/O_2/N_2$: 4/1/95 vol %. $F_{cat/geo}$ is assumed to be 1 for all cases. Effect of flow velocity is presented for 0.274 SLPM (a), 0.548 SLPM (b) and 1.096 SLPM (c).

For high temperature regimes over 573 K, the model underestimates the O_2 conversion rates. Due to the reactor configuration, external mass transport limitations take place in the reaction, which results in a higher discrepancy between experiments and simulations with higher flow rates. A similar tendency was also observed with lumped kinetic model simulations by Tavazzi et al. [188] and elementary-step-like reaction model presented by Maestri et al. [186].

5.2.5 Conclusion

The aim of this study is twofold. First, to provide a better understanding of H_2 oxidation kinetics on Rh surfaces, which is a critical step for fuel processing technologies such as partial oxidation, steam reforming, and auto thermal reforming of hydrocarbons.

H_2 oxidation experiments are carried out for varying fuel/oxygen ratios and temperatures. Experimental data are used to assist development of a thermodynamically consistent elementary-step-like reaction kinetics.

Sensitivity analyses showed that hydrogen adsorption and desorption steps are the crucial steps and the kinetics is highly sensitive to the concentrations of gas-phase H_2O, adsorbed H_2O and OH species.

The proposed reaction mechanism is tested by reproducing the H_2 oxidation measurement data created in a laboratory scale flow reactor with different flow rates taken from Tavazzi et al.[188].

5.3 CO/O_2 systems: Direct oxidation of CO by O_2

In this chapter, an investigation of direct oxidation of CO over Rh/Al_2O_3 is presented. Experiments are carried out in the stagnation-flow reactor at low, moderate, and high temperatures to evaluate the surface reaction kinetics over a wide range of temperature. The reaction kinetics is further tested by comparison of experimental light-off temperatures with numerical simulations for varying CO/O_2 mixtures in a continuous-flow reactor.

5.3.1 Theoretical Background

Catalytic CO oxidation on noble metal surfaces is one of the most studied reactions in literature [121, 135, 189-193]. Although it is assumed to be a simple oxidation reaction with only a few reaction steps, Gerhard Ertl earned the Nobel Prize in 2007 with his studies on CO oxidation on solid surfaces [124, 131, 193, 194].

The simplicity of the reaction makes it possible to understand the relation between fundamental surface science and practical applications by searching the effect of influence of structure sensitivity on kinetics and reaction rates. Understanding the CO oxidation kinetics has also of a practical importance. CO oxidation takes place in three-way catalysts (TWC) for removal of CO in the exhaust gas [107, 195]. Besides, for fuel cell applications, CO at the ppm level needs to be removed by catalytic oxidation in a H_2-rich effluent gas stream (preferential oxidation) because the polymer electrolit membrane is sensitive to CO impurities [196, 197]. Furthermore, CO oxidation is a crucial step for catalytic partial oxidation of hydrocarbons in synthesis gas production studies at high temperatures. Recently there has been an open discussion about the reaction pathways for the formation of H_2 and CO during partial oxidation and reforming of hydrocarbons. It is still under debate whether the oxidation of CO by atomic oxygen or OH originating from dissociation of H_2O is more favorable [33, 36, 198, 199] .

CO oxidation on Rh surfaces follows a Langmuir-Hinshelwood mechanism. Studies on single crystals show that CO oxidation on Rh surfaces is structure insensitive [200]. Studies under realistic operating conditions also confirm that the trend is similar for catalytic oxidation of CO on Rh(111) and Rh(100) surfaces [201]. Besides, the reaction kinetics on silica and alumina supported Rh catalysts are identical to those of bulk Rh [200].

5.3.2 Experimental

CO oxidation measurements are carried out at 523 K, 673 K, and 873 K at steady-state. In contrast to the general measurement procedure, only the mass spectrometer is used for the detection of the species. The carrier gas flow rate in the sampling loop is chosen to be 600 ml/min. The reaction conditions are given in Table 5.3.

Table 5.3. Reaction conditions for CO oxidation.

	Temperature [K]	CO [% vol.]	O_2 [% vol.]
Case 1	523	2.67	2.33
Case 2	673	5.67	2.89
Case 3	873	5.66	2.83

At low temperatures, oxygen-rich condition is selected to avoid the external mass transport limitations and examine the kinetic effects (Case 1). However, for moderate and high temperature regimes (Case 2 and Case 3) the reactions are examined under stoichiometric conditions.

5.3.3 Results and Discussion

Surface Reaction Kinetics

The surface reaction mechanism presented here only includes the reaction steps of CO and O_2 species (direct oxidation of CO). The reaction mechanism involves ten elementary-step surface reactions in which four surface species and there gas-phase species are involved. The reaction steps of adsorption, desorption of oxygen and reaction of adsorbed oxygen (O(s)) speices have been taken from the hydrogen oxidation kinetics scheme without further modification (Table 5.1).

The reaction mechanism of Hartmann et al. [88] and Schwiedernoch et al. [33] are taken as references for the reaction steps and enthalpy values.
Reaction rate parameters involvin CO, CO_2 species are also re-evaluated. Since the preliminary purpose here is development of a unified surface reaction kinetics, the reaction steps of CO and CO_2 are evaluated, for CO oxidation as well as the reforming reactions at which the CO oxidation reaction steps are involved. However, the previous reaction mechanisms [33, 88] were developed for catalytic partial oxidation of methane, they were not especially evaluated for CO_2 reforming systems.. McGuire et al. [27] have studied the dry reforming of CH_4 over a Rh surface by using the mechanism of Hartmann et al.[88]. They emphasized that, for a reasonable dry reforming activity on Rh while avoiding deactivation of the catalyst by carbon deposition, the CO_2 adsorption rate should be much higher ($4.80\text{x}10^{-2}$) than in the model [88] ($1.00\text{x}10^{-5}$). The simulation with corrected CO_2 adsorption/desorption parameters has been reported to show a good agreement with methane dry reforming experiments in a stagnation-flow reactor [27]. Furthermore, Horn et al.[34] also pointed that the model [50] does not show a good prediction of the dry reforming activity of CH_4 due to the low sticking probability of CO_2. Referring to these studies [27, 34], the sticking coefficient of CO_2 is altered from $1.00\text{x}10^{-5}$ [33, 50, 88] to be $4.80\text{x}10^{-2}$. Besides the pre-exponential factor of CO_2 desorption is altered to be $3.92\text{x}10^{11}$.

According to catalytic ignition studies [187], due to the high sticking probability of CO, at low temperatures, the surface is fully covered in CO that blocks the active sites for subsequent oxygen or water coverage, which prevents the ignition for oxidation or WGS reactions [31]. Therefore, coverage dependency of CO with 47 kJ/mol is introduced to sustain sufficient adsorption site for oxygen. This value is calculated empirically on the basis of the stagnation-flow reactor experiments. The proposed reaction mechanism is presented in Table 5.4. The reaction kinetics is thermodynamically consistent at temperatures of 273-1273 K.

Table 5.4. Proposed reaction mechanism for CO oxidation on Rh.

	Reaction	$A^{\dagger}$(cm, mol,s)	β(-)‡	Ea(kJ/mol)
R1	$O_2 + Rh(s) + Rh(s) \longrightarrow O(s) + O(s)$	1.000×10^{-2b}	stick. coeff.	
R2	$CO_2 + Rh(s) \longrightarrow CO_2(s)$	4.800×10^{-2b}	stick. coeff.	
R3	$CO + Rh(s) \longrightarrow CO(s)$	4.971×10^{-1b}	stick. coeff.	
R4	$O(s) + O(s) \longrightarrow Rh(s) + Rh(s) + O_2$	5.329×10^{22}	-0.137	387.00
R5	$CO(s) \longrightarrow CO + Rh(s)$	1.300×10^{13}	0.295	$134.07-47\theta_{CO}$
R6	$CO_2(s) \longrightarrow CO_2 + Rh(s)$	3.920×10^{11}	0.315	20.51
R7	$CO_2(s) + Rh(s) \longrightarrow CO(s) + O(s)$	5.752×10^{22}	-0.175	106.49
R8	$CO(s) + O(s) \longrightarrow CO_2(s) + Rh(s)$	6.390×10^{21}	0.000	$174.76-47\theta_{CO}$
R9	$CO(s) + Rh(s) \longrightarrow C(s) + O(s)$	6.183×10^{22}	0.034	$129.98-47\theta_{CO}$
R10	$C(s) + O(s) \longrightarrow CO(s) + Rh(s)$	1.173×10^{22}	0.000	92.14

The rate coefficients are given in the form of $k=AT^{\beta}\exp(-E_a/RT)$; adsorption kinetics is given in the form of sticking coefficients; the surface site density is $\Gamma=2.72 \times 10^{-9}$ mol cm^{-2}.

The fidelity of the reaction kinetics is shown by using the stagnation-flow reactor data. Experimental results and numerical simulations are compared in Figure 5.13 and Figure 5.14.

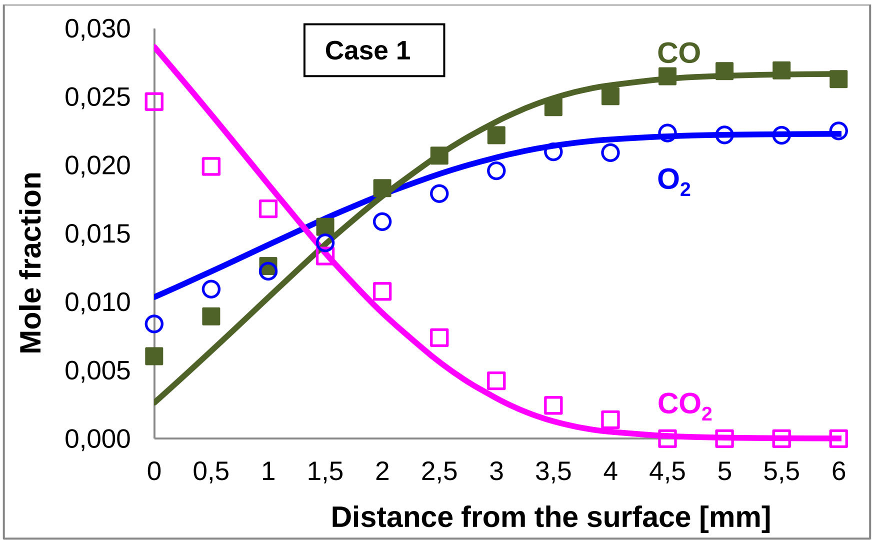

Figure 5.13. Comparison of experimental (symbols) and simulation results (lines) for catalytic oxidation of CO at 523 K and at 500 mbar with an inlet velocity of 51cm/s (Case 1).$F_{cat/geo}$ =0.6 is used in numerical simulations

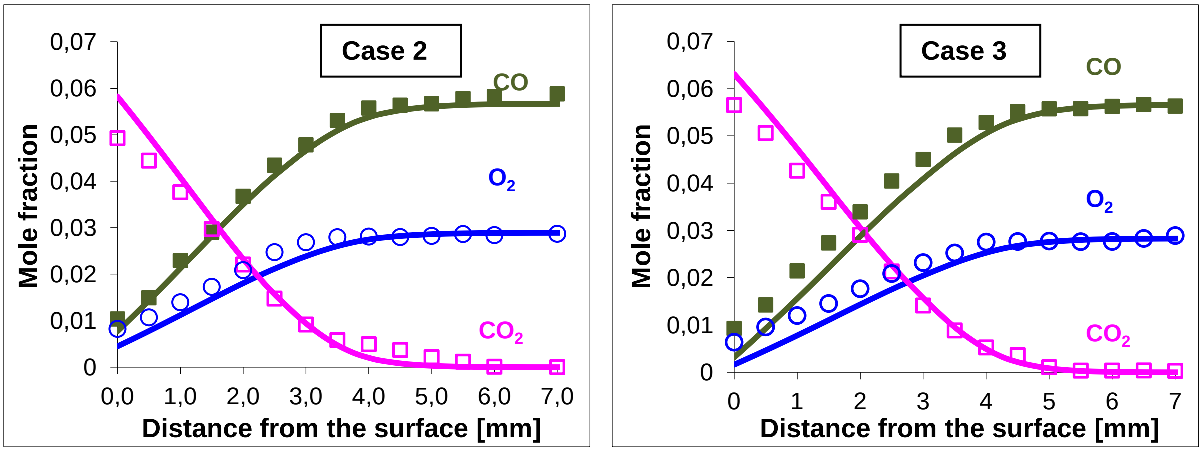

Figure 5.14. Comparison of experimental (symbols) and simulation results (lines) for catalytic oxidation of CO at 673 K (Case 2) and 873 K (Case 3) at 500 mbar with an inlet velocity of 51cm/s. $F_{cat/geo}$ =0.6 is used in numerical simulations.

For all cases investigated, the simulation results agree well with the experiments. At 523 K, the reaction is already ignited but the full conversion is not achieved. The boundary-layer thickness is measured to be 4.5 mm. At high temperatures, the boundary-layer thickness expands to 5 mm at 673 K and to 5.5 mm at 873 K, which is due to an increased reaction temperature and increased reaction rate. At 873 K, the reaction rate reaches its maximum value. CO and O_2 are completely consumed on the surface.

Application of the Kinetics

The reaction kinetics is used to model light-off measurements of CO/O_2 mixtures in N_2 dilution with a total flow rate of 5 SLPM.

Reactions are carried out in a continuous-flow reactor (Figure 5.15) for varying fuel/oxygen ratios in the form of α value which is expressed as the mole fraction of CO and O_2 (Eq. 5.6)

$$\alpha = \frac{x_{\mathrm{CO}}}{x_{\mathrm{CO}} + x_{\mathrm{O_2}}} \quad . \qquad 5.6$$

Reaction kinetics is tested for fuel lean (α=0.4,0.60) and fuel rich (α=0.71) conditions (Table 5.5).

Table 5.5. Reaction conditions for CO oxidation in a continuous-flow reactor.

Case	**% vol. CO**	**%vol. O_2**	α
1	2	3	0.40
2	3	2	0.60
3	5	2	0.71

A quartz glass tube (ID=2.0 cm) is used (Figure 5.15) as a reactor. A 0.28 wt.Rh/γ-Al_2O_3 catalyst in monolithic structure with 900 cpsi is used for the catalytic measurement. The active metal surface area is measured to be 0.63 m^2/g based on the continuous-flow CO

chemisorption measurements. $F_{\mathrm{cat/geo}}$ is calculated to be 60. Detailed information on the CO chemisorption measurement is given in Chapter 4.2.5.
The catalyst is placed in the center of the reactor and is housed in a temperature-controlled furnace. The temperature inside the catalyst bed is measured by two K-type thermocouples (NiCr-Ni, 3 mm thick) which are placed close to the catalyst´s front and back. The temperature is raised with a ramp of 5 K/min. CO and CO_2 outlet mole fractions are measured by an FTIR detector at 300-523 K. The temperature difference between front and back thermocouple was be less than 10 K for each temperature point. Thus, isothermal conditions are assumed.

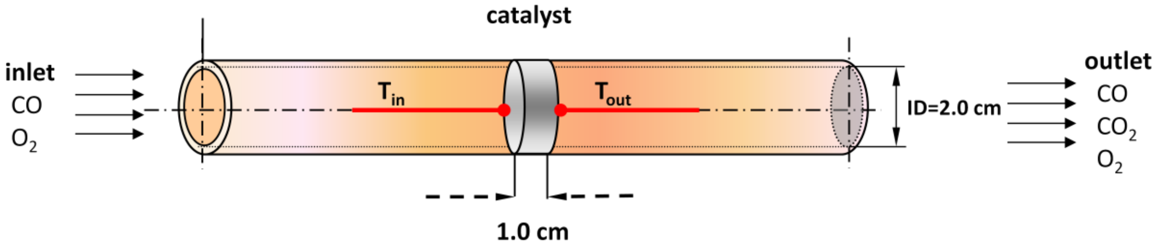

Figure 5.15. Continuous-flow reactor for CO oxidation measurements.

2D numerical simulation of the system is performed by using DETCHEM$^{\mathrm{CHANNEL}}$. The hydraulic radius of a channel is measured to be 0.48 mm and axial flow velocity is calculated to be 26.2 cm/s at 293 K. Since the washcoat layer is considerably thin (5-10 µm) [202], no diffusion limitations are taken into account. Therefore the experimentally derived $F_{\mathrm{cat/geo}}$ value is used in the numerical simulations without further adaptation. A good agreement between the experimental data and numerical simulations is presented in Figure 5.16.

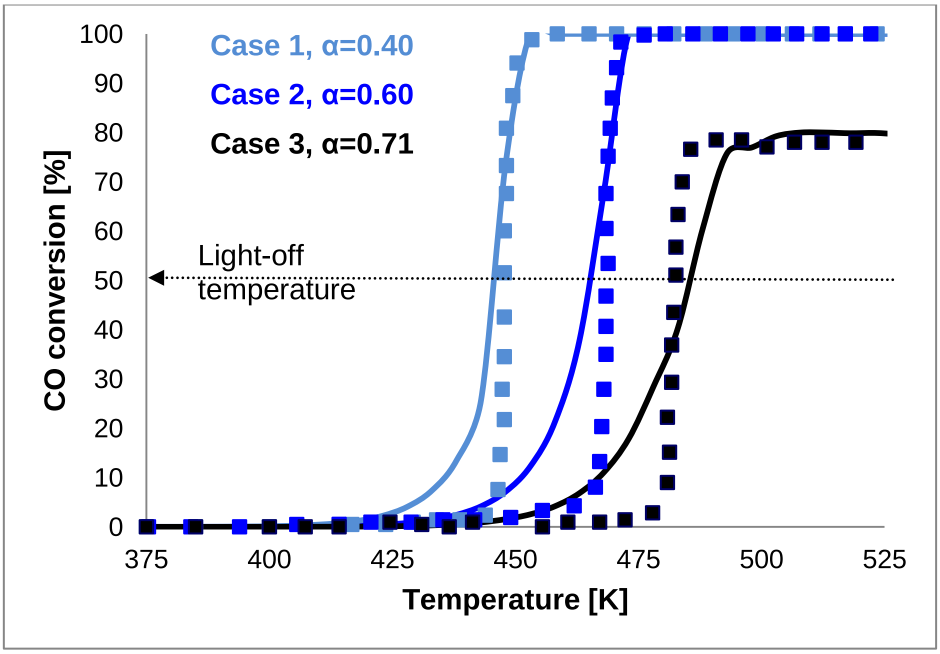

Figure 5.16. Comparison of experimental (dashed lines) and numerical simulations (solid lines) for CO conversion as a function of the catalyst temperature (T_{in}) for varying inlet gas composition of CO/O_2 in a monolithic catalyst.

The CO conversion is calculated according to Eq. 5.7, in which $x\mathrm{CO}_{in}$ and xCO_{out} denote the inlet and outlet mole fractions of CO, respectively.

$$\mathrm{CO\ conversion} = 100 * \frac{x\mathrm{CO}_{in} - x\mathrm{CO}_{out}}{x\mathrm{CO}_{in}} \quad . \tag{5.7}$$

For Case 1 (Table 5.5), in which an excess amount of O_2 is fed to the reactor, full CO conversion has been reached. Although the conversion of CO is complete for Case 2 as well, increasing the mole fraction of CO results in an increase in the light-off temperature (50 % conversion). This is due to the high surface coverage of CO which blocks the subsequent oxygen atoms, results in an increased ignition temperature [187]. At high CO concentrations (Case 3), the reaction is mass transport limited by oxygen. A maximum CO conversion of 80 % has been reached. However, when the conversion of CO is below 20 %, for all cases, a small deviation in the temperature (ΔT =~10 K) is observed between the experimental data and numerical simulations.

5.3.4 Conclusion

Surface reaction kinetics for direct oxidation of CO is developed by using stagnation-flow reactor data. Additionally, CO oxidation measurements are carried out in a continuous-flow reactor. The reaction mechanism has been tested for CO-rich and CO-lean conditions over a wide range of temperature.

5.4 Kinetics of the Water-Gas Shift Reaction

In this chapter, an investigation of water-gas shift (WGS) and reverse water-gas shift (R-WGS) reaction kinetics over Rh/Al_2O_3 is presented. This study is as a sequel to the previous studies in which an elementary-step-like reaction mechanism for H_2/O_2 and CO/O_2 sub-systems over Rh/Al_2O_3 catalysts was presented (Chapter 5.2 and 5.3) Here, the surface reaction mechanism is extended to $CO/CO_2/H_2/H_2O/O_2$ systems. The WGS, R-WGS and the preferential oxidation of CO experiments are carried out in the stagnation-flow reactor. Particularly, high temperature regime reactions are studied to reveal the effect of WGS reaction on partial oxidation and steam/dry reforming of hydrocarbons. The applicability of the reaction kinetics is also tested with the experiments carried out in a laboratory-scale flow reactor a the temperature range of 473-1173 K.

5.4.1 Theoretical Background

The WGS reaction is industrially important for H_2 production technologies.

$$\mathrm{CO} + \mathrm{H_2O} \leftrightarrow \mathrm{CO_2} + \mathrm{H_2} \qquad \Delta_\mathrm{R}\mathrm{H}^\mathrm{o} = -40.4\ \mathrm{kJ/mol} \qquad 5.8$$

Among the possible reaction paths in reforming of hydrocarbons, i.e., total oxidation, steam reforming, and dry reforming, heterogeneously-catalyzed WGS is one of the crucial reaction paths that determine the overall yield of synthesis gas (H_2+CO) [203-206].

In H_2-operated, low-temperature fuel cell power generation systems and in ammonia synthesis plants, in which CO as a by-product should be removed from the product gas, WGS technology is used to purify the synthesis gas [31, 127, 196, 207].

Besides, in after-gas treatment applications, the WGS reaction takes place between CO and H_2O in the effluent gas stream. This reaction has a significant effect on the reduction of CO emissions [130, 206, 208].

Low Temperature Applications: Synthesis Gas Purifications

In commercial applications, in which the removal of CO from the stream is necessary, the WGS reaction takes place in two steps, involving high-temperature shift and low-temperature shift WGS reaction processes, which are known as HTS and LTS, respectively [127]. Iron oxide and chromium oxide catalysts are used for the HTS in the temperature range of 583-723 K [209]. The LTS reaction, however, is mostly carried out as a second step after the HTS. Catalysts based on zinc and copper oxide are used in the temperature range of 473 to 523 K [209, 210].

Even though the reaction efficiency can be increased with this two-stage reactor configuration, there is a renewed interest in a robust catalyst because LTS catalysts are sensitive to air and condensed water as well as easily poisoned by sulfur [130]. Besides, conventional catalysts imply large reactor volumes, in which mostly a packed-bed reactor configuration is used. This limits their application to on-board reforming technologies where smaller systems are required for portable power plants [211].

Noble metal-supported catalysts show promising activity as next generation WGS catalysts because of their high stability in low and high temperature regimes and high tolerance capacity to impurities [130, 206]. Pt, Rh, Pd, and Au-promoted catalysts on different support systems (ceria, La_2O_3) are investigated as new candidates for WGS reactions [196, 206] . Among these metals, Rh is a promising catalyst because, at the same reaction conditions, it has a higher stability and turnover rate (TOR) than others.

Although the general agreement is that Rh is the best catalyst for H_2 purification technologies, a deep understanding of such complex systems and reaction pathways has not been achieved yet [32]. In order to optimize and advance such catalytic systems, it is important to achieve a fundamental understanding of the reaction mechanism over the catalyst (metal) and reveal its interaction with the support on a molecular level [31, 32].

Different reaction mechanisms are proposed for WGS reaction kinetics depending on the metal and support systems and the reaction conditions investigated. For example, for ceria containing automotive three-way catalysts, it was reported that the activity of the catalyst does not only depend on the metal but that the support also plays an important role [31, 127, 130, 196].

Many theoretical and experimental studies are conducted to elucidate the main reaction path of WGS. Three different reaction mechanisms are proposed for WGS reaction, whereas the exact reaction mechanism still remains unsettled [204]. One of the proposed reaction mechanisms relies on the assumptions that the redox mechanism is dominant and CO_2 is generated by a reaction of CO, which is adsorbed on the metal with a CeO_2 surface, and H_2 is formed via re-oxidation of the Ce surface with H_2O. For the second mechanism, it is assumed that the carboxyl mechanism is dominant [31]. For supports containing CeO_2 , regardless of the metal type (Pt or Rh), substraction of H from water leads to OH formation on the support, which is a slow step, and the main reaction path of the CO_2 formation follows the path of the formation of a carboxyl (COOH) intermediate. The reaction proceeds with decomposition of the carboxyl intermediate to form CO_2 and H. The reaction between the chemisorbed CO and O is negligible [31].

Lastly, a formate species (HCOO) is formed, presumably by the reaction of adsorbed CO and OH. Olympiou et al. studied WGS reactions at 623-823 K on Pt, Pd, and Rh supported on γ-Al_2O_3 with similar noble metal dispersions [127]. According to their study, at steady-state, as a result of surface diffusion of H/ OH species present on the alumina support, the reaction is favored for the formation of adsorbed formate (HCOO). This intermediate species resides on the alumina support and/or the metal support intermediate, and this reaction step might be considered a slow step in WGS. Jacobs et al. also studied low temperature WGS reaction kinetics on ceria-supported Au catalysts [196]. They used in-situ steady-state diffuse reflectance infrared Fourier transform spectroscopy (DRIFTS) as the spectroscopic technique for the measurements. According to their study, formates are present on the surface of reduced ceria, being formed by a reaction with geminal OH groups that are present after reduction of the ceria surface shell. Based on the data from Fourier transform infrared (FTIR) spectroscopy, similar explanations have been given for Rh/MgO, Rh/ZnO, and Rh/CeO_2 catalysts by Shido and Iwasawa [212],for Pt/MgO and Pt/ZrO by Chenu et al [213] and Pt/CeO_2 by Grenoble et al. [214].

Formate (HCOO) is the isomer of carboxyl (COOH) and both structures have been detected experimentally within the framework of FTIR and DRIFTS and steady-state isotropic transient kinetic analysis (SSITKA). However, there is a disagreement in the interpretation of the experimental data as to whether it is a carboxyl or a formate species. According to Hilaire et al., based on the spectra, the band which appears in the range of 1000–1700 cm^{-1} originates from OCO asymmetric and symmetric stretching vibrations [215]. Therefore, it is difficult to distinguish whether the bands in this region correspond to carbonates or formates, because both species contain OCO vibrations. Besides, theoretical calculations also favor the formation of carboxyl species [204, 205].

High Temperature Applications: Effect of WGS Reaction on Synthesis Gas Production

For high-temperature applications, Rh supported on Al_2O_3 catalysts are known as efficient catalysts for synthesis gas production [5, 36, 88]. Recent researches follow two distinct approaches to explain the synthesis gas production and the effect of the WGS reaction on product distribution and reaction yield: direct and indirect mechanisms [35, 216, 217]. The direct reaction mechanism postulates the formation of H_2 and CO via partial oxidation of CH_4 in the presence of gas-phase O_2[183], whereas, for the indirect reaction pathway, a two-zone model is assumed, which means that at the beginning of the reaction zone, total oxidation takes place and the reaction proceeds with H_2O and CO_2 reforming of methane to generate synthesis gas. The WGS and the consecutive combustion of H_2 and CO also take place in this reaction zone [188].

The literature addresses different types of mechanism for WGS reaction and its effect on catalytic partial oxidation (CPOx) and reforming of hydrocarbons, depending on the reactor types in which the kinetic investigations are carried out, on operating conditions, and on the sampling technique used [30]. Horn et al. have studied the effect of the WGS in CPOx over Rh catalysts by using the spatial profiles technique which enables monitoring concentration and temperature profiles along the catalyst bed under transient and steady-state conditions. They claimed that the WGS has only a minor effect since the amount of CO_2 does not change in the absence of O_2 and the contribution of the WGS varies with the C/O feed ratio [5].

Michael et al. have studied the effects of H_2O and CO_2 as co-reactants on CPOx reactions by using the spatial profile technique as well. They claimed that the feeding of H_2O as a co-reactant has no effect on CH_4 reforming, however the main product distribution is significantly affected by the WGS reaction [218]. However, Maestri et al. have proposed that the WGS reaction is equilibrium limited and the OH species is the main oxidation source to form CO via C generated by pyrolysis of methane. It was concluded that steam reforming and dry reforming reactions of methane always occur with WGS and that the formation of CO_2 is mainly due to the dissociation of the carboxyl COOH species [36].

Wang et al. have studied the WGS reaction over Rh/Al_2O_3 catalysts by using a TAP reactor at isothermal conditions and under vacuum. They claimed that CO_2 formation mainly occurs via fast oxidation of CO with adsorbed oxygen or via a nucleophilic attack of adsorbed OH groups on the alumina support which has an inverse spill-over effect because the water can dissociatively adsorb on alumina by producing O and OH species [139]. According to Wei et al., the isotopic tracer studies show that the step of H_2O dissociation is quasi-equilibrated, i.e., H and OH species recombine rapidly to form H_2, and water forms mainly via the reaction of O, which results in the dissociation of CO_2 [199].

5.4.2 Experimental Procedure

Catalytic Measurements

In order to understand the WGS and R-WGS kinetics, a series of measurements is carried out in the stagnation-flow reactor under a varying fuel/oxygen composition and temperature. Preferential oxidation of CO with varying H_2 and O_2 mixtures is also studied. Detailed descriptions of the experimental conditions are given in Table 5.6-5.8 Reactor operating pressure is selected to be 500 mbar to obtain an optimum boundary-layer thickness. The same catalyst which was used for H_2 oxidation measurement (Chapter 5.2) is used.

Preferential Oxidation of CO in H_2/O_2 Mixtures

The CO oxidation behavior of the catalyst is tested in the presence of H_2 at varying O_2 concentrations.

Table 5.6. Experimental conditions for preferential oxidation of CO in H_2/O_2 mixtures.

	Temperature (K)	H_2 Mole Fraction (%)	CO Mole Fraction (%)	O_2 Mole Fraction (%)
Case 1	873	6.00	5.20	5.20
Case 2	873	6.00	5.20	2.65
Case 3	873	2.57	2.57	4.00

Ar-diluted gas mixtures are fed to the reactor with a total flow rate of 15.5 standard liter per minute (SLPM, at 20 ^{o}C and 1 atm), which results in a flow velocity of 51 cm/s at the inlet at 500 mbar. The experimental conditions are summarized in Table 5.6. Boundary-layer profiles of the species are measured at steady-state. The thickness of the boundary layer and the data points collected vary depending on the temperature and fuel (H_2+CO) to oxygen ratios.

WGS and R-WGS reactions

The WGS reaction is carried out at a temperature ranges of 873-1073 K with the steam/carbon (S/C) ratios of 1.1 for all cases. A detailed explanation for the experimental conditions is given in Table 5.7. CO is dosed via MFC and whereas 11.2 μL/s water is supplied by LFC. Total flow rate is calculated to be 17.2 SLPM. The gas feeding lines and evaporator are heated to 423 K to evaporate the water and avoid the condensation through the lines. Under these conditions the calculated flow velocity is 74 cm/s at the inlet of the reaction chamber at 500 mbar.

Table 5.7. Experimental conditions for WGS reaction.

	Temperature (K)	H_2O Mole Fraction (%)	CO Mole Fraction (%)
Case 1	873	4.75	5.18
Case 2	1008	4.75	5.18
Case 3	1073	4.75	5.18

The efficiency of R-WGS efficiency is also tested at temperature points of 873 K and 973 K (Table 5.8). Ar-diluted CO_2 and H_2 gases (CO_2/H_2 =1.00) are fed to the reactor at an inlet temperature of 313 K and a pressure of 500 mbar. To avoid the possible C formation, the measurement time is decreased by enlarging the measurement distance to 1 mm.

Table 5.8. Experimental conditions for R-WGS reaction.

	Temperature (K)	H_2 Mole Fraction (%)	CO_2 Mole Fraction (%)
Case 1	873	5.20	5.20
Case 2	973	5.20	5.20

5.4.3 Surface Reaction Mechanism

The heterogeneous reaction mechanism presented here is a continuation of the previous chapters (5.1-5.3). By following the hierarchy, here the surface mechanism is extended by including CO, CO_2 species and their reaction between O_2, H_2 and H_2O. The small differences in the H_2 oxidation steps between the previously presented mechanism and this mechanism arise due to the adjustment of the thermodynamic consistency.

The continuous-flow reactor experiments show that only a ppm level of CH_4 is formed during the WGS and R-WGS reaction and that no CH_4 is detected in the stagnation-flow experiments. Therefore, CH_4 and its reaction with other species are excluded from the reaction mechanism presented here. The reaction mechanism is thermodynamically consistent at both the entalphic and the entropic level.

Table 5.9. Proposed reaction mechanism for the WGS kinetics.

	Reaction	**A†(cm, mol,s)**	**β(-)‡**	**E_a(kJ/mol)**
R1	$H_2 + Rh(s) + Rh(s) \longrightarrow H(s) + H(s)$	3.000 x 10-2	stick. coeff.	
R2	$O_2 + Rh(s) + Rh(s) \longrightarrow O(s) + O(s)$	1.000 x 10-2	stick. coeff.	
R3	$H_2O + Rh(s) \longrightarrow H_2O(s)$	1.000 x 10-1	stick. coeff.	
R4	$CO_2 + Rh(s) \longrightarrow CO_2(s)$	4.800 x 10-2	stick. coeff.	
R5	$CO + Rh(s) \longrightarrow CO(s)$	4.971 x 10-1	stick. coeff.	
R6	$H(s) + H(s) \longrightarrow Rh(s) + Rh(s) + H_2$	5.574 x1 0^{19}	0.239	59.69
R7	$O(s) + O(s) \longrightarrow Rh(s) + Rh(s) + O_2$	5.329 x 10^{22}	-0.137	387.00
R8	$H_2O(s) \longrightarrow H_2O + Rh(s)$	6.858 x 10^{14}	-0.280	44.99
R9	$CO(s) \longrightarrow CO + Rh(s)$	1.300 x 10^{13}	0.295	$134.07- 47.00\theta_{CO}$
R10	$CO_2(s) \longrightarrow CO_2 + Rh(s)$	3.920 x 10^{11}	0.315	20.51
R11	$H(s) + O(s) \longrightarrow OH(s)+ Rh(s)$	8.826 x 10^{21}	-0.048	73.37
R12	$OH(s)+ Rh(s) \longrightarrow H(s) + O(s)$	1.000 x 10^{21}	0.045	48.04
R13	$H(s) + OH(s) \longrightarrow H_2O(s)+ Rh(s)$	1.743 x 10^{22}	-0.127	41.73
R14	$H_2O(s) + Rh(s) \longrightarrow H(s) + OH(s)$	5.408 x 10^{22}	0.129	98.22
R15	$OH(s) + OH(s) \longrightarrow H_2O(s) + O(s)$	5.735 x 10^{20}	-0.081	121.59
R16	$H_2O(s) +O(s) \longrightarrow OH(s) + OH(s)$	1.570 x 10^{22}	0.081	203.41
R17	$CO_2(s) + Rh(s) \longrightarrow CO(s) + O(s)$	5.752 x 10^{22}	-0.175	106.49
R18	$CO(s) + O(s) \longrightarrow CO_2(s) + Rh(s)$	6.183 x 10^{22}	0.034	$129.98- 47.00\theta_{CO}$
R19	$CO(s) + Rh(s) \longrightarrow C(s) + O(s)$	6.390 x 10^{21}	0.000	$174.76- 47.00\theta_{CO}$
R20	$C(s) + O(s) \longrightarrow CO(s) + Rh(s)$	1.173 x 10^{22}	0.000	92.14
R21	$CO(s) + OH(s) \longrightarrow COOH(s) + Rh(s)$	2.922 x 10^{20}	0.000	$55.33- 47.00\theta_{CO}$
R22	$COOH(s) + Rh(s) \longrightarrow CO(s) + OH(s)$	2.738 x 10^{21}	0.000	48.38
R23	$COOH(s) + Rh(s) \longrightarrow CO_2(s) + H(s)$	1.165 x 10^{19}	0.160	5.61
R23	$CO_2(s) + H(s) \longrightarrow COOH(s) + Rh(s)$	1.160 x 10^{20}	-0.160	14.48
R25	$COOH(s) + H(s) \longrightarrow CO(s) + H_2O(s)$	5.999 x 10^{19}	-0.188	33.55
R26	$CO(s) + H_2O(s) \longrightarrow COOH(s) + H(s)$	2.258 x 10^{19}	0.051	$97.08- 47.00\theta_{CO}$
R27	$CO(s) + OH(s) \longrightarrow CO_2(s) + H(s)$	3.070 x 10^{19}	0.000	$82.94- 47.00\theta_{CO}$
R28	$CO_2(s) + H(s) \longrightarrow CO(s) + OH(s)$	2.504 x 10^{21}	-0.301	84.77
R29	$C(s) + OH(s) \longrightarrow CO(s) + H(s)$	4.221 x 10^{20}	0.078	30.04
R30	$CO(s) + H(s) \longrightarrow C(s) + OH(s)$	3.244 x 10^{21}	-0.078	$138.26- 47.00\theta_{CO}$

The rate coefficients are given in the form of $k=AT^{\beta}\exp(-E_a/RT)$; adsorption kinetics is given in form of sticking coefficients; the surface site density is Γ=2.72 x 10^{-9} mol cm^{-2}

The reaction mechanism consists of five gas-phase and eight surface species and their reversible elementary-step reactions that are based on the Langmuir-Hinshelwood kinetics (Table 5.9). The mean-field approximation is used, i.e., the surface is assumed to be uniform and adsorbates are randomly distributed on the surface. The adsorption of the gas species is considered to be non-activated in accordance with previously-published reaction mechanisms [88, 151, 183]. The initial sticking coefficients of O_2, H_2, H_2O, CO, and CO_2 are taken to be 1.00x10^{-2}, 3.00x10^{-2}, 1.00x10^{-1}, 4.97x10^{-1} and 4.80x10^{-2}, respectively.

H_2 oxidation kinetics and CO oxidation kinetics rate parameters which are derived in Chapter 5.2 and 5.3 are incorporated into mechanism. Activation energies listed in Table 5.9 is taken on the basis of the reaction mechanism previously published [33, 88]. Temperature dependent activation energies are introduced to ensure thermodynamic consistency.

Dissociation steps of adsorbed CO (R19, 20; R29, 30) are introduced in the mechanism to take into account the possible carbon formation from CO. Moreover, reactions of CO and OH groups are introduced into the reaction steps as a WGS and consecutively R-WGS reaction steps (Figure 5.17).

Several proposals have been made to explain the WGS reaction pathway over nobel metal supported catalysts. Although there is a disagreement in the literature as to whether the redox formate or carboxyl mechanism is the dominant reaction path of the WGS, recent researches favor the carboxyl mechanism [204, 205, 219]. According to this mechanism, the reaction between the adsorbed CO and OH may yield carboxyl (COOH) groups with a very small activation barrier [205] The kinetic data show that the rate of the carboxyl mechanism proposed in this work is very close to the experimental value and is much faster than that of the formate and redox mechanisms.

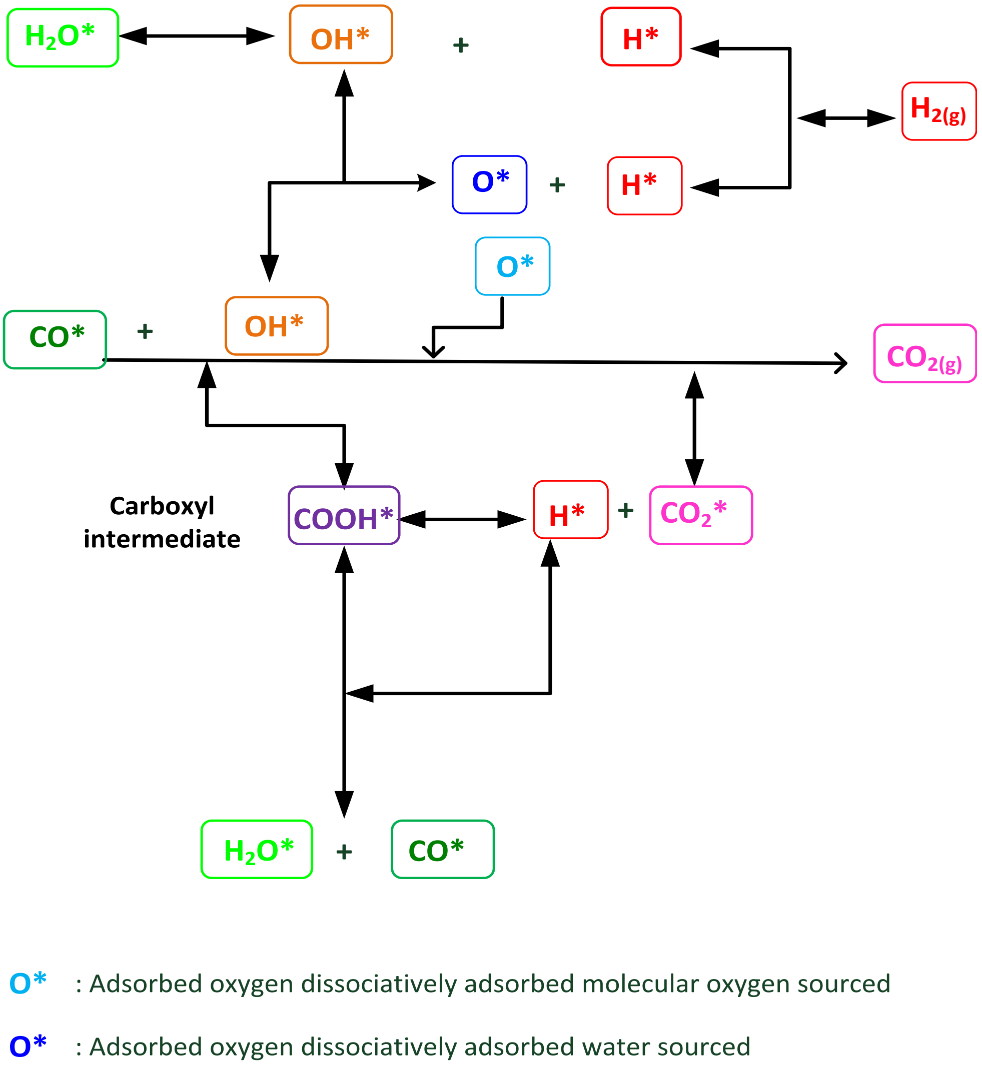

Figure 5.17. Reaction pathways for formation of CO_2.

Grabow et al. have presented a micro-kinetic model as well as experimental data for the WGS reaction catalyzed by Pt at temperatures from 523 to 573 K and for various gas compositions [219]. The authors show that the most significant reaction channel proceeds via a carboxyl (COOH) intermediate. Formate (HCOO), which has been experimentally observed and thought in the literature to be the key WGS intermediate, is shown to act only as a spectator species.

A detailed analysis of the evidence for and against a formate-based mechanism for the water-gas shift reaction has been carried out by Burch et al. [220]. It was shown that with very few exceptions, the published results cannot be used to provide any mechanistic evidence either for or against a formate model. The authors emphasize that, where reliable quantitative data are available; these show that the contribution of IR-observable formate to the production of CO_2 is of only minor importance for all high-activity catalysts.

In the reaction mechanism in Table 5.9, the carboxylate scheme is introduced into the reaction mechanism as it is proposed at the theoretical studies [205, 219] and assumed to be dominant in the WGS reaction. The formation of COOH species proceeds as a reaction between the adsorbed CO and OH species derived from the dissociation of water (Eq. 5.9, R21, 22) (Table 5.9).

$$\mathrm{CO(s) + OH(s) \rightarrow COOH(s) + Rh(s)} \tag{5.9}$$

It is assumed that all the species adsorb only on the active metal. The alumina support does not function as an active site.

Adsorbed carboxyl (COOH) follows two possible further reaction paths. Firstly, a reaction to form CO and water with the adsorbed H is possible (Eq. 5.10, R25, 26) and secondly, it may follow the step of dissociation to form CO_2 and a hydrogen atom (Eq. 5.11, R23, 24).

$$\mathrm{COOH(s) + H(s) \rightarrow CO(s) + H_2O(s)} \tag{5.10}$$

$$\mathrm{COOH(s) + Rh(s) \rightarrow CO_2(s) + H(s)} \tag{5.11}$$

All reactions are described as reversible elementary reaction pairs. The dissociation of CO_2 by surface H is also included in the reaction paths (R28) because it was reported that hydrogen enhances the CO_2 dissociation [221, 222]. The activation barriers of the reactions R21 – R28 were obtained based on a thermochemical analysis and using the unity bond index-quadratic exponential potential (UBI-QEP) method [223, 224].

$$\mathrm{CO(s) + OH(s) \rightarrow CO_2(s) + Rh(s)} \tag{5.12}$$

Figure 5.18-5.19 show the sensitivity analyses of the gas-phase concentrations of CO_2 and H_2O for WGS and R-WGS reactions with the proposed reaction mechanism, respectively. The sensitivity analyses are performed at the four temperature points of 473 K, 673 K, 773 K and 973 K at which conversions of reactants from low to high values were observed. CHEMKIN SPIN software is used for the sensitivity analyses. The results show that for all temperature points investigated, gas-phase CO_2 and H_2O concentrations are highly sensitive to H_2O adsorption and dissociation as well as to CO_2 adsorption and desorption steps. The reaction steps for the the COOH (R21) has an important effect on the gas-phase concentration of CO_2 (Figure 5.18) and this effect is decreases at higher temperatures. This is in accordance with the data from the sensitivity analysis of Maestri et al.[36]. They used a reaction mechanism of Mhadeshwar et al. for the investigation of methane steam and dry reforming on a Rh catalyst [151]. The authors pointed out that CO_2 formation via the formate reaction path is negligible and that the main reaction paths are direct CO oxidation (R27) and COOH pathways.

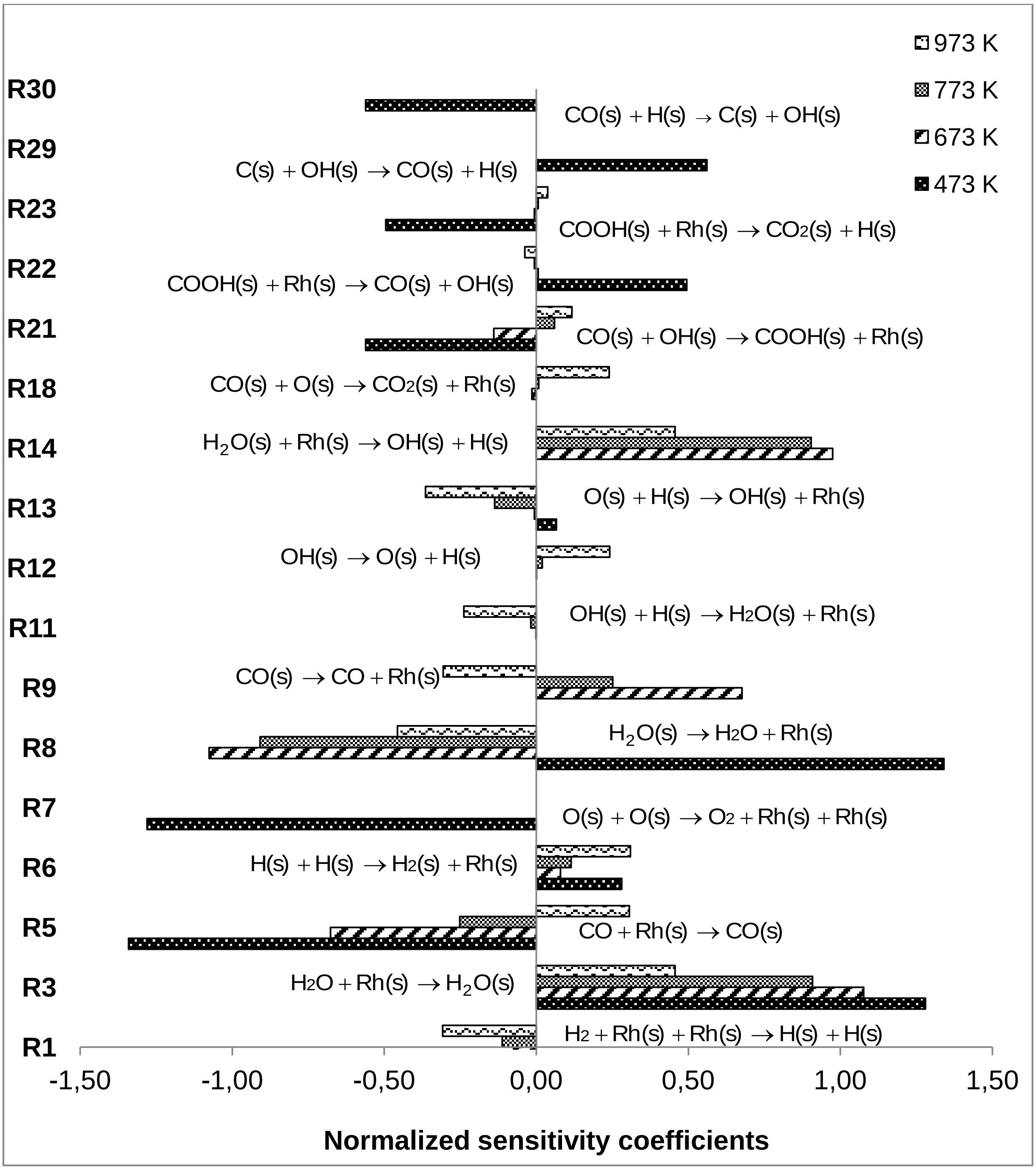

Figure 5.18. Sensitivity analyses of CO_2 gas-phase concentration for WGS reaction at different temperature points. Inlet mole composition is chosen to be 4.76 vol.% CO and 5.18 vol.% H_2O in Ar dilution.

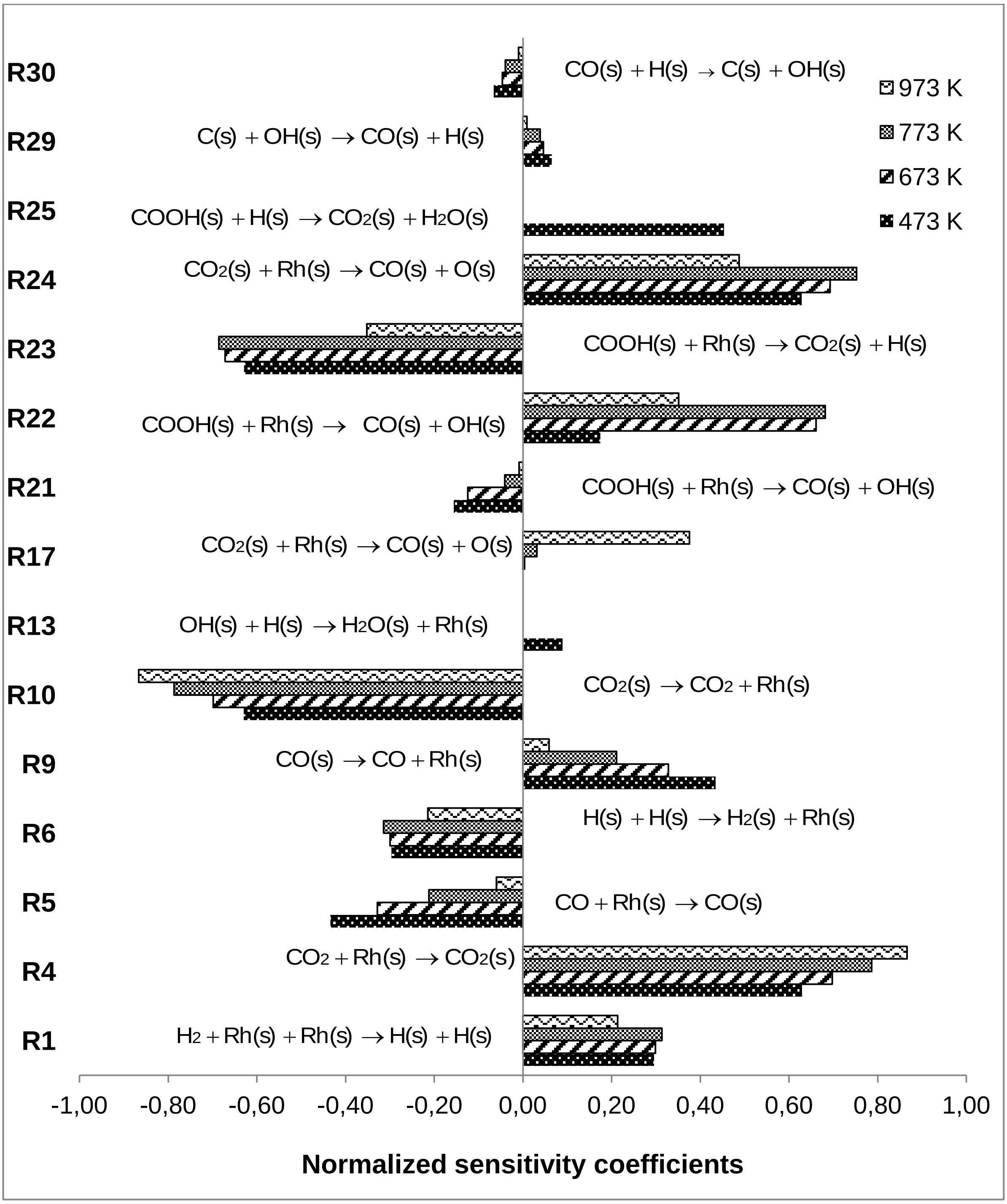

Figure 5.19. Sensitivity analyses of H_2O gas-phase concentration for R-WGS reaction at different temperature points. Inlet mole composition is chosen to be 5.20 vol.% CO_2 and 5.20 vol.% H_2 in Ar dilution.

On the other hand, sensitivity analyses for the R-WGS reaction show that the formation of gas-phase H_2O is highly dominated by CO_2 adsorption (R4), desorption (R10), and dissociation (R17, R24) reaction steps (Figure 5.19). Besides, the main pathway of H_2O production is via carboxyl formation (R21) and dissociation (R22, R23) steps. The adsorption (R5) and desorption (R9) steps of CO also have a significant effect on H_2O formation, because the radical concentration of COOH is related to the concentration of the adsorbed CO. Carboxyl reaction steps have a minor effect on the formation of H_2O at high temperatures. The rate-determining steps are adsorption (R4) and desorption (R10) steps of CO_2. A similar tendency is observed for the sensitivity analysis of gas-phase CO concentrations.

5.4.4 Results and Discussion

5.4.4.1 Stagnation-flow Reactor Experiments

Comparison of the experimental and numerical simulation results are presented here. The CHEMKIN SPIN and DETCHEM^{STAG} softwares are used for numerical solution of the stagnation-flow reactor data.
For all the stagnation-flow reactor experiments including preferential oxidation as well as WGS and R-WGS reactions, presented in this chapter, the an effective $F_{\mathrm{cat/geo}}$ value of 1 (Chapter 4.2.6) is used for numerical simulation.

Preferential Oxidation of H_2 in CO/O_2 Mixtures

To understand the possible oxidation reactions between H_2 and CO, selective CO oxidation reactions are carried out in H_2 and O_2 mixtures. For the sake of comparison, based on the flow experiments, 873 K is selected as a moderate temperature at which the reaction rate is considerably high but not equilibrated.

Figure 5.20, Figure 5.21 and Figure 5.22 show a comparison of the experimental (symbols) and predicted boundary-layer concentration profiles of the reactants and of CO_2 as products in wet basis. The mole fraction of H_2O is calculated to be 0.058 via oxygen balance on the catalyst surface. A minimum C balance of 95 % is ensured for all experiments.

.

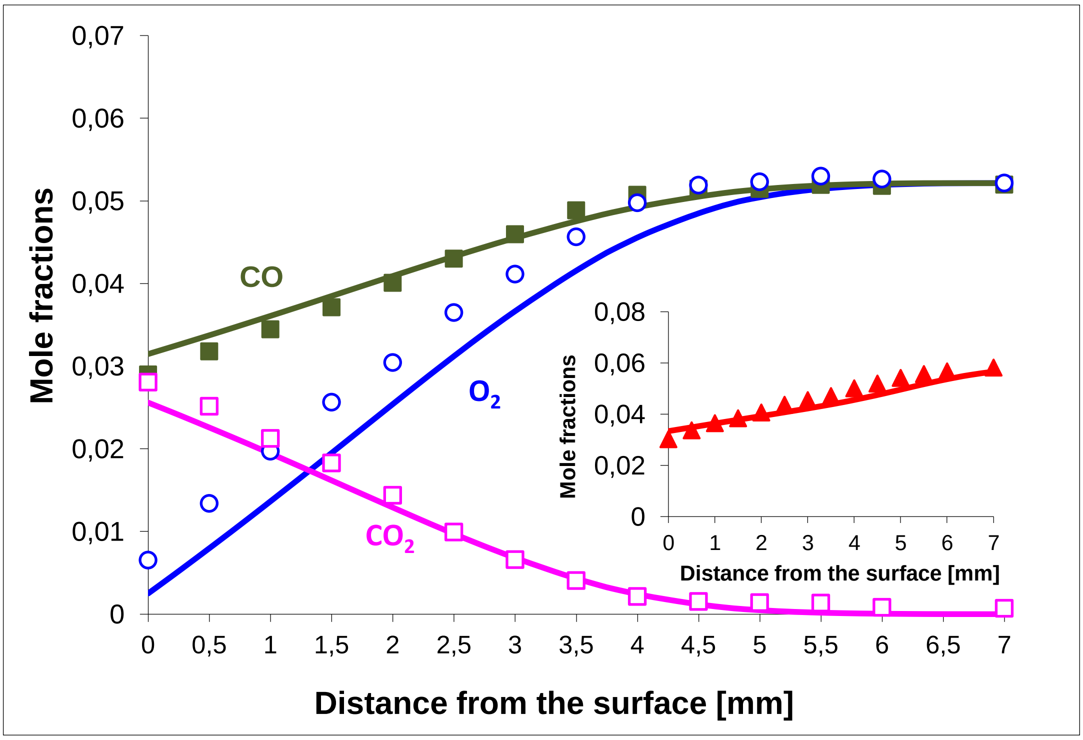

Figure 5.20. Comparison of the boundary-layer mole fractions of simulations (lines) and experiments (symbols) for preferential oxidation of CO in H_2/O_2 mixtures at 873 K with the inlet velocity of 51 cm/s and inlet composition of 6.00 vol.% H_2 5.20 vol.% CO and 5.20 vol.% O_2 diluted in Ar.

An inlet composition of 5.20 vol. % CO, 5.20 vol. % O_2, and 6.0 vol. % H_2 is accepted as baseline conditions (Case 1 in Table 5.6). The model predictions show a rather good agreement between the experimental data and the linear boundary-layer profiles of CO, CO_2, and O_2 species (Figure 5.20) After 5 mm, the boundary layer for CO, H_2O, and CO_2 species is reached. However, the concentration profile of H_2 is flatter and tends to produce a thicker boundary-layer. This behavior is due to the fast diffusion of H_2 molecules. Besides, a small difference between the measured and the predicted H_2 concentrations on the catalyst surface is observed. This difference can be attributed to sampling inaccuracy due to a possible gap between the microprobe tip and the catalyst surface. Although the measured fluxes of CO and H_2 are equal on the catalyst surface, the stagnation-flow reactor data show considerably high amounts of CO and H_2 on the catalyst surface, which are due to the diffusion limitations of the reactants.

Secondly (Case 2 in Table 5.6), the oxygen mole fraction is decreased to understand the selective oxidation of H_2 in CO-rich conditions (Figure 5.21). Halving the oxygen concentration results in a decreased reaction rate of CO_2 and H_2O formation in the same order of magnitude. No significant selective oxidation behavior is observed for either CO or CO_2.

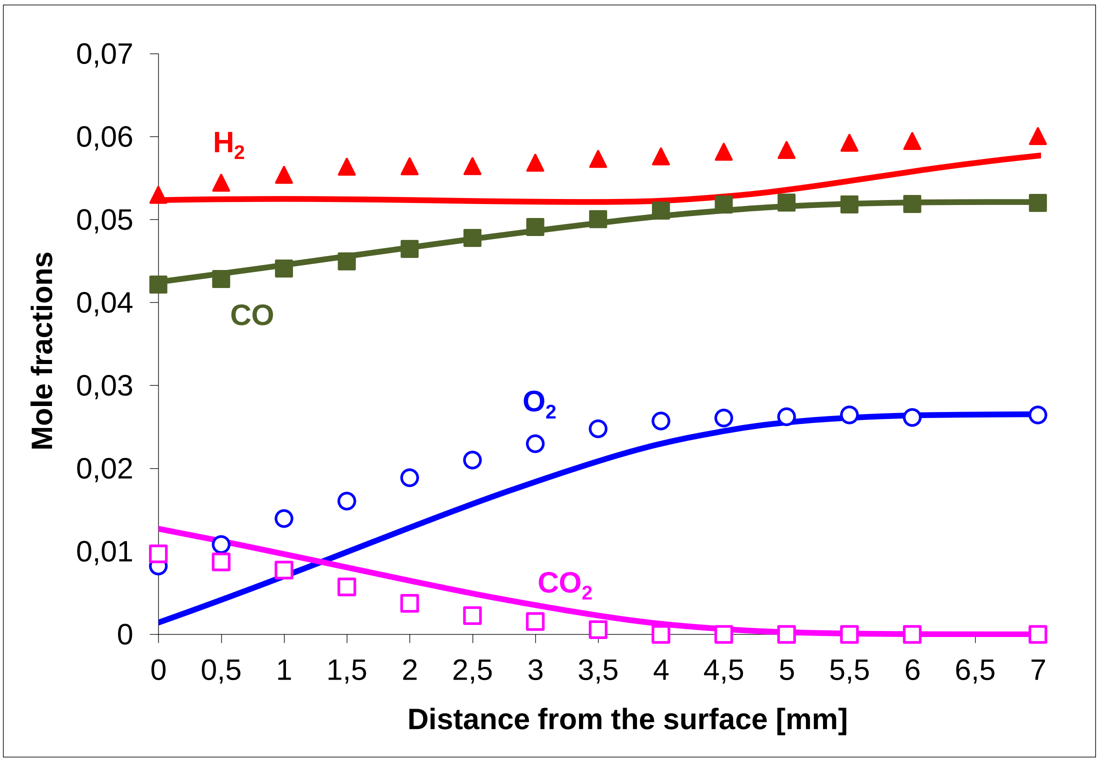

Figure 5.21. Comparison of the boundary-layer mole fractions of simulations (lines) and experiments (symbols) for preferential oxidation of CO in H_2/O_2 mixtures at 873 K with the inlet velocity of 51 cm/s and inlet composition of 6.00 vol.% H_2, 5.20 vol. % CO and 2.65 vol.% O_2 in Ar dilution.

Lastly the oxygen concentration in the gas mixture is increased by 50 vol.% (Case 3 in Table 5.6) to investigate the mass transport limitations (Figure 5.22). Similar to Case 2, no preferential oxidation behaviour is observed here. The reaction is O_2 mass transport limited because of the fast diffusion of H_2 molecules.

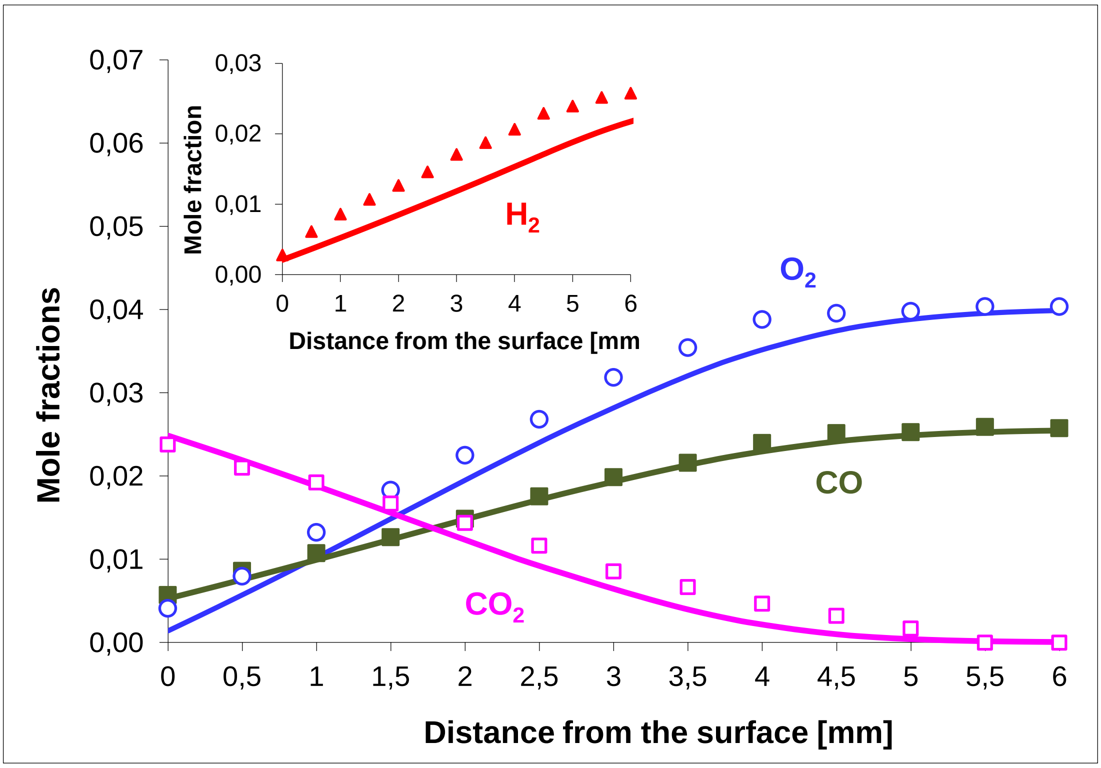

Figure 5.22. Comparison of the boundary-layer mole fractions of simulations (lines) and experiments (symbols) for preferential oxidation of CO in H_2/O_2 mixtures at 873 K with the inlet velocity of 51 cm/s and inlet composition of 2.57 vol.% H_2, 2.55 vol.% CO and 4.00 vol.% O_2 in Ar dilution.

The mol fraction of water on the catalyst surface is calculated to be 0.054 via C and oxygen mass balance, which is in good agreement with the predicted value of 0.052. Even though the detected surface concentrations of the species are in good agreement with the experimental values, the concentration profile of H_2 within the boundary layer slightly differs from the predicted values.

It is worth mentioning that, here, the gas concentrations and the temperatures selected for the preferential oxidation are unrealistic. The preliminary aim here is to develop a unified reaction mechanism for a wide range of temperatures and varying concentrations of fuel/oxygen mixtures. To this end, the reaction kinetics of CO and H_2 oxidation was examined under mild conditions. Unlike the preferential oxidation of CO in H_2-rich conditions in which CO at the ppm level is selectively oxidized in 30-60 % H_2-rich conditions for Polymer Electrolyte Membrane (PEM) fuel cell applications [225] a high number of CO/H_2 ratios are examined.

In the ignition study (Chapter 5.1) It has been shown that in case of H_2 oxidation, the reaction is carried out under stoichiometric conditions; ignition occurs at 457 K and results in a total H_2 conversion at adiabatic conditions Besides, recent studies showed that CO can be totally oxidized at 398 K under oxygen-rich conditions (1 vol. % CO and 1 vol. % O_2) [226]. For this reason, it is concluded that, no preferential oxidation behavior between H_2 and CO is observed at 873 K at which the reaction is neither thermodynamically nor kinetically limited. However, both reactants (CO, H_2) have an ignition-inhibiting effect on each other. If O_2 is the limiting reactant (Case 2 in Table 5.6), neither a total CO nor total H_2 oxidation are observed. The reaction proceeds in the path of both CO and H_2 oxidation at an equal reaction rate.

WGS-and R-WGS Reactions

WGS activity of the catalyst is tested at three different surface temperatures (Table 5.7) with an inlet composition of 4.75 vol. % CO and 5.18 vol. % H_2O diluted in an Ar flow. The inlet flow velocity is calculated to be 74 cm/s at an inlet temperature of 423 K and the pressure of 500 mbar. Figure 5.23 shows a comparison of the measured and the predicted boundary-layer concentration profiles at 873 K. The mole fractions of CO, CO_2, and H_2 are measured, whereas the mole fractions of H_2O at each measurement point are calculated via oxygen mass balance. Boundary-layer thickness is measured to be 4.5 mm. CO, CO_2, and H_2 concentrations linearly decrease as expected because there is no gas-phase reaction effect at this temperature. On the other hand, the concentration profile of H_2O is flatter and reaches its inlet value within the boundary layer of 3.5 mm.

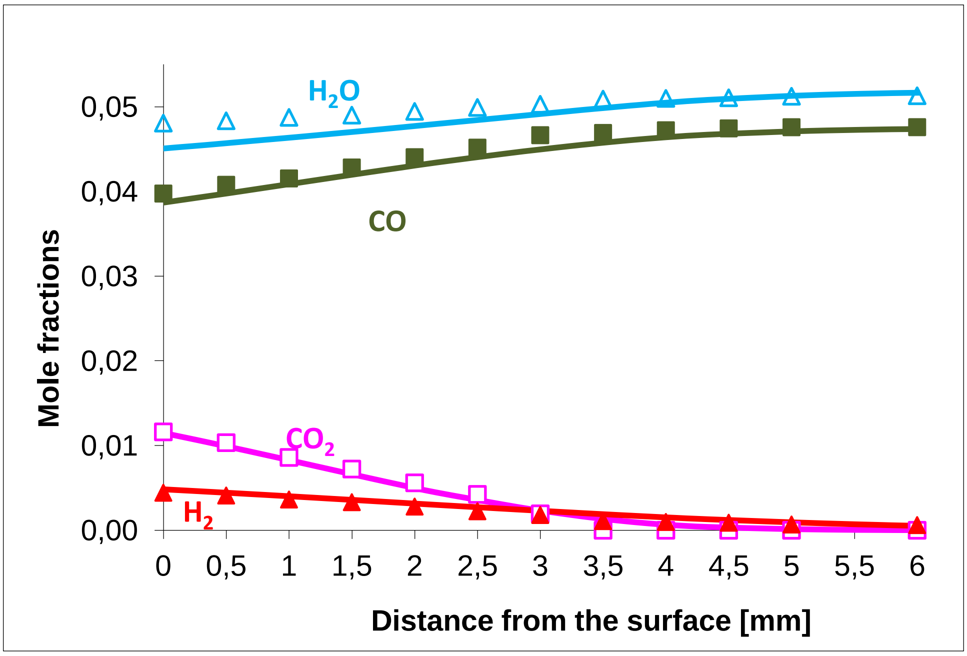

Figure 5.23. Comparison of measured (symbols) and predicted (lines) boundary-layer profiles for WGS reaction carried out with H_2O/CO ratio of 1.1 and the surface temperature of 873 K .

Increasing the temperature to 1008 K significantly increases the WGS activity (Figure 5.24 a) whereas the effect on product distribution is poor at 1073 K (Figure 5.24 b). At this temperature point, the reaction is closed to the equilibrium. For all three cases, the model predictions are in good agreement with the experimental data.

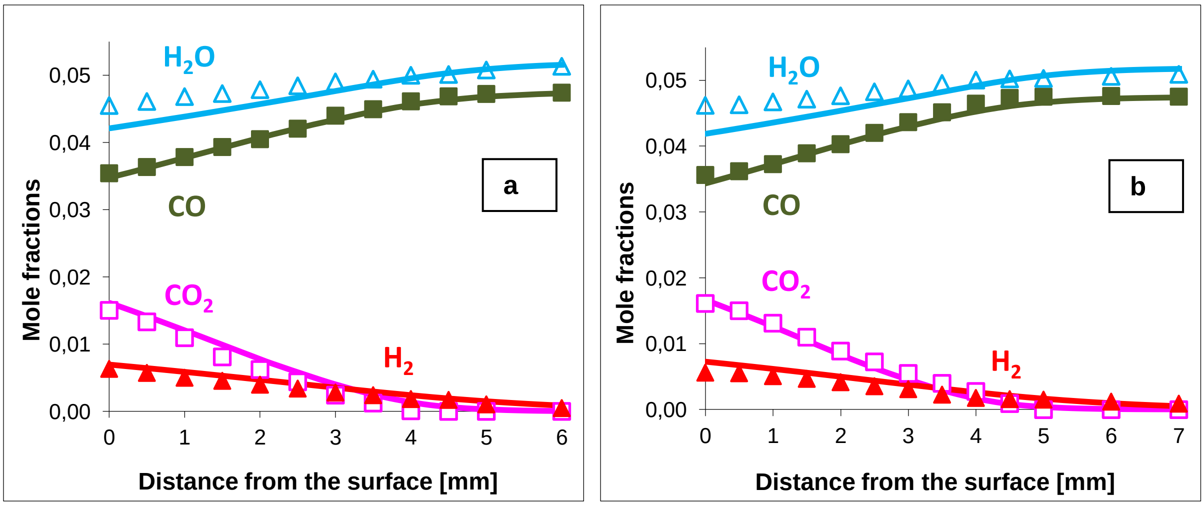

Figure 5.24. Comparison of measured (symbols) and predicted (lines) boundary-layer mole composition profiles for WGS reaction carried out with H_2O/CO ratio of 1.1 and the surface temperature of 1008 K (a) and 1073 K (b).

Lastly R-WGS activity is tested at surface temperatures of 873 K and 973 K with a flow composition of 5.2 vol.% CO_2 and % 5.2 % H_2 diluted in Ar. Inlet gas temperature is 313 K resulting in an inlet velocity of 51 cm/s at 500 mbar. The boundary-layer concentration profile of the species is shown in Figure 5.25 a, b. No significant R-WGS activity is detected at 873 K (Figure 5.25, a)

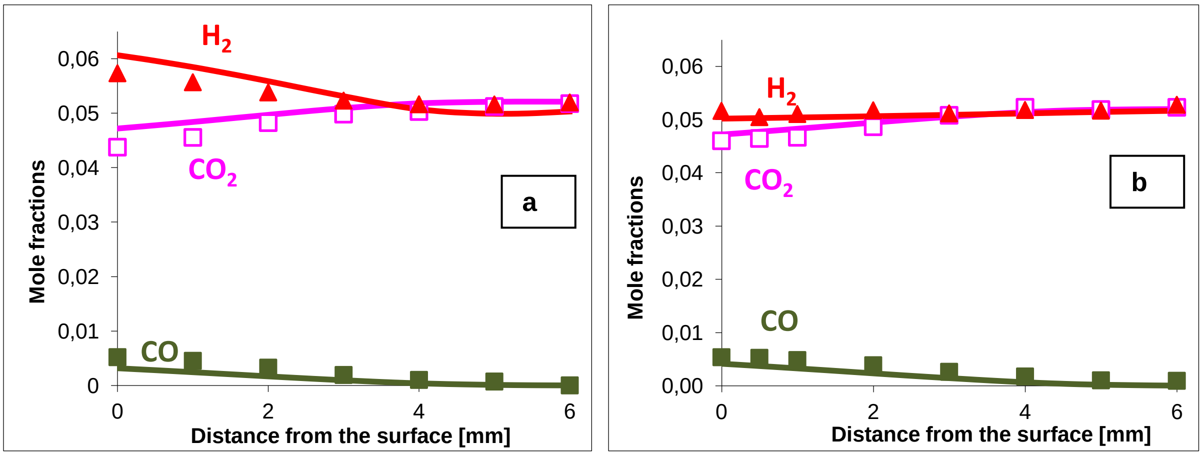

Figure 5.25. Comparison of measured (symbols) and predicted (lines) boundary-layer mole composition profiles for R-WGS reaction with CO_2/H_2 ratio of 1.0 and the surface temperature of 873 K (a) and 973 K (b).

The boundary-layer thickness is considerably small (4 mm). the maximum level of H_2O is calculated to be 2800 ppm on the catalyst surface. The observed reaction rate is much smaller than diffusion rate. Therefore, the reaction is diffusion controlled.

At 973 K, H_2 shows almost a linear concentration profile along the boundary-layer. The maximum level of H_2O is detected on the catalyst surface to be 3500 ppm. Within the 5 mm, the boundary-layer is reached (Figure 5.25, b)

5.4.4.2 Application of the Reaction Kinetics:

Channel Reactor Experiments

The fidelity of reaction mechanism is tested by reproducing the experimental data of Otterstätter et. al [227]. Experiments were carried out in a flow reactor configuration under steady-state conditions at atmospheric pressure. WGS, R-WGS reactions at temperatures of 473 -1173 K are examined. The co-feeding effect of the products CO_2 and CO for the WGS and R-WGS reaction, respectively, is also investigated. A technical 1.2 wt % Rh/γ-Al_2O_3 catalyst with 600 cells per square inch (cpsi) of monolithic structure and dimensions of 19 mm in OD and 10 mm in length was used. On the basis of CO chemisorption measurements $F_{cat/geo}$ value is calculated to be 19. All measurements are carried out at atmospheric pressure with a total flow rate of 5 SLPM that corresponds to a gas hourly space velocity (GHSV) of 100000 h^{-1}. Detailed information about the experimental set-up and the reaction conditions are given elsewhere [227, 228] .

Comparison of the experimental values and model predictions are presented. The numerical simulations are performed based on the 2D boundary-layer model of the channel with a hydraulic diameter of 1.0 mm and the 1 cm channel length by using DETCHEM^{CHANNEL} code [58]. Axial flow velocity is calculated to be 28.75 cm/s in the channel.

Similar to the stagnation-flow reactor simulations, the effectiveness factor has been calculated for channel reactor experiments presented in this chapter. Examplarily, WGS reaction is considered. Porosity and tortuosity values are assumed to be 0.6 and 3 respectively. The pore diameter is measured to be 25 nm [229]. The reaction temperature has been chosen to be 813 K at which the reaction is neither kinetically nor thermodynamically limited. The inlet concentrations are chosen to be 11.6 vol. % H_2O and 11.2 vol. % CO diluted in N_2. Under the given reaction conditions the CO flux at the catalyst surface is calculated to be -2.4x10^{-2} mole/m^2s and the reaction rate of the consumption of CO is calculated to be 1.75x10^8 mole/m^3s. With the given catalyst properties the effectiveness factor is calculated to be 0.03 and. It is worth to mention that the effectivess factor varies as function of temperature. For the same reactive fuel composition (11.6 vol. % H_2O and 11.2 vol. % CO diluted in N_2), the effectiveness factor is calculated to be 0.05 at 723 K. Therefore an effective $F_{\mathrm{cat/geo}}$= 2 is used for all channel reactor simulations in this chapter.

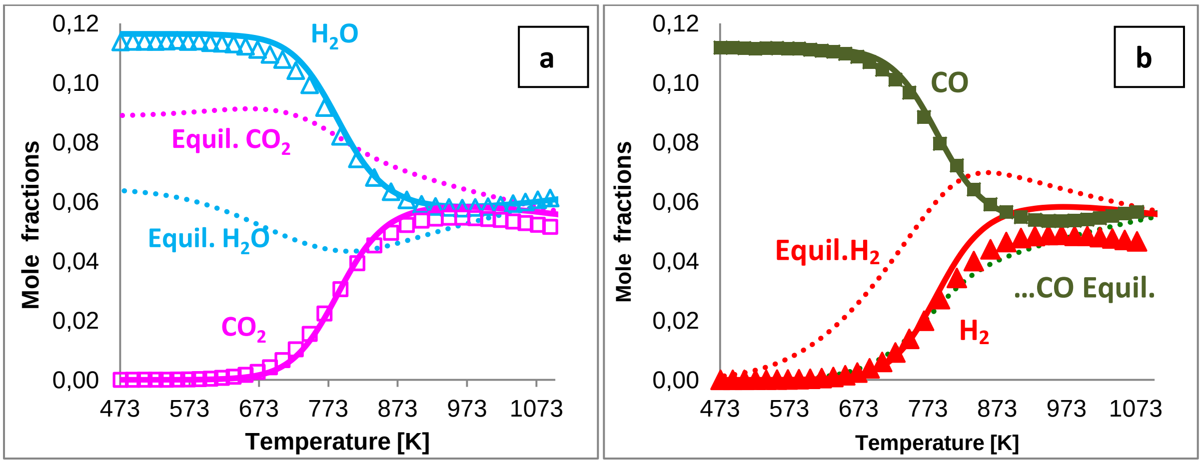

Figure 5.26. WGS reaction carried out in a flow reactor with inlet mole composition of 11.6 vol.% H_2O and 11.2 vol.% CO diluted in N_2. Comparsion of experimental [227] (symbols) and predicted values (lines) of H_2O- CO_2 and CO-H_2 mole fractions as a function of temperature.

Figure 5.26 a, b shows a comparisons between the predicted and experimental values of CO_2 -H_2O and CO-H_2 mole fractions in the outlet gas stream for the WGS reaction. An inlet mole composition of 11.6 vol.% H_2O and 11.2 vol.% CO diluted in N_2 was fed to the reactor. The temperature is raised by a ramp of 7 K/min and the mole fractions of CO, CO_2, H_2, H_2O and CH_4 species in the outlet gas stream were detected. Maximum 100 ppm level of CH_4 was formed at around 813 K, therefore, the methanation is excluded in the reaction steps. The WGS activity starts 673 K and the reaction reaches the equilibrium at 1043. The model predicts the WGS activity in a good agreement with the experimental results over a wide range of temperatures.

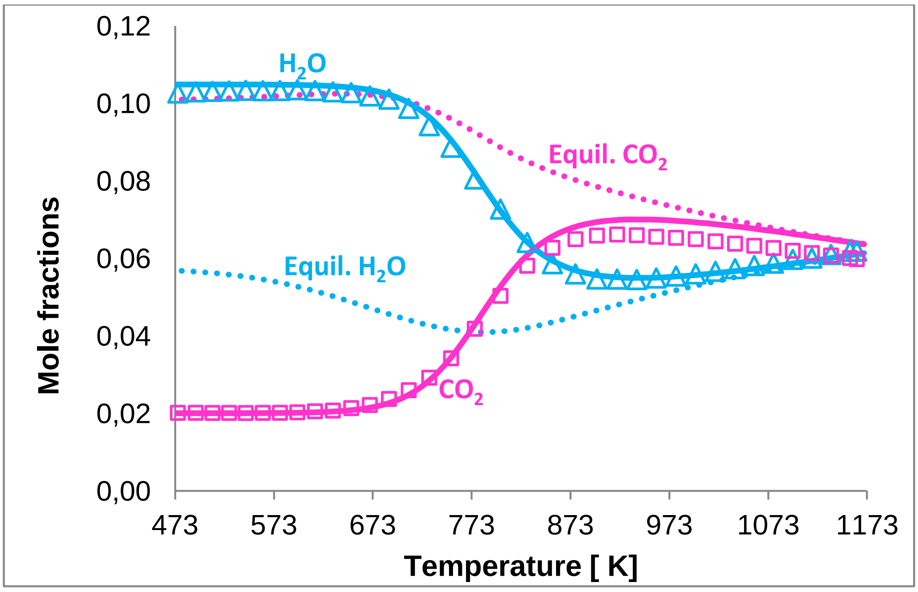

Figure 5.27. CO_2 cofeeding effect in WGS reaction which is carried out in flow reactor with the inlet mole composition of 10.49 vol.% H_2O, 10.08 vol.% CO and 2.0 vol.% CO_2 in N_2 dilution. Comparsion of experimental [227] (symbols) and predicted values (lines) of H_2O and CO_2 mole fractions.

An addition of 2.0 vol. % CO_2 to the flow composition of 10.49 vol. % H_2O and 10.08 vol. % CO diluted in N_2 was also tested (Figure 5.27). No significant effect was observed on the rate of the forward reaction. The reaction rate was independent of the CO_2 concentration.

The equilibrium temperature was slightly shifted to 1083 K According to the reaction mechanism, the forward reaction path of WGS is CO oxidation by OH radicals and the rate-determining step is water dissociation. An addition of CO_2 is expected to increase the R-WGS reaction rate and, consequently the dry reforming rate that leads the consumption of CH_4 [36]. A maximum amount of 80 ppm CH_4 was detected at 803 K.

Similarly, the proposed surface reaction mechanism is validated for R-WGS reactions as well. The channel reactor experiments of Otterstätter are reproduced [227]. A comparison of the experimental and the predicted values of H_2 and CO for the R-WGS reaction carried out in a flow reactor is shown in Figure 5.28. The inlet mole composition was chosen to be 10.40 vol. % H_2 and 10.88 vol. % CO_2 diluted in N_2.

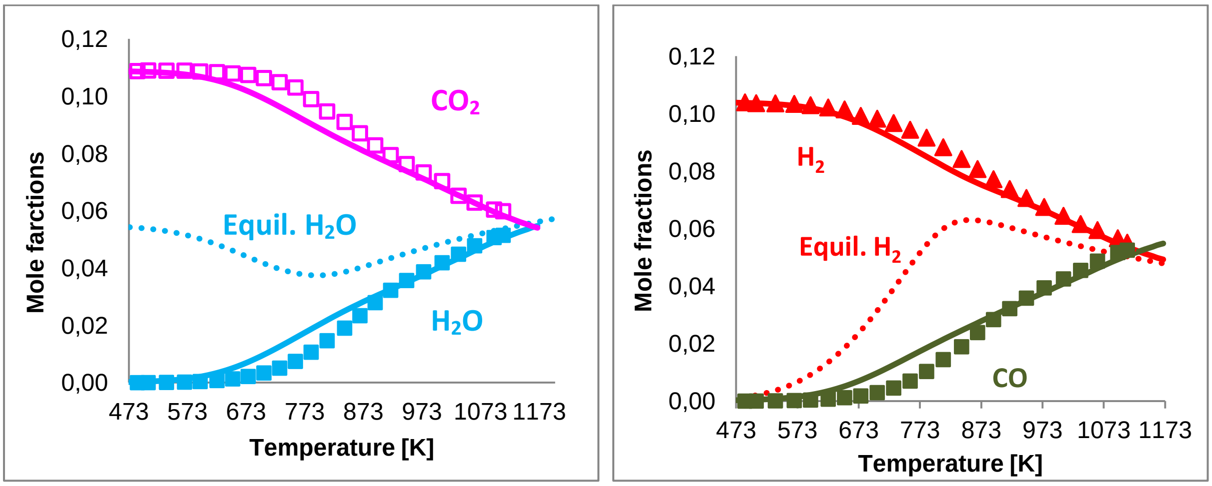

Figure 5.28. Comparison of experimental [227] (symbols) and predicted values (lines) of CO_2-H_2O and CO-H_2 outlet mole fractions for R-WGS reaction carried out in flow reactor. Inlet mole composition is chosen to be 10.40 vol.% H_2 and 10.88 vol.% CO_2 in N_2 dilution.

Low activity was observed below 773 K and increasing the reaction temperature resulted in a linear increase in CO formation which was due to endothermic reaction behaviour of R-WGS reaction. Reaction was closed to the equilibrium at around 1163 K.

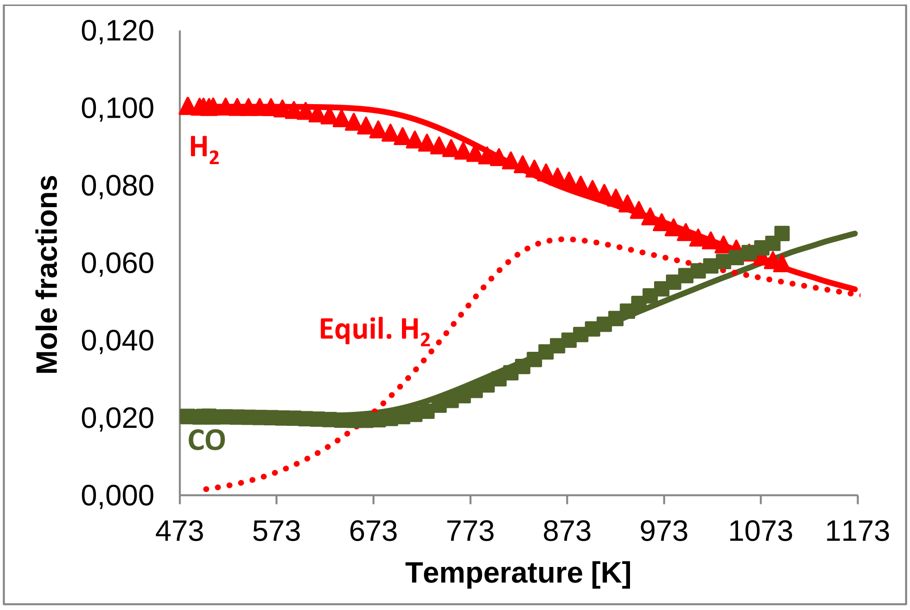

Figure 5.29. Effect of CO co-feeding in R-WGS reaction carried out in flow reactor with the inlet mole compostion of 10.03 vol.% H_2 and 9.52 vol.% CO_2 and 2.04 vol.% CO in N_2 dilution: comparsion of experiments [227] (symbols) and predicted values (lines).

Effect of CO co-feeding was also examined with addition of 2.04 vol.% CO in to the mixture of 10.03 vol.% H_2 and 9.52 vol.% CO_2 in N_2 dilution (Figure 5.29). As expected, the addition of CO has no significant effect on the forward reaction rate. Overall reaction rate for formation of CO has first order dependency of CO_2 concentration and 0.5 order dependency of H_2 concentration [230].

Comparison of the Reaction Rates

Measured and predicted reaction rates in terms of cumulative TOR are compared for WGS and R-WGS reactions.

$$\mathrm{TOR} = \frac{\text{converted product molecules at the reactor exit}}{\text{residence time. catalyst site}} \quad . \qquad 5.13$$

$$\text{converted product molecules at the reactor exit} = \Delta\text{molecules}_{\text{formed}} \quad . \qquad 5.14$$

$$\Delta\text{molecules}_{\text{formed}} = \frac{\text{mole fraction of the product.}\, n_{\text{total}}}{N_A} \quad . \qquad 5.15$$

$$n_{\text{total}} = \frac{p * V}{R * T} \quad . \qquad 5.16$$

$$\text{catalyst site} = \frac{A_{\text{geometric}} \cdot F_{\text{cat/geo}} \cdot}{N_A} \quad . \qquad 5.17$$

The experiments for WGS reaction carried out in a flow reactor with inlet mole composition of 11.6 vol.% H_2O and 11.2 vol.% CO diluted in N_2 and CO_2 cofeeding effect in WGS reaction which is carried out in flow reactor with the inlet mole composition of 10.49 vol.% H_2O, 10.08 vol.% CO and 2.0 vol.% CO_2 in N_2 dilution.

A parity diagram is created for H_2 TOR values for WGS reactions (Figure 5.30, a). Similarly, for R-WGS reaction, TOR calculations are performed based on H_2O concentration in the outlet gas stream (Figure 5.30, b). Experiments are carried out with the inlet mole composition is chosen to be 10.40 vol.% H_2 and 10.88 vol.% CO_2 in N_2 dilution and effect of CO co-feeding in R-WGS reaction was investigated with the inlet mole composition of 10.03 vol.% H_2 and 9.52 vol.% CO_2 and 2.04 vol.% CO in N_2 dilution.

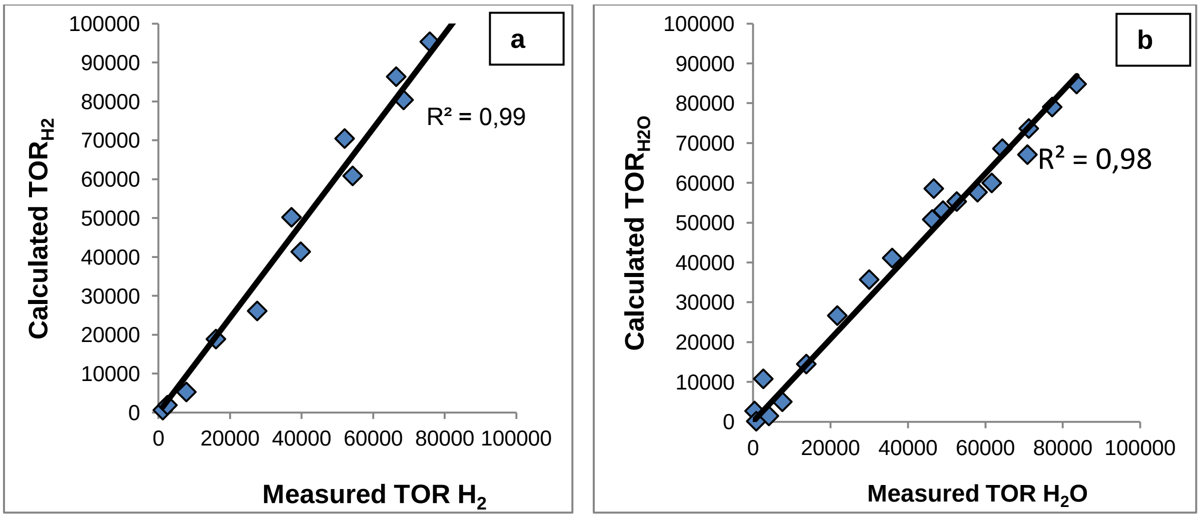

Figure 5.30. Comparison of calculated and measured TOR values of H_2 (a) and H_2O (b) for WGS and R-WGS reactions respectively carried out in the flow reactor.

For both cases linear correlations ($R^2 \geq 0.98$) between measured and calculated TOR values are observed. Thus, the applicability and the fidelity of the proposed reaction mechanism are successfully tested for WGS and R-WGS reactions in a wide temperature range.

5.4.5 Conclusion

Water-gas shift and reverse water-gas shift reaction kinetics over Rh/Al_2O_3 catalyst are investigated experimentally and numerically.

The stagnation-flow reactor is used for catalytic measurements, which facilitates the computational modeling of heterogeneous surface chemistry coupled with 1D convective and diffusive transport properties within the gas-phase boundary layer. A microprobe sampling technique is used to measure the gas-phase composition in the boundary layer adjacent to the catalyst surface.

WGS, R-WGS, and preferential oxidation of CO reactions are carried out in order to understand the reaction kinetics. The obtained data are used to assist in the development of a surface reaction mechanism for water-gas shift and reverse water-gas shift reactions under varying fuel/oxygen ratios and over a wide range of temperature. A new, thermodynamically consistent reaction kinetics is proposed for low and high temperature applications of WGS and R-WGS reactions. Since experimentally, CH_4 is detected only at the ppm level, the formation of CH_4 and its reaction with the other species are excluded from the reaction mechanism.

A major difference between the present reaction pathway and the previous reaction kinetics [33, 88] is the formation of CO_2 at low temperatures, which is not well-covered with the previous reaction kinetics. Here, the reaction steps of formation of carboxyl group (COOH) and its elementary-step-like reactions are inlcuded. According to the sensitivity analyses, at low temperatures, formation of carboxlyl (COOH) has major effect on WGS reactions and CO_2 forms via dissociation of carboxlyl (COOH) to adsorbed CO_2 and H species. Whereas for high temperature regimes, direct oxidation of adsorbed CO species by adsorbed oxygen is favoured. The rate determining step is dissociation of H_2O and gas-phase CO_2 concentration is highly effected by the reaction steps of H_2O dissociation as well as the adsorption and desorption steps of CO_2. On the other hand, for R-WGS reaction, main reaction path is the formation and dissociation of COOH group at low and high temperatures. The reaction rate of H_2O formation is sensitive to dissociation of CO_2 since it is the rate determining step.

The reaction kinetics is successfully tested by simulating the experiments carried out in a channel reactor over Rh/Al_2O_3 monolithic catalyst. WGS, R-WGS, and co-feeding of CO_2 and CO respectively are also examined.

5.5 Catalytic Partial Oxidation and Reforming of CH_4

This chapter focuses on development of the surface reaction kinetics for catalytic partial oxidation and reforming of methane. Following the hierarchy, the reaction mechanism (Table 5.9) is extended by CH_x species. Partial oxidation, steam reforming and dry reforming of CH_4 reactions are examined. The stagnation-flow reactor data are used to establish the reaction rate parameters. Thermodynamic consistency of the reaction kinetics is ensured for temperatures of 273-1273 K. The application of the reaction mechanism is shown by also reproducing continuous-flow reactor data from the literature [30, 35] .

5.5.1 Theoretical Background

Synthesis gas production technology via catalytic partial oxidation and reforming of methane has been studied extensively. Hickmann and Schmidt showed that CH_4 can be converted to synthesis gas in an efficient way (> 90 % yield) over Rh in millisecond-contact-times by partial oxidation of methane [183].

Although this technique is used at the industrial level in small scales, today´s driving force behind studying CPOx and reforming of methane is the necessity to understand the reaction kinetics at the elementary-level, which can be used for optimal reactor designs with efficient yield and low costs.

Studies show that partial oxidation of methane is a complex process where total oxidation and reforming zones exist [5, 33]. Furthermore, there is a strong competition between total oxidation, direct partial oxidation and steam reforming in the reactor [33]. Similarly, for dry reforming of methane, studies show that a steam reforming zone exists and that the reaction follows the path of reverse water-gas shift and steam reforming reactions. The water-gas shift reaction also takes place [32].

Even though global reactions of CPOx, SR and DR are separate processes there is no distinct boundary between these reactions. Besides, reactors are designed to operate in combination of different reforming or oxidation processes, e.g., ATR, a combination of partial oxidation and steam reforming, to optimize the heat management of the overall process yield and the product selectivity. Recently, there is a continuing interest in the development of new reactors and catalysts for dry reforming. Furthermore, the environmental benefits i.e., that the CO_2 can be used as a reactant, the dry reforming process is preferred because a synthesis gas with a lower H_2/CO ratio can be optained (compared to the steam reforming process) which is a suitable gas composition for the production of oxygenated compounds. Furthermore, a combination of steam reforming and dry reforming reactions allows producing the synthesis gas in a desired range of H_2/CO, as well as increasing the product yield.

$$\mathrm{CH_4} + {}^{1}\!/_{2}\,\mathrm{O_2} \rightarrow \mathrm{CO} + 2\mathrm{H_2} \qquad \Delta_{\mathrm{R}}\mathrm{H^o} = -35.9\ \mathrm{kJ/mol} \tag{5.18}$$

$$\mathrm{CH_4} + 2\mathrm{O_2} \rightarrow \mathrm{CO_2} + 2\mathrm{H_2O_{(g)}} \qquad \Delta_{\mathrm{R}}\mathrm{H^o} = -802.6\ \mathrm{kJ/mol} \tag{5.19}$$

$$\mathrm{CH_4} + \mathrm{H_2O_{(g)}} \rightarrow \mathrm{CO} + 3\mathrm{H_2} \qquad \Delta_{\mathrm{R}}\mathrm{H^o} = +205.9\ \mathrm{kJ/mol} \tag{5.20}$$

$$\mathrm{CH_4} + \mathrm{CO_2} \rightarrow 2\mathrm{CO} + 2\mathrm{H_2} \qquad \Delta_{\mathrm{R}}\mathrm{H^o} = +247.0\ \mathrm{kJ/mol} \tag{5.21}$$

$$\mathrm{CO} + \mathrm{H_2O_{(g)}} \leftrightarrow \mathrm{CO_2} + \mathrm{H_2O_{(g)}} \qquad \Delta_{\mathrm{R}}\mathrm{H^o} = -41.1\ \mathrm{kJ/mol} \tag{5.22}$$

$$\mathrm{CO} + {}^{1}\!/_{2}\,\mathrm{O_2} \rightarrow \mathrm{CO_2} \qquad \Delta_{\mathrm{R}}\mathrm{H^o} = -232.9\ \mathrm{kJ/mol} \tag{5.23}$$

$$\mathrm{H_2} + {}^{1}\!/_{2}\,\mathrm{O_2} \rightarrow \mathrm{H_2O_{(g)}} \qquad \Delta_{\mathrm{R}}\mathrm{H^o} = -241.8\ \mathrm{kJ/mol} \tag{5.24}$$

Therefore, a proposed reaction mechanism for partial oxidation of methane should also particularly predict the dry reforming and steam reforming of methane as well as the oxidation of methane and products of CO and H_2. This conclusion emerges the necessity of a unified reaction mechanism for partial oxidation and reforming of methane under varying reaction conditions.

5.5.2 Experimental Procedure

CPOx, SR and DR of methane have been studied in the stagnation-flow reactor under varying fuel composition and temperature. A 5 wt.% Rh/Al_2O_3 catalyst is used which was also used in H_2 and CO oxidation and WGS experiments. The operating pressure is selected to be 500 mbar and the reactive gas mixtures are diluted in Ar gas. Boundary-layer profiles of the species are measured at steady-state conditions. A detailed description of the measurement procedure is given in Chapter 3.1.5.

Catalytic Partial Oxidation of CH_4

The studied reaction conditions for CPOx of CH_4 are presented in Table 5.10. A total gas flow rate of 15.5 SLPM is selected which corresponds to an inlet velocity of 51 cm/s at the stagnation-flow reactor inlet at 313 K. The temperature of 973 K is selected to be the reference temperature and the C/O ratio is varied to yield total oxidation and fuel-rich partial oxidation reactions conditions. Gas-phase reactions are neglected, because the maximum reaction temperature studied here is 1023 K which is considerably low for the ignition of the gas-phase reactions.

Table 5.10. Reaction conditions for CPOx of CH_4.

Case	Reaction Temp (K)	% vol. CH_4	% vol. O_2	C/O
1	873	5.30	2.57	1.03
2	973	5.32	2.78	0.99
3	973	5.20	4.90	0.53
4	973	5.30	3.50	0.76
5	973	4.38	7.80	0.28
6	1023	5.20	2.79	0.93

Steam Reforming of CH_4

Steam reforming of methane is studied at 973 K and 1008 K. 11.2 µl/min water is fed to the evaporator. The gas feeding lines and the evoparator are heated up to 423 K to avoid the condensation of water. The total gas flow rate is calculated to be 17.2 SLPM which corresponds to 71 cm/s gas velocity at the stagnation-flow reactor inlet. The reaction conditions are given below.

Table 5.11. Steam reforming reaction conditions.

Reaction Temp (K)	% vol. CH_4	% vol.H_2 O	S/C
973	5.06	5.38	1.06
1008	5.16	5.38	1.04

Dry Reforming of CH_4

Dry reforming of CH_4 is studied at 973 K with a fuel composition of 5.45 vol.% CH_4 and 4.97 vol.% CO_2 diluted in Ar. To avoid the possible formation of carbon on the surface, 1 vol.% O_2 is added in to the feed. A total flow rate of 15.5 SLPM is fed to the reactor. Besides, the dry reforming experiment of McGuire et al. [27] is reproduced. In that study, the reaction was carried out in a stagnation-flow reactor at 1073 K at 300 mbar. A reactive gas compostion of 15 vol.% CO_2 and 10 vol.% CH_4 diluted in Ar was fed to the reactor. The calculated flow velocity was 90 cm/s at the stagnation reactor inlet at 333 K.

5.5.3 Results and Discussion

As a continuation of the hierarchical development of surface reaction kinetics, the reaction mechanism that includes the $H_2/O_2/CO/CO_2/H_2O$ species (Table 5.9) is extended to methane. Adsorption and desorption of CH_4, thermal dehydrogenation and oxidative dehydrogenation of CH_x species as well as their reactions with adsorbed OH species are included. The study of Hartmann et al. [88] is taken as a reference for the elementary reaction steps and enthalpy values. The stagnation-flow reactor data are used to calculate the reaction rates and determine the pre-exponential factors. A carbon coverage dependent activation energy of 120 kJ/mol has been introduced for the reaction $\mathrm{C}(s) + \mathrm{H}(s) \rightarrow \mathrm{CH}(s)$ to avoid surface poising by carbon during dry reforming reaction in the model. The enthalpy value is determined empirically on the basis of the stagnation-flow reactor data. The thermodynamic consistency has been ensured at a temperature range of 273-1273 K. The proposed reaction mechanism is given in Table 5.12.

Table 5.12. Proposed reaction mechanism for partial oxidation and reforming of CH_4.

	Reaction	$A^{\dagger}$(cm, mol,s)	β(-)‡	Ea(kJ/mol)
R1	$H_2 + Rh(s) + Rh(s) \longrightarrow H(s) + H(s)$	3.000×10^{-2b}	stick. coeff.	
R2	$O_2 + Rh(s) + Rh(s) \longrightarrow O(s) + O(s)$	1.000×10^{-2b}	stick. coeff.	
R3	$H_2O + Rh(s) \longrightarrow H_2O(s)$	1.000×10^{-1b}	stick. coeff.	
R4	$CO_2 + Rh(s) \longrightarrow CO_2(s)$	4.800×10^{-2b}	stick. coeff.	
R5	$CO + Rh(s) \longrightarrow CO(s)$	4.971×10^{-1b}	stick. coeff.	
R6	$CH_4 + Rh(s) \longrightarrow CH_4(s)$	1.300×10^{-2b}	Stick .coeff.	
R7	$H(s) + H(s) \longrightarrow Rh(s) + Rh(s) + H_2$	5.574 x1 0^{19}	0.239	59.69
R8	$O(s) + O(s) \longrightarrow Rh(s) + Rh(s) + O_2$	5.329×10^{22}	-0.137	387.00
R9	$H_2O(s) \longrightarrow H_2O + Rh(s)$	6.858×10^{14}	-0.280	44.99
R10	$CO(s) \longrightarrow CO + Rh(s)$	1.300×10^{13}	0.295	$134.07\text{-}47\theta_{CO}$
R11	$CO_2(s) \longrightarrow CO_2 + Rh(s)$	3.920×10^{11}	0.315	20.51
R12	$CH_4(s) \longrightarrow CH_4 + Rh(s)$	1.523×10^{13}	-0.110	26.02
R13	$H(s) + O(s) \longrightarrow OH(s) + Rh(s)$	8.826×10^{21}	-0.048	73.37
R14	$OH(s) + Rh(s) \longrightarrow H(s) + O(s)$	1.000×10^{21}	0.045	48.04
R15	$H(s) + OH(s) \longrightarrow H_2O(s) + Rh(s)$	1.743×10^{22}	-0.127	41.73
R16	$H_2O(s) + Rh(s) \longrightarrow H(s) + OH(s)$	5.408×10^{22}	0.129	98.22
R17	$OH(s) + OH(s) \longrightarrow H_2O(s) + O(s)$	5.735×10^{20}	-0.081	121.59
R18	$H_2O(s) + O(s) \longrightarrow OH(s) + OH(s)$	1.570×10^{22}	0.081	203.41
R19	$CO_2(s) + Rh(s) \longrightarrow CO(s) + O(s)$	5.752×10^{22}	-0.175	106.49
R20	$CO(s) + O(s) \longrightarrow CO_2(s) + Rh(s)$	6.183×10^{22}	0.034	$129.98\text{-} 47.00\theta_{CO}$
R21	$CO(s) + Rh(s) \longrightarrow C(s) + O(s)$	6.390×10^{21}	0.000	$174.76\text{-} 47.00\theta_{CO}$
R22	$C(s) + O(s) \longrightarrow CO(s) + Rh(s)$	1.173×10^{22}	0.000	92.14
R23	$CO(s) + OH(s) \longrightarrow COOH(s) + Rh(s)$	2.922×10^{20}	0.000	$55.33\text{-} 47.00\theta_{CO}$
R24	$COOH(s) + Rh(s) \longrightarrow CO(s) + OH(s)$	2.738×10^{21}	0.000	48.38
R25	$COOH(s) + Rh(s) \longrightarrow CO_2(s) + H(s)$	1.165×10^{19}	0.160	5.61
R26	$CO_2(s) + H(s) \longrightarrow COOH(s) + Rh(s)$	1.160×10^{20}	-0.160	14.48
R27	$COOH(s) + H(s) \longrightarrow CO(s) + H_2O(s)$	5.999×10^{19}	-0.188	33.55
R28	$CO(s) + H_2O(s) \longrightarrow COOH(s) + H(s)$	2.258×10^{19}	0.051	$97.08\text{-} 47.00\theta_{CO}$
R29	$CO(s) + OH(s) \longrightarrow CO_2(s) + H(s)$	3.070×10^{19}	0.000	$82.94\text{-} 47.00\theta_{CO}$
R30	$CO_2(s) + H(s) \longrightarrow CO(s) + OH(s)$	2.504×10^{21}	-0.301	84.77
R31	$C(s) + OH(s) \longrightarrow CO(s) + H(s)$	4.221×10^{20}	0.078	30.04
R32	$CO(s) + H(s) \longrightarrow C(s) + OH(s)$	3.244×10^{21}	-0.078	$138.26\text{-} 47.00\theta_{CO}$
R33	$CH_4(s) + Rh(s) \longrightarrow CH_3(s) + H(s)$	4.622×10^{21}	0.136	72.26
R34	$CH_3(s) + H(s) \longrightarrow CH_4(s) + Rh(s)$	2.137×10^{21}	-0.058	46.77
R35	$CH_3(s) + Rh(s) \longrightarrow CH_2(s) + H(s)$	1.275×10^{24}	0.078	107.56
R36	$CH_2(s) + H(s) \longrightarrow CH_3(s) + Rh(s)$	1.073×10^{22}	-0.078	39.54
R37	$CH_2(s) + Rh(s) \longrightarrow CH(s) + H(s)$	1.275×10^{24}	0.078	115.39
R38	$CH(s) + H(s) \longrightarrow CH_2(s) + Rh(s)$	1.073×10^{22}	-0.078	52.61
R39	$CH(s) + Rh(s) \longrightarrow C(s) + H(s)$	1.458×10^{20}	0.078	23.09
R40	$C(s) + H(s) \longrightarrow CH(s) + Rh(s)$	1.122×10^{23}	-0.078	$170.71\text{-}120\theta_{C}$
R41	$CH_4(s) + O(s) \longrightarrow CH_3(s) + OH(s)$	3.465×10^{23}	0.051	77.71
R42	$CH_3(s) + OH(s) \longrightarrow CH_4(s) + O(s)$	1.815×10^{22}	-0.051	26.89
R43	$CH_3(s) + O(s) \longrightarrow CH_2(s) + OH(s)$	4.790×10^{24}	0.000	114.52
R44	$CH_2(s) + OH(s) \longrightarrow CH_3(s) + O(s)$	2.858×10^{21}	0.000	20.88
R45	$CH_2(s) + O(s) \longrightarrow CH(s) + OH(s)$	4.790×10^{24}	0.000	141.79
R46	$CH(s) + OH(s) \longrightarrow CH_2(s) + O(s)$	2.858×10^{21}	-0.000	53.41
R47	$CH(s) + O(s) \longrightarrow C(s) + OH(s)$	5.008×10^{20}	0.000	26.79
R48	$C(s) + OH(s) \longrightarrow CH(s) + O(s)$	2.733×10^{22}	0.000	$148.81\text{-}120\theta_{C}$

The rate coefficients are given in the form of $k=AT^{\beta}\exp(-E_a/RT)$; adsorption kinetics is given in the form of sticking coefficients; the surface site density is $\Gamma=2.72 \times 10^{-9}$ mol cm^{-2}

Applications of the reaction mechanism are tested by conducting CPOx, SR, and DR reactions in the stagnation-flow reactor. The reaction mechanism is used without any modification whatsoever for all investigated CPOx, SR and DR reactions.

CPOx of CH_4

A comparison of the experimental data and the simulation results is shown in Figure 5.31-5.34. CH_4, CO, CO_2 and H_2 mole fractions are measured by measns of FTIR, MS and H-Sense. H_2O mole fractions are calculated via an oxygen mole balance for each measurement point. The maximum boundary-layer thickness is measured to be 8 mm at a temperature of 1023 K (Case 6).

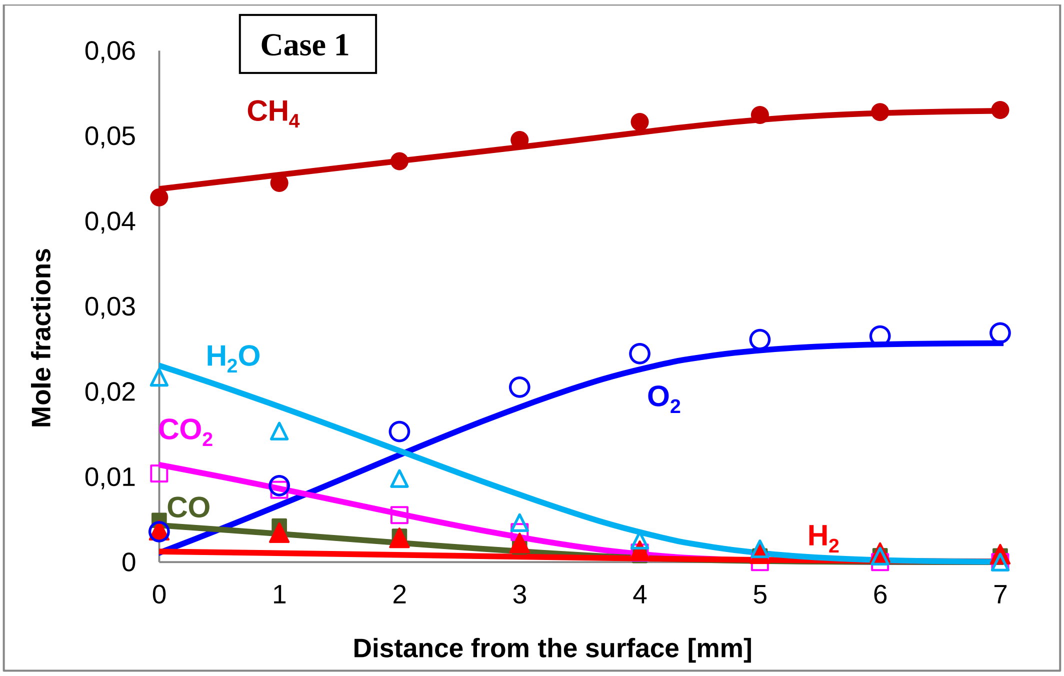

Figure 5.31. Comparison of experimental (symbols) and mumerical simulations (lines) for CPOx of CH_4 studied at 873 K with a C/O ratio of 1.03 (Case 1). $F_{cat/geo}$=0.8 used in the numerical simulations.

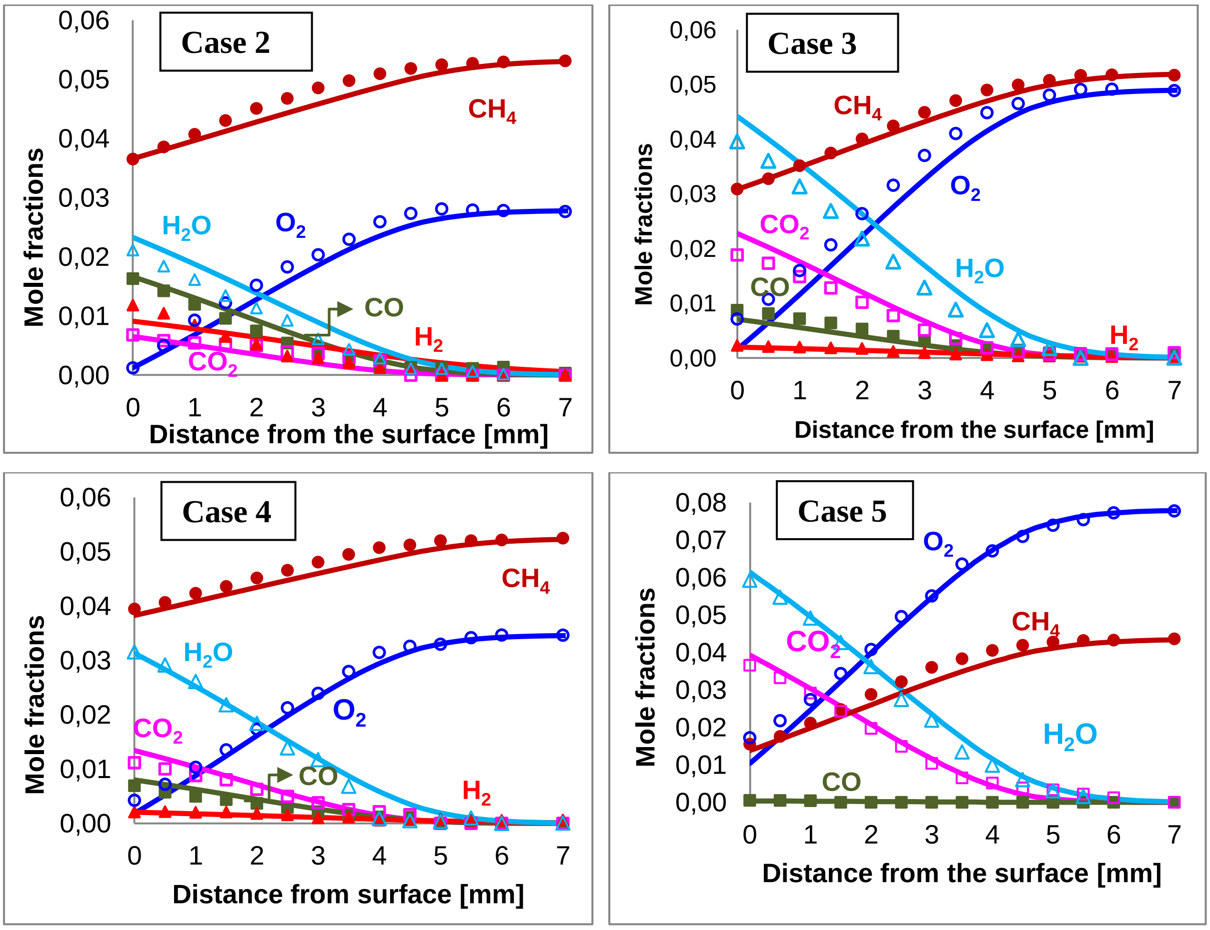

Figure 5.32. Comparison of experimental (symbols) and mumerical simulations (lines) for partial oxidation of CH_4 at 973 K under varying C/O ratios (Cases 2-5 in Table 5.10). Numerical simulations are performed by using $F_{ca/tgeo}$=0.8 for Case 2, $F_{ca/tgeo}$=1.0 for Case 3, and $F_{ca/tgeo}$=0.6 for Case 4,5.

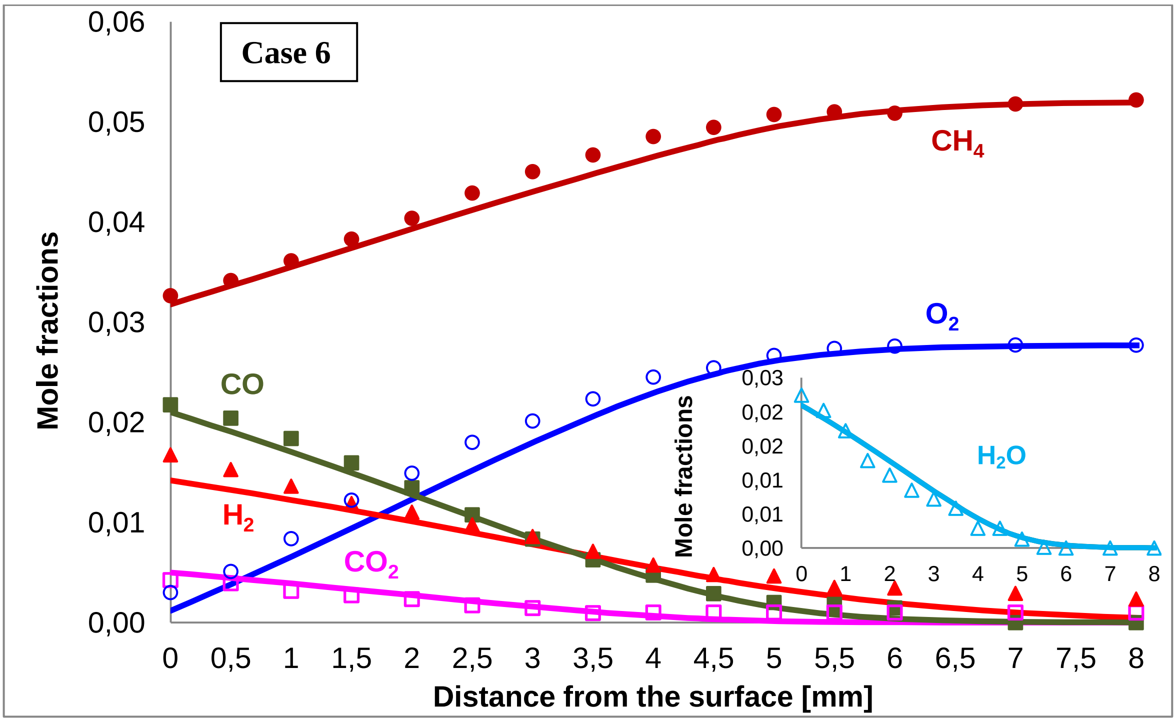

Figure 5.33. Comparison of experimental (symbols) and mumerical simulations (lines) for partial oxidation of CH_4 at 1023 K for a C/O ratio of 0.93. $F_{ca/tgeo}$=0.8 is used in the numerical simulations.

The synthesis gas yield is low at the reaction temperature of 873 K (Figure 5.31). CO_2 and H_2O are detected to be the main products on the catalyst surface. In this case, the reaction is mass transport limited because O_2 is completely consumed on the catalyst surface. Increasing the reaction temperature to 973 K increases the synthesis gas product yield (Figure 5.32, Case 2) as expected. Although O_2 and CH_4 mole fractions on the catalyst surface do not vary considerably (compared to Case 1), the product distribution changes remarkably. Here, H_2 and CO are the main products. On the other hand, increasing the oxygen amount in the feed (Case 3 and Case 4) yields more total oxidation products and results in an increased methane conversion rate.

No partial oxidation products are generated in Case 5 in which a stoichiometric amount of O_2 is fed to the reactor. Although the reaction (total oxidation) is completed at 973 K, O_2 and CH_4 are not completely consumed on the catalyst surface. This is due to the fast diffusion of CH_4 compared to CO_2 and O_2. Since CH_4 diffuses faster than O_2 (relatively 1.4 times), there is a back diffusion of CH_4 that results in a higher mole fraction on the catalyst surface than expected [231].

Lastly, the temperature is increased to 1023 K by ensuring a C/O ratio of 0.93 at the reactor inlet (Case 6). Compared to Case 2, the synthesis gas product yield is increased. Besides, CH_4 and O_2 mole fractions show similar profiles compared to Case 2. That is, the reaction is mass transport limited due to the O_2 amount in the feed.

For all reaction conditions investigated, the numerical simulations are in a good agreement with the experiments with regard to the prediction of the reaction rates of CH_4 and O_2 as well as the prediction of the selectivity of hydrogen and carbon-containing species. Compared to the reaction mechanism of Hartmann et al. [88], the implementation of carboxyl species (COOH) into the mechanism scheme results in a better prediction of carbon selectivities (CO/CO_2).

Application of the Kinetics

The application of the mechanism for CPOx reaction condition is shown for two different reactor types from different research groups.

Example 1: Steady-State Experiments in a Tubular Reactor

Donazzi et al.[30] have studied CPOx of CH_4 in an annular type of a reactor shown in Figure 5.11. The reaction was carried out with 1 vol.% CH_4 and 0.56 vol.% O_2. The reactive gases were diluted in N_2 with the total flow rate of 0.299 SLPM. A 4 wt.% Rh α-Al_2O_3 catalyst was used. With the catalyst amount given and the dispersion measured, an $F_{\mathrm{cat/geo}}$value of 30 is calculated. Steady-state concentration profiles of the species were detected at temperatures of 573-1123 K at atmospheric pressure. The numerical simulation of the system is performed by using the DETCHEM$^{\mathrm{CHANNEL}}$ code. The flow velocity is calculated to be 0.2 m/s at 298 K. A comparison of the numerical simulations and the experimental data is shown in Figure 5.34.

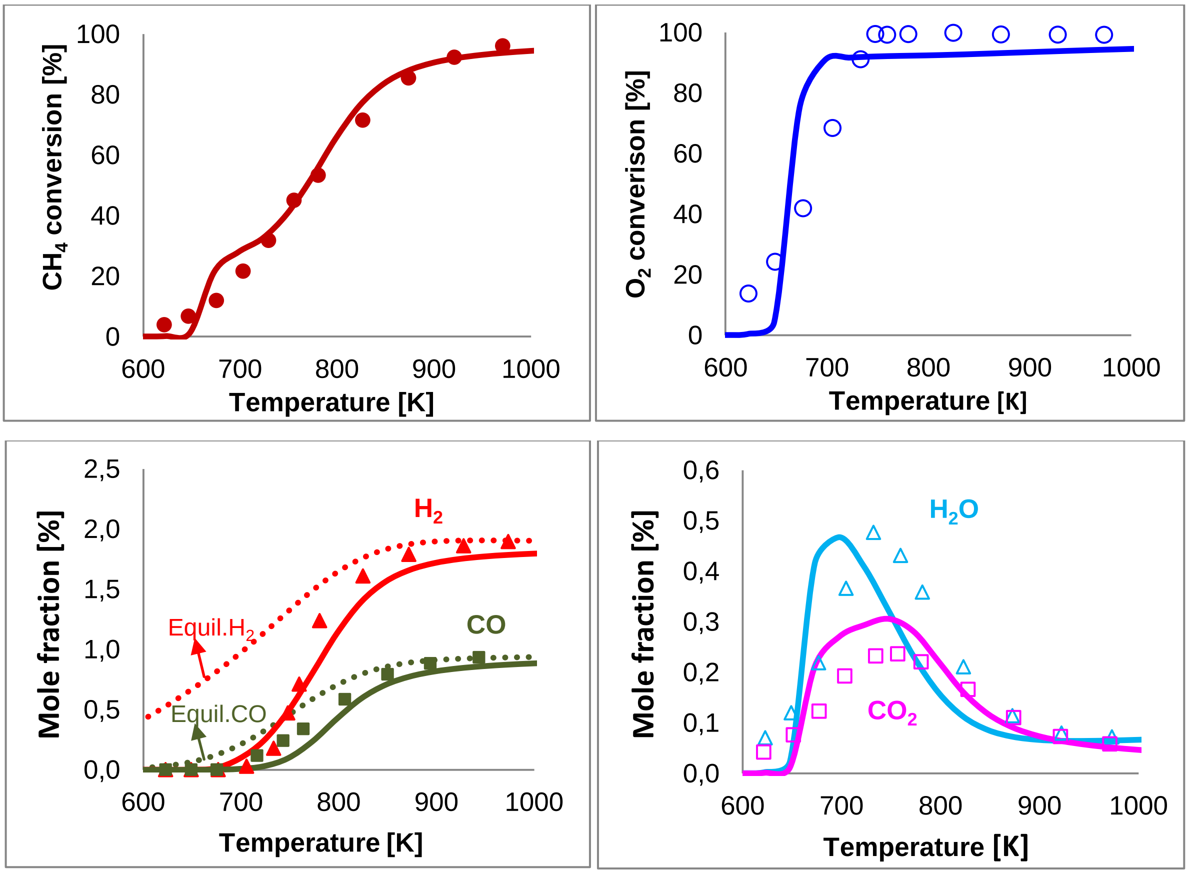

Figure 5.34. Comparison of experimental (symbols) and numerical simulation results (lines) for CPOx of CH_4. Experimental data of Donazzi et al. [30] is reproduced.

Results indicate a good agreement between experimental data and simulation results. A slight difference between experimental and numerical values of CO_2 and H_2O is observed at low temperatures, below 750 K. However a similar tendency was observed by the numerical simulations of Donazzi et al.[30] in which a lumped kinetic model (global reaction kinetics) was used. This difference was attributed to the non-homogeneous coating of the catalyst which also caused hot spot generation on the catalyst bed. Methane and oxygen conversions start slightly at around 650 K and the conversion increases with increasing temperature. At low temperatures, below 700 K, the main products are CO_2 and H_2O. As the conversion of O_2 is completed, synthesis gas production starts. At higher temperature regimes, decomposition of H_2O and CO_2 takes place and as a result, H_2 and CO concentrations increase until the reaction reaches the equilibrium.

Morover the similarities of stagnation-flow reactor data and the work of Donazzi et al. [30] are worth mentioning. At low temperature regimes, total oxidation of CH_4 is favored; however as the temperature increases decomposition of CO_2 and H_2O takes place. The reaction is mass transport limited due to the fast diffusion and consumption of O_2.

Example 2: Spatial Profile Measurement along the Catalyst Bed

Recently, Horn et al. have developed a model for the measurement of axial species profiles of the reactants and temperature profiles in foam structured monoliths for catalytic partial oxidation of CH_4 in millisecond-contact-time reactors at atmospheric pressure [34]. By using a capillary technique they were able to answer the question whether the synthesis gas production follows the direct or the indirect path. The answer was that, neither of them were followed but a combination of indirect and direct paths [5, 34, 35].

Here, a study of Nogare et al. [35] is reproduced and it is compared with the numerical solution using the reaction mechanism presented in Table 5.12.

In that study, CPOx of CH_4 was studied over Rh catalysts. The details of the experimental conditions are given in Table 5.13.

Table 5.13. Reaction conditions for CPOx of CH_4 studied by Nogare et al. [35].

Catalyst	Pore diameter	Lenght	Flow velocity	% CH_4	% O_2	% Ar	C/O
5 wt.Rh/α-Al_2O_3	500 µm	10 mm	1.29 m/s at 900 K	28.94	14.96	56.10	1.0

The numerical simulation of the system is performed by using DETCHEM^{CHANNEL} code in 2D. However, the average concentration profiles in the channel diameter are plotted against the channel length.

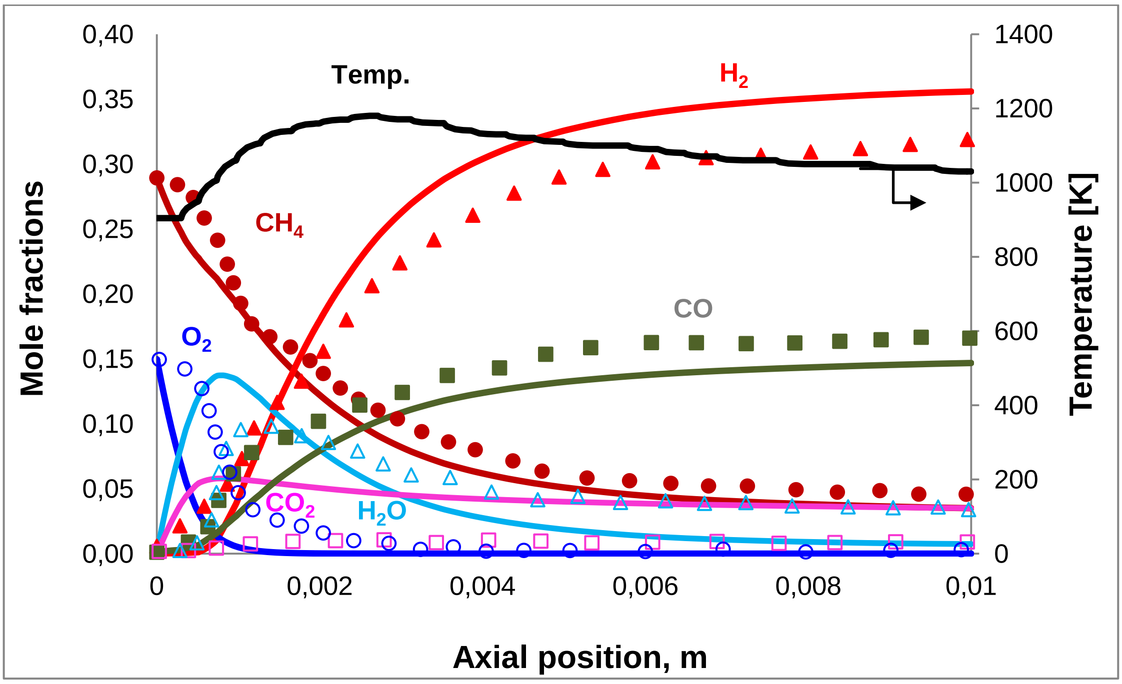

Figure 5.35. Spatial resolved temperature and concentration profile of CPOx of CH_4. Comparison of experimental [35] (symbols) and numerical data (lines.)

The experimental and the simulation results show good agreement in the prediction of the concentration profile along the catalyst bed as well as the outlet gas composition (Figure 5.35). However, the simulation results predict a faster oxidation zone than the experiments (1 mm vs. 2 mm). CO_2 and H_2O are formed in this oxidation zone. The reaction temperature increases due to the exothermicity of the reaction. A small amount of synthesis gas is produced in this zone. Further downstream, a sharp decrease in water concentration and CH_4 results in an increase in H_2 and CO concentrations. This indicates that the steam reforming reaction is active in this zone. The temperature slightly decreases, but the CO_2 concentration does not vary considerably. After the oxygen is completely consumed, CO_2 concentration remains constant. Neither dry reforming (CO_2 reforming) nor WGS reaction activities are detected for this case. On the other hand, Horn et al. [34] pointed out that, the WGS reaction becomes important for C/O ratios of 0.8 and 0.7

Although a good agreement between the experimental and numerical values of CH_4, O_2, CO and H_2 concentrations is presented in Figure 5.35, the model overestimates the maximum concentration levels of CO_2 and the H_2O. It should be noted that, the reaction on the porous foam catalyst is simulated by using an isothermal 2D channel code. The heat transport is not included in the model. It is believed that the deviations can be attributed to the disparateness' of the model system and the experimental set-up.

Methanation

Horn et al. measured CPOx activity of Rh/Al_2O_3 catalysts under different reaction conditions by using their capillary technique [34]. They detected CH_4 formation at the axial positions of 4 mm and 4.5 mm of the catalyst for C/O ratios of 0.7 and 1.3, respectively. The total flow rate was 5 SLPM for both reaction condition examined. Similarly, for the experiments with a C/O ratio of 1.0 and 10 SLPM, they detected methanation at the axial position of ~ 7.5 mm inside the catalyst. At these measurement points, the reaction yields a decrease in H_2 and CO as well as an increase of CH_4 and H_2O concentrations which is a significant sign of the methanation reaction (Eq. 5.28)

$$3H_2 + CO \leftrightarrow CH_4 + H_2O \qquad 5.25$$

The formation of intermediate methane has not been exactly explained by Horn et al.[34] but it has been attributed to the washcoat and possibly reproducible feature of all species in the oxidation zone.

Wheeler et al. [211] have studied the WGS reaction over a series of noble metals including aluminium oxide and ceria-supported Rh catalysts. They showed that a considerable amount of CH_4 is formed on Rh/Al_2O_3 catalyst during WGS reactions in millisecond-contact-time. No detail explanation is given on the methanation kinetics.

In the proposed reaction mechanism in this study (Table 5.12), the methane is formed via R-WGS reaction. In the reforming zone of CPOx, WGS and R-WGS reactions take place. The methane is formed by the reaction of CO with H_2. The gas-phase methane concentration is sensitive to the reaction step in which the surface carbon and hydrogen forms an adsorbed CH(s) species (R40).

$$\text{R40:} \quad C(s) + H(s) \rightarrow CH(s) \qquad 5.26$$

The sensitivity analyses show that, the main C source for the methanation is CO which is formed by the dissociation of CO_2. Besides, it was shown in Chapter 5.4 that, increasing the CO content in the R-WGS reaction yields more methane. In this chapter, the numerical simulations of CH_4 formation during WGS and R-WGS reactions are presented. Detailed information on the experiments and the numerical simulation conditions are given in Chapter 5.4.4.2. Here, only the data of CH_4 formation are shown.

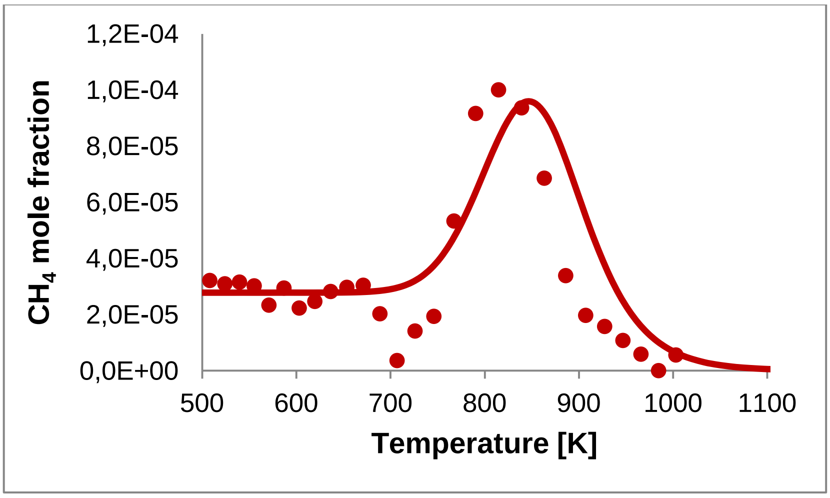

Figure 5.36. Comparison of experimental [227] (symbols) and the predicted values (lines) of CH_4 formation during the WGS reaction carried out in the flow reactor. The reactor inlet mole composition is chosen to be 11.6 vol.% H_2O and 11.2 vol.% CO diluted in N_2.

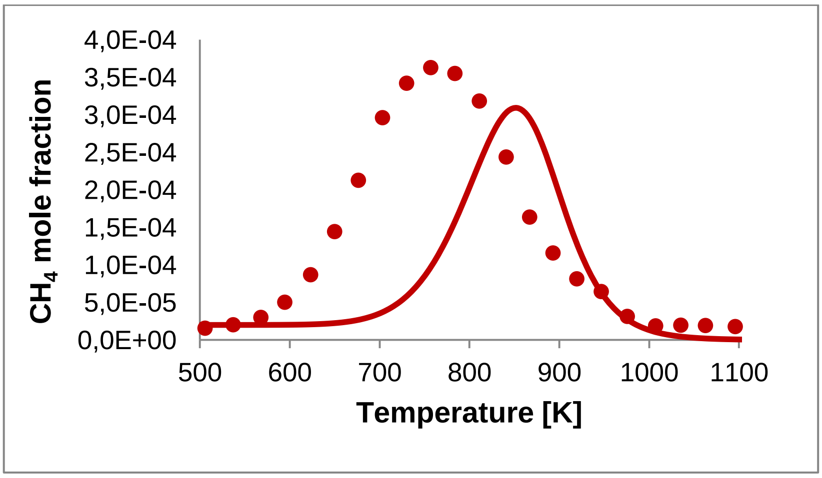

Figure 5.37. Comparison of the experimental [227] (symbols) and the predicted values (lines) of CH_4 formation during the R-WGS reaction carried out in the flow reactor. The reactor inlet mole composition is chosen to be 10.40 vol.% H_2 and 10.88 vol.% CO_2 diluted in N_2.

Steam Reforming of CH_4

A comparison of the experimental and the predicted mole fractions along the boundary-layer is presented in Figure 5.38 and Figure 5.39 for the reaction temperatures of 973 and 1008 K, respectively. CH_4, CO, CO_2 and H_2 concentrations are measured by FTIR and H-Sense whereas H_2O concentration is calculated via the atom balance.

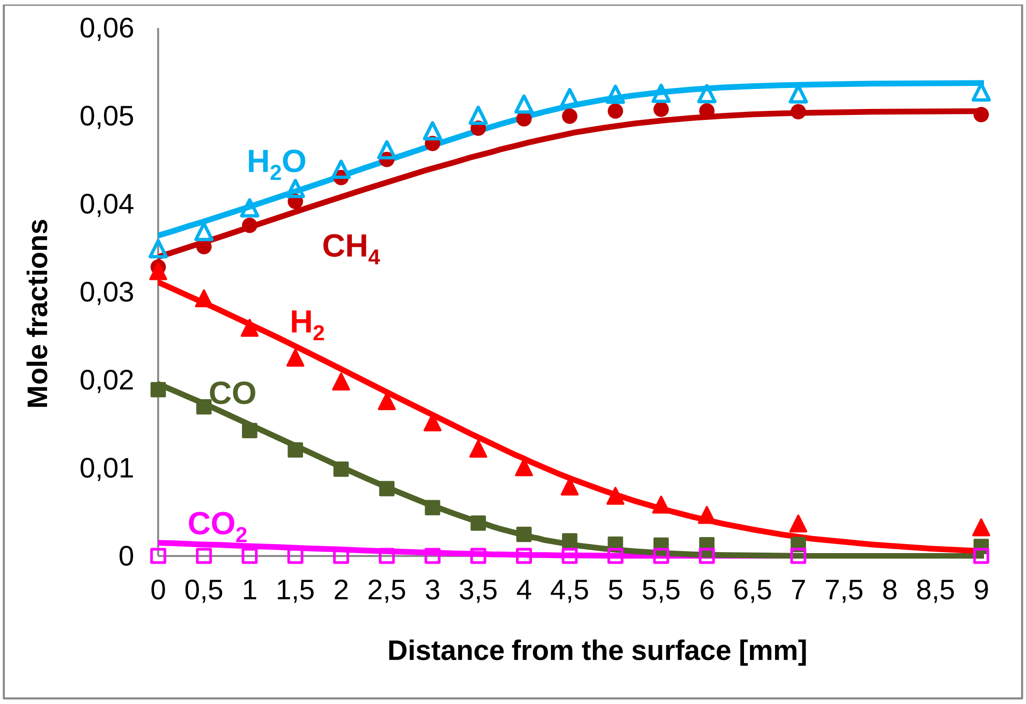

Figure 5.38. Comparison of the experimental (symbols) and the predicted (lines) mole fractions along the boundary-layer for steam reforming of CH_4, S/C=1.06, and the reaction temperature is 973 K. $F_{ca/tgeo}$=1.0 is used in the numerical simulations

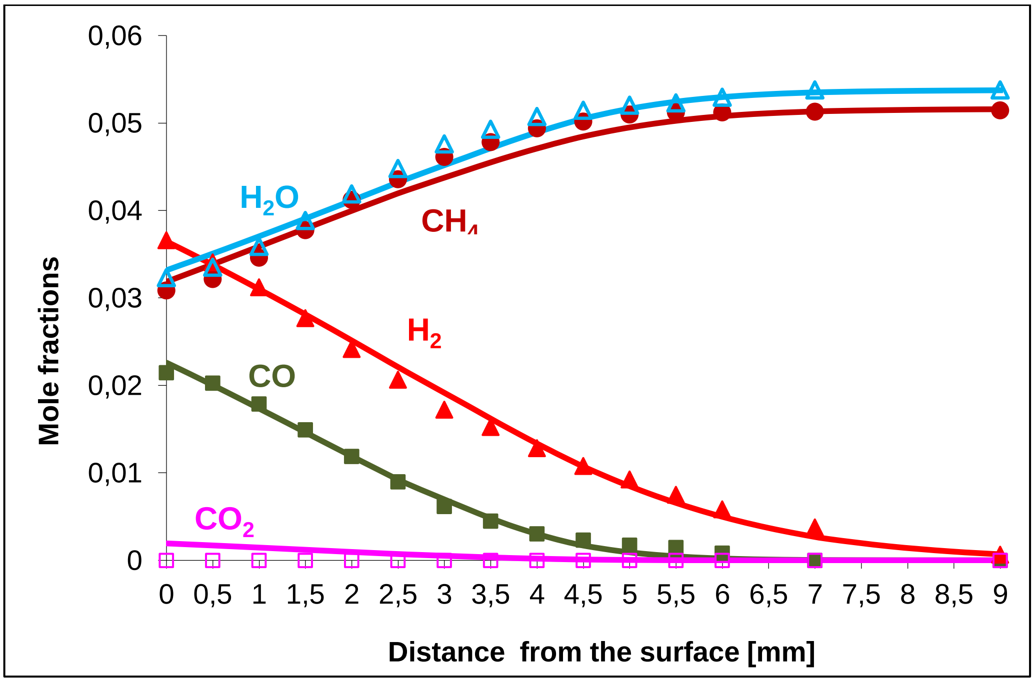

Figure 5.39. Comparison of the experimental (symbols) and the predicted (lines) mole fractions along the boundary-layer for steam reforming of CH_4, S/C=1.04, reaction temperature is 1008 K. $F_{ca/tgeo}$=1.0 is used in the numerical simulations.

A high synthesis gas reaction yield is detected at 973 K. An increase in the temperature leads to an increased reaction rate of CH_4 and H_2O. For both reaction conditions investigated, the reactions are kinetically limited because the the reactants are not completely consumed on the catalyst surface. Although the boundary-layer is completely resolved after 6 mm for CO, CH_4 and H_2O, further boundary-layer resolution measurements are carried out to detect H_2 by 9 mm.

The main reaction products are CO and H_2, for both of which the reaction conditions are examined. Simulation results show that CO_2 at the ppm level (maximum ~1900 ppm at 1008 K) is formed, whereas no CO_2 is detected experimentally.

To analyze the main reaction path of steam reforming of CH_4, sensitivity analyses are carried out by using the CHEMKIN SPIN code. Three temperature points (773 K, 900 K and 1000 K) are selected at which low, moderate and high conversions of the reactants are expected on the basis of the numerical simulations in 600 cpsi channel geometry over Rh/Al_2O_3 catalyst (the detail description of the catalyst in given in Chapter 5.4.4.2).

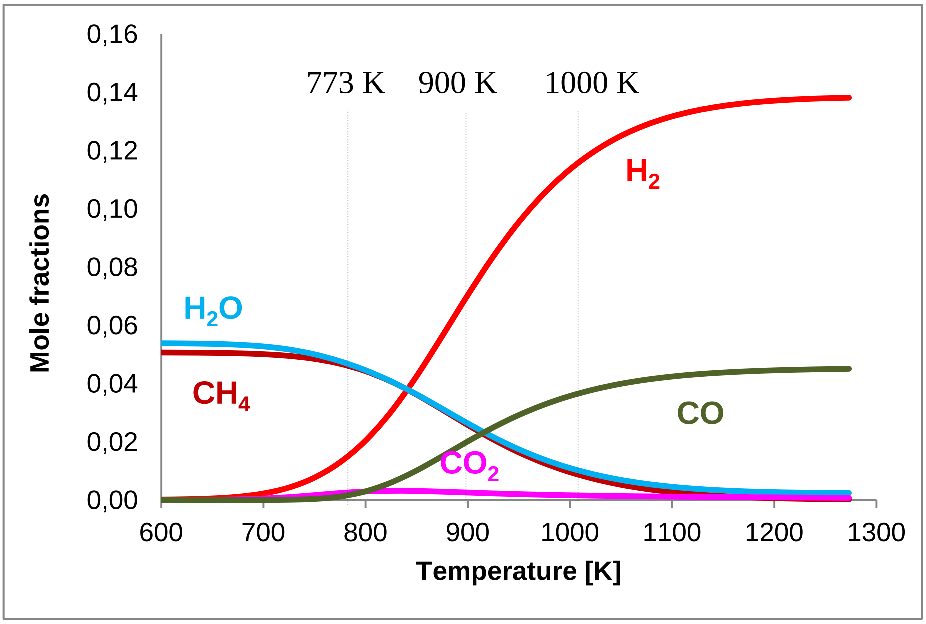

Figure 5.40. Simulation of steam reforming of CH_4 over 600 cpsi monolithic Rh/Al_2O_3 catalyst with 5.06 vol.% CH_4 and 5.38 vol.%H_2O diluted in N_2. Steady-state reaction conditions are assumed at 573-1273 K. Inlet velocity is 0.2875 m/s at 298 K and $F_{cat/geo}$ is assumed to be 2. The numerical simulation is performed by using DETCHEM^{CHANNEL} code.

The sensitivity analyses (Figure 5.41) show that the main reaction paths may vary depending on the reaction temperature. At a low temperature (773 K), the gas-phase CO concentration is sensitive to adsorbed and gas-phase CO and H_2O as well as their reaction steps in which the WGS reaction path is dominant. Besides, the adsorption, desorption and the dehydrogenation steps of CH_4 are dominant reaction paths for the production of gas-phase CO. Similar to WGS reaction path analysis (Figure 5.18and Figure 5.19), it is shown that the formation of carboxyl species (COOH) is an important reaction step for steam reforming reactions at low temperature regimes.

At high temperature regimes, the formation of gas-phase CO is sensitive to the adsorption and desorption steps of CH_4. Furthermore, the dehydrogenation step of CH_4 is an important reaction step (R33). Similar trends are also valid in the sensitivity analyses of the formation of gas-phase H_2 at low and high temperature regimes.

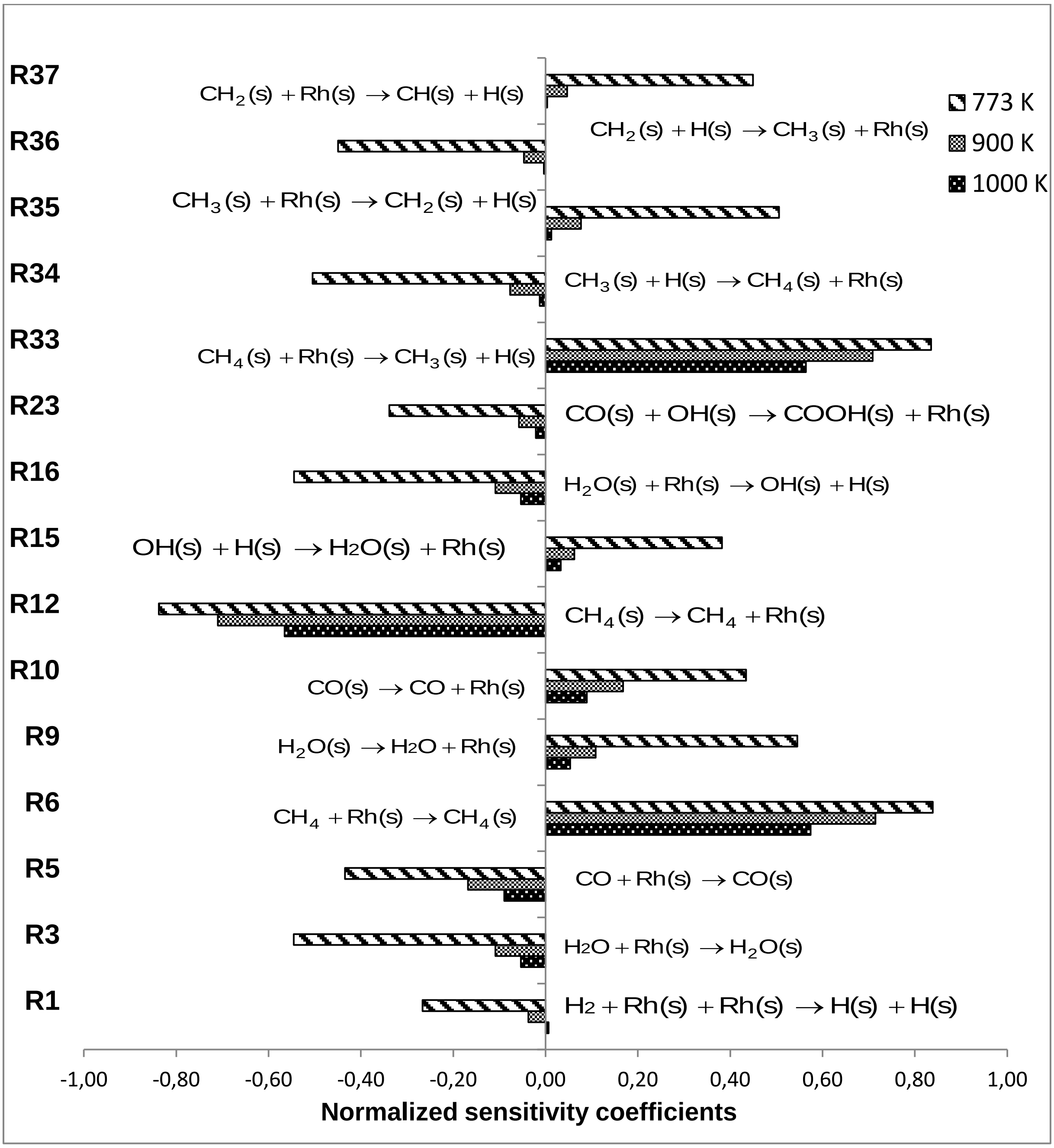

Figure 5.41. Sensitivity analyses of CO gas-phase concentrations for steam reforming reactions at different temperature points. Inlet mole composition is chosen to be 5.06 vol.% CH_4 and 5.38 vol.% H_2O diluted in Ar.

To identify which reaction steps are in equilibrium and which reaction step is the rate determining step reaction in this sensitivity diagram, the reaction path analysis of Maestri et al. [36] is applied. A partial equilibrium ratio, $\varphi = \frac{r_f}{r_f + r_b}$ in which r_f and r_b are forward and backward reaction rates for each elementary-step, is defined. Given in definition, if φ=0.5 the reaction is in partially equilibrium and if φ deviated from 0.5 the reaction is not in partial equilibrium.

According to this analysis, for the reactions in which relatively high sensitivity coefficient are reported for the adsorption (R6) and the desorption steps (R12) of CH_4, the partial equilibrium ratio φ is calculated to be 0 for all the reaction temperatures under investigation.

Thus, the reaction is far from the equilibrium. However, for the dehydrogenation reaction of CH_4 (R33) φ is calculated to be close to 1. Therefore, this reaction is also not in equilibrium. According to Maestri et al. [36], the rate determining step becomes the most sensitive reaction step through the sensitivity analyses. By using this definition, it has been concluded that the adsorption, desorption and dehydrogenation steps of CH_4 are rate determining steps because they are far from the equilibrium and they have almost the same normalized sensitivity coefficients.

Furthermore, the reaction rate seems to be independent of the reaction steps of H_2O (R3 and R9) at moderate and high temperatures. It only has an influence on the gas-phase CO concentration at the temperature of 773 K at which WGS reaction steps (R5, R10, R16 and R23) are the dominant reaction paths for CO formation.

A similar conclusion was postulated by Donazzi et al. [30]. They studied steam reforming of CH_4 in an annular type of reactor and showed that the reaction rate is independent of H_2O concentration. Furthermore, they concluded that, the rate determining step is related to the methane pyrolysis reaction step. Wei and Iglesia [199] have also pointed out that, whether it is a catalytic partial oxidation or steam reforming reaction, the kinetically relevant step is the C-H activation step.

Application of the Kinetics

The application of the presented reaction kinetics is shown by reproducing the experimental steam reforming data of Donazzi et al. [30]. The reaction was carried out at 573-1123 K in an annular type of reactor with 1 vol.% CH_4 and 2 vol.% H_2O diluted in N_2.

In this study, the numerical simulation of the system is performed by using DETCHEM^{CHANNEL} code. The steady-state average concentration profiles in the channel outlet are calculated for each species and compared with the experimental data of Donazzi et al. [30].

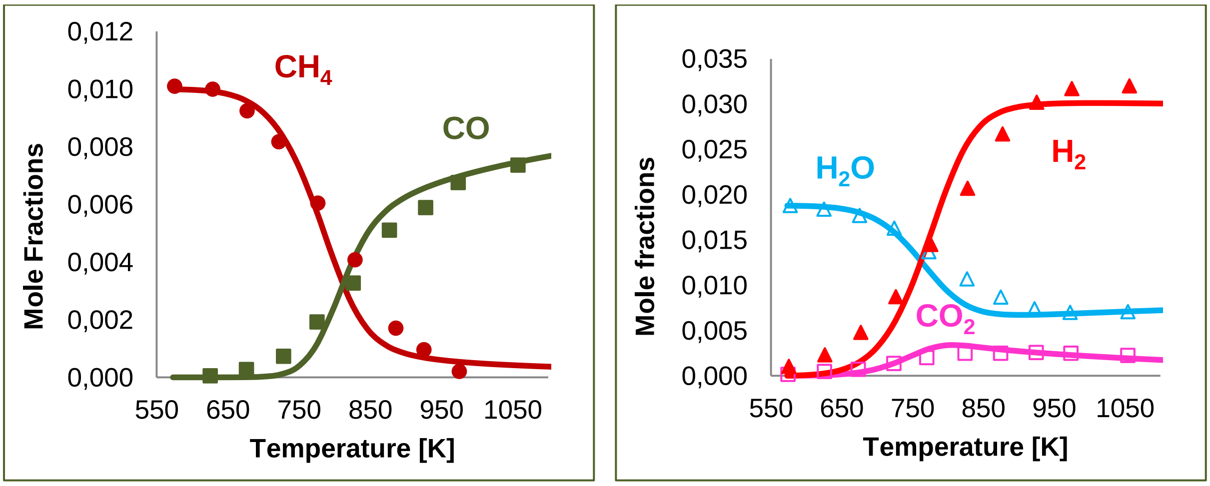

Figure 5.42. Comparison of the experimental [30] (symbols) data and the numerical simulations (lines) for steam reforming of CH_4. The reactive gas composition includes1 vol.% CH_4 and 2 vol.% of H_2O diluted in N_2. The flow velocity is calculated to be 0.2 m/s at 298 K and $F_{cat/geo}$ is assumed to be 30.

According to Figure 5.42, the reaction starts at around 700 K and the total combustion of CH_4 has reached at around 950 K. The concentration profiles of the main products of H_2 and CO are predicted in a good agreement with the experimental data. The same is true for the CO_2 which is only at the ppm level.

Dry Reforming of CH_4

Comparisons of the experimental data and the numerical results for dry reforming reactions are shown in Figure 5.43 and Figure 5.44.

Figure 5.43 shows a relatively small dry reforming activity at 973 K. 1 vol.% O_2 is added to the reactive gas mixture to avoid possible carbon formation and consequently the deactivation of the catalyst. The boundary-layer is reached at 5 mm. Besides the dry reforming products of H_2 and CO, H_2O is formed via partial oxidation of CH_4. The reaction is kinetically limited since a comparably small dry reforming activity is measured at this temperature.

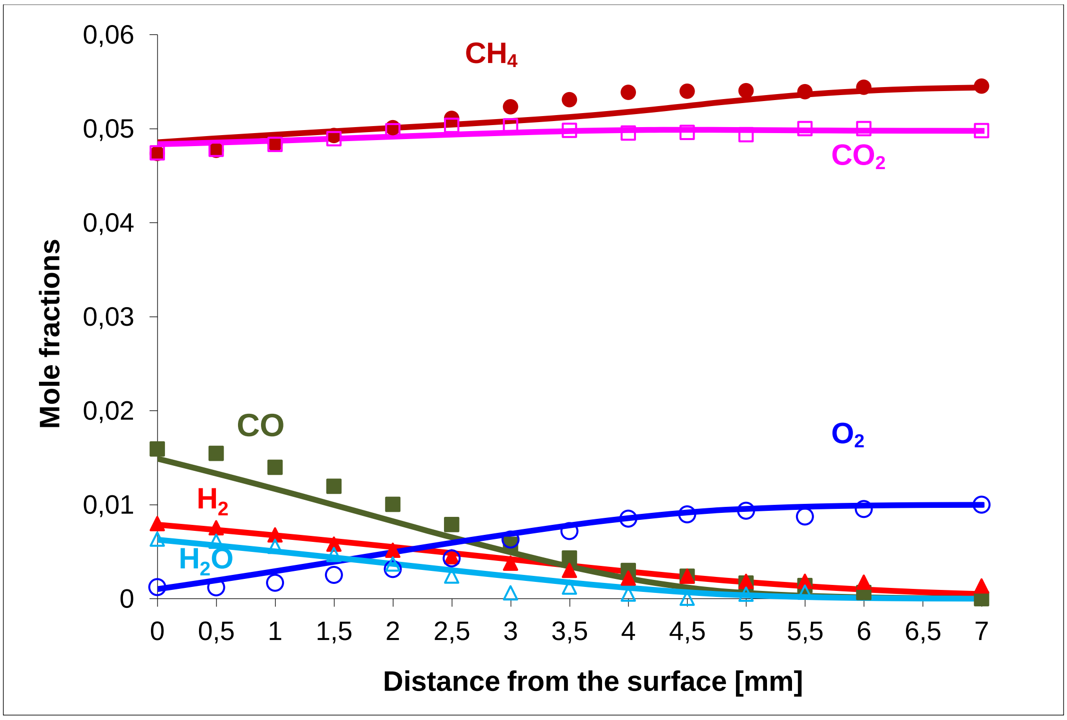

Figure 5.43. Comparison of the experimental (symbols) and the numerical simulations for dry reforming of CH_4. The inlet gas composition is chosen to be 5.45 vol.% CH_4, 4.97 vol.% CO_2 and 1 vol.% O_2 diluted in Ar. The reactor is operated at 500 mbar and the inlet velocity is calculated to be 51 cm/s. $F_{cat/geo}$ is assumed to be 1.

For analyzing the reaction at high temperature regimes, the experimental data of McGuire et al. [27] are reproduced. A comparison of the experimental data and the numerical simulations is shown in Figure 5.44. A similar stagnation-flow reactor was developed by Colorado Fuel Cell Center (Colorado School of Mines). A series of dry reforming experiments were reported by McGuire et al. on a Rh surface supported on strontium-substituted hexaaluminates [27]. Although the support was different from Al_2O_3, they showed that the surface reaction mechanism developed by Deutschmann et al. [50] for Rh/Al_2O_3 surfaces can be used for $Rh/SrAl_{12}O_{19}$ systems as well [83].

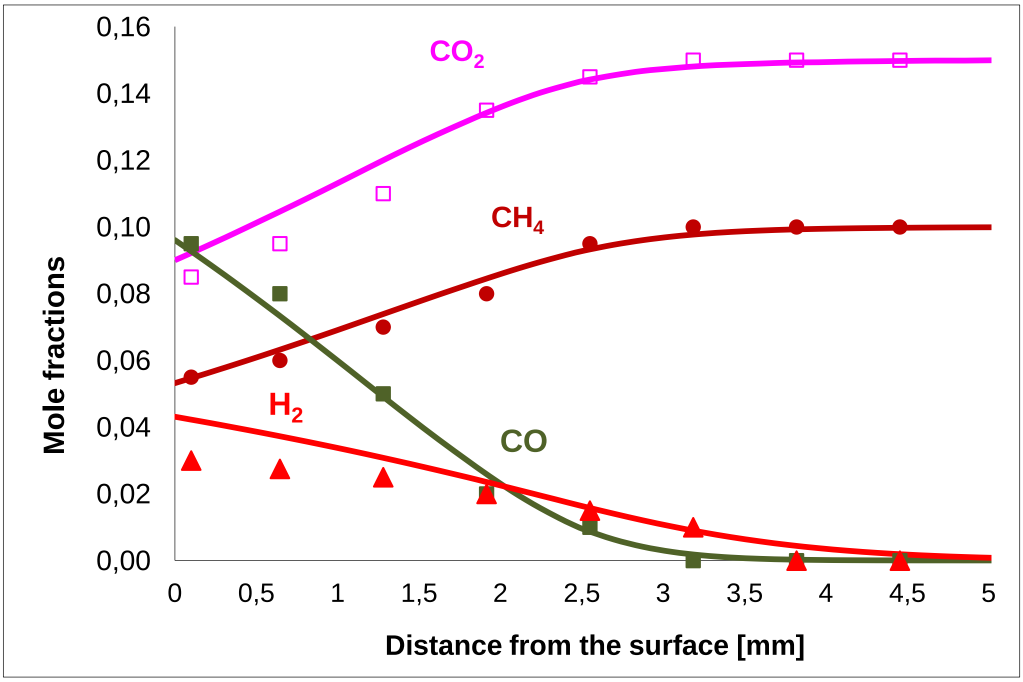

Figure 5.44. Dry reforming of CH_4 at 1073 K. Experimental data (symbols) of McGuire et al.[27] is reproduced. The reactive gas mixture contains 10 vol.% CH_4 and 15 vol.% CO_2 diluted in Ar. The reactor is operated at 395 mbar and the inlet velocity is calculated to be 90 cm/s. An $F_{cat/geo}$ value of 56 is used in the numerical simulations.

Although a highly concentrated reactive gas mixture is fed to the reactor, the boundary-layer is completely resolved by 4.5 mm which is due to the fact that the working pressure is lower than in Figure 5.43. Only H_2 and CO are detected to be the reaction products. Therefore, it can be concluded that H_2O was formed via CPOx of CH_4. The elementary-step reaction mechanism given in Table 5.12 is used for the numerical simulations.

In literature, several kinetic models have been reported to explain the main reaction pathways of dry reforming of CH_4. Many of the published kinetic data agree that the rate determining step is related to dehydrogenation steps of CH_4 [27, 36, 199, 232, 233]. However, the main argument is about the reaction path of CO formation. Nakamura et al. have suggested a reaction path for CH4 activation based on the Rideal-Eley reaction kinetics. In their reaction scheme, CH_4 dissociatively adsorbs on Rh active sites and yields an adsorbed CH_2 and H_2 in the gas-phase. The reaction step is the rate determining step [232]. Subsequently, the dissociatively adsorbed CO_2 is converted to CO by the R-WGS reaction. Furthermore, H_2O reacts with CH_2 and forms an adsorbed CO and H_2 in the gas-phase. The reaction scheme is shown in Eq. 5.27-5.31. (Here ↔ denotes a quasi-equilibrium reaction)

$$\mathrm{CH_4 + Rh(s) \rightarrow CH_2(s) + H_2} \tag{5.27}$$

$$\mathrm{CO_2 + Rh(s) \leftrightarrow CO + O(s)} \tag{5.28}$$

$$\mathrm{O(s) + H_2 \leftrightarrow H_2O + Rh(s)} \tag{5.29}$$

$$\mathrm{CH_2(s) + H_2O \leftrightarrow CO(s) + 2H_2} \tag{5.30}$$

$$\mathrm{CO(s) + Rh(s) \leftrightarrow CO + Rh(s)} \quad 5.31$$

However, FTIR studies revealed that rather than CH_2 only, also CH_x-containing species are formed via dissociation of CH_4 [221, 234]. The studies show that the adsorbed hydrogen atoms enhance the disscociation of CO_2 that results in the formation of gas-phase CO (Eq. 5.32) [235].

$$\mathrm{CO_2 + H(s) \leftrightarrow CO + HO(s)} \quad 5.32$$

A similar conclusion was reported by Rostrupnielsen and Hansen. According to their study, the R-WGS reaction is the most important reaction step because of its dependence on the product H_2 [236]. Later, Maestri et al. postulated a reaction scheme based on the Langmuir-Hinshelwood kinetics and showed that, dry reforming of methane occurs via R-WGS reaction [36].

Mark and Maier have proposed an alternative reaction path for the formation of CO on Rh surfaces which is based on the Rideal-Eley kinetics. [237]. They postulated a reaction scheme in which CO is generated by the reaction of surface carbon, $C(s)$, with gas-phase CO_2. This step is assumed to be a fast step. $C(s)$ is formed via pyrolysis of CH_4 and this step is assumed to be the rate determining step.

$$\mathrm{CH_4 + Rh(s) \rightarrow C(s) + 2H_2} \quad 5.33$$

$$\mathrm{C(s) + CO_2 \rightarrow 2CO + Rh(s)} \quad 5.34$$

Recently, Hartmann et al. [88], Mhadeshwar and Vlachos [152] and Wei and Iglesia [199] have proposed reaction schemes for dry reforming of methane based on the Langmuir-Hinshelwood mechanism kinetics. They all agreed that CH_4 produces the surface carbon via its dehydrogenation steps. On the other hand, the main differences between these studies are on the definition of the oxidation path of the surface carbon thus the formation of adsorbed CO species. According to Wei and Iglesia [199], CO is formed via oxidation of the surface carbon via oxygen atoms which are formed via the dissociative adsorption of CO_2. Furthermore, H_2 is formed via rapid combination of hydrogen atoms. On the other hand, Hartmann et al. [88] proposed a reaction mechanism in which the oxidation of the surface carbon may occur via adsorbed oxygen which is generated via the dissociation of CO_2 and HCO species. McGuire et al. [27] applied this mechanism to dry reforming of CH_4 and showed that surface carbon is oxidized by oxygen which originates from dissociation of HCO rather than CO_2. Maestri et al. [36] performed a reaction path analysis for dry reforming of CH_4 by using the mechanism of Mhadeshwar and Vlachos [152]. They revealed that, the oxidation of surface carbon occurs by the reaction with adsorbed hydroxyl (OH) and furthermore, that OH species does not mainly originate from the reaction of hydrogen and oxygen $[\mathrm{O(s) + H(s) \rightarrow OH(s) + Rh(s)}]$ but the reaction of adsorbed CO_2 and H (Eq.5.36).

$$\mathrm{C(s) + OH(s) \rightarrow CO(s) + H(s)} \quad 5.35$$

$$\mathrm{CO_2(s) + H(s) \rightarrow CO(s) + OH(s)} \quad 5.36$$

In addition, Shustorovich and Bell calculated the activation barrier for the two elementary-steps reactions: $\mathrm{C(s) + OH(s) \rightarrow CO(s) + H(s)}$ and $\mathrm{C(s) + O(s) \rightarrow CO(s) + Pt(s)}$ on Pt(111) surface using UBI-QEP. They showed that, theoretically, oxidation of surface carbon via OH species is more favored [238].

The reaction mechanism proposed in this study (Table 5.12) involves the direct oxidation of the surface carbon by oxygen as well as by OH species. To understand the main reaction path for the formation of CO, the sensitivity analyses are performed at three different reaction temperatures, 723 K, 823 K and 923 K. The reaction inlet conditions are assumed to be 10 vol.% CH_4 and 15 vol.% CO_2 diluted in Ar. Reaction is carried out at 395 mbar.

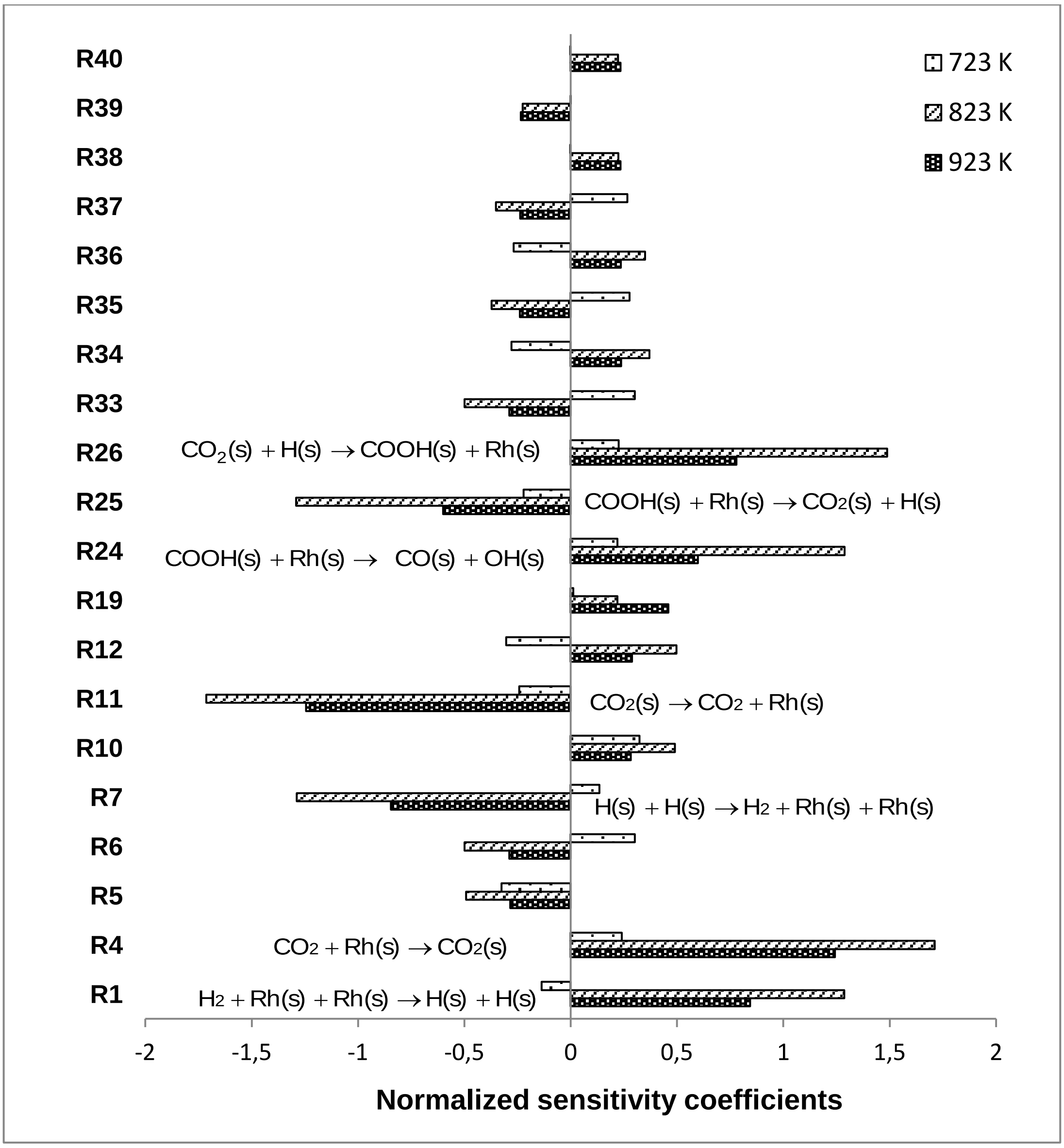

Figure 5.45. Sensitivity analyses for the gas-phase CO concentrations for dry reforming of CH_4. The reactive gas mixture contains 10 vol.% CH_4 and 15 vol.% CO_2 diluted in Ar. The reactor is operated at 395 mbar and the inlet velocity is calculated to be 90 cm/s.

The sensitivity analyses reveal that, the main reaction path for dry reforming of CH_4 follows the R-WGS reaction pathway under the reaction conditions investigated. Gas-phase CO is formed via decomposition steps of carboxyl intermediate (R24 and R25). The reaction is sensitive to the adsorption and desorption steps of H_2 and CO_2. The direct oxidation of the surface carbon by oxygen (R22) does not have a significant effect. Besides, unlike in the study of Maestri et al.[36] no significant effect of the reaction of the hydroxyl species (OH) with the surface carbon on gas-phase CO formation is detected.

Lastly, the reaction mechanism is validated by reproducing the experimental data of Donazzi et al. [216]. The experiments were carried out in the annular type of reactor which is described in detail in Chapter 5.2.4. The dry reforming activity of a 4 wt.% Rh/Al_2O_3 catalyst was measured. The inlet gas composition was selected to be 1 vol.% CH_4 and 2 vol.% CO_2 diluted in N_2 with the total flow rate of 0.299 SLPM. The outlet mole composition of the reactor was measured under steady-state temperatures. The numerical simulation of the system is performed using 2D DETCHEM^{CHANNEL} code. $F_{cat/geo}$ is calculated to be 30 on the basis of the given information on the catalyst properties and the coating. The results are presented in Figure 5.46.

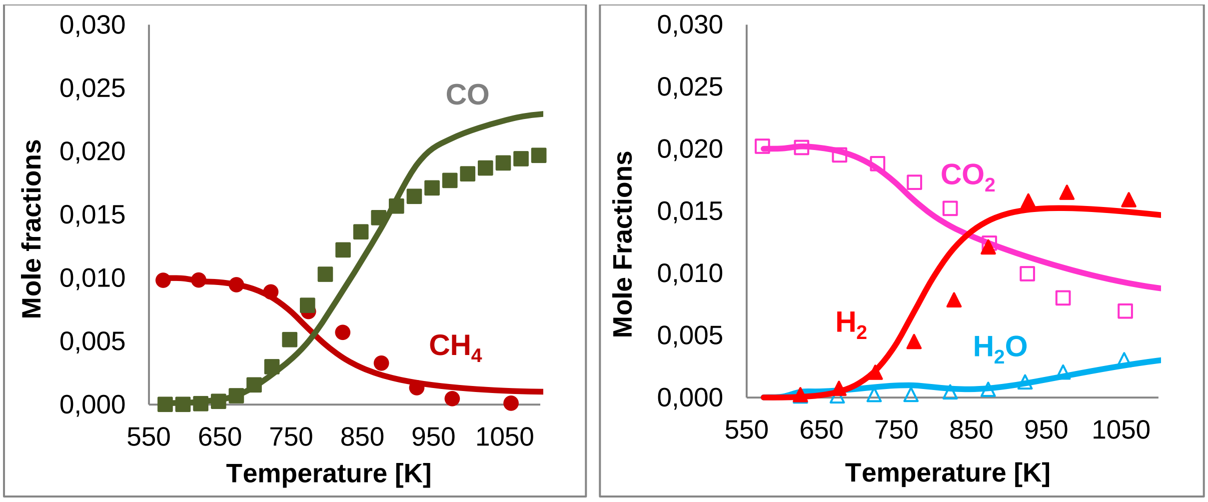

Figure 5.46. Comparison of the experimental data [216] (symbols) and the numerical simulations (lines) of dry reforming of CH_4. The reactive gas mixture contains 1 vol.% CH_4 and 2 vol.% CO_2 diluted in N_2. The total flow rate is 0.279 SLPM.

The model predicts the experimental data well over a wide range of temperatures. At high temperature regimes (> 950 K), CO and CO_2 concentrations slightly differ from the predicted values. This is due to the mass transport limitations resulting from a non-uniform coating of the catalyst. Maestri et al. [36] simulated these experiments by using the elementary-step reaction mechanism of Mhadeshwar and Vlachos [152]. Similar to the data presented in Figure 5.46, the predicted CO and CO_2 concentrations slightly differ from the experiments at high temperatures (> 900 K).

5.5.4 Conclusion

A unified reaction mechanism for catalytic partial oxidation and reforming of CH_4 has been presented. The stagnation-flow reactor experiments are used to assist a 1D steady-state solution of the reactive flow. CPOx, SR and DR experiments are carried out in the stagnation-flow reactor under varying reaction conditions. The reaction mechanism is thermodynamically consistent at a temperature regime of 273-1273 K. The proposed reaction mechanism is validated by using the data derived from experimental in different reactor types and with different catalyst configurations by different research groups.

The following conclusions have been made:

- The synthesis gas production via CPOx of CH_4 is a combination of total oxidation (indirect path) and partial oxidation (direct path) reactions. Based on the axial spatial measurement profiles inside a catalyst bed [34], the reaction mechanism confirms that there is a total oxidation of CH_4 at the beginning of the reaction. CO_2 and H_2O are produced in this zone and small amounts of H_2 and CO are also produced. Afterwards, the rest of the CH_4 is consumed in the reforming zone in which SR, WGS and R-WGS reactions may also take place.
- Introducing the formation of carboxyl species (COOH) improves the mechanism, now a better prediction of carbon selectivities (CO/CO_2) in CPOx of CH_4 is possible.
- A good agreement between the experiments and the numerical simulations are detected with regard to the prediction of synthesis gas mole concentrations as well as the side product (CH_4). It was concluded that CH_4 is formed in the reforming zone in which WGS and R-WGS reactions take place.
- The sensitivity analyses are performed to examine SR reaction path at different reaction temperatures. The results reveal that, the rate-determining steps are the adsorption, desorption and the dehydrogenation steps of CH_4. H_2O concentration does not have a large influence on the concentration of gas-phase CO at high temperatures. However, at temperature regimes below 773 K, the reaction is sensitive to the formation of carboxyl species (COOH) and H_2O concentration.
- The reaction path analyses are performed for DR reactions as well. It has been shown that, the reaction follows the path of the R-WGS reaction. The gas-phase CO is formed by the decomposition of carboxyl intermediates. The hydrogen concentration has a significant effect on the concentration of gas-phase CO because the formation of COOH is favored by the reaction of the adsorbed CO and hydroxyl species.

5.6 Catalytic Partial Oxidation and Reforming of Propane (C_3H_8)

CPOx and reforming of C_3H_8 reactions were conducted in the stagnation-flow reactor. The reaction mechanism (Table 5.12) has been extended to propane. The reaction rate parameters are evaluated on basis of the data derived from the stagnation-flow reactor experiments.

5.6.1 Theoretical Background

Propane is one of the most abundant species in natural gas (0.1-1.5 vol.%) [239]. It is also used for domestic and industrial purposes [240]. It can be liquefied at approximately 9 bar, which enables easy storage and transportation of the gas. For instance, in Norway, no infrastructure exists for the transportation of natural gas. The natural gas is not directly used. Instead, it is first converted to propane and liquefied in large amounts to facilitate easy transportation and storage of the gas [241]. Liquefied petroleum gas (LPG) is used in automobiles in all around the world as an alternative fuel, because it is considerably cheaper than oil [240, 242]. Furthermore, propane is considered as an alternative fuel for synthesis gas production technologies. However, the number of studies in literature is limited. Huff et al. have examined the partial oxidation reaction of propane over Pt, Pd, Rh, Ir and Ni coated monolithic catalysts in millisecond-contact-time reactors under auto-thermal operating conditions at 1273-1473 K [243]. They reported that using Ir faces sintering problem and Ni volatizes. They concluded that Rh provides the best synthesis gas selectivity. Pt yields more H_2O and the formation of ethylene (C_2H_4) is observed under fuel-rich conditions. However, solid carbon formation is reported on Pd and Rh catalysts [243]. Similarly, Beretta and Forzatti have studied partial oxidation of propane over Rh and Pt catalyst by means of a 1D isothermal annular duct type reactor [244]. They showed that Rh is a more selective catalyst than Pt for synthesis gas production. Pt yields more total oxidation products since the reaction follows the direct oxidation path. Secondary reactions i.e., SR and DR were found to be negligible during CPOx of C_3H_8 over Pt catalyst. On the other hand, CPOx of C_3H_8 over Rh shows a different behavior. Reforming of C_3H_8 also takes place during CPOx, and thus, indirect path as well as the direct oxidation paths exists. C_3H_8 is converted to CO and H_2 by means of O_2 in the direct oxidation zone. Besides, H_2O which is formed in the direct oxidation zone activates the synthesis gas formation via steam reforming reaction in the downstream of the catalyst. By products i.e., C_2H_4 and CH_4 formation is observed on Pt. No C_2H_4 is formed and formation of CH_4 is observed only at the ppm level over Rh catalysts [244].

Silberova et al. have studied CPOx and oxidative steam reforming (OSR) of C_3H_8 over Rh impregnated Al_2O_3 foam catalysts [241]. They showed that a reaction temperature of 973 K is the optimum reaction temperature for hydrogen production by CPOx as well as oxidative steam reforming (OSR). A relatively low CH_4 formation was reported at this temperature. Furthermore, a higher H_2 yield was obtained by OSR than CPOx.

Aside from the experimental studies, no detailed surface reaction mechanism has been proposed for CPOx and reforming of C_3H_8. Recently, Schädel et al. have studied steam reforming of C_3H_8 as well as C_2H_6 and C_4H_{10} over a technical Rh/Al_2O_3 catalyst in a monolithic structure [245]. By using the experimental data which are derived from a continuous-flow reactor, they revised the catalytic partial oxidation reaction mechanism of Schwiedernoch et al. [33]. They implemented a series of reaction steps for a better prediction of the reforming activity. Furthermore, they incorporated global reaction kinetics of C_3H_8, C_2H_6 and C_4H_{10} in to the reaction mechanism. Later on, Hartmann et al. studied CPOx of iso-octane and proposed a detailed surface reaction mechanism for C_1-C_3 species including the global reaction kinetics of iso-octane [88]. But, even though, the validation of the reaction mechanism for CPOx of iso-octane had been successfully shown, no detailed investigations on CPOx and reforming of C_3H_8 have been conducted.

In this study, as a sequel to the previous chapters (5.2-5.5), the reaction mechanism is extended and unified for CPOx and reforming of C_3H_8 by using the stagnation-flow reactor data.

5.6.2 Experimental Procedure

The CPOx and SR reactions are carried out in the stagnation-flow reactor under varying fuel compositions and reaction temperatures. A fresh 5 wt.% Rh/Al_2O_3 catalyst is prepared for this study. The operating pressure is selected to be 500 mbar and the reactive gas mixtures are diluted in Ar gas. The boundary-layer profiles of the species are measured under steady-state conditions.

CPOx of C_3H_8

CPOx of C_3H_8 has been studied under varying C/O ratios and temperatures. The fuel composition is chosen to yield stoichiometric, fuel-lean or fuel-rich conditions for the partial oxidation reaction.

$$\mathrm{C_3H_8} + \frac{3}{2}\mathrm{O_2} \rightarrow 3\mathrm{CO} + 4\mathrm{H_2} \qquad \Delta_\mathrm{R}\mathrm{H}^\mathrm{o} = -227.6\ \mathrm{kJ/mol} \tag{5.37}$$

The total gas flow rate is measured to be 16.1 SLPM, which corresponds to an axial flow velocity of 53 cm/s at 313 K at the reactor inlet. To avoid gas-phase reactions, the surface reaction temperature is kept below 973 K which is lower than the ignition temperature of gas-phase reactions. The experimental conditions which are investigated are listed as a case study in Table 5.14 . The orders of the reactions are given according to how they were conducted in reality.

Table 5.14. Experimental conditions for CPOx of C_3H_8.

Case	ReactionTemp. [K]	% vol. C_3H_8	%vol. O_2	C/O
1	823	6.06	9.04	1.01
2	873	6.06	9.04	1.01
3	883	6.60	7.93	1.25
4	933	5.70	8.85	0.97
5	933	4.87	9.56	0.76
6	933	6.63	8.09	1.23

The boundary-layer concentration profiles of O_2, H_2, CO, CO_2, CH_4, C_2H_6, C_2H_4, C_2H_2, and C_3H_8 species are detected simultaneously by means of the MS (for O_2), H-Sense (for H_2), and FTIR (for C containing species). Detailed information about the measurement technique is given in Chapter 3.1.5.

SR of C_3H_8

SR of C_3H_8 studied under stoichiometric conditions (S/C ratio of 1) at the surface temperature of 883 and 923 K.

$$\mathrm{C_3H_8 + 3H_2O \rightarrow 3CO + 7H_2} \qquad \Delta_\mathrm{R}\mathrm{H^o} = 498\ \mathrm{kJ/mol} \tag{5.38}$$

11.2 µl/min water is fed to the evaporator. The gas feeding lines and the evaporator are heated up to 423 K to avoid a possible condensation of the water. The total flow rate is calculated to be 18.9 SLPM that corresponds to an axial gas velocity of 77 cm/s at the stagnation-flow reactor inlet at 423 K.

Table 5.15. Reaction conditions for SR of C_3H_8.

Case	Reaction temp. [K]	vol.% C_3H_8	vol.%H_2O	S/C
1	883	2.45	7.38	1.00
2	923	2.44	7.42	0.99

5.6.3 Results and Discussion

Numerical Model

The surface reaction mechanism which was previously presented in Table 5.12 is extended by including propane and its surface reaction steps into the reaction scheme. The study of Hartmann et al. is taken as a reference for the elementary-step reactions of C_3H_8 and their enthalpy values [88]. 14 surface reaction steps of the adsorption, desorption and the dehydrogenation steps of C_3H_8 are included (Table 5.16). The kinetic parameters are re-evaluated on the basis of the stagnation-flow reactor data.

Table 5.16. Surface reactions of C_3H_8.

	Reaction	$A^{\dagger}$(cm, mol,s)	β(-)‡	Ea(kJ/mol)
R1	$C_3H_8 + Rh(s) \longrightarrow C_3H_8(s)$	2.000×10^{-2b}	stick. coeff.	
R2	$C_3H_8(s) \longrightarrow C_3H_8 + Rh(s)$	1.000×10^{13}	-0.500	30.10
R3	$C_3H_8(s) + Rh(s) \longrightarrow C_3H_7(s) + H(s)$	1.300×10^{21}	0.000	52.00
R4	$C_3H_7(s) + H(s) \longrightarrow C_3H_8(s) + Rh(s)$	1.349×10^{21}	0.156	46.77
R5	$C_3H_7(s) + Rh(s) \longrightarrow C_3H_6(s) + H(s)$	5.028×10^{21}	-0.118	84.05
R6	$C_3H_6(s) + H(s) \longrightarrow C_3H_7(s) + Rh(s)$	2.247×10^{22}	0.115	65.25
R7	$C_3H_8(s) + O(s) \longrightarrow C_3H_7(s) + OH(s)$	7.895×10^{24}	-0.124	69.65
R8	$C_3H_7(s) + OH(s) \longrightarrow C_3H_8(s) + O(s)$	1.087×10^{24}	0.124	33.24
R9	$C_3H_7(s) + O(s) \longrightarrow C_3H_6(s) + OH(s)$	1.276×10^{22}	-0.162	88.97
R10	$C_3H_6(s) + OH(s) \longrightarrow C_3H_7(s) + O(s)$	1.875×10^{20}	0.162	45.03
R11	$C_3H_6(s) + Rh(s) \longrightarrow C_2H_3(s) + CH_3(s)$	1.370×10^{24}	-0.280	94.63
R12	$C_2H_3(s) + CH_3(s) \longrightarrow C_3H_6(s) + Rh(s)$	9.113×10^{24}	0.279	44.88
R13	$C_2H_3(s) + Rh(s) \longrightarrow CH_3(s) + C(s)$	1.370×10^{22}	-0.280	46.53
R14	$CH_3(s) + C(s) \longrightarrow C_2H_3(s) + Rh(s)$	1.563×10^{23}	0.280	$107.78 - 120\theta_{CO}$

The rate coefficients are given in the form of $k = AT^{\beta} \exp(-E_a/RT)$; adsorption kinetics is given in the form of sticking coefficients; the surface site density is $\Gamma = 2.72 \times 10^{-9}$ mol cm^{-2}

Compared to the study of Hartmann et al. [88], the adsorption rate of C_3H_8 is increased by increasing the sticking coefficient of C_3H_8 by 3 orders of magnitude (Table 5.16). The desorption rate parameters have not been altered, and thus, the reaction rate of the consumption of C_3H_8 was increased. The enthalpy values of each reaction step differs from the reaction mechanism of Hartmann et al. [88]. However, the thermodynamic consistency has been ensured in entalphic manner as well. The surface reaction mechanism for C_1 and C_3 species is presented in Appendix A, Table 1.

According to the presented surface reaction mechanism, no gas-phase C_2H_2, C_2H_4 and C_3H_6 species are produced. This was confirmed experimentally since no by-product, except CH_4 was detected.

CH_4 is formed at the ppm level during CPOx and SR reactions. A similar conclusion was drawn in the literature as well [241, 244, 246]. According to the reaction mechanism presented (Table 5.16), the main source of the methanation is the adsorbed CH_3 species that reacts with adsorbed hydrogen and forms methane. The concentration of the gas-phase CH_4 is sensitive to decomposition of $C_3H_6(s)$ (R11) by which $CH_3(s)$ and $C_2H_3(s)$ species are formed.

CPOx of C_3H_8

A comparison of the numerical simulations and the experimental data is presented in Figure 5.48-5.51 At 823 K and for C/O =1.0 (Case-1) no partial oxidation activity was detected. The only reaction products measured on the catalyst surface are the total oxidation products, i.e., CO_2 and H_2O. This was confirmed by numerical simulations as well. The boundary-layer was not completely resolved. However, the numerical simulation of complete boundary-layer is presented here (Figure 5.47).

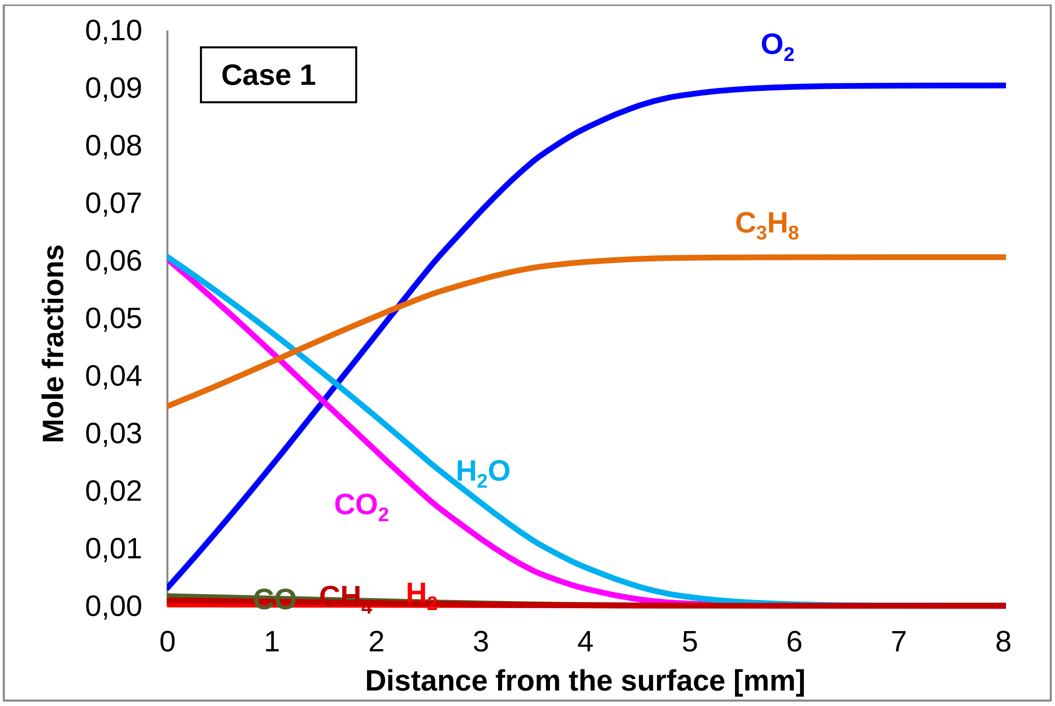

Figure 5.47. Numerical simulations of CPOx of C_3H_8 at 823 K. Inlet mole 6.06 vol.% C_3H_8 and 9.04 vol.% O_2 in Ar dilution. Inlet gas velocity is 53 cm/s. $F_{cat/geo}$ is assumed to be 1.0.

Increasing the reaction temperature to 873 K (Case 2) does not have a significant influence on the reaction rate of C_3H_8. However, product distribution significantly changes and the reaction yields the partial oxidation products, i.e., CO and H_2.

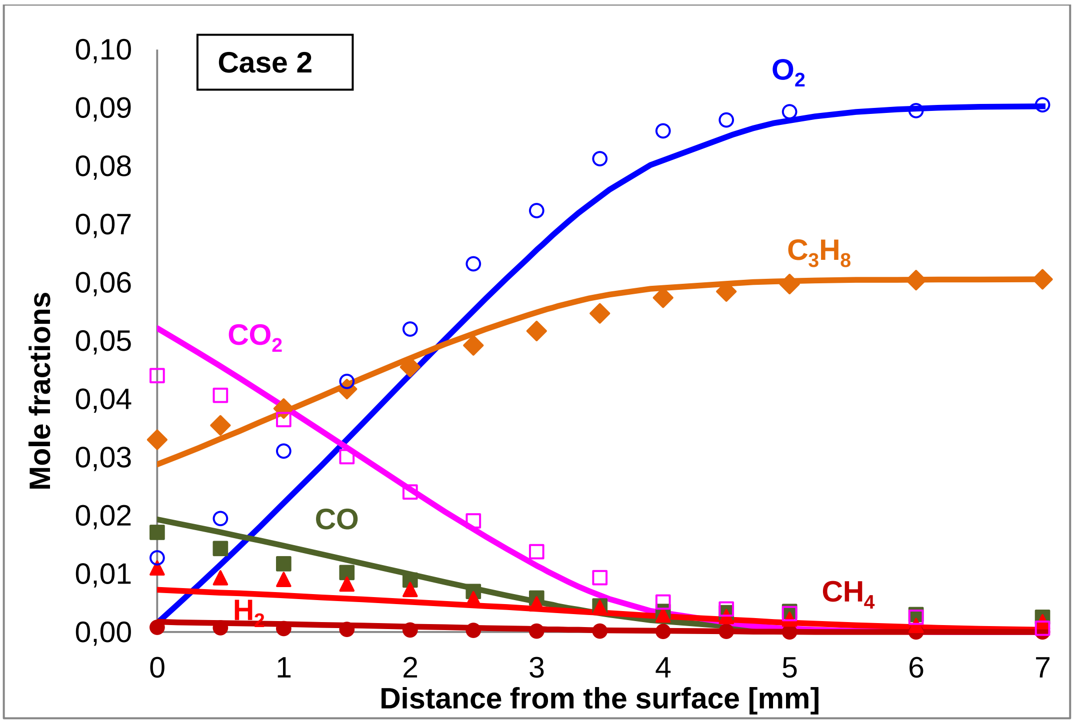

Figure 5.48. Comparison of the numerical simulations (lines) and the experimental data (symbols) of CPOx of C_3H_8 at 873 K. The inlet mole composition is chosen to be 6.06 vol.% C_3H_8 and 9.04 vol.% O_2 diluted in Ar (C/O=1.01, Case 2). The axial flow velocity at the reactor inlet is 53 cm/s at 313 K. $F_{cat/geo}$ is assumed to be 2.4.

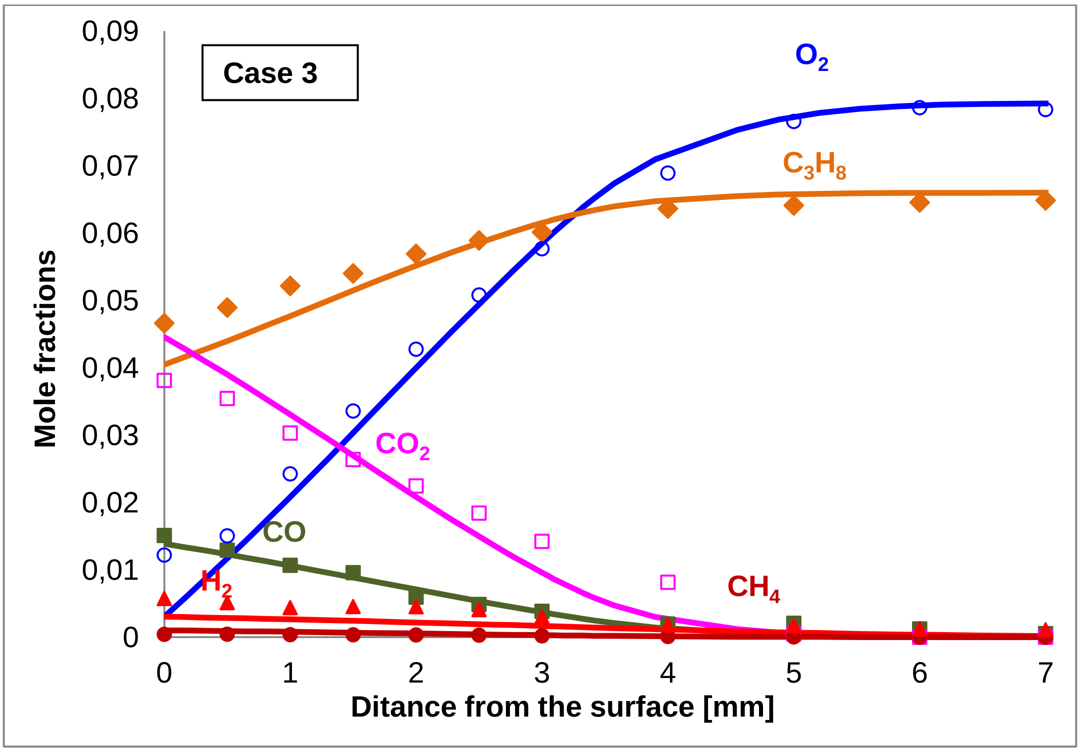

Figure 5.49. Comparison of the numerical (lines) and experimenta (symbols) values of CPOx of C_3H_8 at 883 K. The inlet mole composition is chosen to be 6.60 vol.% C_3H_8 and 7.93 vol.% O_2 diluted in Ar (C/O=1.25, Case-3). The axial flow velocity at the reactor inlet is 53 cm/s at 313 K. $F_{cat/geo}$ is assumed to be 1.

The effect of the inlet fuel composition on CPOx of C_3H_8 is investigated by varying the C/O ratios. A fuel-rich condition (Case 3) is selected and the reaction is carried out at 873 K with C/O=1.25 (Figure 5.49). Under these conditions, the reaction is mass transport limited because O_2 is completely consumed on the catalyst surface and the consumption of C_3H_8 is decreased compared to Case 2. However, the formation rate of the products and their selectivities do not vary significantly as that of Case 2. Total combustion products of CO_2 and H_2O are the main reaction products. The methane formation rate is also in the same range with Case-2. The main influence of decreasing the oxygen ratio is the rate of carbon formation on the surface. The formation of surface carbon and the deactivation of Rh surface were also observed experimentally by Huff et al. [243].

After a change in the reaction conditions between Case 2 and Case 3, steady-state conditions are achieved after 1h. which is a considerably long reaction time. After the first 30 min., the mole fractions on the catalyst surface were measured. A sharp decrease in H_2 and CO mole fractions and a slight increase in C_3H_8 mole fraction were noticed. The reactor was held at these conditions for a further 30 min. After the boundary-layer was completely resolved, the microprobe was positioned at the catalyst surface again, and the mole composition was measured. By doing so, possible deviations in the boundary-layer mole fractions of the speices which are due to the deactivation during the measurements, were eliminated.

The formation of carbon on the surface physically results in a color change on the catalyst surface as black spots appear on the catalyst surface. It is believed that, a fast deactivation of the catalyst occurs at the beginning of the reaction within the first 30-40 min., afterwards, the reaction is stable and no further catalyst deaction takes place. As result of the deactivation of the active metal surface area, $F_{\mathrm{cat/geo}}$ which is used in numerical simulations is decreased from 2.4 to 1.0.

Prior to the next measurements, the catalyst is regenerated. In contrast to the regeneration procedure previously discussed in Chapter 3.1.5, the oxidation and the reduction time are extended to 1h. Further measurements are carried out to examine the effect of the reaction temperature on the product selectivity (Cases 4-6).

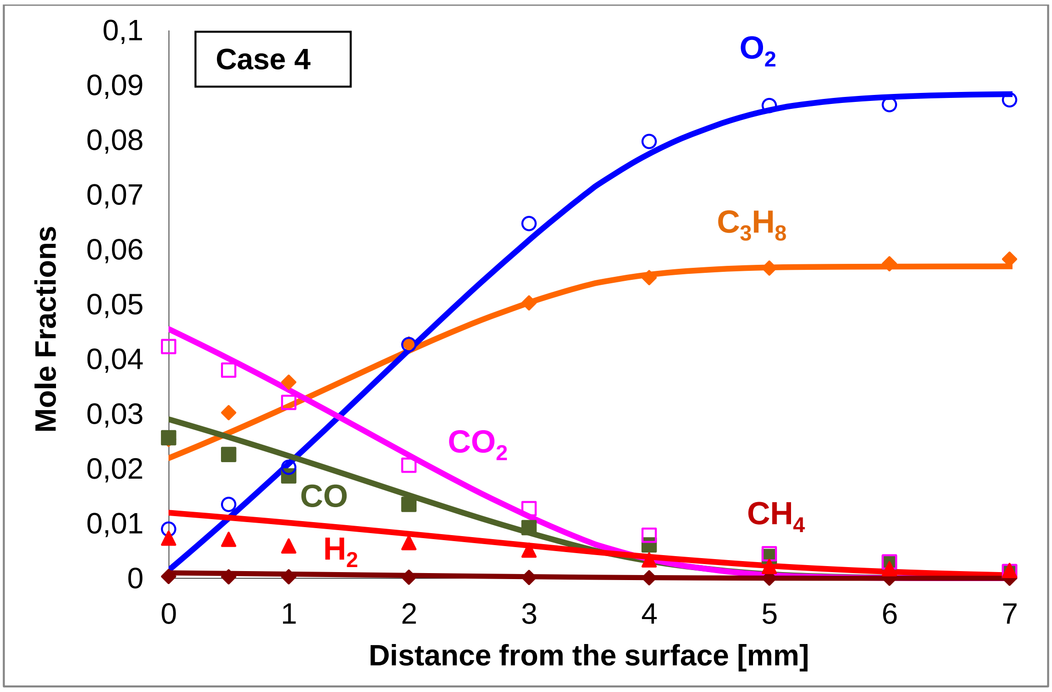

Figure 5.50. Comparison of the numerical (lines) and the experimental data (symbols) of CPOx of C_3H_8 at 933 K. The inlet mole composition is selected to be 5.70 vol.% C_3H_8 and 8.85 vol.% O_2 diluted in Ar (C/O=0.97, Case 4). The axial flow velocity at the reactor inlet is 53 cm/s at 313 K. $F_{cat/geo}$ is assumed to be 1.0.

As expected, increasing the reaction temperature increases the synthesis gas yield. Although no large influence on the consumption rate of C_3H_8 was observed, the major difference between Case 2 and Case 4 is in the measured gas-phase CO concentration.

CO_2 concentration does not change significantly whereas H_2O concentration slightly decreases; 6.4 vol.% H_2O and 5.2 vol.% H_2O are calculated on the catalyst surface in Case 2 and Case 4 respectively. Therefore, during partial oxidation, a steam reforming reaction of C_3H_8 also takes place at 883 K.

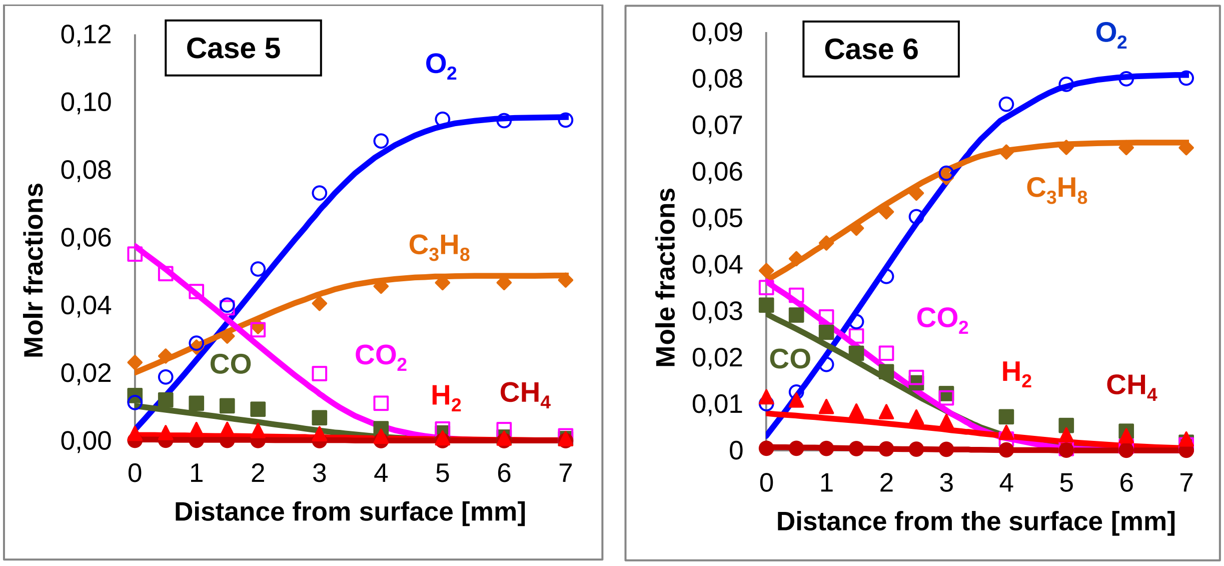

Figure 5.51. Comparison of the numerical (lines) and experimental data (symbols) of CPOx of C_3H_8 at 933 K. The inlet mole composition is selected to be 4.87 vol.% C_3H_8 and 9.56 vol.% O_2 diluted in Ar (C/O=0.76, Case 5) and 6.63 vol.% C_3H_8 and 8.09 vol.% O_2 diluted in Ar (C/O=1.23, Case 6). The axial flow velocity at the reactor inlet is 53 cm/s at 313 K for both cases. $F_{cat/geo}$ is assumed to be 1.0.

Taking Case 4 as a baseline condition for 933 K, further measurements are carried out at varying fuel/oxygen ratios. The synthesis gas production yield is decreased by increasing the oxygen amount (Case 5, C/O=0.76) because the reaction yields more total oxidation producs (CO_2, H_2O) than synthesis gas. The reaction rate of consumption of C_3H_8 is increased and the oxygen is completely consumed at the catalyst surface. If fuel-rich conditions is studied (Case 6, C/O=1.23), the synthesis gas production rate is slightly increased. Compared to Case 4, a slight increase in CO and H_2 concentrations is detected.

For all reaction conditions examined, good agreement is achieved between the experimental and the numerical data. CH_4 is measured to be the only by-product.
Under the reaction conditions investigated, the optimum operating conditions for CPOx of C_3H_8 are defined in Case 4 in which the reaction is carried out with a stoichimoteric amount of fuel and oxygen (C/O=1.0) at 933 K. Although a higher synthesis gas production was observed for fuel-rich conditions (Case 6), the reaction suffers from the deactivation of active metal which is due to the formation of surface carbon.

Steam Reforming of C_3H_8

SR of C_3H_8 is studied at 883 and 923 K under stoichiometric conditions. The stagnation-flow reactor data are used to predict the reaction rate parameters for the calculation of the exact reaction rates on the catalyst surface. Comparisons of the experimental data and the numerical simulations are presented in Figure 5.52 and Figure 5.53. The reaction mechanism (Appendix A, Table 1) is used without any modification.

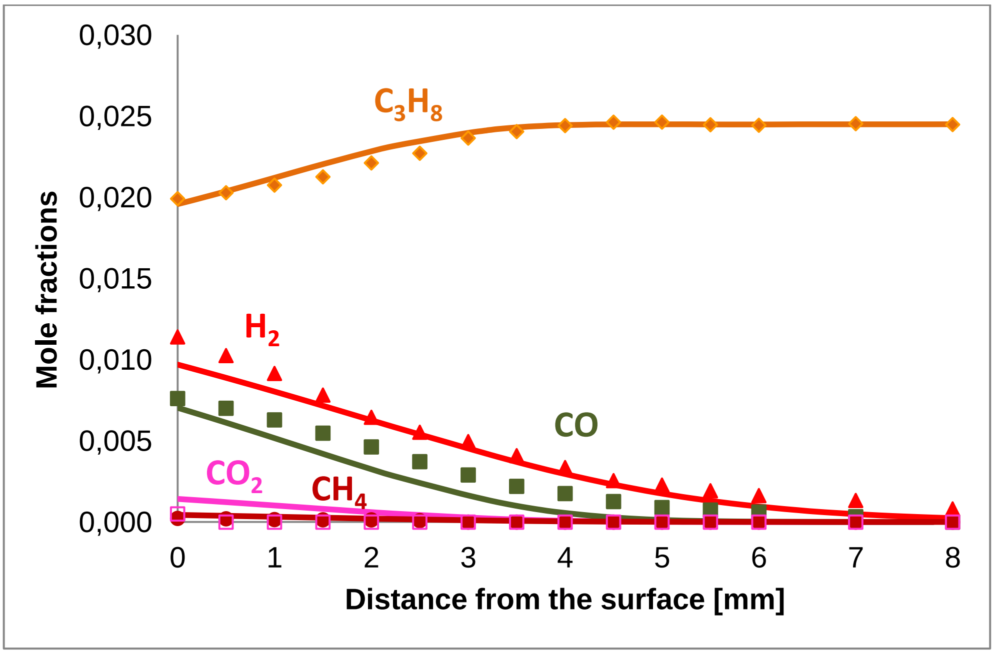

Figure 5.52. Comparison of numerical (lines) and experimental (symbols) values for SR of C_3H_8 at 883 K. The inlet mole composition is selected to be 2.45 vol.% C_3H_8 and 7.38 vol.% H_2O diluted in Ar. The axial flow velocity was measured to be 77 cm/s at 423 K. $F_{cat/geo}$ is assumed to be 1.0.

A high synthesis gas production rate is observed at both reaction temperatures investigated. The main reaction products are measured to be CO and H_2. CH_4 and CO_2 species are detected only as by-products at the ppm level. Similar to the CPOx measurements, no C_2H_2, C_2H_4 and C_3H_6 are detected. The boundary-layer was reached at maximum 6 mm for CO, C_3H_8. However, further measurements were carried out for H_2 by 8 mm.

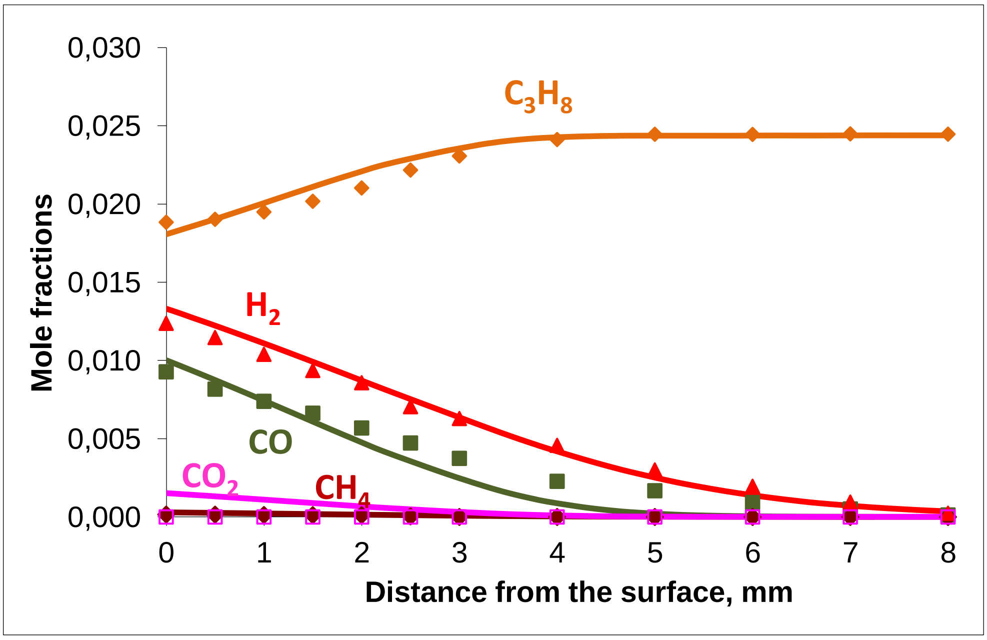

Figure 5.53. Comparison of the numerical (lines) and the experimental (symbols) data for SR of C_3H_8 at 923 K. The inlet mole composition is selected to be 2.45 vol.% C_3H_8 and 7.42 vol.% H_2O diluted in Ar. The axial flow velocity was measured to be 77 cm/s at 423 K. $F_{cat/geo}$ is assumed to be 1.0.

The reaction is kinetically limited for both cases (Table 5.15) since neither C_3H_8 nor H_2O are completely consumed at the catalyst surface. Increasing the reaction temperature increases the consumption rate of C_3H_8 and H_2O as well as the rate of synthesis gas production.
Although a good agreement between the experimental data and the numerical simulations is achieved, the model slightly overestimates the CO_2 concentration for both reaction conditions investigated. However, it is worth mentioning that the maximum CO_2 concentration predicted by the numerical simulations was at ppm level (~1500 at 923 K). Although CO_2 was also experimentally detected by the FTIR, no accurate data analysis was possible since the amount was under the detection limit of the analytic.

5.6.4 Conclusion

A new reaction kinetics is presented for silumation of partial oxidation and reforming of C_3H_8 (Appendix A, Table 1). The 1D steady-state stagnation-flow reactor data is used for the evaluation of the kinetic parameters. The reaction mechanism includes no formation of by-product such as C_2H_2, C_2H_4, C_2H_6 and C_3H_6, which is also experimentally confirmed under varying C/O and S/C ratios. CH_4 is the only by-product and it is only detected at ppm level. The decomposition of C_3H_6 is a sensitive reaction path for the formation of CH_4.
The studied reaction temperature is selected to be below 973 K to avoid ignition of possible gas-phase reactions [244] during CPOx and SR reactions. The experimental results indicate that the total oxidation (indirect path) as well as the partial oxidation (direct path) reactions takes place during CPOx of C_3H_8. At low temperatures, below 873 K,, the reaction yields only total oxidation products i.e., CO_2 and H_2O. Increasing the temperature also increase the synthesis gas production yield. The result indicate that steam reforming reaction also takes place during CPOx of C_3H_8 at 883 K and with C/O=1.0. At fuel-rich conditions at which C/O≤ 1.0, carbon formation was observed whicht causes the deactivation active metal. Under the reaction conditions investigated, the optimum operating conditions for CPOx of C_3H_8 are determined to be C/O=1.0 at 933 K. Although high energy cost, which are due to the endothermicity of the reaction, decrease the overall reaction efficiency, SR of C_3H_8 is more effective way for synthesis gas production.

Further investigations are necessary at high temperature regimes at which gas-phase reactions can be coupled with the surface reaction mechanism. Additionally, a crusial evaluation of the surface reaction mechanism in a continuous-flow reactor is higly recommended.

6. CONCLUSIONS AND OUTLOOK

The primary objective of this study was the development of thermodynamically consistent surface reaction kinetics for partial oxidation and reforming of methane and propane. A stagnation-flow reactor has been developed to study heterogeneous kinetics over a wide range of temperature. The reactor configuration allowed mathematical modeling of the system in 1D by coupling heterogeneous chemistry with diffusive and convective transport within the gas-phase boundary layer.

A stagnation disk was coated with Rh/Al_2O_3 catalyst by a spin-spray technique. Light microscopy, scanning electron microscopy, and transmission electron microscopy were applied to reveal the interaction between support and active phase. A new CO chemisorption TPD technique was developed for the measurement of the catalytic surface area of the stagnation disk. $F_{\mathrm{cat/geo}}$ was calculated based on the CO chemisorption data. This technique makes it possible to use a continuous-flow reactor set-up under atmospheric conditions without using any sophisticated apparatus, e.g., UHV. Furthermore, the technique enabled characterizing the entire catalyst structure before and after the catalytic test, whereby aging effects of the catalyst can be explored and integrated into the kinetics.

The experiments were conducted in the stagnation-flow reactor following a hierarchical approach. It means that, all possible reaction paths of partial oxidation and reforming of CH_4 and C_3H_8 were considered. The complexity of the reaction was augmented by increasing the complexity of the fuel type and the number of species in the reactive gas composition. This methodlogy is presented as a flow diagram in Figure 6.1.
Experimental conditions, i.e., fuel composition, flow rates and operating pressure by considering the detection ranges of the analytics as well as by ensuring the stagnation-flow regimes. Gas-phase reactions were eliminated by ensuring that the reaction temperature was below the ignition temperature of gas-phase reactions for each case. Therefore, only heterogeneous reactions were examined. Numerical simulations of the system were performed using CHEMKIN SPIN [69] and DETCHEM$^{\mathrm{STAG}}$ [58] softwares.

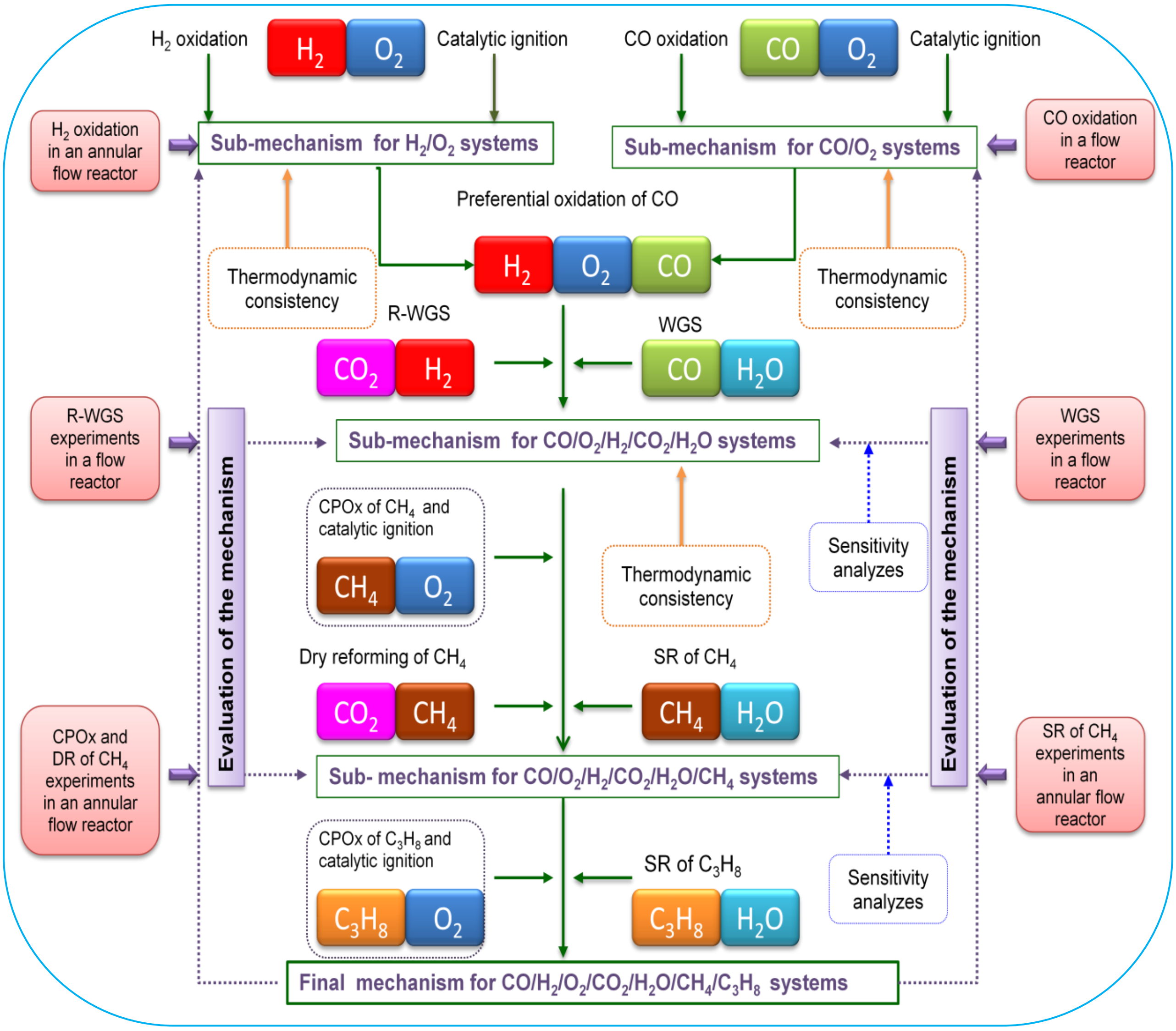

Figure 6.1. The methodology of the work

The catalytic ignition of the oxidation of H_2, CO, CH_4, C_2H_6, and C_3H_8 fuels was investigated under varying fuel/oxygen ratios in the stagnation-flow reactor. It has been shown that CO has a different ignition tendency than H_2, CH_4, C_2H_6, and C_3H_8. Increasing the CO ratio in the CO/O_2 feed composition results in an increase in the ignition temperature. However, an opposite trend was observed for H_2, CH_4, C_2H_6, and C_3H_8. That is, increasing the O_2 concentration in the feed results in an increase in the ignition temperature. This was explained by the different surface coverage tendencies of the fuels. In low O_2 concentrations, CO tends to easily cover the free adsorption site, which blocks the subsequent oxygen adsorption. Therefore, a coverage-dependent activation barrier for CO desorption has been introduced in the reaction kinetics. Furthermore, it has been shown that H_2 ignition shows an opposite trend on Rh than on Pt catalyst, because in the latter case, increasing the oxygen content shifts the ignition temperature to a lower value. The tendency of an increasing ignition temperature with increasing oxygen content in H_2/O_2 systems could further be explained by the surface poisoning effect of oxygen that blocked the subsequent hydrogen adsorption.

Firstly, an elementary-step-like surface reaction kinetics was presented for hydrogen oxidation. The reaction mechanism of Hartmannn et al. [88] and Schiwiedernoch et al. [33] was used as a reference for the reaction paths and the enthalpic values. The reaction kinetics was further improved based on the stagnation-flow reactor data under varying fuel/oxygen ratios over a wide range of temperature. The reaction rates were calculated and the kinetic parameters were altered. It has been shown that adsorption and desorption of H_2 and O_2 are critical steps in the reaction mechanism and the reaction mechanism is highly sensitive to OH and gas-phase H_2O species. A good agreement was shown between the stagnation-flow experimental data and the numerical simulations. Furthermore, the reaction kinetics was tested using DETCHEM^{CHANNEL} simulations for H_2 oxidation measurements by Tavazzi et al. [188], which were carried out in an annular type of reactor with different flow rates. A sub-mechanism for $H_2/O_2/Rh/Al_2O_3$ system is proposed.

Using the reaction mechanism of Hartmannn et al. [88] and Schwiedernoch et al. [33] as references, the complexity of the reaction mechanism was augmented by introducing CO, CO_2, and H_2O species into the mechanism. Firstly direct oxidation of CO was studied and a sub-mechansim for $CO/O_2/Rh/Al_2O_3$ system was presented. Furthermore, preferential oxidation of CO as well as WGS and R-WGS reactions were examined over a wide range of operating condition (fuel/oxygen ratio, temperature). The formation of the carboxyl intermediate species (COOH) and its elementary-step-like reactions were introduced to improve the WGS and R-WGS reaction behavior of the reaction mechanism at low temperatures, below 873 K. The rate parameters of the reaction steps were estimated by UBI-QUEP techniques [224, 238] Furthermore, the adsorption and desorption rate parameters of CO_2 were altered. It has been shown that for the WGS reactions, CO_2 is mainly formed via dissociation of carboxyl species (COOH) at low temperature regimes, whereas at high temperature regimes, direct oxidation of CO by adsorbed oxygen is favored. On the other hand, the effect of carboxyl species on the R-WGS reaction rate is crucial because the CO concentration was highly effected by the formation COOH species.
The reaction kinetics was also tested by numerical simulations of the continuous-flow reactor data of CO oxidation as well as WGS and R-WGS reactions, in which a technical Rh/Al_2O_3 catalyst was used in a channel configuration. The DETCHEM^{CHANNEL} software was used for the simulations.

CPOx, SR, and DR of CH_4 have been studied in order to develop a reaction kinetics for oxidation and reforming of methane. The results showed that the introduction of the formation of carboxyl species (COOH) into the reaction mechanism has a significant, positive effect on the predictability of the selectivity of CO and CO_2 in CPOx. Numerical simulations confirmed the spatial profile measurements of the species along the catalyst bed by Horn et al. [34] and Nogare et al. [35]. That is, the formation of partial oxidation products follows the combination of the direct and the indirect path [33-35, 137]. A small amount of H_2 and CO is formed in the oxidation zone, in which total oxidation products, i.e., CO_2 and H_2O, are also formed. Further downstream, a reforming zone exists, in which steam reforming of CH_4 takes place, which yields CO and H_2. The WGS reaction may also take place (depending on the reaction condition). Aside from the good agreement regarding the prediction of the synthesis gas mole concentrations, the formation of a side product (CH_4) was also predicted correctly. It was concluded that CH_4 is formed in the reforming zone, in which WGS and R-WGS reactions take place.

SR reaction path analyses were performed based on the sensitivity analyses at different reaction temperatures. The results showed that the rate-determining steps are the adsorption, desorption, and dehydrogenation steps of CH_4. The H_2O concentration does not have a large influence on the concentration of gas-phase CO at high temperatures (> 773 K). However, at temperatures below 773 K, the reaction is sensitive to the formation of the carboxyl species (COOH) and to the H_2O concentration. Furthermore, it has been shown that the SR reaction follows the path of the R-WGS reaction. CO is formed by the decomposition of the carboxyl intermediate. The hydrogen concentration has a significant effect on the concentration of gas-phase CO, because the formation of COOH is favored by the reaction of $\mathrm{CO_2}(s) + \mathrm{H}(s) \rightarrow \mathrm{COOH}(s) + \mathrm{Rh}(s)$. Reaction path analys showed that there is no significant effect on the formation of CO by $\mathrm{CO_2}(s) + \mathrm{H}(s) \rightarrow \mathrm{CO}(s) + \mathrm{OH}(s)$ or by direct oxidation (by adsorbed oxygen).

The proposed reaction kinetics was tested for CPOx, SR, and DR reactions carried out in an annular type of reactor under steady-state conditions over a wide range of temperature [216]. Eventually, a thermodynamically consistent reaction mechanism is presented for $H_2/O_2/CO/CO_2/H_2O/CH_4/Rh/Al_2O_3$ sub-systems.

The reaction mechanism was further extended to C_3H_8. The study of Hartmann et al. [88] was taken as a reference; in this study, the reaction mechanism includes the adsorption, desorption, and dehydrogenation reaction steps of C_xH_y species. No by-product formation, i.e., C_2H_2, C_2H_4, C_2H_6 and C_3H_6, is included in the reaction path.
CPOx and SR reactions of propane were conducted in the stagnation-flow reactor. The reaction temperature was chosen to be lower than 973 K so that gas-phase reactions were eliminated [244].

Fuel-lean and fuel-rich conditions were examined for CPOx of propane. The experimental results indicated that, the synthesis gas production starts at temperatures above 873 K. Increasing the reaction temperature results in an increase in the synthesis gas yield. Steam reforming of C_3H_8 also took place during CPOx of C_3H_8 at 883 K for C/O=1.0 because the reaction products showed an increase in H_2 concentration together with a decrease in C_3H_8 and H_2O mole fractions on the catalyst surface. This result can be interpreted as evidence of an indirect path together with the direct oxidation path during the CPOx of C_3H_8.
Under fuel-rich conditions (C/O≤ 1.0), deactivation of the catalyst occured due to the surface carbon formation. The surface carbon formation physically appeared on the catalyst surface as black spots. Although, the consumption rate of oxygen did not vary, it is completely consumed on the catalyst surface, the selectivity of the synthesis gas was decreased because the reaction fovoured more total oxidation products (i.e., H_2O, CO_2) than synthesis gas. It is believed that a fast deactivation of the catalyst occurred within the first 30-40 min. after the beginning of the reaction. Afterwards, the reaction was stable and no further catalyst deactivation took place.

Under the reaction conditions investigated, it has been shown that the optimum operating conditions for CPOx of C_3H_8 is C/O = 1.0 at 933 K. Furhermore, despite the high energy costs due to the endothermicity of the SR reaction, it has been shown that a higher synthesis gas production rate can be achieved by SR of C_3H_8 than by CPOx.

The experiments under varying C/O and S/C ratios confirmed that the only by-product is CH_4 at the ppm level. Further measurements of CPOx, SR, and DR of propane in a laboratory-scale continuous-flow reactor are highly recommended for the evaluation of the model.

The work presented here showed that a stagnation-flow reactor is a useful tool for studying reaction kinetics, as it facilitates one-dimensional modeling of the flow-field and zero-dimensional modeling of the surface kinetics. Although good agreement was presented between the experimental data and the numerical predictions, some uncertainties remain. The major open question in modeling the stagnation flow reactor is the effect of internal diffusion within the catalytic disk. Since the disk has a considerably high washcoat thickness, diffusion limitations may occur. However, so far, there are no tools avalaible for the resolution of concentration profiles inside the washcoat in both the numerical codes, CHEMKIN SPIN [69] and DETCHEM^{STAG} [58]. Only an effectiveness factor based on he Thile modulus is avalaible, which, however, is an estimation. In further applications, it will be necessary to introduce a detailed washcoat model for revealing the interaction between reaction kinetics and mass transport limitations. Furthermore, it has been shown that the catalyst prepared here differs from commercially-available ones because of its washcoat thickness and active metal dispersion. For future applications, an optimization of the catalyst coating is necessary. For future applications, an optimization of the catalyst coating is necessary. It is proposed to use a thinner alumina substrate for the optimization of the coating layer. By doing so, the heat transfer between the resistive heater and the catalyst surface can also be improved. Furthermore, together with the spatial profile measurement of the species within the boundary-layer, temperature profile measurement can be conducted in the reactor. Although only heterogeneous reactions have been considered here, the stagnation-flow reactor can be used to investigate gas-phase reactions as coupled with heterogenous reactions in high-temperature catalysis. Furthermore, the stagnation-flow reactor constructed here has been configured to allow optical access, thus, an in-situ measurement technique (i.e., laser Raman spectroscopy) can be implemented.

A detailed investigation of carbon formation is necessary to understand the deactivation process of the catalyst and its effect on the synthesis gas production. A dynamic measurement of CPOx of C_3H_8 and a detailed investigation of the surface by scanning electron microscopy and transmission electron microscopy are recommended.

The reaction mechanism can also be validated against complex reactive systems such as oxidative steam reforming of CH_4 and C_3H_8, in which CPOx and SR reactions are simultaneously generated.

Following the hierarchical approach presented here, the reaction mechanism can be extended to oxygenated fuels and higher hydrocarbons, i.e., ethanol, methanol and iso-octane.

Appendix

Table 1. Proposed reaction mechanism for C_1-C_3 species.

	Reaction	$A^{\dagger}$(cm, mol,s)	$\beta(-)^{\ddagger}$	Ea(kj/mol)
R1	$H_2 + Rh(s) + Rh(s) \longrightarrow H(s) + H(s)$	3.000×10^{-2b}	stick. coeff.	
R2	$O_2 + Rh(s) + Rh(s) \longrightarrow O(s) + O(s)$	1.000×10^{-2b}	stick. coeff.	
R3	$H_2O + Rh(s) \longrightarrow H_2O(s)$	1.000×10^{-1b}	stick. coeff.	
R4	$CO_2 + Rh(s) \longrightarrow CO_2(s)$	4.800×10^{-2b}	stick. coeff.	
R5	$CO + Rh(s) \longrightarrow CO(s)$	4.971×10^{-1b}	stick. coeff.	
R6	$CH_4 + Rh(s) \longrightarrow CH_4(s)$	1.300×10^{-2b}	stick.coeff.	
R7	C_3H_8+ Rh(s) $C_3H_8(s)$	2.000×10^{-2b}	stick.coeff.	
R8	$H(s) + H(s) \longrightarrow Rh(s) + Rh(s) + H_2$	5.574 x1 0^{19}	0.239	59.69
R9	$O(s) + O(s) \longrightarrow Rh(s) + Rh(s) + O_2$	5.329×10^{22}	-0.137	387.00
R10	$H_2O(s) \longrightarrow H_2O + Rh(s)$	6.858×10^{14}	-0.280	44.99
R11	$CO(s) \longrightarrow CO + Rh(s)$	1.300×10^{13}	0.295	$134.07-47\theta_{CO}$
R12	$CO_2(s) \longrightarrow CO_2 + Rh(s)$	3.920×10^{11}	0.315	20.51
R13	$CH_4 (s) \longrightarrow CH_4 + Rh(s)$	1.523×10^{13}	-0.110	26.02
R14	$C_3H_8(s) \longrightarrow C_3H_8 + Rh(s)$	1.000×10^{13}	-0.500	30.10
R15	$H(s) + O(s) \longrightarrow OH(s) + Rh(s)$	8.826×10^{21}	-0.048	73.37
R16	$OH(s) + Rh(s) \longrightarrow H(s) + O(s)$	1.000×10^{21}	0.045	48.04
R17	$H(s) + OH(s) \longrightarrow H_2O(s) + Rh(s)$	1.743×10^{22}	-0.127	41.73
R18	$H_2O(s) + Rh(s) \longrightarrow H(s) + OH(s)$	5.408×10^{22}	0.129	98.22
R19	$OH(s) + OH(s) \longrightarrow H_2O(s) + O(s)$	5.735×10^{20}	-0.081	121.59
R20	$H_2O(s) + O(s) \longrightarrow OH(s) + OH(s)$	1.570×10^{22}	0.081	203.41
R21	$CO_2(s) + Rh(s) \longrightarrow CO(s) + O(s)$	5.752×10^{22}	-0.175	106.49
R22	$CO(s) + O(s) \longrightarrow CO_2(s) + Rh(s)$	6.183×10^{22}	0.034	$129.98-47\ \theta_{CO}$
R23	$CO(s) + Rh(s) \longrightarrow C(s) + O(s)$	6.390×10^{21}	0.000	$174.76-47\ \theta_{CO}$
R24	$C(s) + O(s) \longrightarrow CO(s) + Rh(s)$	1.173×10^{22}	0.000	92.14
R25	$CO(s) + OH(s) \longrightarrow COOH(s) + Rh(s)$	2.922×10^{20}	0.000	$55.33-47\ \theta_{CO}$
R26	$COOH(s) + Rh(s) \longrightarrow CO(s) + OH(s)$	2.738×10^{21}	0.000	48.38
R27	$COOH(s) + Rh(s) \longrightarrow CO_2(s) + H(s)$	1.165×10^{19}	0.160	5.61
R28	$CO_2(s) + H(s) \longrightarrow COOH(s) + Rh(s)$	1.160×10^{20}	-0.160	14.48
R29	$COOH(s) + H(s) \longrightarrow CO(s) + H_2O(s)$	5.999×10^{19}	-0.188	33.55
R30	$CO(s) + H_2O(s) \longrightarrow COOH(s) + H(s)$	2.258×10^{19}	0.051	$97.08-47\ \theta_{CO}$
R31	$CO(s) + OH(s) \longrightarrow CO_2(s) + H(s)$	3.070×10^{19}	0.000	$82.94-47\ \theta_{CO}$
R32	$CO_2(s) + H(s) \longrightarrow CO(s) + OH(s)$	2.504×10^{21}	-0.301	84.77
R33	$C(s) + OH(s) \longrightarrow CO(s) + H(s)$	4.221×10^{20}	0.078	30.04
R34	$CO(s) + H(s) \longrightarrow C(s) + OH(s)$	3.244×10^{21}	-0.078	$138.26-47\ \theta_{CO}$
R35	$CH_4(s) + Rh(s) \longrightarrow CH_3(s) + H(s)$	4.622×10^{21}	0.136	72.26
R36	$CH_3(s) + H(s) \longrightarrow CH_4(s) + Rh(s)$	2.137×10^{21}	-0.058	46.77
R37	$CH_3(s) + Rh(s) \longrightarrow CH_2(s) + H(s)$	1.275×10^{24}	0.078	107.56
R38	$CH_2(s) + H(s) \longrightarrow CH_3(s) + Rh(s)$	1.073×10^{22}	-0.078	39.54
R39	$CH_2(s) + Rh(s) \longrightarrow CH(s) + H(s)$	1.275×10^{24}	0.078	115.39
R40	$CH(s) + H(s) \longrightarrow CH_2(s) + Rh(s)$	1.073×10^{22}	-0.078	52.61
R41	$CH(s) + Rh(s) \longrightarrow C(s) + H(s)$	1.458×10^{20}	0.078	23.09
R42	$C(s) + H(s) \longrightarrow CH(s) + Rh(s)$	1.122×10^{23}	-0.078	$170.71-120\ \theta_{C}$
R43	$CH_4(s) + O(s) \longrightarrow CH_3(s) + OH(s)$	3.465×10^{23}	0.051	77.71
R44	$CH_3(s) + OH(s) \longrightarrow CH_4(s) + O(s)$	1.815×10^{22}	-0.051	26.89
R45	$CH_3(s) + O(s) \longrightarrow CH_2(s) + OH(s)$	4.790×10^{24}	0.000	114.52
R46	$CH_2(s) + OH(s) \longrightarrow CH_3(s) + O(s)$	2.858×10^{21}	0.000	20.88
R47	$CH_2(s) + O(s) \longrightarrow CH(s) + OH(s)$	4.790×10^{24}	0.000	141.79
R48	$CH(s) + OH(s) \longrightarrow CH_2(s) + O(s)$	2.858×10^{21}	-0.000	53.41
R49	$CH(s) + O(s) \longrightarrow C(s) + OH(s)$	5.008×10^{20}	0.000	26.79
R50	$C(s) + OH(s) \longrightarrow CH(s) + O(s)$	2.733×10^{22}	0.000	$148.81-120\ \theta_{C}$
R51	$C_3H_8(s) + Rh(s) \longrightarrow C_3H_7(s) + H(s)$	2.000×10^{-2b}	0.000	52.00

R52	$C_3H_7(s) + H(s) \longrightarrow C_3H_8(s) + Rh(s)$	1.000×10^{13}	0.156	46.77
R53	$C_3H_7(s) + Rh(s) \longrightarrow C_3H_6(s) + H(s)$	1.300×10^{21}	-0.118	84.05
R54	$C_3H_6(s) + H(s) \longrightarrow C_3H_7(s) + Rh(s)$	1.349×10^{21}	0.115	65.25
R55	$C_3H_8(s) + O(s) \longrightarrow C_3H_7(s) + OH(s)$	5.028×10^{21}	-0.124	69.65
R56	$C_3H_7(s) + OH(s) \longrightarrow C_3H_8(s) + O(s)$	2.247×10^{22}	0.124	33.24
R57	$C_3H_7(s) + O(s) \longrightarrow C_3H_6(s) + OH(s)$	7.895×10^{24}	-0.162	88.97
R58	$C_3H_6(s) + OH(s) \longrightarrow C_3H_7(s) + O(s)$	1.087×10^{24}	0.162	45.03
R59	$C_3H_6(s) + Rh(s) \longrightarrow C_2H_3(s) + CH_3(s)$	1.276×10^{22}	-0.280	94.63
R60	$C_2H_3(s) + CH_3(s) \longrightarrow C_3H_6(s) + Rh(s)$	1.875×10^{20}	0.279	44.88
R61	$C_2H_3(s) + Rh(s) \longrightarrow CH_3(s) + C(s)$	1.370×10^{24}	-0.280	46.53
R62	$CH_3(s) + C(s) \longrightarrow C_2H_3(s) + Rh(s)$	9.113×10^{24}	0.280	$107.78-120\ \theta_C$

The rate coefficients are given in the form of $k = AT^{\beta} \exp(-E_a/RT)$; adsorption kinetics is given in the form of sticking coefficients; the surface site density is $\Gamma = 2.72 \times 10^{-9}$ mol cm^{-2}

Table 2. Thermodynamic data for the surface and gas-phase species used in this work.

```
AR                120186AR  1               G  0300.00   5000.00  1000.00      1
 0.02500000E+02 0.00000000E+00 0.00000000E+00 0.00000000E+00 0.00000000E+00    2
-0.07453750E+04 0.04366001E+02 0.02500000E+02 0.00000000E+00 0.00000000E+00    3
 0.00000000E+00 0.00000000E+00-0.07453750E+04 0.04366001E+02                   4
N2                121286N   2               G  0300.00   5000.00  1000.00      1
 0.02926640E+02 0.01487977E-01-0.05684761E-05 0.01009704E-08-0.06753351E-13    2
-0.09227977E+04 0.05980528E+02 0.03298677E+02 0.01408240E-01-0.03963222E-04    3
 0.05641515E-07-0.02444855E-10-0.01020900E+05 0.03950372E+02                   4
Rh(s)                   Rh  1               S    300.0    3000.0  1000.0       1
 0.00000000E+00 0.00000000E+00 0.00000000E+00 0.00000000E+00 0.00000000E+00    2
 0.00000000E+00 0.00000000E+00 0.00000000E+00 0.00000000E+00 0.00000000E+00    3
 0.00000000E+00 0.00000000E+00 0.00000000E+00 0.00000000E+00                   4
O(s)               92491O   1Rh  1          I    300.00   3000.00 1000.00      1
 0.19454180E+01 0.91761647E-03-0.11226719E-06-0.99099624E-10 0.24307699E-13    2
-0.14005187E+05-0.11531663E+02-0.94986904E+00 0.74042305E-02-0.10451424E-05    3
-0.61120420E-08 0.33787992E-11-0.13209912E+05 0.36137905E+01                   4
O2                121386O   2               G  0300.00   5000.00  1000.00      1
 0.03697578E+02 0.06135197E-02-0.01258842E-05 0.01775281E-09-0.01136435E-13    2
-0.01233930E+05 0.03189166E+02 0.03212936E+02 0.01127486E-01-0.05756150E-05    3
 0.01313877E-07-0.08768554E-11-0.01005249E+05 0.06034738E+02                   4
H(s)               92491H   1Rh  1          I    300.00   3000.00 1000.00      1
 0.10696996E+01 0.15432230E-02-0.15500922E-06-0.16573165E-09 0.38359347E-13    2
-0.50546128E+04-0.71555238E+01-0.13029877E+01 0.54173199E-02 0.31277972E-06    3
-0.32328533E-08 0.11362820E-11-0.42277075E+04 0.58743238E+01                   4
H2                121286H   2               G  0300.00   5000.00  1000.00      1
 0.02991423E+02 0.07000644E-02-0.05633829E-06-0.09231578E-10 0.01582752E-13    2
-0.08350340E+04-0.01355110E+02 0.03298124E+02 0.08249442E-02-0.08143015E-05    3
-0.09475434E-09 0.04134872E-11-0.01012521E+05-0.03294094E+02                   4
H2O                20387H   2O   1          G  0300.00   5000.00  1000.00      1
 0.02672146E+02 0.03056293E-01-0.08730260E-05 0.01200996E-08-0.06391618E-13    2
-0.02989921E+06 0.06862817E+02 0.03386842E+02 0.03474982E-01-0.06354696E-04    3
 0.06968581E-07-0.02506588E-10-0.03020811E+06 0.02590233E+02                   4
H2O(s)             92491O   1H   2Rh  1     I    300.00   3000.00 1000.00      1
 0.25803051E+01 0.49570827E-02-0.46894056E-06-0.52633137E-09 0.11998322E-12    2
-0.38302234E+05-0.17406322E+02-0.27651553E+01 0.13315115E-01 0.10127695E-05    3
-0.71820083E-08 0.22813776E-11-0.36398055E+05 0.12098145E+02                   4
OH(s)              92491O   1H   1Rh  1     I    300.00   3000.00 1000.00      1
 0.18249973E+01 0.32501565E-02-0.31197541E-06-0.34603206E-09 0.79171472E-13    2
-0.26685492E+05-0.12280891E+02-0.20340881E+01 0.93662683E-02 0.66275214E-06    3
-0.52074887E-08 0.17088735E-11-0.25319949E+05 0.89863186E+01                   4
CH4               121286C   1H   4          G  0300.00   5000.00  1000.00      1
 0.01683479E+02 0.01023724E+00-0.03875129E-04 0.06785585E-08-0.04503423E-12    2
-0.01008079E+06 0.09623395E+02 0.07787415E+01 0.01747668E+00-0.02783409E-03    3
 0.03049708E-06-0.01223931E-09-0.09825229E+05 0.01372219E+03                   4
CH4(s)                 0C   1H   4Rh  1     I    300.00   3000.00 1000.00      1
 0.30016165E+01 0.54084505E-02-0.40538058E-06-0.53422466E-09 0.11451887E-12    2
-0.32752722E+04-0.10965984E+02 0.12919217E+01 0.72675603E-02 0.98179476E-06    3
-0.20471294E-08 0.90832717E-13-0.25745610E+04-0.11983037E+01                   4
CO(s)                  0C   1O   1Rh  1     S    300.00   3000.00 1000.00      1
 0.47083778E+01 0.96037297E-03-0.11805279E-06-0.76883826E-10 0.18232000E-13    2
-0.32311723E+05-0.16719593E+02 0.48907466E+01 0.68134235E-04 0.19768814E-06    3
 0.12388669E-08-0.90339249E-12-0.32297836E+05-0.17453161E+02                   4
CO2(s)            081292C   1O   2Rh  1     I   300.00   3000.00  1000.00      1
 0.46900000E+00 0.62660000E-02 0.00000000E-00 0.00000000E-00 0.00000000E-00    2
-0.50458700E+05-0.45550000E+01 0.46900000E+00 0.62662000E-02 0.00000000E-00    3
 0.00000000E-00 0.00000000E-00-0.50458700E+05-0.45550000E+01                   4
```

```
CO                121286C   1O   1          G  0300.00   5000.00  1000.00      1
 0.03025078E+02 0.01442689E-01-0.05630828E-05 0.01018581E-08-0.06910952E-13    2
-0.01426835E+06 0.06108218E+02 0.03262452E+02 0.01511941E-01-0.03881755E-04    3
 0.05581944E-07-0.02474951E-10-0.01431054E+06 0.04848897E+02                   4
CO2               121286C   1O   2          G  0300.00   5000.00  1000.00      1
 0.04453623E+02 0.03140169E-01-0.01278411E-04 0.02393997E-08-0.01669033E-12    2
-0.04896696E+06-0.09553959E+01 0.02275725E+02 0.09922072E-01-0.01040911E-03    3
 0.06866687E-07-0.02117280E-10-0.04837314E+06 0.01018849E+03                   4
C(s)                   0C   1Rh  1          I    300.00   3000.00 1000.00      1
 0.15792824E+01 0.36528701E-03-0.50657672E-07-0.34884855E-10 0.88089699E-14    2
 0.99535752E+04-0.30240495E+01 0.58924019E+00 0.25012842E-02-0.34229498E-06    3
-0.18994346E-08 0.10190406E-11 0.10236923E+05 0.21937017E+01                   4
CH(s)                  0C   1H   1Rh  1     I    300.00   3000.00 1000.00      1
-0.48242472E-02 0.30446239E-02-0.16066099E-06-0.29041700E-09 0.57999924E-13    2
 0.22595219E+05 0.56677818E+01 0.84157485E+00 0.13095380E-02 0.28464575E-06    3
 0.63862904E-09-0.42766658E-12 0.22332801E+05 0.11452305E+01                   4
CH2(s)                 0C   1H   2Rh  1     I    300.00   3000.00 1000.00      1
 0.74076122E+00 0.48032533E-02-0.32825633E-06-0.47779786E-09 0.10073452E-12    2
 0.10443752E+05 0.40842086E+00-0.14876404E+00 0.51396289E-02 0.11211075E-05    3
-0.82755452E-09-0.44572345E-12 0.10878700E+05 0.57451882E+01                   4
CH3(s)                 0C   1H   3Rh  1     I    300.00   3000.00 1000.00      1
 0.30016165E+01 0.54084505E-02-0.40538058E-06-0.53422466E-09 0.11451887E-12    2
-0.32752722E+04-0.10965984E+02 0.12919217E+01 0.72675603E-02 0.98179476E-06    3
-0.20471294E-08 0.90832717E-13-0.25745610E+04-0.11983037E+01                   4
C3H7(s)                0C   3H   7Rh  1     I    300.00   3000.00 1000.00      1
 0.30016165E+01 0.54084505E-02-0.40538058E-06-0.53422466E-09 0.11451887E-12    2
-0.32752722E+04-0.10965984E+02 0.12919217E+01 0.72675603E-02 0.98179476E-06    3
-0.20471294E-08 0.90832717E-13-0.25745610E+04-0.11983037E+01                   4
C3H6(s)                0C   3H   6Rh  1     I    300.00   3000.00 1000.00      1
 0.30016165E+01 0.54084505E-02-0.40538058E-06-0.53422466E-09 0.11451887E-12    2
-0.32752722E+04-0.10965984E+02 0.12919217E+01 0.72675603E-02 0.98179476E-06    3
-0.20471294E-08 0.90832717E-13-0.25745610E+04-0.11983037E+01                   4
C2H3(s)                0C   2H   3Rh  1     I    300.00   3000.00 1000.00      1
 0.30016165E+01 0.54084505E-02-0.40538058E-06-0.53422466E-09 0.11451887E-12    2
-0.32752722E+04-0.10965984E+02 0.12919217E+01 0.72675603E-02 0.98179476E-06    3
-0.20471294E-08 0.90832717E-13-0.25745610E+04-0.11983037E+01                   4
C3H8(s)                0C   3H   8Rh  1     I    300.00   3000.00 1000.00      1
 0.30016165E+01 0.54084505E-02-0.40538058E-06-0.53422466E-09 0.11451887E-12    2
-0.32752722E+04-0.10965984E+02 0.12919217E+01 0.72675603E-02 0.98179476E-06    3
-0.20471294E-08 0.90832717E-13-0.25745610E+04-0.11983037E+01                   4
C3H8              120186C   3H   8          G  0300.00   5000.00  1000.00      1
 0.07525217E+02 0.01889034E+00-0.06283924E-04 0.09179373E-08-0.04812410E-12    2
-0.01646455E+06-0.01784390E+03 0.08969208E+01 0.02668986E+00 0.05431425E-04    3
-0.02126001E-06 0.09243330E-10-0.01395492E+06 0.01935533E+03                   4
COOH(s)                 C   1H   1O   2Rh  1I    300.00   3000.00 1000.00      1
 0.30016165E+01 0.54084505E-02-0.40538058E-06-0.53422466E-09 0.11451887E-12    2
-0.32752722E+04-0.10965984E+02 0.12919217E+01 0.72675603E-02 0.98179476E-06    3
-0.20471294E-08 0.90832717E-13-0.25745610E+04-0.11983037E+01                   4
```

List of Symbols

Symbol	Description	Unit
$A_{catalytic}$	catalytic surface area	m^{2}
$A_{geometric}$	gerometrical surface area	m^{2}
A_k	pre-exponential factor	cm, mol, s
C_i	concentration of species i	mol.m^{-3}
c_p	Specific enthalpy of the mixture	J.kg^{-1}
D_i	diffusion coefficient of species i	m^{2}·s^{-1}
D_{ij}	the multi-component diffusion coefficient of species i	m^{2}/s
D_i^T	thermal diffusion coefficient of i	m^{2}·s^{-1}
E_a	activation energy	kJ.mol^{-1}
$F_{\mathrm{cat/geo}}$	surface scaling factor	-
G_i	Gibb´s free energy of species i	kJmol^{-1}
h_i	specific entalph of species i	
J_i	diffusive flux of species i	
$k_{f\mathrm{k}}$	reaction rate coefficient	mol, m,s
M_i	molecluer weight of speices i	kg.mol^{-1}
M	moleculer weight of the mixture	kg.mol^{-1}
n_i	number of moles of species i	mol
N_A	Avogadro´s number	6.02x10^{23} mol^{-1}
N_g	number of gas-phase species	-
N_s	number of surface species	-
N_b	number of bulk species	*
p	pressure	Pa
r	radius	m
R	gas constant	8.314 J.(mol.K)$^{-1}$
$\dot{s}_i$	molar reaction rate of species i	mol.m^{-2}.s^{-1}
T	temperature	K
t	time	s
u	axial velocity	m.s^{-1}
v	radial velocity	m.s^{-1}
V_i	diffusion velocity of species i	m.s^{-1}
x_i	mole fraction of species i	-
X_i	conversion of species i	
t	time	s
Y_i	mass fraction of species i	m.s^{-1}
Γ	surface site density	mol.m^{2}
β_k	temperature exponent	-
ε_i	coverage dependent activation energy	kJmol^{-1}
θ_i	surface coverage of species i	-
λ	thermal conductivity	W.(m.K)$_{-1}$

μ	voscosity	kg.(m.s)$^{-1}$
v_{ik}	stoichiometric coefficients	-
$\dot{\omega}_\iota$	Molar reaction rate of gas-phase reaction of species i	mol.m^{-3}.s^{-1}

Abbreviations

AES	Auger Electron Spectroscopy
APU	Auxilary Power Unit
ATR	Autothermal Reforming
BET	Brunauer-Emmett-Teller
BOC-MP	Bond-Order Conservation-Morse Potential
C/O	Carbon to Oxygen
cpsi	Cell Per Square Inch
CPOx	Catalytic Partical Oxidation
DFT	Density Functional Theory
DR	Dry Reforming
FTIR	Fourier Transform Infrared Spectroscopy
GHSV	Gas Hourly Space Velocity
h	hour
IR	Infrared
LM	Light Microscopy
MARI	Most Abundant Reaction Intermediate
MS	Mass Spectrometer
PEM	Polymer Electrolit Membrane
R-WGS	Reverse Water-Gas Shift
s	second
S/C	Steam to Carbon
SEM	Scanning Electron Microscopy
SLPM	Standard Liter Per Minutes
SR	Steam Reforming
TEM	Transmission Electron Miscroscopy
TOR	Turnover Rate
TPD	Temeperature Programmed Desorption
UBI-QUEP	Unit-Bond Quadratic Exponential Potential
WGS	Water-Gas Shift
XRD	X-Ray Diffraction
XPS	X-Ray Photoelectron Spectroscopy

References

[1] O. Deutschmann, High Temperature Catalysis: Efficient Way for Chemical Conversion of Logistic Fuels, Chem. Ing. Tech., 83 (2011) 1954-1964.

[2] K.A. Williams, R. Horn, L.D. Schmidt, Performance of mechanisms and reactor models for methane oxidation on Rh, AIChE Journal, 53 (2007) 2097-2113.

[3] O. Deutschmann, Interactions between transport and chemistry in catalytic reactors, Habilitation thesis, in: Fakultat für Chemie der Ruprecht-Karls-Universität Heidelberg, Heidelberg, 2001.

[4] K. Aasberg-Petersen, I. Dybkjær, C.V. Ovesen, N.C. Schjødt, J. Sehested, S.G. Thomsen, Natural gas to synthesis gas - Catalysts and catalytic processes, Journal of Natural Gas Science and Engineering, 3 (2011) 423-459.

[5] R. Horn, K.A. Williams, N.J. Degenstein, A. Bitsch-Larsen, D. Dalle Nogare, S.A. Tupy, L.D. Schmidt, Methane catalytic partial oxidation on autothermal Rh and Pt foam catalysts: Oxidation and reforming zones, transport effects, and approach to thermodynamic equilibrium, Journal of Catalysis, 249 (2007) 380-393.

[6] M. Bizzi, G. Saracco, R. Schwiedernoch, O. Deutschmann, Modeling the partial oxidation of methane in a fixed bed with detailed chemistry, AIChE Journal, 50 (2004) 1289-1299.

[7] V.M. Janardhanan, S. Appari, S. Jayanti, O. Deutschmann, Numerical study of on-board fuel reforming in a catalytic plate reactor for solid-oxide fuel cells, Chemical Engineering Science, 66 (2011) 490-498.

[8] M. Krumpelt, T.R. Krause, J.D. Carter, J.P. Kopasz, S. Ahmed, Fuel processing for fuel cell systems in transportation and portable power applications, Catalysis Today, 77 (2002) 3-16.

[9] A.L. Dicks, Hydrogen generation from natural gas for the fuel cell systems of tomorrow, Journal of Power Sources, 61 (1996) 113-124.

[10] T. Kaltschmitt, O. Deutschmann, Chapter 1 - Fuel Processing for Fuel Cells, in: S. Kai (Ed.) Advances in Chemical Engineering, Academic Press, 2012, pp. 1-64.

[11] M.A. Peña, J.P. Gómez, J.L.G. Fierro, New catalytic routes for syngas and hydrogen production, Applied Catalysis A: General, 144 (1996) 7-57.

[12] L. Ma, D.L. Trimm, Alternative catalyst bed configurations for the autothermic conversion of methane to hydrogen, Applied Catalysis A: General, 138 (1996) 265-273.

[13] S.S. Bharadwaj, L.D. Schmidt, Catalytic partial oxidation of natural gas to syngas, Fuel Processing Technology, 42 (1995) 109-127.

[14] O. Deutschmann, L.D. Schmidt, Modeling the partial oxidation of methane in a short-contact-time reactor, Aiche Journal, 44 (1998) 2465-2477.

[15] M. Prettre, C. Eichner, M. Perrin, The catalytic oxidation of methane to carbon monoxide and hydrogen, Transactions of the Faraday Society, 42 (1946) 335b-339.

[16] A. Donazzi, M. Maestri, B.C. Michael, A. Beretta, P. Forzatti, G. Groppi, E. Tronconi, L.D. Schmidt, D.G. Vlachos, Microkinetic modeling of spatially resolved autothermal CH(4) catalytic partial oxidation experiments over Rh-coated foams, Journal of Catalysis, 275 (2010) 270-279.

[17] D.A. Hickman, E.A. Haupfear, L.D. Schmidt, SYNTHESIS GAS-FORMATION BY DIRECT OXIDATION OF METHANE OVER RH MONOLITHS, Catal. Lett., 17 (1993) 223-237.

[18] O. Deutschmann, R. Schwiedernoch, L.I. Maier, D. Chatterjee, Natural Gas Conversion in Monolithic Catalysts: Interaction of Chemical Reactions and Transport Phenomena, Natural Gas Conversion VI, Studies in Surface Science and Catalysis 136 251-258.

[19] K. Supat, S. Chavadej, L.L. Lobban, R.G. Mallinson, Combined steam reforming and partial oxidation of methane to synthesis gas under electrical discharge, Ind. Eng. Chem. Res., 42 (2003) 1654-1661.

[20] D.Y. Qin, J. Lapszewicz, X.Z. Jiang, Comparison of partial oxidation and steam-CO2 mixed reforming of CH4 to syngas on MgO-supported metals, Journal of Catalysis, 159 (1996) 140-149.

[21] D. Li, Y. Nakagawa, K. Tomishige, Methane reforming to synthesis gas over Ni catalysts modified with noble metals, Applied Catalysis A: General, 408 (2011) 1-24.

[22] G. Kolb, R. Zapf, V. Hessel, H. Lowe, Propane steam reforming in micro-channels - results from catalyst screening and optimisation, Appl. Catal. A-Gen., 277 (2004) 155-166.

[23] T. Boeltken, M. Belimov, P. Pfeifer, T.A. Peters, R. Bredesen, R. Dittmeyer, Fabrication and testing of a planar microstructured concept module with integrated palladium membranes, Chemical Engineering and Processing: Process Intensification, (2012).

[24] S.H. Chan, O.L. Ding, D.L. Hoang, A Thermodynamic View of Partial Oxidation, Steam Reforming, and Autothermal Reforming on Methane, International Journal of Green Energy, 1 (2004) 265-278.

[25] S. Ayabe, H. Omoto, T. Utaka, R. Kikuchi, K. Sasaki, Y. Teraoka, K. Eguchi, Catalytic autothermal reforming of methane and propane over supported metal catalysts, Applied Catalysis A: General, 241 (2003) 261-269.

[26] L.S.F. Feio, C.E. Hori, L.V. Mattos, D. Zanchet, F.B. Noronha, J.M.C. Bueno, Partial oxidation and autothermal reforming of methane on Pd/CeO2–Al2O3 catalysts, Applied Catalysis A: General, 348 (2008) 183-192.

[27] N.E. McGuire, N.P. Sullivan, O. Deutschmann, H. Zhu, R.J. Kee, Dry reforming of methane in a stagnation-flow reactor using Rh supported on strontium-substituted hexaaluminate, Applied Catalysis A: General, 394 (2011) 257-265.

[28] Ş. Özkara-Aydınoğlu, E. Özensoy, A.E. Aksoylu, The effect of impregnation strategy on methane dry reforming activity of Ce promoted Pt/ZrO2, International Journal of Hydrogen Energy, 34 (2009) 9711-9722.

[29] Z. Hou, P. Chen, H. Fang, X. Zheng, T. Yashima, Production of synthesis gas via methane reforming with CO on noble metals and small amount of noble-(Rh-) promoted Ni catalysts, International Journal of Hydrogen Energy, 31 (2006) 555-561.

[30] A. Donazzi, A. Beretta, G. Groppi, P. Forzatti, Catalytic partial oxidation of methane over a 4% Rh/α-Al2O3 catalyst. Part I: Kinetic study in annular reactor, Journal of Catalysis, 255 (2008) 241-258.

[31] A. Boisen, T.V.W. Janssens, N. Schumacher, I. Chorkendorff, S. Dahl, Support effects and catalytic trends for water gas shift activity of transition metals, Journal of Molecular Catalysis A: Chemical, 315 (2010) 163-170.

[32] M. Maestri, K. Reuter, Molecular-level understanding of WGS and reverse WGS reactions on Rh through hierarchical multiscale approach, Chemical Engineering Science, 74 (2012) 296-299.

[33] R. Schwiedernoch, S. Tischer, C. Correa, O. Deutschmann, Experimental and numerical study on the transient behavior of partial oxidation of methane in a catalytic, monolith, Chemical Engineering Science, 58 (2003) 633-642.

[34] R. Horn, K.A. Williams, N.J. Degenstein, L.D. Schmidt, Syngas by catalytic partial oxidation of methane on rhodium: Mechanistic conclusions from spatially resolved measurements and numerical simulations, Journal of Catalysis, 242 (2006) 92-102.

[35] D.D. Nogare, N.J. Degenstein, R. Horn, P. Canu, L.D. Schmidt, Modeling spatially resolved data of methane catalytic partial oxidation on Rh foam catalyst at different inlet compositions and flowrates, Journal of Catalysis, 277 (2011) 134-148.

[36] M. Maestri, D.G. Vlachos, A. Beretta, G. Groppi, E. Tronconi, Steam and dry reforming of methane on Rh: Microkinetic analysis and hierarchy of kinetic models, Journal of Catalysis, 259 (2008) 211-222.

[37] S. Hannemann, J.-D. Grunwaldt, N. van Vegten, A. Baiker, P. Boye, C.G. Schroer, Distinct spatial changes of the catalyst structure inside a fixed-bed microreactor during the partial oxidation of methane over Rh/Al2O3, Catalysis Today, 126 (2007) 54-63.

[38] S.F. Rice, A.H. McDaniel, E.S. Hecht, A.J.J. Hardy, Methane partial oxidation catalyzed by platinum and rhodium in a high-temperature stagnation flow reactor, Ind. Eng. Chem. Res., 46 (2007) 1114-1119.

[39] V. Balakotaiah, N. Gupta, D.H. West, Simplified model for analyzing catalytic reactions in short monoliths, Chemical Engineering Science, 55 (2000) 5367-5383.

[40] S. Tischer, O. Deutschmann, Recent advances in numerical modeling of catalytic monolith reactors, Catalysis Today, 105 (2005) 407-413.

[41] A. Güthenke, D. Chatterjee, M. Weibel, B. Krutzsch, P. Kočí, M. Marek, I. Nova, E. Tronconi, Current status of modeling lean exhaust gas aftertreatment catalysts, in, 2007, pp. 103-211,280-283.

[42] T.C. Ho, Kinetic modeling of large-scale reaction systems, Catalysis Reviews - Science and Engineering, 50 (2008) 287-378.

[43] O. Deutschmann, Modeling and simulation of heterogeneous catalytic reactions : from the molecular process to the technical system, in, Wiley-VCH, Weinheim, 2012, pp. 354.

[44] V.P. Zhdanov, Impact of surface science on the understanding of kinetics of heterogeneous catalytic reactions, Surface Science, 500 (2002) 966-985.

[45] F. Zaera, The surface chemistry of heterogeneous catalysis: Mechanisms, selectivity, and active sites, Chemical Record, 5 (2005) 133-144.

[46] F. Zaera, Outstanding mechanistic questions in heterogeneous catalysis, Journal of Physical Chemistry B, 106 (2002) 4043-4052.

[47] T. Johannessen, J.H. Larsen, I. Chorkendorff, H. Livbjerg, H. Topsøe, Catalyst dynamics: Consequences for classical kinetic descriptions of reactors, Chemical Engineering Journal, 82 (2001) 219-230.

[48] R. Schwiedernoch, Partial and Total Oxidation of Methane in Monolithic Catalysts at Short Contact Times, in: Naturwissenschaftlichen-Mathematishen Gesamtfakultät der Ruprecht-Karls-Universität Heidelberg, Ruprecht-Karls-Universität Heidelberg, Heidelberg, 2005.

[49] H.S. Fogler, Elements of Chemical Reaction Engineering, Fourth edition ed., Pearson International Edition, Michigan, 2006.

[50] O. Deutschmann, R. Schwiedernoch, L.I. Maier, D. Chatterjee, Natural gas conversion in monolithic catalysts: Interaction of chemical reactions and transport phenomena, in: J.J.S. E. Iglesia, T.H. Fleisch (Eds.) Studies in Surface Science and Catalysis, Elsevier, 2001, pp. 251-258.

[51] H. Lynggaard, A. Andreasen, C. Stegelmann, P. Stoltze, Analysis of simple kinetic models in heterogeneous catalysis, Progress in Surface Science, 77 (2004) 71-137.

[52] D.J. Dooling, J.E. Rekoske, L.J. Broadbelt, Microkinetic models of catalytic reactions on nonuniform surfaces: application to model and real systems, Langmuir, 15 (1999) 5846-5856.

[53] O. Deutschmann, H. Knözinger, K. Kochloefl, T. Turek, Heterogeneous Catalysis and Solid Catalysts, in: Ullmann's Encyclopedia of Industrial Chemistry, Wiley-VCH Verlag GmbH & Co. KGaA, 2000.

[54] A.K. Mukherjee, I. Sinha, Effect of the Eley–Rideal step on catalytic oxidation of CO under periodic external pressure, Applied Surface Science, 255 (2009) 6168-6172.

[55] B.L.M. Hendriksen, J.W.M. Frenken, CO Oxidation on Pt(110): Scanning Tunneling Microscopy Inside a High-Pressure Flow Reactor, Physical Review Letters, 89 (2002) 046101.

[56] J.D. Grunwaldt, A.M. Molenbroek, N.Y. Topsøe, H. Topsøe, B.S. Clausen, In situ investigations of structural changes in Cu/ZnO catalysts, Journal of Catalysis, 194 (2000) 452-460.

[57] R. Turton, M. Colakyan, THE EFFECTIVENESS FACTORS FOR VARIOUS SIZE DISTRIBUTIONS OF CATALYST PARTICLES, Chemical Engineering Communications, 35 (1985) 75-79.

[58] O. Deutschmann, S. Tischer, Stefan Kleditzsch, V. Janardhanan, C. Correa, D. Chatterjee, N. Mladenov, H.D. Minh, H. Karadeniz, DETCHEM User Manual Version 2.4, Germany, 2012.

[59] A.B. Mhadeshwar, H. Wang, D.G. Vlachos, Thermodynamic Consistency in Microkinetic Development of Surface Reaction Mechanisms, Journal of Physical Chemistry B, 107 (2003) 12721-12733.

[60] L. Maier, B. Schädel, K.H. Delgado, S. Tischer, O. Deutschmann, Steam reforming of methane over nickel: Development of a multi-step surface reaction mechanism, Topics in Catalysis, 54 (2011) 845-858.

[61] R.B. Bird, W.E. Stewart, E.N. Lightfoot, Transport Phenomena, John Wiley & Sons, 2006.

[62] L.L. Raja, R.J. Kee, O. Deutschmann, J. Warnatz, L. D. Schmidt, A critical evaluation of Navier–Stokes, boundary-layer, and plug-flow models of the flow and chemistry in a catalytic-combustion monolith, Catalysis Today, 59 (2000) 47-60.

[63] J.D. Anderson, Jr, Ludwig Prandtl's Boundary Layer, Physics Today, 58 (2005) 42-48.

[64] R.J.Kee, M.E.Coltrin, P.Glarborg, Chemically Reacting Flow, Theory and Practice 2005.

[65] T. Yuan, Y.-H. Lai, C.-K. Chang, Numerical studies of heterogeneous reaction in stagnation flows using one-dimensional and two-dimensional Cartesian models, Combustion and Flame, 154 (2008) 557-568.

[66] R.W. Sidwell, H. Zhu, R.J. Kee, D.T. Wickham, C. Schell, G.S. Jackson, Catalytic combustion of premixed methane/air on a palladium-substituted hexaluminate stagnation surface, Proceedings of the Combustion Institute, 29 (2002) 1013-1020.

[67] J. Warnatz, M.D. Allendorf, R.J. Kee, M.E. Coltrin, A model of elementary chemistry and fluid-mechanics in the combustion of hydrogen on a platinium surfaces, Combust. Flame, 96 (1994) 393-406.

[68] S. Joh, G.H. Evans, Heat transfer and flow stability in a rotating disk stagnation flow chemical vapor deposition reactor, Numer. Heat Tranf. A-Appl., 31 (1997) 867-879.

[69] R.J. Kee, F.M. Rupley, J.A. Miller, M.E. Coltrin, J.F. Grcar, E. Meeks, H.K. Moffat, A.E. Lutz, G. Dixon-Lewis, M.D. Smooke, J. Warnatz, Evans G.H., R.S. Larson, R.E. Mitchell, L.R. Petzold, W.C. Reynolds, M. Caracotsios, W.E. Stewart, P. Glarborg, C. C. Wang, O. Adigun, Technical Report Release 4.0, Reaction Design, Inc, in, San Diego, CA, 2005.

[70] C. Houtman, D.B. Graves, K.F. Jensen, CVD in a stagnation point flow-An evauation of the classical 1D-Treatment, J. Electrochem. Soc., 133 (1986) 961-970.

[71] I.H. Oh, C.G. Takoudis, G.W. Neudeck, Mathematical-modeling of epitaxial silicon growth in pancake chemical vapor-deposition reactors, J. Electrochem. Soc., 138 (1991) 554-567.

[72] N. Memon, Y. Jaluria, Flow Structure and Heat Transfer in a Stagnation Flow CVD Reactor, J. Heat Transf.-Trans. ASME, 133 (2011).

[73] F. Behrendt, O. Deutschmann, B. Ruf, J. Warnatz, Numerical study of apparent activation energies of diamond growth rates in hot filament chemical vapor deposition systems, in, AVS, 1996, pp. 1604-1608.

[74] B. Ruf, F. Behrendt, O. Deutschmann, J. Warnatz, Simulation of reactive flow in filament-assisted diamond growth including hydrogen surface chemistry, Journal of Applied Physics, 79 (1996) 7256-7263.

[75] S. Ljungström, B. Kasemo, A. Rosen, T. Wahnström, E. Fridell, An experimental study of the kinetics of OH and H_2O formation on Pt in the $H_2 + O_2$ reaction, Surface Science, 216 (1989) 63-92.

[76] X. Song, L.D. Schmidt, R. Aris, The Ignition Criteria for Stagnation-Point Flow: SemenovFrank-Kamenetski or van't Hoff, Combustion Science and Technology, 75 (1991) 311-331.

[77] O. Deutschmann, F. Behrendt, J. Warnatz, Modelling and simulation of heterogeneous oxidation of methane on a platinum oil, Catal. Today, 21 (1994) 461-470.

[78] H. Ikeda, J. Sato, F.A. Williams, Surface kinetics for catalytic combustion of hydrogen-air mixtures on platinum at atmospheric pressure in stagnation flows, Surface Science, 326 (1995) 11-26.

[79] O. Deutschmann, R. Schmidt, F. Behrendt, J. Warnatz, Numerical modeling of catalytic ignition, Symposium (International) on Combustion, 26 (1996) 1747-1754.

[80] V. Dupont, S.H. Zhang, A. Williams, Experiments and simulations of methane oxidation on a platinum surface, Chemical Engineering Science, 56 (2001) 2659-2670.

[81] A.H. McDaniel, A.E. Lutz, M.D. Allendorf, S.F. Rice, Effects of methane and ethane on the heterogeneous production of water from hydrogen and oxygen over platinum in stagnation flow, Journal of Catalysis, 208 (2002) 21-29.

[82] J.D. Taylor, M.D. Allendorf, A.H. McDaniel, S.F. Rice, In situ diagnostics and modeling of methane catalytic partial oxidation on Pt in a stagnation-flow reactor, Ind. Eng. Chem. Res., 42 (2003) 6559-6566.

[83] N.E. McGuire, N.P. Sullivan, R.J. Kee, H. Zhu, J.A. Nabity, J.R. Engel, D.T. Wickham, M.J. Kaufman, Catalytic steam reforming of methane using Rh supported on Sr-substituted hexaaluminate, Chemical Engineering Science, 64 (2009) 5231-5239.

[84] N.E. Fernandes, Y.K. Park, D.G. Vlachos, The autothermal behavior of platinum catalyzed hydrogen oxidation: Experiments and modeling, Combustion and Flame, 118 (1999) 164-178.

[85] M. Försth, F. Gudmundson, J.L. Persson, A. Rosén, The influence of a catalytic surface on the gas-phase combustion of H2 + O2, Combustion and Flame, 119 (1999) 144-153.

[86] O. Deutschmann, R. Schmidt, F. Behrendt, J. Warnat, Numerical modeling of catalytic ignition, Symposium (International) on Combustion, 26 (1996) 1747-1754.

[87] R.W. Sidwell, H. Zhu, R.J. Kee, D.T. Wickham, Catalytic combustion of premixed methane-in-air on a high-temperature hexaaluminate stagnation surface, Combust. Flame, 134 (2003) 55-66.

[88] M. Hartmann, L. Maier, H.D. Minh, O. Deutschmann, Catalytic partial oxidation of iso-octane over rhodium catalysts: An experimental, modeling, and simulation study, Combust. Flame, 157 (2010) 1771-1782.

[89] D.S. Dandy, J. Yun, Momentum and Thermal Boundary-layer Thickness in a Stagnation Flow Chemical Vapor Deposition Reactor, Journal of Materials Research, 12 (1997) 1112-1121.

[90] R.J. Kee, M.E. Coltrin, P. Glarborg, Chemically Reacting Flow: Theory and Practice, Wiley, 2005.

[91] J. Thormann, P. Pfeifer, K. Schubert, U. Kunz, Reforming of diesel fuel in a micro reactor for APU systems, Chemical Engineering Journal, 135, Supplement 1 (2008) S74-S81.

[92] C.L. Bridges, An experimental study of catalytic partial oxidaion of CH4 on rhodium-strontium hexaaluminate in a stagnation-flow boundary layer, in: Division of Engineering, Colorado School of Mines
2006.

[93] Airsense: High Speed Multi-component Gas Analyzer, in, V&F Instruments Inc., Michigan, 2012, pp. http://www.vandfna.com/airsense.htm.

[94] Process Mass Spectrometer, Model H-Sense, in, V&F Instruments Inc., Michigan, 2012, pp. http://www.vandfna.com/hsense.htm.

[95] G.E.A. Swann, S.V. Patwardhan, Application of Fourier Transform Infrared Spectroscopy (FTIR) for assessing biogenic silica sample purity in geochemical analyses and palaeoenvironmental research, Climate of the Past, 7 (2011) 65-74.

[96] B. Stuart, Infrared Spectroscopy: Fundamentals and Applications, John Wiley & Sons, Ltd, West Sussex, 2004.

[97] N. Dyson, Peak distortion, data sampling errors and the integrator in the measurement of very narrow chromatographic peaks, J. Chromatogr. A, 842 (1999) 321-340.

[98] R.M. Vanhardeveld, P.L.J. Gunter, L.J. Vanijzendoorn, W. Wieldraaijer, E.W. Kuipers, J.W. Niemantsverdriet, Deposition of Inorganic salts from solution on flat substrates by spin-coating-Theory, guantification and application to model catalysts, Applied Surface Science, 84 (1995) 339-346.

[99] P.C. Thune, J.W. Niemantsverdriet, Surface science models of industrial catalysts, Surface Science, 603 (2009) 1756-1762.

[100] U. Manual, Leica MEF4A/MEF4M Widefield Metallographs, in: L.M.W. GmbH (Ed.), Wetzlar, 2012.

[101] R.F. Egerton, Physical Principles of Electron Microscopy: An Introduction to TEM, SEM, and AEM, Springer, Edmonton, 2005.

[102] N.B. Winter, Understanding Cement, in: An introduction to cement production, cement hydration and deterious process in concrete, WHD Microanalysis Consultants Suffolk, UK, 2012.

[103] B. Fultz, J.M. Howe, The TEM and its Optics
Transmission Electron Microscopy and Diffractometry of Materials, in, Springer Berlin Heidelberg, 2008, pp. 61-118.

[104] A. Marshall, A.L. Koh, Transmission Electron Microscope (TEM) Facility in, Stanford Nano Shared Facilities, 2012, pp. http://www.stanford.edu/group/snl/tem.htm.

[105] F. Eigenmann, M. Maciejewski, A. Baiker, Gas adsorption studied by pulse thermal analysis, Thermochim. Acta, 359 (2000) 131-141.

[106] S. Komai, Y. Yazawa, A. Satsuma, T. Hattori, Determination of Metal Dispersion of Pt/CeO2 Catalyst by CO-pulse Method, Journal of the Japan Petroleum Institute, 48 (1995) 173-177.

[107] W. Boll, S. Tischer, O. Deutschmann, Loading and Aging Effects in Exhaust Gas After-Treatment Catalysts with Pt As Active Component, Ind. Eng. Chem. Res., 49 (2010) 10303-10310.

[108] S.B. Kang, H.J. Kwon, I.-S. Nam, Y.I. Song, S.H. Oh, Activity Function for Describing Alteration of Three-Way Catalyst Performance over Palladium-Only Three-Way Catalysts by Catalyst Mileage, Ind. Eng. Chem. Res., 50 (2011) 5499-5509.

[109] G. Bergeret, P. Gallezot, Particle Size and Dispersion Measurements, in: Handbook of Heterogeneous Catalysis, Wiley-VCH Verlag GmbH & Co. KGaA, 2008, pp. 738-765.

[110] M.S. Chen, Y. Cai, Z. Yan, K.K. Gath, S. Axnanda, D.W. Goodman, Highly active surfaces for CO oxidation on Rh, Pd, and Pt, Surface Science, 601 (2007) 5326-5331.

[111] H.-J. Freund, Principles of Chemisorption, in: H.K. G. Ertl, F. Schüth, and J. Weitkamp (Ed.) Handbook of Heterogeneous Catalysis, Wiley-VCH Verlag GmbH & Co. KGaA, 2008, pp. 1375-1415.

[112] K. Foger, J.R. Anderson, TEMPERATURE PROGRAMMED DESORPTION OF CARBON-MONOXIDE ADSORBED ON SUPPORTED PLATINUM CATALYSTS, Applied Surface Science, 2 (1979) 335-351.

[113] H. Dropsch, M. Baerns, CO adsorption on supported Pd catalysts studied by adsorption microcalorimetry and temperature programmed desorption, Appl. Catal. A-Gen., 158 (1997) 163-183.

[114] T. Lear, N.G. Hamilton, D. Lennon, The application of temperature-programmed desorption, adsorption isotherms and temperature-programmed oxidation to investigate the interaction of CO with alumina-supported palladium catalysts, Catalysis Today, 126 (2007) 219-227.

[115] K. Fottinger, R. Schlogl, G. Rupprechter, The mechanism of carbonate formation on Pd-Al2O3 catalysts, Chemical Communications, (2008) 320-322.

[116] M. Arai, M. Fukushima, N. Nishiyama, The Surface Heterogeneity of Supported Platinum Catalysts as Studied by the Interrupted Temperature-Programmed Desorption of Carbon Monoxide, Bulletin of the Chemical Society of Japan, 70 (1997) 1545-1549.

[117] T. Tanabe, Y. Nagai, T. Hirabayashi, N. Takagi, K. Dohmae, N. Takahashi, S. Matsumoto, H. Shinjoh, J.N. Kondo, J.C. Schouten, H.H. Brongersma, Low temperature CO pulse adsorption for the determination of Pt particle size in a Pt/cerium-based oxide catalyst, Appl. Catal. A-Gen., 370 (2009) 108-113.

[118] J. Koop, O. Deutschmann, Detailed surface reaction mechanism for Pt-catalyzed abatement of automotive exhaust gases, Appl. Catal. B-Environ., 91 (2009) 47-58.

[119] G. C. Bond, P. B. Wells, Characterization of the standard platinum/silica catalyst europt-1 1.philosophy and achievement, Applied Catalysis, 18 (1985) 221-224.

[120] K. Arnby, A. Törncrona, B. Andersson, M. Skoglundh, Investigation of Pt/[gamma]-Al2O3 catalysts with locally high Pt concentrations for oxidation of CO at low temperatures, Journal of Catalysis, 221 (2004) 252-261.

[121] A. Bourane, D. Bianchi, Oxidation of CO on a Pt/Al2O3 catalyst: from the surface elementary steps to light-off tests: V. Experimental and kinetic model for light-off tests in excess of O2, Journal of Catalysis, 222 (2004) 499-510.

[122] A. Bourane, D. Bianchi, Oxidation of CO on a Pt/Al2O3 Catalyst: From the Surface Elementary Steps to Lighting-Off Tests: III. Experimental and Kinetic Model for Lights-Off Tests in Excess CO, Journal of Catalysis, 209 (2002) 126-134.

[123] A. Bourane, D. Bianchi, Oxidation of CO on a Pt/Al2O3 Catalyst: From the Surface Elementary Steps to Light-Off Tests: I. Kinetic Study of the Oxidation of the Linear CO Species, Journal of Catalysis, 202 (2001) 34-44.

[124] C.T. Campbell, G. Ertl, H. Kuipers, J. Segner, A MOLECULAR-BEAM STUDY OF THE CATALYTIC-OXIDATION OF CO ON A PT(111) SURFACE, J. Chem. Phys., 73 (1980) 5862-5873.

[125] S.N. Pavlova, V.A. Sadykov, V.A. Razdobarov, E.A. Paukshtis, The influence of support on the low-temperature activity of Pd in the reaction of CO oxidation .2. Adsorption properties and reactivity of adsorbed species, Journal of Catalysis, 161 (1996) 507-516.

[126] A. Holmgren, B. Andersson, D. Duprez, Interactions of CO with Pt/ceria catalysts, Applied Catalysis B: Environmental, 22 (1999) 215-230.

[127] G.G. Olympiou, C.M. Kalamaras, C.D. Zeinalipour-Yazdi, A.M. Efstathiou, Mechanistic aspects of the water-gas shift reaction on alumina-supported noble metal catalysts: In situ DRIFTS and SSITKA-mass spectrometry studies, Catalysis Today, 127 (2007) 304-318.

[128] C.M. Kalamaras, G.G. Olympiou, A.M. Efstathiou, The water-gas shift reaction on Pt/[gamma]-Al2O3 catalyst: Operando SSITKA-DRIFTS-mass spectroscopy studies, Catalysis Today, 138 (2008) 228-234.

[129] G. C. Bond, P. B. Wells, Characterization of the standard platinum/silica catalyst europt-1 2. preparation, physical properties, and chemical composition, Applied Catalysis, 18 (1985) 225-230.

[130] A.A. Phatak, N. Koryabkina, S. Rai, J.L. Ratts, W. Ruettinger, R.J. Farrauto, G.E. Blau, W.N. Delgass, F.H. Ribeiro, Kinetics of the water-gas shift reaction on Pt catalysts supported on alumina and ceria, Catalysis Today, 123 (2007) 224-234.

[131] J. Segner, C.T. Campbell, G. Doyen, G. Ertl, Catalytic oxidation of CO on Pt(111): The influence of surface defects and composition on the reaction dynamics, Surface Science, 138 (1984) 505-523.

[132] W. Boll, Korrelation zwischen Umsatzverhalten und katalytisher Oberfläche von Dieseloxidationskatalysatoren unter Variation von Beladung und Alterungzustand, in: Techical Chemistry and Polymer Chemistry, Karlsruhe Institute of Technology, Karlsruhe, 2011.

[133] R. Kissel-Osterrieder, F. Behrendt, J. Warnatz, Detailed modeling of the oxidation of CO on platinum: A Monte-Carlo model, Symposium (International) on Combustion, 27 (1998) 2267-2274.

[134] P. Thormählen, M. Skoglundh, E. Fridell, B. Andersson, Low-Temperature CO Oxidation over Platinum and Cobalt Oxide Catalysts, Journal of Catalysis, 188 (1999) 300-310.

[135] J.Z. Xu, J.T. Yates, CATALYTIC-OXIDATION OF CO ON PT(335) - A STUDY OF THE ACTIVE-SITE, J. Chem. Phys., 99 (1993) 725-732.

[136] E. Finocchio, G. Busca, P. Forzatti, G. Groppi, A. Beretta, State of Supported Rhodium Nanoparticles for Methane Catalytic Partial Oxidation (CPO): FT-IR Studies, Langmuir, 23 (2007) 10419-10428.

[137] J.-D. Grunwaldt, L. Basini, B.S. Clausen, In Situ EXAFS study of Rh/Al_2O_3 catalysts for Catalytic Partial Oxidation of Methane, J. Catal., 200 (2001) 321-329.

[138] S. Hannemann, J.-D. Grunwaldt, N. Van Vegten, A. Baiker, P. Boye, C.G. Schroer, Distinct spatial changes of the catalyst structure inside a fixed-bed microreactor during the partial oxidation of methane over Rh/Al_2O_3, Catal. Today, 126 (2007) 54-63.

[139] D. Wang, O. Dewaele, A.M. De Groote, G.F. Froment, Reaction mechanism and role of the support in the partial oxidation of methane on Rh/Al2O3, Journal of Catalysis, 159 (1996) 418-426.

[140] E.P.J. Mallens, J.H.B.J. Hoebink, G.B. Marin, The reaction mechanism of the partial oxidation of methane to synthesis gas: A transient kinetic study over rhodium and a comparison with platinum, Journal of Catalysis, 167 (1997) 43-56.

[141] A.G. Salinger, G. Eigenberger, The direct calculation of periodic states of the reverse flow reactor .1. Methodology and propane combustion results, Chemical Engineering Science, 51 (1996) 4903-4913.

[142] G. Veser, L.D. Schmidt, Ignition and Extinction in the Catalytic Oxidation of Hydrocabons over Platinum, AIChE J., 42 (1996) 1077-1087.

[143] M. Rinnemo, O. Deutschmann, F. Behrendt, B. Kasemo, Experimental and numerical investigation of the catalytic ignition of mixtures of H_2 and O_2 on Pt, Combust. Flame, 111 (1997) 312-326.

[144] M. Rinnemo, M. Fassihi, B. Kasemo, The critical condition for catalytic ignition H2/O2 on Pt, Chem. Phys. Lett., 211 (1993) 60-64.

[145] M. Rinnemo, D. Kulginov, S. Johansson, K.L. Wong, V.P. Zhdanov, B. Kasemo, Catalytic ignition in the CO-O_2 reaction on platinum: experiment and simulation, Surf. Sci., 376 (1997) 297-309.

[146] B.K. Warren, S.T. Oyama, Heterogeneous Hydrocarbon Oxidation, in: F. Behrendt, O. Deutschmann, R. Schmidt, J. Warnatz (Eds.) Ignition and Extinction of Hydrogen-Air and Methane-Air Mixtures over Platinum and Palladium, American Chemical Society, Washington D.C., 1996, pp. 48.

[147] O. Deutschmann, R. Schmidt, F. Behrendt, J. Warnatz, Comparison between calculated and experimentally determined catalytic ignition temperatures for a) stagnation point flows on an electrically heated platinum foils b) flows around an electrically heated platinum wires, Proc. Combust. Inst., 26 (1996) 1747-1754.

[148] K.L. Hohn, C.-C. Huang, C. Cao, Catalytic ignition of light hydrocarbons, J. Nat.Gas Chem., 18 (2009) 115-123.

[149] M. Ziauddin, G. Veser, L.D. Schmidt, Ignition-extinction of ethane-air mixtures over noble metals, Catal. Lett., 46 (1997) 159-167.

[150] R. Sant, E.E. Wolf, Elementary-step modeling and transient FTIR studies of CO-Oxidation on Rh/SiO_2, Chem. Eng. Sci., 45 (1990) 3137-3147.

[151] A.B. Mhadeshwar, D.G. Vlachos, Hierarchical, multiscale surface reaction mechanism development: CO and H_2 oxidation, water-gas shift and preferential oxidation of CO on Rh, J. Catal., 234 (2005) 48-63.

[152] A.B. Mhadeshwar, D.G. Vlachos, Hierarchical Multiscale Mechanism Development for Methane Partial Oxidation and Reforming and for Thermal Decomposition of Oxygenates on Rh, J. Phys. Chem. B, 109 (2005) 16819-16835.

[153] P. Cho, C.K. Law Catalytic Ignition of Fuel/Oxygen/Nitrogen Mixtures over Platinum, Combust. Flame, 66 (1986) 159-170.

[154] F. Behrendt, O. Deutschmann, R. Schmidt, J. Warnatz, Heterogeneous Hydrocarbon Oxidation, in: B.K. Warren, S.T. Oyama (Eds.) Ignition and Extinction of Hydrogen-Air and Methane-Air Mixtures over Platinum and Palladium, American Chemical Society, Washington D.C., 1996.

[155] G. Veser, M. Ziauddin, L.D. Schmidt, Ignition in alkane oxidation on noble-metal catalysts, Catal. Today, 47 (1999) 219-228.

[156] I. Chorkendorff, J.W. Niemantsverdriet, Concepts of modern catalysis and kinetics, Wiley-VCH, Weinheim, 2007.

[157] O. Deutschmann, F. Behrendt, J. Warnatz, Modelling and simulation of heterogeneous oxidation of methane on a platinum foil, Catalysis Today, 21 (1994) 461-470.

[158] P.A. Thiel, J.T. Yates Jr, W.H. Weinberg, The interaction of oxygen with the Rh(111) surface a, Surface Science, 82 (1979) 22-44.

[159] J.T. Yates Jr, P.A. Thiel, W.H. Weinberg, The chemisorption of hydrogen on Rh(111), Surface Science, 84 (1979) 427-439.

[160] J.T. Yates Jr, P.A. Thiel, W.H. Weinberg, The catalytic reaction between adsorbed oxygen and hydrogen on Rh(111), Surface Science, 82 (1979) 45-68.

[161] L.K. Verheij, M.B. Hugenschmidt, B. Poelsema, G. Comsa, The hydrogen-oxygen reaction on the Pt(111) surface; influence of adsorbed oxygen on the sticking of hydrogen, Surface Science, 233 (1990) 209-222.

[162] D.F. Padowitz, S.J. Sibener, Kinetics of hydrogen oxidation to water on the Rh(111) surface using multiple source modulated molecular beam techniques, Surface Science, 254 (1991) 125-143.

[163] R. Löber, D. Hennig, Interaction of hydrogen with transition metal fcc(111) surfaces, Physical Review B - Condensed Matter and Materials Physics, 55 (1997) 4761-4765.

[164] S. Völkening, K. Bedürftig, K. Jacobi, J. Wintterlin, G. Ertl, Dual-Path Mechanism for Catalytic Oxidation of Hydrogen on Platinum Surfaces, Physical Review Letters, 83 (1999) 2672-2675.

[165] C. Treviño, Catalytic ignition of very lean mixtures of hydrogen, International Journal of Hydrogen Energy, 36 (2011) 8610-8618.

[166] S. Wilke, V. Natoli, M.H. Cohen, Theoretical investigation of water formation on Rh and Pt surfaces, J. Chem. Phys., 112 (2000) 9986-9995.

[167] G. Veser, Experimental and theoretical investigation of H2 oxidation in a high-temperature catalytic microreactor, Chemical Engineering Science, 56 (2001) 1265-1273.

[168] J. Zhou, Y. Wang, W. Yang, J. Liu, Z. Wang, K. Cen, Combustion of hydrogen–air in catalytic micro-combustors made of different material, International Journal of Hydrogen Energy, 34 (2009) 3535-3545.

[169] W. Choi, S. Kwon, H. Dong Shin, Combustion characteristics of hydrogen–air premixed gas in a sub-millimeter scale catalytic combustor, International Journal of Hydrogen Energy, 33 (2008) 2400-2408.

[170] B.I. Whittington, C.J. Jiang, D.L. Trimm, Vehicle exhaust catalysis: I. The relative importance of catalytic oxidation, steam reforming and water-gas shift reactions, Catalysis Today, 26 (1995) 41-45.

[171] V. Yakhnin, M. Menzinger, Stationary and traveling hot spots in the catalytic combustion of hydrogen in monoliths, Chemical Engineering Science, 57 (2002) 4559-4567.

[172] J.D. Holladay, J. Hu, D.L. King, Y. Wang, An overview of hydrogen production technologies, Catalysis Today, 139 (2009) 244-260.

[173] M. Hartmann, L. Maier, O. Deutschmann, Hydrogen production by catalytic partial oxidation of iso-octane at varying flow rate and fuel/oxygen ratio: From detailed kinetics to reactor behavior, Appl. Catal. A, 391 (2011) 144-152.

[174] A. Beretta, A. Donazzi, D. Livio, M. Maestri, G. Groppi, E. Tronconi, P. Forzatti, Optimal design of a CH4 CPO-reformer with honeycomb catalyst: Combined effect of catalyst load and channel size on the surface temperature profile, Catalysis Today, 171 (2011) 79-83.

[175] Y.-H. Chin, C. Buda, M. Neurock, E. Iglesia, Selectivity of chemisorbed oxygen in C–H bond activation and CO oxidation and kinetic consequences for CH4–O2 catalysis on Pt and Rh clusters, Journal of Catalysis, 283 (2011) 10-24.

[176] R. Chakrabarti, J.L. Colby, L.D. Schmidt, Effects of biomass inorganics on rhodium catalysts: I. Steam methane reforming, Applied Catalysis B: Environmental, 107 (2011) 88-94.

[177] M.P. Zum Mallen, W.R. Williams, L.D. Schmidt, Steps in H2 oxidation on Rh: OH desorption at high temperatures, Journal of Physical Chemistry, 97 (1993) 625-632.

[178] T.A. Germer, W. Ho, Direct characterization of the hydroxyl intermediate during reduction of oxygen on Pt(111) by time-resolved electron energy loss spectroscopy, Chemical Physics Letters, 163 (1989) 449-454.

[179] A.B. Anton, D.C. Cadogan, The mechanism and kinetics of water formation on Pt(111), Surface Science, 239 (1990) L548-L560.

[180] W.R. Williams, C.M. Marks, L.D. Schmidt, Steps in the reaction H2 + O-2-Reversible-Arrow-H2O on PT - OH deposition at high temperatures, Journal of Physical Chemistry, 96 (1992) 5922-5931.

[181] J. Mantzaras, R. Bombach, R. Schaeren, Hetero-/homogeneous combustion of hydrogen/air mixtures over platinum at pressures up to 10 bar, in, 2009, pp. 1937-1945.

[182] P.A. Thiel, J.T. Yates Jr, W.H. Weinberg, The co-adsorption of oxygen and hydrogen on Rh(111), Surface Science, 90 (1979) 121-132.

[183] D.A. Hickman, L.D. Schmidt, Production of syngas by direct catalytic oxidation of methane, Science, 259 (1993) 343-346.

[184] O. Dewaele, D. Wang, G.F. Froment, TAP study of the sorption of H2 and O2 on Rh/γ-Al2O3, Journal of Molecular Catalysis A: Chemical, 149 (1999) 263-273.

[185] M. Maestri, A. Beretta, T. Faravelli, G. Groppi, T. Enrico, Role of gas-phase chemistry in the rich combustion of H2 and CO over a Rh / Al2 O3 catalyst in annular reactor, Chemical Engineering Science, 62 (2007) 4992-4997.

[186] M. Maestri, A. Beretta, T. Faravelli, G. Groppi, E. Tronconi, D.G. Vlachos, Two-dimensional detailed modeling of fuel-rich combustion over catalyst, Chemical Engineering Science, 63 (2008) 2657-2669.

[187] Bär J., Karakaya C., Deutschmann O., Catalytic ignition of light hydrocarbons over Rh/Al2O3 studied in a stagnation point flow reactor, Proceedings of the Combustion Institute, In press. (2012).

[188] I. Tavazzi, A. Beretta, G. Groppi, P. Forzatti, Development of a molecular kinetic scheme for methane partial oxidation over a Rh/α-Al2O3 catalyst, Journal of Catalysis, 241 (2006) 1-13.

[189] M.J.P. Hopstaken, J.W. Niemantsverdriet, Structure sensitivity in the CO oxidation on rhodium: Effect of adsorbate coverages on oxidation kinetics on Rh(100) and Rh(111), J. Chem. Phys., 113 (2000) 5457-5465.

[190] J.Y. Park, H. Lee, J.R. Renzas, Y.W. Zhang, G.A. Somorjai, Probing hot electron flow generated on Pt nanoparticles with Au/TiO2 Schottky diodes during catalytic CO oxidation, Nano Lett., 8 (2008) 2388-2392.

[191] X.C. Su, P.S. Cremer, Y.R. Shen, G.A. Somorjai, High-pressure CO oxidation on Pt(111) monitored with infrared-visible sum frequency generation (SFG), Journal of the American Chemical Society, 119 (1997) 3994-4000.

[192] J.A. Anderson, CO OXIDATION ON RH/AL2O3 CATALYSTS, J. Chem. Soc.-Faraday Trans., 87 (1991) 3907-3911.

[193] G. Ertl, M. Neumann, K.M. Streit, Chemisorption of CO on the Pt(111) surface, Surface Science, 64 (1977) 393-410.

[194] T. Engel, G. Ertl, Surface residence times and reaction mechanism in the catalytic oxidation of CO on Pd(111), Chemical Physics Letters, 54 (1978) 95-98.

[195] D. Chatterjee, O. Deutschmann, J. Warnatz, Detailed surface reaction mechanism in a three-way catalyst, Faraday Discussions, 119 (2002) 371-384.

[196] G. Jacobs, P.M. Patterson, L. Williams, E. Chenu, D. Sparks, G. Thomas, B.H. Davis, Water-gas shift: In situ spectroscopic studies of noble metal promoted ceria catalysts for CO removal in fuel cell reformers and mechanistic implications, Applied Catalysis A: General, 262 (2004) 177-187.

[197] L.V. Mattos, F.B. Noronha, Hydrogen Production for fuel cell applications by ethanol partial oxidation on Pt/CeO2 catalysts: the effect of the reaction conditions and reaction mechanism, J. Catal., 233 (2005) 453-463.

[198] D.A. Hickman, E.A. Haupfear, L.D. Schmidt, Synthesis gas formation by direct oxidation of methane over Rh monoliths, Catal. Lett., 17 (1993) 223-237.

[199] J. Wei, E. Iglesia, Structural requirements and reaction pathways in methane activation and chemical conversion catalyzed by rhodium, Journal of Catalysis, 225 (2004) 116-127.

[200] T. Bunluesin, H. Cordatos, R.J. Gorte, Study of CO Oxidation Kinetics on Rh/Ceria, Journal of Catalysis, 157 (1995) 222-226.

[201] J. Gustafson, R. Westerström, A. Mikkelsen, X. Torrelles, O. Balmes, N. Bovet, J.N. Andersen, C.J. Baddeley, E. Lundgren, Sensitivity of catalysis to surface structure: The example of CO oxidation on Rh under realistic conditions, Physical Review B, 78 (2008) 045423.

[202] C. Essmann, Untersuchung der Verkokung von Rhodiumkatalysatoren während der Wasserdampfreformierung von Erdgas, in: der Fakultät für Chemie und Biowissenschaften, Karlsruher Institut für Technologie (KIT), Karlsruhe, 2011.

[203] Y. Chen, J. Cheng, P. Hu, H. Wang, Examining the redox and formate mechanisms for water-gas shift reaction on Au/CeO2 using density functional theory, Surface Science, 602 (2008) 2828-2834.

[204] A.A. Gokhale, J.A. Dumesic, M. Mavrikakis, On the Mechanism of Low-Temperature Water Gas Shift Reaction on Copper, Journal of the American Chemical Society, 130 (2008) 1402-1414.

[205] Y. Chen, H. Wang, R. Burch, C. Hardacre, P. Hu, New insight into mechanisms in water-gas-shift reaction on Au/CeO2(111): A density functional theory and kinetic study, Faraday Discussions, 152 (2011) 121-133.

[206] C.A. Cornaglia, J.F. Múnera, E.A. Lombardo, Kinetic study of a novel active and stable catalyst for the water gas shift reaction, Industrial and Engineering Chemistry Research, 50 (2011) 4381-4389.

[207] J. Sun, J. Desjardins, J. Buglass, K. Liu, Noble metal water gas shift catalysis: Kinetics study and reactor design, International Journal of Hydrogen Energy, 30 (2005) 1259-1264.

[208] J. Barbier Jr, D. Duprez, Steam effects in three-way catalysis, Applied Catalysis B: Environmental, 4 (1994) 105-140.

[209] B. Smith R J, M. Loganathan, M.S. Shantha, A review of the water gas shift reaction kinetics, International Journal of Chemical Reactor Engineering, 8 (2010).

[210] D. Mendes, A. Mendes, L.M. Madeira, A. Iulianelli, J.M. Sousa, A. Basile, The water-gas shift reaction: From conventional catalytic systems to Pd-based membrane reactors- A review, Asia-Pacific Journal of Chemical Engineering, 5 (2010) 111-137.

[211] C. Wheeler, A. Jhalani, E.J. Klein, S. Tummala, L.D. Schmidt, The water-gas-shift reaction at short contact times, Journal of Catalysis, 223 (2004) 191-199.

[212] T. Shido, Y. Iwasawa, Reactant-Promoted Reaction Mechanism for Water-Gas Shift Reaction on Rh-Doped CeO2, Journal of Catalysis, 141 (1993) 71-81.

[213] E. Chenu, G. Jacobs, A.C. Crawford, R.A. Keogh, P.M. Patterson, D.E. Sparks, B.H. Davis, Water-gas shift: An examination of Pt promoted MgO and tetragonal and monoclinic ZrO2 by in situ drifts, Applied Catalysis B: Environmental, 59 (2005) 45-56.

[214] D.C. Grenoble, M.M. Estadt, D.F. Ollis, The chemistry and catalysis of the water gas shift reaction. 1. The kinetics over supported metal catalysts, Journal of Catalysis, 67 (1981) 90-102.

[215] S. Hilaire, X. Wang, T. Luo, R.J. Gorte, J. Wagner, A comparative study of water-gas-shift reaction over ceria supported metallic catalysts, Applied Catalysis A: General, 215 (2001) 271-278.

[216] A. Donazzi, A. Beretta, G. Groppi, P. Forzatti, Catalytic partial oxidation of methane over a 4% Rh/α-Al2O3 catalyst Part II: Role of CO2 reforming, Journal of Catalysis, 255 (2008) 259-268.

[217] M. Hartmann, L. Maier, O. Deutschmann, Hydrogen production by catalytic partial oxidation of iso-octane at varying flow rate and fuel/oxygen ratio: From detailed kinetics to reactor behavior, Applied Catalysis A: General, 391 (2011) 144-152.

[218] B.C. Michael, A. Donazzi, L.D. Schmidt, Effects of H2O and CO2 addition in catalytic partial oxidation of methane on Rh, Journal of Catalysis, 265 (2009) 117-129.

[219] L.C. Grabow, A.A. Gokhale, S.T. Evans, J.A. Dumesic, M. Mavrikakis, Mechanism of the Water Gas Shift Reaction on Pt: First Principles, Experiments, and Microkinetic Modeling, J Phys Chem C Nanomater Interfaces, 112 (2008) 4608-4617.

[220] R. Burch, A. Goguet, F.C. Meunier, A critical analysis of the experimental evidence for and against a formate mechanism for high activity water-gas shift catalysts, Applied Catalysis A: General, 409–410 (2011) 3-12.

[221] A.M. Efstathiou, A. Kladi, V.A. Tsipouriari, X.E. Verykios, Reforming of Methane with Carbon Dioxide to Synthesis Gas over Supported Rhodium Catalysts: II. A Steady-State Tracing Analysis: Mechanistic Aspects of the Carbon and Oxygen Reaction Pathways to Form CO, Journal of Catalysis, 158 (1996) 64-75.

[222] C.M. Kalamaras, G.G. Olympiou, A.M. Efstathiou, The water-gas shift reaction on Pt/γ-Al2O3 catalyst: Operando SSITKA-DRIFTS-mass spectroscopy studies, Catalysis Today, 138 (2008) 228-234.

[223] E. Shustorovich, H. Sellers, The UBI-QEP method: A practical theoretical approach to understanding chemistry on transition metal surfaces, Surface Science Reports, 31 (1998) 1-119.

[224] E. Shustorovich, A.V. Zeigarnik, The UBI–QEP treatment of polyatomic molecules without bond-energy partitioning, Surface Science, 527 (2003) 137-148.

[225] C. Galletti, S. Fiorot, S. Specchia, G. Saracco, V. Specchia, Activity of rhodium-based catalysts for CO preferential oxidation in H_2-rich gases, Topics in Catalysis, 45 (2007) 15-19.

[226] N. Rankovic, A. Nicolle, D. Berthout, P. Da Costa, Kinetic modeling study of the oxidation of carbon monoxide-hydrogen mixtures over Pt/Al2O3 and Rh/Al2O3 catalysts, Journal of Physical Chemistry C, 115 (2011) 20225-20236.

[227] R. Otterstätter, Untersuchung der Wassergas-Shift-Reaktion über Ptund Rh-Katalysatoren, in: Institut für Technische Chemie und Polymerchemie, Fakultät für Chemie und Biowissenschaften, Karlsruher Institüt für Technologie, Karlsruhe, 2012, pp. 89.

[228] T. Kaltschmitt, C. Diehm, O. Deutschmann, Catalytic partial oxidation of isooctane to hydrogen on rhodium catalysts: effect of tail-gas recycling, . Industrial & Engineering Chemistry Research, Accepted (2012).

[229] M. Hartmann, Erzeugung von Wasserstoff mittels katalytischer Partialoxidation höherer Kohlenwasserstoffe an Rhodium, in: Fakultät für Chemie und Biowissenschaften, der Universität Karlsruhe (TH), Karlsruhe, 2009.

[230] W.M. Graven, F.J. Long, KINETICS AND MECHANISMS OF THE 2 OPPOSING REACTIONS OF THE EQUILIBRIUM CO + H_2O = CO_2 + H_2^1, Journal of the American Chemical Society, 76 (1954) 2602-2607.

[231] E.T. Hashim, H.N.A. Al-Shorachi, Prediction of Diffusion Coefficients for Binary Gas System, Petroleum Science and Technology, 25 (2007) 983-989.

[232] J. Nakamura, K. Aikawa, K. Sato, T. Uchijima, Role of support in reforming of CH_4 with CO_2 over Rh catalysts, Catal. Lett., 25 (1994) 265-270.

[233] H.Y. Wang, C.T. Au, Carbon dioxide reforming of methane to syngas over SiO2-supported rhodium catalysts, Applied Catalysis A: General, 155 (1997) 239-252.

[234] A. Erdöhelyi, J. Cserényi, E. Papp, F. Solymosi, Catalytic reaction of methane with carbon dioxide over supported palladium, Applied Catalysis A: General, 108 (1994) 205-219.

[235] A. Erdohelyi, J. Cserenyi, F. Solymosi, Activation of CH4 and Its Reaction with CO2 over Supported Rh Catalysts, Journal of Catalysis, 141 (1993) 287-299.

[236] J.R. Rostrupnielsen, J.H.B. Hansen, CO2-Reforming of Methane over Transition Metals, Journal of Catalysis, 144 (1993) 38-49.

[237] M.F. Mark, W.F. Maier, CO2-Reforming of Methane on Supported Rh and Ir Catalysts, Journal of Catalysis, 164 (1996) 122-130.

[238] E. Shustorovich, A.T. Bell, Oxygen-assisted cleavage of O□H, N□H, and C□H bonds on transition metal surfaces: bond-order-conservation-Morse-potential analysis, Surface Science, 268 (1992) 397-405.

[239] Chemical Composition of Natural Gas, in, Union Gas Limited
Ontario, 2012.

[240] A. Demirbaş, Fuel properties of hydrogen, liquefied petroleum gas (LPG), and compressed natural gas (CNG) for transportation, Energy Sources, 24 (2002) 601-610.

[241] B. Silberova, H.J. Venvik, A. Holmen, Production of hydrogen by short contact time partial oxidation and oxidative steam reforming of propane, Catalysis Today, 99 (2005) 69-76.

[242] M. Masi, Experimental analysis on a spark ignition petrol engine fuelled with LPG (liquefied petroleum gas), Energy, 41 (2012) 252-260.

[243] M. Huff, P.M. Torniainen, D.A. Hickman, L.D. Schmidt, Partial Oxidation of CH4, C2H6, and C3H8 on Monoliths at Short Contact Times, in: H.E. Curry-Hyde, R.F. Howe (Eds.) Studies in Surface Science and Catalysis, Elsevier, 1994, pp. 315-320.

[244] A. Beretta, P. Forzatti, Partial oxidation of light paraffins to synthesis gas in short contact-time reactors, Chemical Engineering Journal, 99 (2004) 219-226.

[245] B.T. Schädel, M. Duisberg, O. Deutschmann, Steam reforming of methane, ethane, propane, butane and natural gas over a rhodium-based catalyst, Catal. Today, 142 (2009) 42-51.

[246] B. Silberova, H.J. Venvik, J.C. Walmsley, A. Holmen, Small-scale hydrogen production from propane, Catalysis Today, 100 (2005) 457-462.

Acknowledgements

First and foremost, I am gratefully thankful Prof. Olaf Deutschmann, for giving me the opportunity to work in his research group. He gave me the freedom to explore the things that truly amaze me and to do this according to my own way of thinking, and he has always been there to point me in the right direction. His support as well as his encouragement made me believe in continuing my career in the scientific field.

I would also like to thank Dr. Lubow Maier for fruitful discussions and her help with the part about the development of the mechanism.

Furthermore, I want to thank Julian N. Bär for performing the catalytic ignition experiments. I wish him all the best for his PhD.

I would like to especially thank Dr. Steffen Tischer for his support in using the DETCHEM tool. Moreover, I would like to thank him for his friendship and moral support; he has been more than a colleague to me.

I am deeply grateful to Professor Robert J. Kee for his help during the reactor development and fruitful discussions on introducing me to the stagnation-flow reactor concept. I would like to thank him and his research group at Colorado Fuel Cell Center (Colorado School of Mines) for their hospitality; I spent a wonderful 3 weeks there in June 2009. A special thanks goes out to Nicholas McGuire and Prof. Neal P. Sullivan for their collaboration.

Additionally, I would like to thank Sven Lichtenberg, Alexander Jacks, and Jörg Finterle for their help in building up the stagnation-flow reactor. And I also thank Hans Weickenmeier for his technical support and Kathrin Schäfer and Jasmin Heck for the CO oxidation measurements. Furthermore, I would like to thank Robin Otterstätter for the collaboration and for sharing his experimental data with me. I also owe my thanks to Dr. Boris Reznik for the LM and SEM measurements and Hüseyin Karadeniz for his support in using the DETCHEM^{STAG} software.

I owe many thanks to Yvonne Dedecek, Ursula Schwald, Andrea Rösel, and Dr. Matthias Hettel for their constant help and affection throughout my stay in Germany. I appreciate the help of Dr. Steffen Tischer and Dr. Lubow Maier in proof-reading my thesis and of Rebecca Klinkig in correcting the English in this thesis.

Also, I thank my friends Willi Boll, Thomas Siegfried, Ingo F.Naue, Michael Kempf and all the group members who made my life in Karlsruhe enjoyable. Especially, thanks to my dear friend Claudia Essman who has always been supportive and encouraging.

My dear friend Deniz Gökdeniz Özdemir – I would not have succeeded without her support.

Lastly, I would like to thank my parents, who always supported me and encouraged me to follow my dreams. And especially, thanks to my dear brother Kenan – he was the hero of this story by taking on the whole responsibility for the family when I was not there.

CURRICULUM VITAE

CANAN KARAKAYA

PERSONAL

Date of Birth: 01.04.1981
Birth Place: Ardahan/Turkey
Marital Status: Single

EDUCATION

Master of Science: Kocaeli University, Chemical Engineering Dept., TURKEY, September 2005-July 2008
Thesis: Investigation of Methane Catalytic Activity and Modeling of Kinetic Constants on $La_{(1-x)}AgxB_{(1-y)}B'yO_{3\pm\delta}$ Type Perovskite Catalysts

Bachelor of Science: Kocaeli University, Chemical Engineering Dept., TURKEY, June 2003

High School: Neset Yalcin High School, TURKEY, 1999

JOB EXPERIENCES

Karlsruhe Institute of Technology, GERMANY
Research assistant since 27/10/2008

Colorado School of Mines; USA
Visiting researcher in Colorado Fuel Center 10/06/2009 – 26/06/2009

Kocaeli University, TURKEY
Research Assistant in Chemical Engineering Dept. 12/2005-07/2008
Classes Assisted: Heat Transfer, Chemical Kinetics and Reaction Engineering, Numeric Analyze (Matlab)

Sandoz Pharmaceuticals Company, TURKEY
Analyst, 09/2003-10/2005
R&D Department, Analytical Method Development Laboratory

PUBLICATIONS

1. A. Celepci, C. Karakaya, N. Machin, Catalytic Combustion of Methane on La, Ce, Co Based Mixed Oxides, Energy &Fuels, 22 (4), 2166–2171, 2008.

2. Julian N. Bär, Canan Karakaya, Olaf Deutschmann, Ignition and Extinction Studies of Light hydrocarbons, Hydrogen and Carbonmonoxide on Rhodium with a Stagnation Point Flow Reactor, Proceedings of the Combustion Institute (34th), 2012, in press, DOI: 10.1016/j.proci.2012.06.115.

3. Canan Karakaya, Olaf Deutschmann, A Simple Method for CO Chemisorption Studies under Continuous-Flow: Adsorption and Desorption Behavior of Pt/Al_2O_3 Catalysts, Applied Catalysis A, in press, DOI: 10.1016/j.apcata.2012.08.022.

4. Canan Karakaya, Olaf Deutschmann, Kinetics of Hydrogen Oxidation on Rh/Al_2O_3 Catalysts Studied in a Stagnation-flow Reactor, Chemical Engineering Science, accepted.

5. Canan Karakaya, Robin Otterstätter, Lubow Maier, Olaf Deutschmann, Kinetics of the water-gas shift reaction on Rh/Al_2O_3 catalysts, submitted to Journal of Catalysis.

6. Canan Karakaya, Lubow Maier, Olaf Deutschmann, Development of a unified surface reaction mechanism for oxidation and reforming of CH_4 on Rh/Al_2O_3 catalysts, in preparation.

7. Canan Karakaya, Lubow Maier, Olaf Deutschmann, Oxidation and reforming of C_3H_8 on Rh/Al_2O_3 catalysts , in preparation

8. Hüseyin Karadeniz, Canan Karakaya, Olaf Deutschmann, Numerical modeling of a stagnation-flow reactor: Evaluation of CO oxidation kinetics, in preparation.

Oral Presentations

1. Karakaya C., Maier L., Deutschmann O., (KIT) and McGuire N.E., Sullivan N.P., Kee R.J., (CSM), Oxidation and reforming of light hydrocarbons over Rh/Al_2O_3 catalysts: a fundamental study using a stagnation-flow reactor (8th ECCE), Berlin 25-29 September, 2012

2. Karakaya C., Maier L., Deutschmann O., (KIT) and McGuire N.E., Sullivan N.P., Kee R.J., (CSM), Oxidation and reforming of light hydrocarbons over Rh/Al_2O_3 catalyst studied in a stagnation-flow reactor, 15th International Congress on Catalysis (15th ICC), Munich, 1-6 July,2012

3. Karakaya C., Maier L., Deutschmann O., (KIT) and McGuire N.E., Sullivan N.P., Kee R.J., (CSM), Development of a unified surface reaction mechanism on Rh surfaces for reforming of C1-C3 species, 22. International Symposium on Chemical Reaction Engineering (22nd ISCRE), Maastricht , September 2-5, 2012

Poster Presentations (selected):

1. Karakaya C., Deutschmann O., Catalytic Oxidation of CO over Rh/Al_2O_3 and Ni/Al_2O_3 Catalysts in a Stagnation-Flow Reactor, *poster winner*, 44. Jahrestreffen Deutscher Katalytiker, Weimar/Germany, 16-18 March, 2011.

2. Karakaya C., Maier L., Deutschmann O., (KIT) and McGuire N.E., Sullivan N.P., Kee R.J., (CSM)., Oxidation and reforming of light hydrocarbons over Rh/Al_2O_3 catalysts: A fundamental study using a stagnation-flow reactor, EuropaCat X, Glasgow / Scotland, 28 August - 2 September, 2011.

3. Karakaya C., Deutschmann O., A simple method to measure the active catalytic surface area: CO ChemisorptionsTPD studies, International Symposium on Modeling of Exhaust-Gas After-Treatment (MODEGAT II), Bad Herrenalb / Germany 19-20 September, 2011.

4. Karakaya C., Maier L., Deutschmann O., (KIT) and McGuire N.E., Sullivan N.P., Kee R.J., (CSM), Oxidation and reforming of light hydrocarbons over Rh/Al_2O_3 catalyst by using a stagnation-flow reactor, 45. Jahrestreffen Deutscher Katalytiker, Weimar / Germany, 14-16 March, 2012.

5. Bär J.N., Karakaya C., Deutschmann O., Catalytic ignition of light hydrocarbons over Rh/Al_2O_3 studied in a stagnation point flow reactor, 45. Jahrestreffen Deutscher Katalytiker, Weimar / Germany, 14-16 March, 2012.